

ISSN 2074-272X

**науково-практичний  
журнал**

**2023/3**



# **ЕІЕ** **Електротехніка і** **ЕІЕ** **електромеханіка**

**Electrical Engineering**

**& Electromechanics**

**Електричні машини та апарати**  
**Електротехнічні комплекси та системи**  
**Промислова електроніка**  
**Інженерна електрофізика.**

**Техніка сильних електричних та магнітних полів**  
**Електричні станції, мережі і системи**

**Журнал включено до найвищої категорії «А»**  
**Переліку фахових видань України**

**З 2021 р. журнал індексується у Scopus**

**З 2015 р. журнал індексується**  
**у Web of Science Core Collection:**  
**Emerging Sources Citation Index**



# Electrical Engineering & Electromechanics

Scientific Journal was founded in 2002

Founder – National Technical University «Kharkiv Polytechnic Institute» (Kharkiv, Ukraine)

## EDITORIAL BOARD

<b>Sokol Ye.I.</b>	<b>Editor-in-Chief</b> , Professor, Corresponding member of NAS of Ukraine, Rector of National Technical University «Kharkiv Polytechnic Institute» (NTU «KhPI»), Ukraine
<b>Korytchenko K.V.</b>	<b>Deputy Editor</b> , Professor, NTU «KhPI», Ukraine
<b>Rozov V.Yu.</b>	<b>Deputy Editor</b> , Professor, Corresponding member of NAS of Ukraine, A. Pidhorneyi Institute of Mechanical Engineering Problems of NAS of Ukraine, Kharkiv, Ukraine
<b>Bolyukh V.F.</b>	<b>Deputy Editor</b> , Professor, NTU «KhPI», Ukraine
<b>Abu-Siada A.</b>	Professor, Curtin University, Perth, Australia
<b>Aman M.M.</b>	Professor, NED University of Engineering & Technology, Karachi, Pakistan
<b>Baltag O.</b>	Professor, Grigore T. Popa University Medicine and Pharmacy, Romania
<b>Baranov M.I.</b>	Professor, Research and Design Institute «Molniya» of NTU «KhPI», Ukraine
<b>Batygin Yu.V.</b>	Professor, Kharkiv National Automobile and Highway University, Ukraine
<b>Bíró O.</b>	Professor, Institute for Fundamentals and Theory in Electrical Engineering, Graz, Austria
<b>Bouktir T.</b>	Professor, Ferhat Abbas University, Setif 1, Algeria
<b>Buriakovskiy S.G.</b>	Professor, NTU «KhPI», Ukraine
<b>Butkevych O.F.</b>	Professor, Institute of Electrodynamics of NAS of Ukraine (IED of NASU), Kyiv, Ukraine
<b>Colak I.</b>	Professor, Nisantasi University, Istanbul, Turkey
<b>Cruz S.</b>	Professor, University of Coimbra, Portugal
<b>Doležel I.</b>	Professor, University of West Bohemia, Pilsen, Czech Republic
<b>Féliachi M.</b>	Professor, Technological Institute of Saint-Nazaire, University of Nantes, France
<b>Grinchenko V.S.</b>	PhD, A. Pidhorneyi Institute of Mechanical Engineering Problems of NAS of Ukraine, Kharkiv, Ukraine
<b>Gurrero J.M.</b>	Professor, Aalborg University, Denmark
<b>Gurevich V.I.</b>	PhD, Honorable Professor, Central Electrical Laboratory of Israel Electric Corporation, Haifa, Israel
<b>Hajjar A.A.</b>	Professor, Tishreen University, Latakia, Syrian Arab Republic
<b>Ida N.</b>	Professor, The University of Akron, Ohio, USA
<b>Izykowski J.</b>	Professor, Wroclaw University of Science and Technology, Poland
<b>Kildishev A.V.</b>	Associate Research Professor, Purdue University, USA
<b>Klepikov V.B.</b>	Professor, NTU «KhPI», Ukraine
<b>Korzeniewska E.</b>	Professor, Lodz University of Technology, Poland
<b>Ktena A.</b>	Professor, National and Kapodistrian University of Athens, Greece
<b>Kuznetsov B.I.</b>	Professor, A. Pidhorneyi Institute of Mechanical Engineering Problems of NAS of Ukraine, Kharkiv, Ukraine
<b>Kyrylenko O.V.</b>	Professor, Academician of NAS of Ukraine, IED of NASU, Kyiv, Ukraine
<b>Levin B.M.</b>	Professor, Holon Institute of Technology, Tel Aviv-Yafo, Israel
<b>Malik O.P.</b>	Professor, University Of Calgary, Canada
<b>Maslov V.I.</b>	Professor, National Science Center «Kharkiv Institute of Physics and Technology», Ukraine
<b>Mi Zou</b>	PhD, Chongqing University of Posts and Telecommunications, China
<b>Mikhaylov V.M.</b>	Professor, NTU «KhPI», Ukraine
<b>Miljavec D.</b>	Professor, University of Ljubljana, Slovenia
<b>Milykh V.I.</b>	Professor, NTU «KhPI», Ukraine
<b>Nacke B.</b>	Professor, Gottfried Wilhelm Leibniz Universität, Institute of Electrotechnology, Hannover, Germany
<b>Petrushin V.S.</b>	Professor, Odessa National Polytechnic University, Ukraine
<b>Podoltsev A.D.</b>	Professor, IED of NASU, Kyiv, Ukraine
<b>Reutskiy S.Yu.</b>	PhD, A. Pidhorneyi Institute of Mechanical Engineering Problems of NAS of Ukraine, Kharkiv, Ukraine
<b>Rezinkin O.L.</b>	Professor, NTU «KhPI», Ukraine
<b>Rezinkina M.M.</b>	Professor, NTU «KhPI», Ukraine
<b>Shcherbak Ya.V.</b>	Professor, NTU «KhPI», Ukraine
<b>Sikorski W.</b>	Professor, Poznan University of Technology, Poland
<b>Suemitsu W.</b>	Professor, Universidade Federal Do Rio de Janeiro, Brazil
<b>Trichet D.</b>	Professor, Institut de Recherche en Energie Electrique de Nantes Atlantique, France
<b>Vaskovskiy Yu.M.</b>	Professor, National Technical University of Ukraine «Igor Sikorsky Kyiv Polytechnic Institute», Kyiv, Ukraine
<b>Vazquez N.</b>	Professor, Tecnológico Nacional de México en Celaya, Mexico
<b>Vinnikov D.</b>	Professor, Tallinn University of Technology, Estonia
<b>Yagup V.G.</b>	Professor, O.M. Beketov National University of Urban Economy in Kharkiv, Ukraine
<b>Yatchev I.</b>	Professor, Technical University of Sofia, Bulgaria
<b>Zagirnyak M.V.</b>	Professor, Member of NAES of Ukraine, Kremenchuk M.Ostrohradskiy National University, Ukraine
<b>Zgraja J.</b>	Professor, Lodz University of Technology, Poland
<b>Grechko O.M.</b>	<b>Executive Managing Editor</b> , PhD, NTU «KhPI», Ukraine

From no. 1 2021 Journal «Electrical Engineering & Electromechanics» is indexing in **Scopus** and from no. 1 2015 Journal is indexing in **Web of Science Core Collection: Emerging Sources Citation Index (ESCI)**.

Also included in DOAJ (Directory of Open Access Journals), in EBSCO's database, in ProQuest's databases – Advanced Technologies & Aerospace Database and Materials Science & Engineering Database, in Gale/Cengage Learning databases.

### Editorial office address:

National Technical University «Kharkiv Polytechnic Institute», Kyrpychova Str., 2, Kharkiv, 61002, Ukraine

phones: +380 57 7076281, +380 67 3594696, e-mail: a.m.grechko@gmail.com (**Grechko O.M.**)

ISSN (print) 2074-272X

ISSN (online) 2309-3404

© National Technical University «Kharkiv Polytechnic Institute», 2023

Printed 05 May 2023. Format 60 × 90 ½. Paper – offset. Laser printing. Edition 200 copies.

Printed by Printing house «Madrid Ltd» (18, Gudanova Str., Kharkiv, 61024, Ukraine)



**Table of Contents**

***Electrical Machines and Apparatus***

**Abu Ibaid O.Z.I., Belhamdi S., Abid M., Chakroune S., Mouassa S., Al-Sagar Z.S.** Wavelet packet analysis for rotor bar breakage in an inverter induction motor ..... 3

**Milykh V.I., Shaida V.P., Yurieva O.Yu.** Analysis of the thermal state of the electromagnetic mill inductor with oil cooling in stationary operation modes ..... 12

**Sakhara S., Brahimi M., Nacib L., Layadi T.M.** Application of a wavelet neural network approach to detect stator winding short circuits in asynchronous machines..... 21

***Electrotechnical Complexes and Systems***

**Aib A., Khodja D.E., Chakroune S.** Field programmable gate array hardware in the loop validation of fuzzy direct torque control for induction machine drive ..... 28

**Fan J., Lee Y.** Sensorless control of switched reluctance motor based on a simple flux linkage model ..... 36

***Industrial Electronics***

**Boukadoum A., Bouguerne A., Bahi T.** Direct power control using space vector modulation strategy control for wind energy conversion system using three-phase matrix converter..... 40

**Yagup V.G., Yagup K.V.** Acceleration of exit to steady-state mode when modeling semiconductor converters ..... 47

***Engineering Electrophysics. High Electric and Magnetic Fields Engineering***

**Brzhezitsky V.O., Haran Y.O., Trotsenko Y.O., Protsenko O.R., Derzhuk A.O., Dixit M.M.** Ultimate effect of non-identity of resistive elements of high-voltage arm on frequency characteristics of voltage divider (analytical research) ..... 52

**Khrysto O.I.** Energy characteristics for nanosecond current interrupter of semiconductor-magnetic pulse generator's terminal stage..... 59

***Power Stations, Grids and Systems***

**Ayat Y., Badoud A.E., Mekhilef S., Gassab S.** Energy management based on a fuzzy controller of a photovoltaic/fuel cell/Li-ion battery/supercapacitor for unpredictable, fluctuating, high-dynamic three-phase AC load ..... 66

**Kadri M., Hamouda A., Sayah S.** Efficient method for transformer models implementation in distribution load flow matrix..... 76

**Srinivasan G., Mahesh Kumar Reddy V., Venkatesh P., Parimalasundar E.** Reactive power optimization in distribution systems considering load levels for economic benefit maximization..... 83

O.Z.I. Abu Ibaid, S. Belhamdi, M. Abid, S. Chakroune, S. Mouassa, Z.S. Al-Sagar

**Wavelet packet analysis for rotor bar breakage in an inverter induction motor**

**Introduction.** In various industrial processes, squirrel cage induction motors are widely employed. These motors can be used in harsh situations, such as non-ventilated spaces, due to their high strength and longevity. These machines are subject to malfunctions such as short circuits and broken bars. Indeed, for the diagnosis several techniques are offered and used. **Novelty** of the proposed work provides the use of wavelet analysis technology in a continuous and discrete system to detect faults affecting the rotating part of an induction motor fed by a three-phase inverter. **Purpose.** This paper aims to present a novel technique for diagnosing broken rotor bars in the low-load, stationary induction machine proposed. The technique is used to address the problem of using the traditional Techniques like Fourier Transforms signal processing algorithm by analyzing the stator current envelope. The suggested method is based on the use of discrete wavelet transform and continuous wavelet transform. **Methods.** A waveform can be monitored at any frequency of interest using the suggested discrete wavelet transform and continuous wavelet transform. To identify the rotor broken bar fault, stator current frequency spectrum is analyzed and then examined. Based on a suitable index, the algorithm separates the healthy motor from the defective one, with 1, 2 and 3 broken bars at no-load. **Results.** In comparison to the healthy conditions, the recommended index significantly raises under the broken bars conditions. It can identify the problematic conditions with clarity. The possibility of detecting potential faults has been demonstrated (broken bars), using discrete wavelet transform and continuous wavelet transform. The diagnostic method is adaptable to temporary situations brought on by alterations in load and speed. Performance and efficacy of the suggested diagnostic method are demonstrated through simulation in Simulink® MATLAB environment. References 31, figures 11.

**Key words:** squirrel cage induction motors, rotor broken bar, continuous wavelet transform, discrete wavelet transform.

**Вступ.** У різних промислових процесах широко використовуються асинхронні двигуни із короткозамкненим ротором. Ці двигуни можуть використовуватися в суворих умовах, наприклад, в приміщеннях, що не вентилюються, завдяки їх високій міцності і довговічності. Ці машини схильні до несправностей, таких як коротке замикання і зламані стрижні. Зрозуміло, що для діагностики пропонується та використовується кілька методик. **Новизна** запропонованої роботи полягає у використанні технології вейвлет-аналізу в безперервній і дискретній системі для виявлення несправностей, що впливають на частину асинхронного двигуна, що обертається, що живиться від трифазного інвертора. **Мета.** У цій статті представлена нова методика діагностики зламаних стрижнів ротора в малонавантаженої стаціонарній асинхронній машині. Цей метод використовується для вирішення проблеми використання традиційних методів, таких як алгоритм обробки сигналів перетворення Фур'є, шляхом аналізу огибаючої струму статора. Пропонуваний метод заснований на використанні дискретного вейвлет-перетворення та безперервного вейвлет-перетворення. **Методи.** Форма сигналу може відстежуватися на будь-якій частоті, що цікавить, з використанням запропонованого дискретного вейвлет-перетворення і безперервного вейвлет-перетворення. Для виявлення несправності обриву стрижня ротора частотний спектр статора аналізується, а потім досліджується. На основі відповідного індексу алгоритм відокремлює справний двигун від несправного з 1, 2 і 3 зламаними стрижнями на холостому ході. **Результати.** Порівняно із нормальними умовами рекомендований показник значно підвищується за умов зламаних стрижнів. Він може чітко визначити проблемні умови. Було продемонстровано можливість виявлення потенційних несправностей (зламани стрижні) з використанням дискретного вейвлет-перетворення та безперервного вейвлет-перетворення. Метод діагностики адаптується до тимчасових ситуацій, викликаних змінами навантаження та швидкості. Працездатність та ефективність запропонованого методу діагностики продемонстровано за допомогою моделювання у середовищі Simulink® MATLAB. Бібл. 31, рис. 11.

**Ключові слова:** асинхронні двигуни з короткозамкненим ротором, зламаний стрижень ротора, безперервне вейвлет-перетворення, дискретне вейвлет-перетворення.

**Introduction.** Currently, induction motors are very popular in the industry and is of great interest to scientists in the variable speed drive. Since of their robust construction, high power-to-weight ratio, high reliability and easy design, squirrel cage induction motors are used in most industries [1]. They are, however, susceptible to failures, which may be caused by the machine itself or by operating conditions.

They found flaws in the converter and inverter of an induction motor that was functioning. In order to apply variable speed applications to the induction motor, an inverter is necessary [2].

According to failure studies, induction motor component failure is typical:

- Stator related (38 %);
- Rotor related (10 %);
- Bearing related (40 %); and others (12 %) [3].

The induction motor could be saved from catastrophic harm if the defect is detected quickly.

Even early detection of an issue could cut down on the amount of time necessary for maintenance. The most prevalent rotor defects are located at the level of the rotor, where bar breakage is the most common rotor problem. It

might be at the notch or at the end of the rotor ring that connects it to the rotor ring [4].

Damage to the machine may result from the fractured rotor bar's fault, which increases fluctuation and reduces the amplitude of the torque. As a result, additional mechanical vibrations and fluctuation may be produced. Ultimately, the increased number of damaged bars makes their effect more obvious [5]. To avoid such issues, the technique of fault diagnosis and identification has become a crucial step in protecting this sort of electrical machines. The sorts of faults often relate to diagnostic techniques [6-9].

In recent years, many researchers have been drawn to motor current signature analysis because of its benefits. Current spectral analysis as it has been done in [10].

The benefit of signal processing techniques such as Fourier Fast Transformation (FFT) Wavelet theory is that it provides a coherent framework for a variety of approaches developed for distinct signal processing applications [11, 12].

Over the past 15 years, there has been a significant amount of research on the development of different steady-state condition monitoring approaches, most of which are based on the FFT.

This theory is distinguished from others in that it is faster in signal analysis, which provides ease in dealing and saves time. Therefore, it was briefly discussed due to its value in scientific research and the renaissance of industrial maintenance [13].

The wavelet transform (WT) is a signal analysis method for time-varying or non-stationary signals that uses a description of spectral decomposition using the scaling idea for fault detection. This approach works well for both stationary and non-stationary signal processing [14].

In order to improve the broken rotor bar diagnosis in induction motors under low load, the researcher developed [15], which combines the Hilbert transform with the neural network operation. The stator current envelope is extracted using the Hilbert transform. After then, FFT is used to process this signal. The fault frequency must be extracted. Under various stress circumstances, this approach is used to count the number of broken rotor bars.

The study of flaws in another approach is employed for broken rotor bars detection in [16] utilizing a lower sampling rate and fewer samples. To address this issue, a novel method based on the pitch synchronous WT at a reduced sample rate is used.

While [17] took a different approach, he did think about diagnostic strategies utilizing electrical signal spectral analysis. These techniques can be classified into two categories: internal diagnosis using a model of the motor based on its parameters, and external diagnosis utilizing external signals, which does not require knowledge of motor properties.

Additionally, [18] had advanced a broken rotor bar fault detection using the power of the sidebands in his investigation of flaws. When the motor is linked directly to the supply voltage, this method is applied to the line current and instantaneous power of one stator phase.

The degree of the defect (such as partial or multiple broken rotor bars), motor loading, the impacts of the starting rotor position, supply imbalance, and the variations in the 3 phase currents are not examined in these early research. Furthermore, the addition of an inverter to an induction motor represents a variety of technology that was not examined in the investigations. We were obviously focused on how crucial the inverter was for using the induction motor with variable speed applications.

**The goal of the paper** is to use Wavelet Packet Transform on current window frame samples from an induction motor to diagnose and categorize broken rotor bars using Discrete Wavelet Transforms (DWT) and Continuous Wavelet Transform (CWT).

#### Basic calculation relationships and assumptions.

Figure 1 shows the diagram of the impeller failure circuit of the induction machine, with equivalent resistance, in the case of broken bars [19].

According to the reference frame (d-q) fixed to the rotor [19, 20], the model for a three-phase induction motor is:

$$[V] = [R] \cdot [I] + \frac{d}{dt} [[L] \cdot [I]], \quad (1)$$

where:

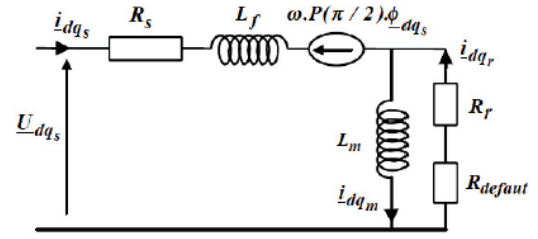


Fig. 1. Broken rotor bars mode

$$\begin{bmatrix} L_{sc}I_2 & -\frac{N_r}{2}M_{sr}I_2 & \vdots & 2 \\ -\frac{3}{2}M_{sr}I_2 & I_{rdq} & \vdots & 0 \\ \dots & \dots & \dots & \dots \\ 0 & 0 & 0 & L_e \end{bmatrix} \frac{d}{dt} \begin{bmatrix} i_{dqs} \\ i_{dqr} \\ \dots \\ i_e \end{bmatrix} = \begin{bmatrix} V_{dqs} \\ V_{dqr} \\ \dots \\ V_e \end{bmatrix} \quad (1)$$

$$\begin{bmatrix} R_s I_2 + \omega_r L_{sc} J_2 & -\frac{N_r}{2} \omega_r M_{sr} J_2 & \vdots & 0 \\ 0 & R_{rdq} J_2 & \vdots & 0 \\ \dots & \dots & \dots & \dots \\ 0 & 0 & \vdots & R_e \end{bmatrix} \begin{bmatrix} i_{dqs} \\ i_{dqr} \\ \dots \\ i_e \end{bmatrix}; \quad (2)$$

$$L_{rdq} = L_{rp} - M_{rr} + \frac{2L_e}{N_r} + 2L_e(1 - \cos(a)); \quad (2)$$

$$R_{rdq} = 2 \cdot \frac{R_e}{N_r} + 2R_b(1 - \cos(a)); \quad (3)$$

$$I_2 = \begin{bmatrix} 1 & 0 \\ 0 & 1 \end{bmatrix}; \quad J_2 = \begin{bmatrix} 0 & -1 \\ 1 & 0 \end{bmatrix}; \quad [R_{rdq}] = \begin{bmatrix} R_{rdd} & R_{rdq} \\ R_{rqd} & R_{rqq} \end{bmatrix},$$

where the 4 terms of this matrix are:

$$R_{rdd} = 2R_b \cdot (1 - \cos(a)) + 2 \cdot \frac{R_e}{N_r} + \frac{2}{N_r} \cdot (1 - \cos(a)) \times \sum_k R_{bfk} (1 - \cos(2k-1)a);$$

$$R_{rqq} = 2R_b \cdot (1 - \cos(a)) + 2 \cdot \frac{R_e}{N_r} + \frac{2}{N_r} \cdot (1 - \cos(a)) \times \sum_k R_{bfk} (1 + \cos(2k-1)a);$$

$$R_{rdq} = -\frac{2}{N_r} \cdot (1 - \cos(a)) \sum_k R_{bfk} \cdot \sin(2k-1)a;$$

$$R_{rqd} = -\frac{2}{N_r} \cdot (1 - \cos(a)) \sum_k R_{bfk} \cdot \sin(2k-1)a.$$

Electromagnetic couples are expressed as:

$$C_e = \frac{3}{2} \cdot p \cdot N_r \cdot M_{sr} \cdot (I_{ds} \cdot I_{qr} - I_{qs} \cdot I_{dr}). \quad (4)$$

**Signal processing methods.** In order to detect problems and overloads in electric devices, especially those used to generate energy and drive high-capacity motors. Advances in microelectronics and signal processing are accelerating the development of contemporary diagnostic technologies [21]. Because temporal patterns don't convey much information, we must rely on signal processing techniques [22]. Spectral analysis has long been used to detect faults in electrical machines, such as asynchronous machine rotor bar breakage, bearing degeneration, eccentricity, and winding short circuits. We'll go over some cutting-edge techniques like FFT and WT briefly in [23].

**Wavelet Transform** is a sophisticated approach for improving stator current data analysis in the transform.

**Continuous Wavelet Transform.** It's common to want to distinguish between lower frequencies bands than DWT permits.

Using the CWT, this is conceivable [24]. The signal's CWT is expressed as follows:

$$CWT(a,b) = \frac{1}{\sqrt{a}} \int_{-\infty}^{+\infty} x(t) \varphi^* \left( \frac{t-b}{a} \right) dt, \quad (5)$$

where  $\varphi(t)$  is the mother wavelet, which represents a disputed function in the time and frequency domains;  $\varphi^*(t)$  is the mother wavelet's complex conjugates, an is the scale value;  $b$  is the translation value. In a more compact form, the normalized wavelet function is:

$$\varphi(a,b) = \frac{1}{\sqrt{a}} \varphi^* \left( \frac{t-b}{a} \right). \quad (6)$$

The integral equation is rewritten as:

$$CWT(a,b) = \int_{-\infty}^{+\infty} x(t) \varphi_{a,b}^*(t) dt. \quad (7)$$

**Discrete Wavelet Transforms.** The wavelet analysis (WT) is a sophisticated approach for improving stator current data analysis in the transitional or stable states [25].

Because of the DWT's automatic filtering, the tool offers a lot of flexibility for analyzing the transient evolution of several different frequency components in the same signal at the same time. The computational needs are low as compared to other tools. Furthermore, the DWT is included in most commercial software packages. As a result, no complex or specific algorithm is necessary [3].

Without data loss or redundancy, this technique provides an approximation coefficient containing low frequencies information and a detail coefficient carrying high frequencies information of the original signal at each level [26].

In other words, a signal's Fourier analysis is the sum of several sinusoidal functions, but a signal's WT is the sum of multiple functions that are displaced and scaled replicas of the main function [27]. The technique can be repeated on multiple levels, resulting in the tree structure depicted in Fig. 2 [10].

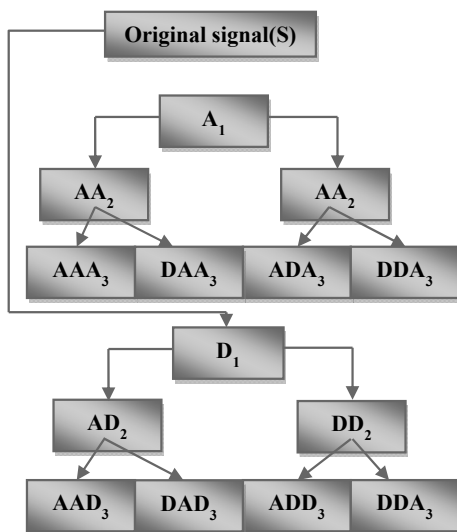


Fig. 2. Decomposition of the signal  $S$  in wavelet packet

DWT decomposes a sampled signal  $S = (S1, S2, \dots, S_n)$  into numerous wavelet signals an approximation signal  $a_n$ , and  $n$  detail signals  $d_j$  ( $j \in [1, n]$ ) [16].

Each frequency band's energy eigenvalue is defined as:

$$E_j = \sum_{k=1}^{k=n} [D_{j,k}(n)]^2; \quad (8)$$

where  $j = 1, 2, 2^{n+1}$ ;  $n$  denotes the discrete wavelet decomposition time;  $D_i$  denotes the amplitude of the wavelet coefficient of the signal in the associated frequency band in each discrete point as shown in Fig. 3 [28].

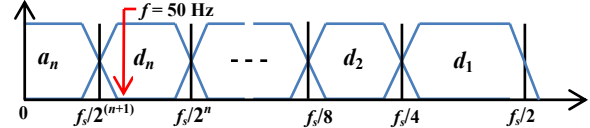


Fig. 3. Filtering process performed by the DWT

FFT is a prominent approach for fault identification in asynchronous devices. It excels in applications requiring great power or steady torque.

The FFT analysis of the bearing fault component will reveal all of the fault's features, including frequency and magnitude responses.

Its purpose is to show how harmonic amplitude grows over time, which is a sign that validates a number of crucial truths [29].

FFT is a technique for decomposing a set of detailed signal spectrum values from one domain to another. Each stage of the procedure consists of a signal spectrum that may be processed with a limited quantity of data to determine the dataset's variation [2 – 22].

The FFT technique can detect flaws in induction motors using this fluctuation. As a result, in signal analysis, the procedure will be faster than DWT [30].

The FFT data can be analyzed as [31]:

$$x(t) = \int_{-\infty}^{+\infty} x(t) \cdot e^{-j \cdot 2 \cdot \pi \cdot f \cdot t} dt. \quad (9)$$

The assessment of a signal is a known interval, which necessitates the selection of a weighting window (Blackmann window, Hanning window, Hamming window, etc.) as well as the window size, which influences the resolution. The frequency accuracy is, in fact, proportional to the sampling frequency and the number of samples  $N$ :

$$\Delta f = f_s / N. \quad (10)$$

**Simulation results and discussion.** We can study the evolution of time elements such as stator currents, torque and speed when the rotor cage shows no failure; starting takes place off-load at nominal voltage with a power supply provided by a three-phase inverter as shown in Fig. 4. The simulation is run over a period of 5 s, with a broken bar occurring at the moment  $t = 2$  s and the machine being exposed to a load torque of 3.5 N·m at the instant  $t = 0.6$  s. Figure 5 presents the simulation results of the model induction motor, squirrel cage induction machine parameters are shown in Table 1.

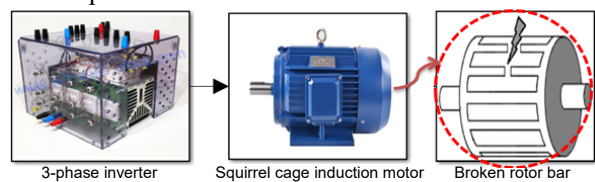


Fig. 4. Simulink block of the induction motor with rotor fault

Table 1

Squirrel cage induction machine parameters	
Parameter	Value
Stator resistance $R_s, \Omega$	7.58
Rotor resistance $R_r, \Omega$	6.3
Number of turns per stator phase, $N_s$	160
Inertia $J, \text{kg}\cdot\text{m}^2$	0.0054
Resistance of a rotor bar $R_b, \text{m}\Omega$	0.15
Leakage inductance of end ring $L_e, \mu\text{H}$	0.1
Length of the rotor $L, \text{mm}$	65
Mutual inductance $L_{1s}, \text{H}$	0.0265
Stator frequency, Hz	50
Number of rotor bars $N_r$	16
Poles number $p$	2
Resistance of end ring segment $R_e, \text{m}\Omega$	0.15
Rotor bar inductance $L_b, \mu\text{H}$	0.1
Air-gap mean diameter $E, \text{mm}$	25
Output power $P, \text{kW}$	1.1

The induction motor was tested under loading conditions first with a healthy rotor, then with 2 broken rotor bars. Every stator current displayed in the study is given in the frequency domain.

The evolution of phase a stator current, electromagnetic torque and phase A current spectrum are illustrated in Fig. 5–7.

We observe from Fig. 5 that the constant current, the electromagnetic torque and the rotational speed that their evolution is constant and also in an excellent and stable condition, so that the speed of the curve increases to reach the ceiling of its peak to settle as a smooth stable plateau.

We notice when 2 adjacent rods are broken, as we note in Fig. 6 in our work, that the speed of rotation decreases gradually, while the ripples also increase more for the constant current in its cover is proportional to the number of broken rods. In a direct relationship, the electromagnetic torque increases with the ripples.

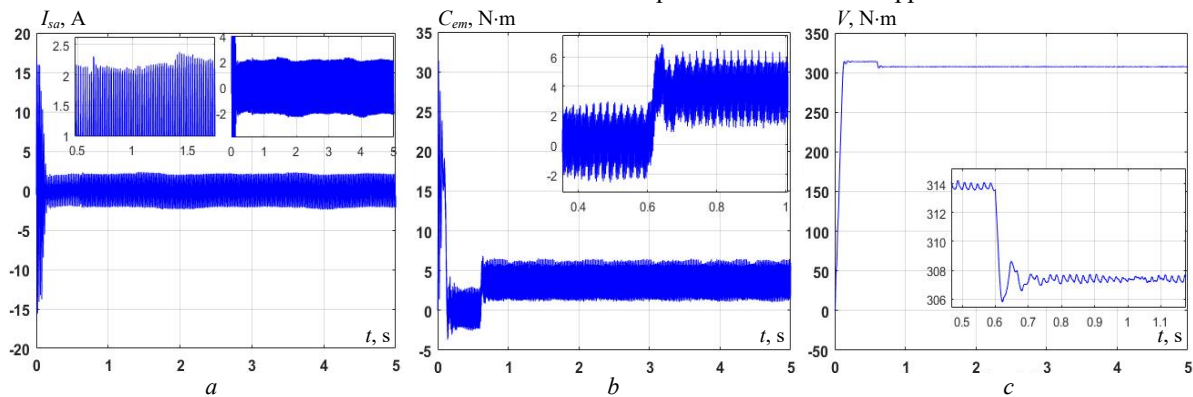


Fig. 5. *a* – evolution of phase A stator current at no-load, on load (healthy); *b* – evolution of the electromagnetic torque on starting, under load (healthy); *c* – rotational speed at start, under load (healthy)

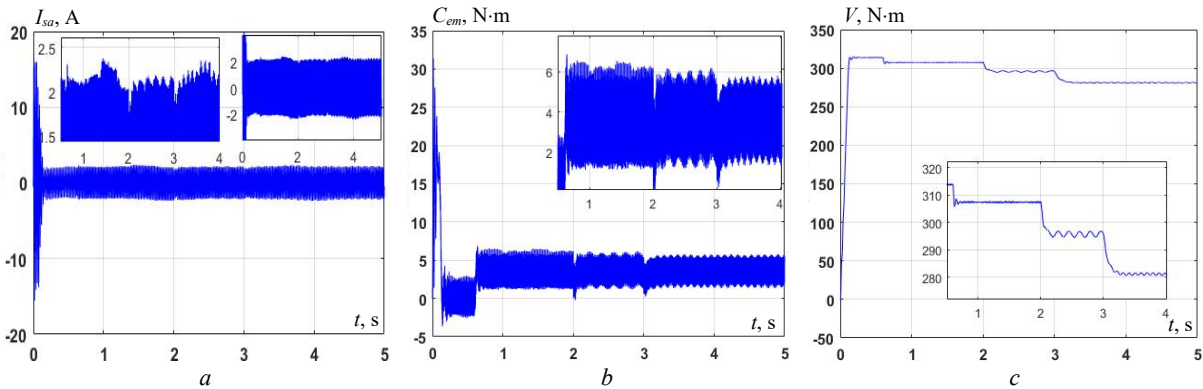


Fig. 6. *a* – evolution of phase A stator current at no-load, on load, then during bar breakage; *b* – evolution of the electromagnetic torque at start-up, under load, then during bar breakage; *c* – rotation speed at start-up, under load, then when the 2 bar breaks

The simulation of the model allowed us to obtain the different characteristics of stator current, speed and electromagnetic torque.

We notice here from Fig. 7,*a* that the spectral stator current in the healthy state does not register any side line around the base line at 50 Hz. As in Fig. 7,*b*, when the machine is loaded, the speed reaches the nominal value and then decreases slightly so that the torque tends to the value of the load torque. It also shows us additional side lines around the base line  $f_s = 50 \text{ Hz}$  at frequencies  $(1 \pm 2 \cdot k \cdot s) \cdot f_s$ .

When analyzing the speed ripple effect, other frequency components of stator current due to rotor asymmetry were observed around the fundamental at the following frequencies  $f_b = (1 + 2 \cdot k \cdot s) \cdot f_s$ .

In the stator current spectrum, more than one higher harmonic component may be induced in the vicinity of the rotor housing harmonics:

$$f_{hk} = Z \left( \frac{N_r}{b} \right) \cdot ((1-s) \pm 1 \pm 2 \cdot k \cdot s). \quad (11)$$

where  $s$  is the slip;  $f_s$  is the supply frequency;  $Z$  is the positive integer;  $N_r$  is the number of rotor bars;  $p$  is the number of pole pairs;  $k = 1, 2, 3 \dots$  and  $h = 1, 3, 5 \dots$

Figure 7,*b* displays the harmonic amplitude's increase as proof that a number of essential criteria are met. The emergence of 2 lateral components with frequencies  $(1 + 2 \cdot s) \cdot f_s$  and  $(1 - 2 \cdot s) \cdot f_s$  to the left and right of the fundamental  $f_s$  is caused by the existence of a broken bar fault, and the degree of gravity of the fault line

amplitudes is  $(1 + 2 \cdot k \cdot s) \cdot f_s$ , suggesting the presence of a two-bar breaking fault.

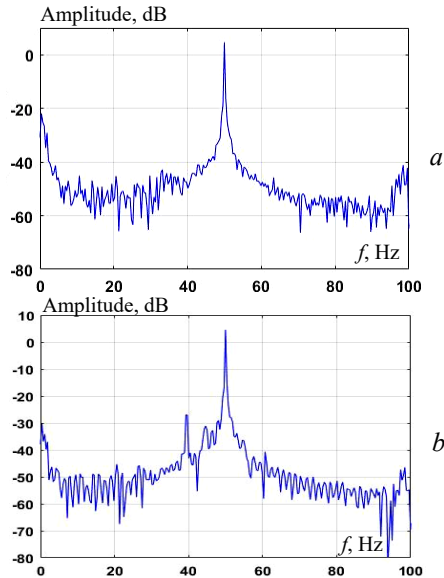


Fig. 7. Phase A current spectrum: a – healthy; b – with bar breaks

Figures 8, 9 demonstrate the use of CWT for stator current for the measurements presented in Fig. 8, 9 for the

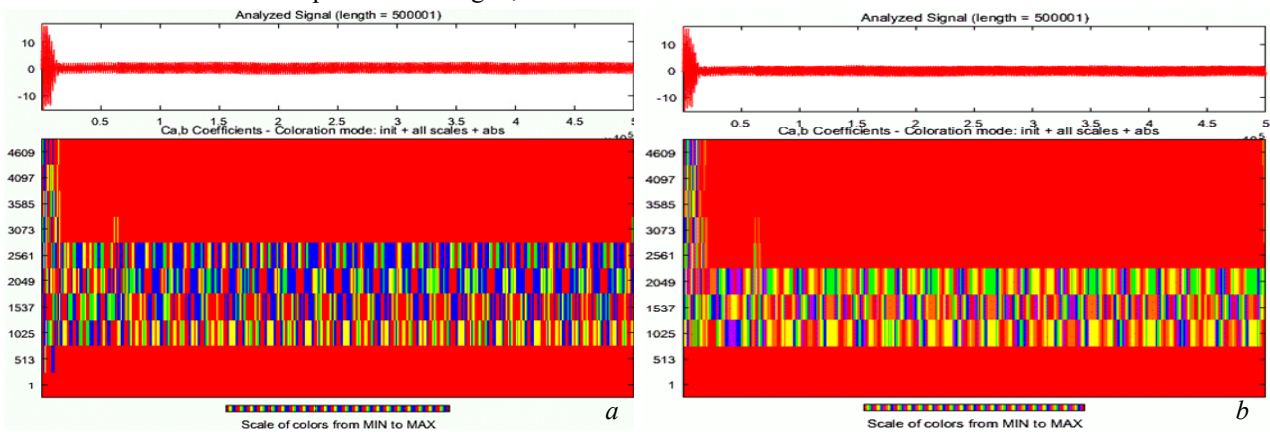


Fig. 8. a – wavelet case of (db); b – wavelet case of (Dmey)

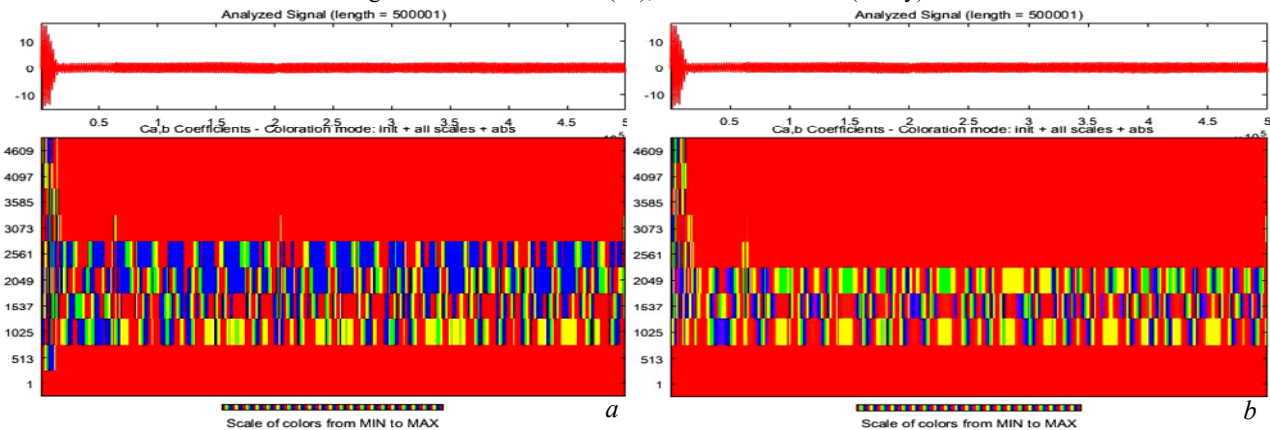


Fig. 9. a – wavelet case of (db) with fault; b – wavelet case of (Dmey) with fault

A closer look at the CWT plots reveals that a healthy motor's starting current displays two patterns under wavelet analysis, the first of which corresponds to the beginning (envelope) and the second of which corresponds to the end (discontinuity) of the signal, while a malfunctioning motor with broken rotor bars displays a third pattern in between the two patterns. It is suggested that this additional pattern can be used to tell a motor that

Meyer family and the family in both a healthy and problematic state of the machine.

Measured using wavelet analysis, the similarity between the signal's fundamental functions (wavelets) and the signal itself is expressed as having the same frequency content. CWT calculated coefficients show how close the signal is to the wave at the current scale.

The current does not alter while the machine is in a healthy state, as opposed to when it is in a damaged one. As the wave coefficients of the kinetic error are stronger than the wave coefficients in the machine's healthy state, we see that the current changes in terms of different degrees of colors and their arrangement in shapes.

These variations show that the wavelet shift may distinguish between the signal components of the healthy and unhealthy motors during the start-up phase. Low frequencies are corresponding to high scales. The higher frequencies match the lower scales.

Another consequence of a broken rotor defect is seen in Fig. 9. The impact is seen in the beginning current envelope plots, where the defective motor starts with a little less current than the healthy motor. This is due to the fact that the defective motor actually has less rotor bars. This is also the cause of the defective motor's decreased torque.

is functioning properly from one that isn't. It is proposed that these variations serve as the distinguishing mark for broken rotor bar fault detection.

Figures 10, 11 show the level signals resulting from the wave decay of the stator current to start in a good health condition of the machine and on the other hand in a defective machine (2 broken bars).

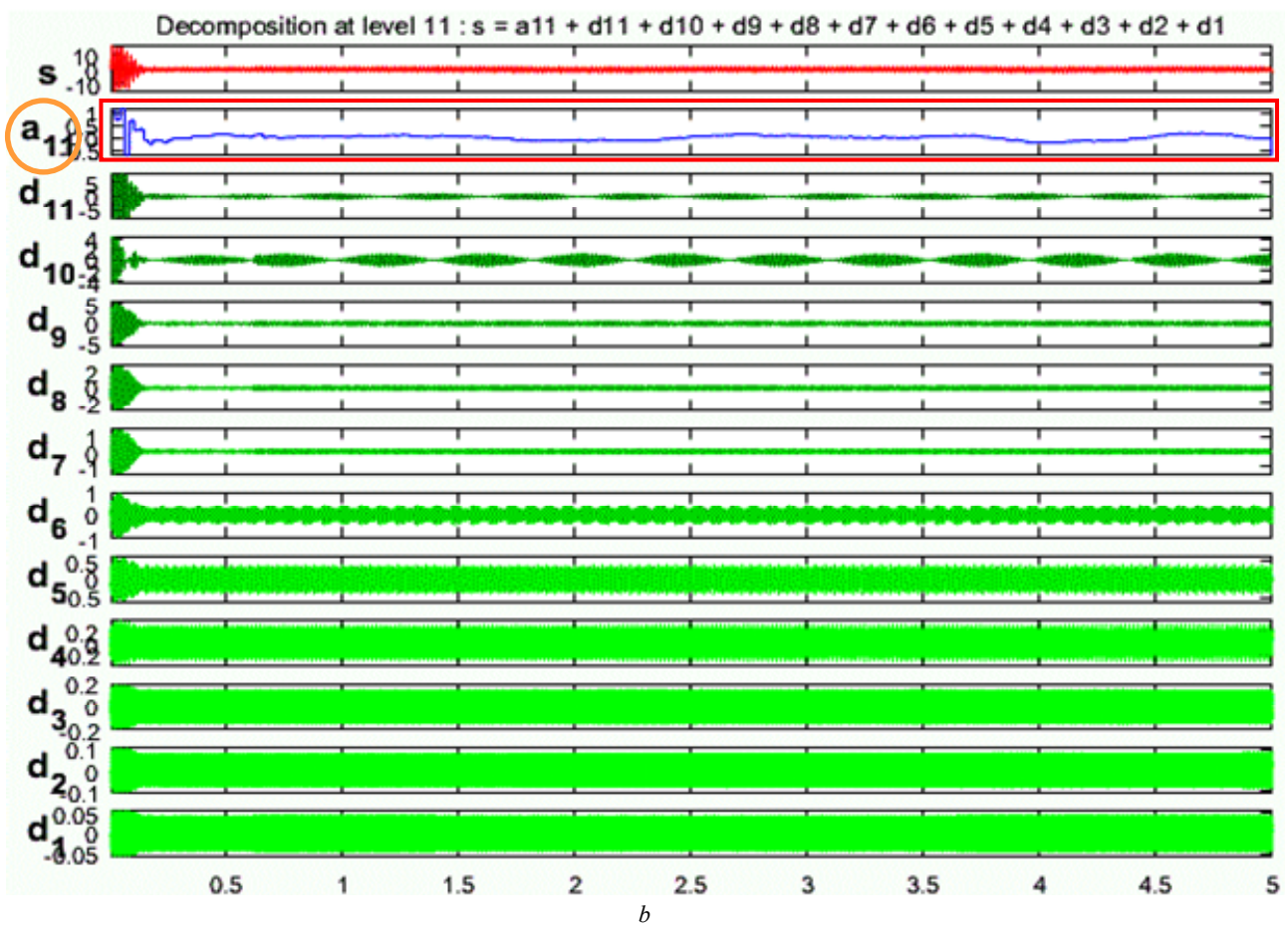
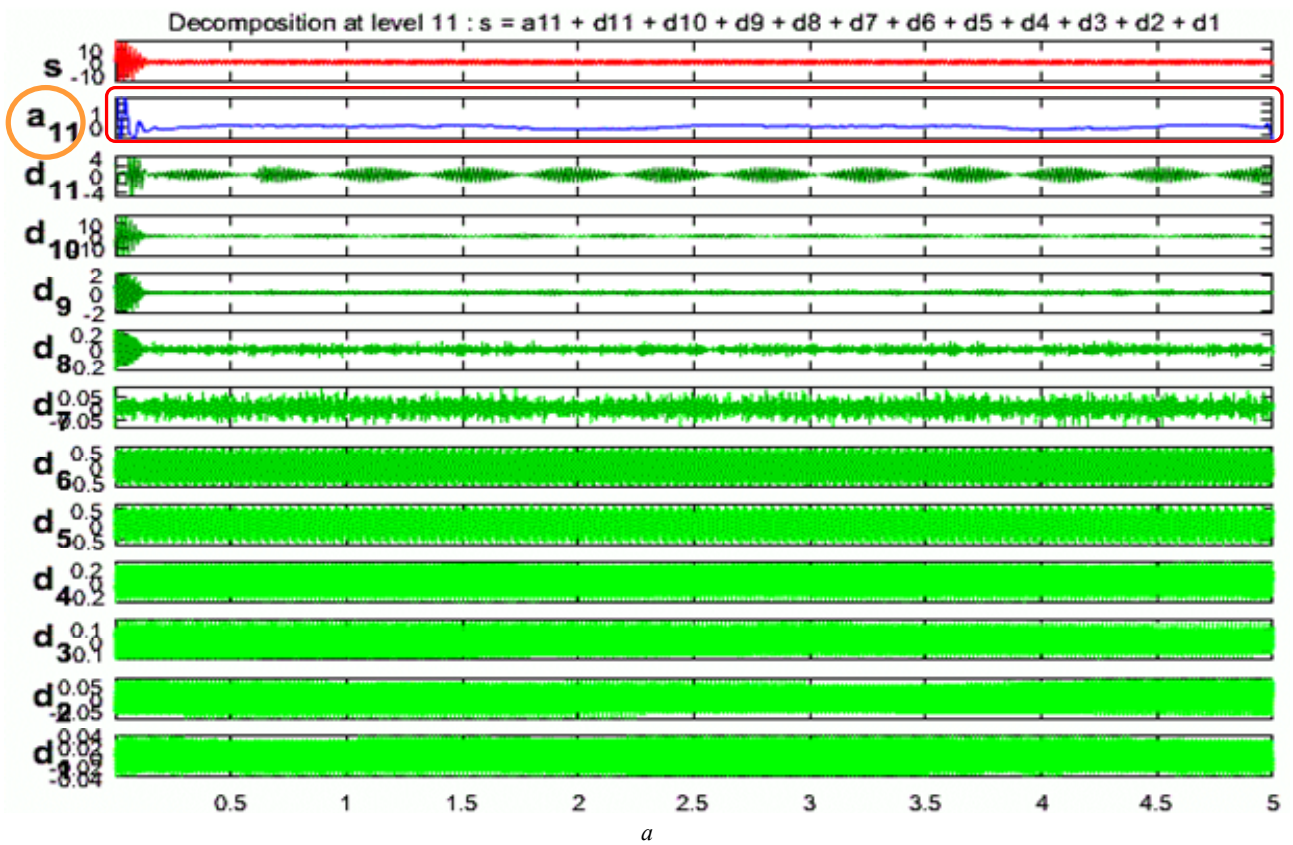


Fig. 10. *a* – wavelet case of sym; *b* – Haar wavelet case

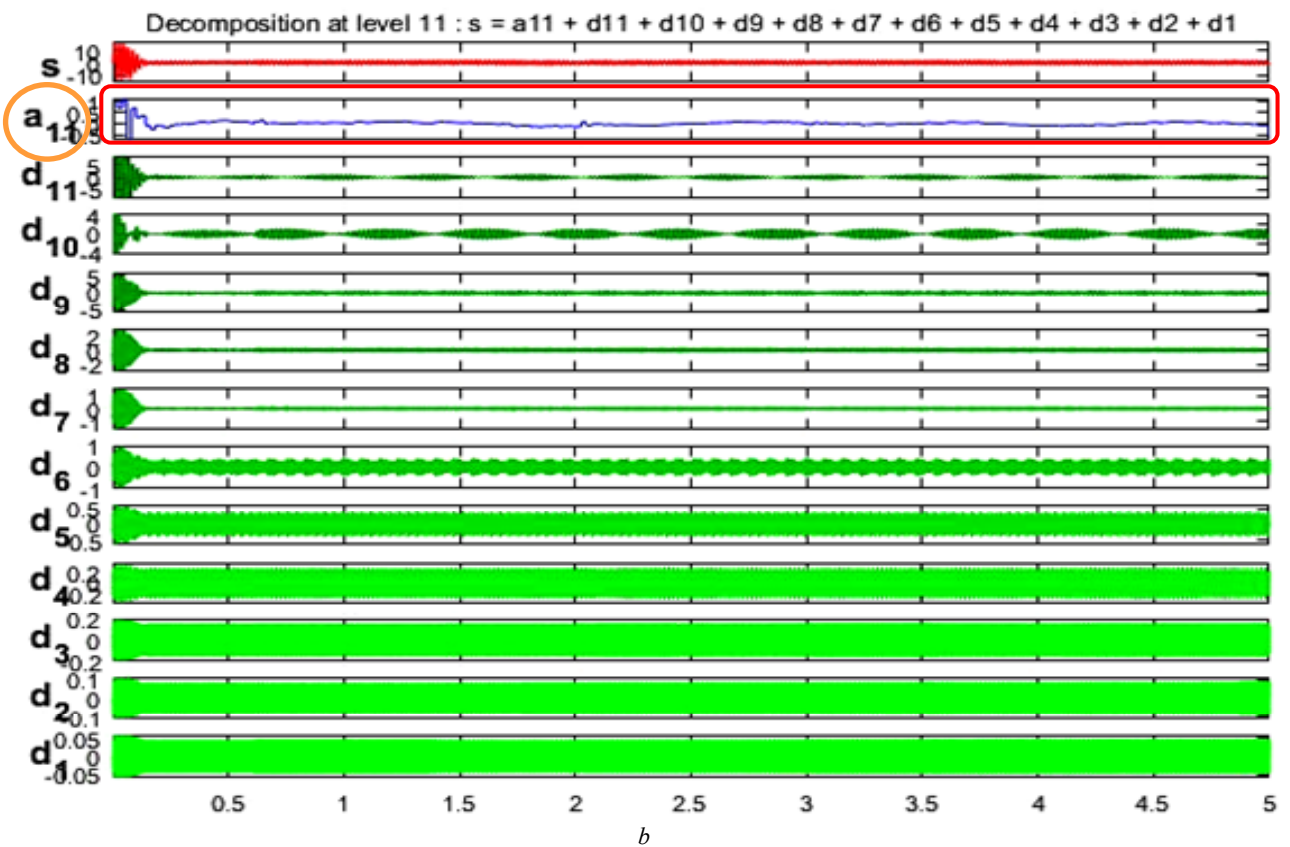
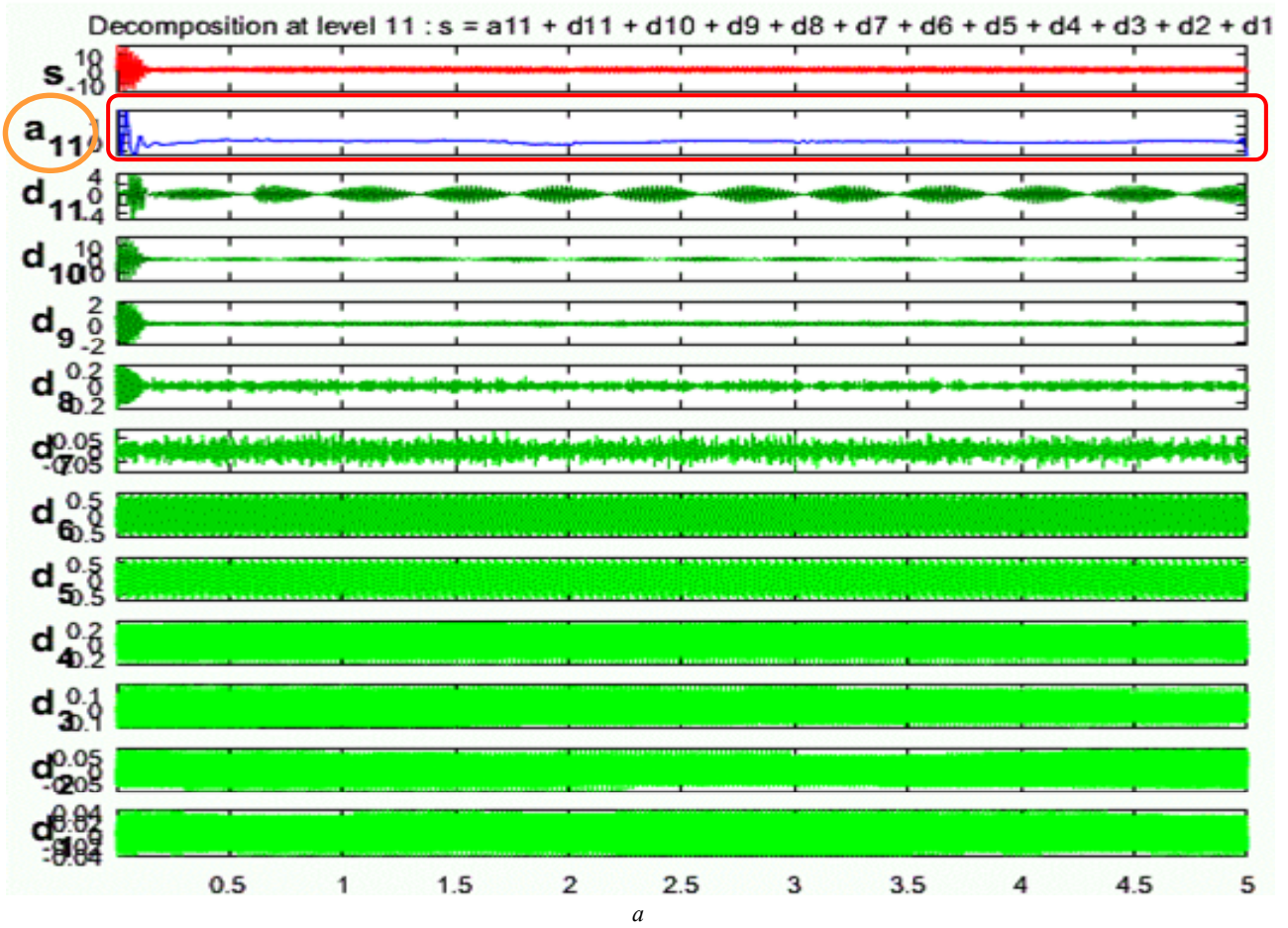


Fig. 11.  $a$  – sym wavelet case with fault;  $b$  – Haar wavelet case with fault

Gives a precise explanation of the variables brought about by the broken rotor bar fault, describing how harmonics develop under transients and steady-state conditions.

The primary factor in the formation of transitional processes is oscillations. When the wavelet signal strength is high, there is no oscillation in the system. Compared to a healthy state, the stator current magnitude in the faulty condition exhibits high-level coefficients and changes in coefficients.

Failure of broken rotor bars affects the effect of frequency bands, increasing the coefficient. The sampling frequency is set to 5 kHz so that the original signal is decomposed at the 11th level.

The high-frequency information is better explained by the detailed signal, while the low-frequency information is better explained by the approximate signal.

The approximation signal for the 11th level has a frequency range of 2.44 to 1.22 which is a very low frequency so it perfectly diagnoses the faults of the rotor bar.

In general, it is noted that the signal in both cases is not the same and can be identified by the disturbances that appear at high levels.

It is noted that the tenth and 11th levels are better in terms of clarity and useful information than the ninth level, which does not have a significant change.

Through the motor signals and graphs that were taken from the samples and using 11 levels of decomposition, it can be concluded that when the reading started, the motor current showed a greater amplitude due to the higher torque, and then it returns to stability. This information for high and low frequencies about the signal is very useful in providing details. Related to error severity and growth in approximation and detail signals, particularly in the corresponding plane of the frequency band, are validated by evaluating the energy stored in each.

The imbalances produced during the fault appear clearly in the signal « $a_{11}$ ».

### Conclusions.

For the purpose of finding faults in squirrel cage induction motors, wavelet packet analysis is an effective tool. The signal is divided into various frequency components using wavelet packets so that any irregularities can be examined. By examining the frequency spectrum of the motor current, the wavelet packet analysis is able to identify broken rotor bar problems. Additionally, it may tell you where the defect is and how serious it is. Wavelet packet analysis can also be used to find other induction motor issues. This makes it a useful tool for identifying and resolving induction motor problems.

In this research, the diagnostic technique is based on the use of discrete wavelet transform and continuous wavelet transform, where it is based on the analysis of the stator current, at the start-up electromagnetic torque.

This method can clearly exhibit the time-frequency characteristic of fault signals. By increasing the peaks of the time domain waveform analysis function, these two techniques' performance was demonstrated by their capacity to produce a local representation of non-stationary current signals for both a functioning machine and one that has a defect.

**Conflict of interest.** The authors declare no conflict of interest.

### REFERENCES

1. Dehina W., Boumehraz M., Kratz F. Diagnosis of Rotor and Stator Faults by Fast Fourier Transform and Discrete Wavelet in Induction Machine. *2018 International Conference on Electrical Sciences and Technologies in Maghreb (CISTEM)*, 2018, pp. 1-6. doi: <https://doi.org/10.1109/CISTEM.2018.8613311>.
2. Rohan A., Kim S.H. Fault Detection and Diagnosis System for a Three-Phase Inverter Using a DWT-Based Artificial Neural Network. *The International Journal of Fuzzy Logic and Intelligent Systems*, 2016, vol. 16, no. 4, pp. 238-245. doi: <https://doi.org/10.5391/IJFIS.2016.16.4.238>.
3. Bessam B., Menacer A., Boumehraz M., Cherif H. DWT and Hilbert Transform for Broken Rotor Bar Fault Diagnosis in Induction Machine at Low Load. *Energy Procedia*, 2015, vol. 74, pp. 1248-1257. doi: <https://doi.org/10.1016/j.egypro.2015.07.769>.
4. Amanuel T., Ghirmay A., Ghebremeskel H., Ghebrehwet R., Bahlibi W. Comparative Analysis of Signal Processing Techniques for Fault Detection in Three Phase Induction Motor. *Journal of Electronics and Informatics*, 2021, vol. 3, no. 1, pp. 61-76. doi: <https://doi.org/10.36548/jei.2021.1.006>.
5. Menacer A., Moreau S., Benakcha A., Said M.S.N. Effect of the Position and the Number of Broken Bars on Asynchronous Motor Stator Current Spectrum. *2006 12th International Power Electronics and Motion Control Conference*, 2006, pp. 973-978. doi: <https://doi.org/10.1109/EPEPEMC.2006.4778526>.
6. Talhaoui H., Ameid T., Kessal A. Energy eigenvalues and neural network analysis for broken bars fault diagnosis in induction machine under variable load: experimental study. *Journal of Ambient Intelligence and Humanized Computing*, 2022, vol. 13, no. 5, pp. 2651-2665. doi: <https://doi.org/10.1007/s12652-021-03172-2>.
7. Ince T. Real-time broken rotor bar fault detection and classification by shallow 1D convolutional neural networks. *Electrical Engineering*, 2019, vol. 101, no. 2, pp. 599-608. doi: <https://doi.org/10.1007/s00202-019-00808-7>.
8. Talhaoui H., Ameid T., Aissa O., Kessal A. Wavelet packet and fuzzy logic theory for automatic fault detection in induction motor. *Soft Computing*, 2022, vol. 26, no. 21, pp. 11935-11949. doi: <https://doi.org/10.1007/s00500-022-07028-5>.
9. Abid M., Laribi S., Larbi M., Allaoui T. Diagnosis and localization of fault for a neutral point clamped inverter in wind energy conversion system using artificial neural network technique. *Electrical Engineering & Electromechanics*, 2022, no. 5, pp. 55-59. doi: <https://doi.org/10.20998/2074-272X.2022.5.09>.
10. Kompella K.C.D., Mannam V.G.R., Rayapudi S.R. DWT based bearing fault detection in induction motor using noise cancellation. *Journal of Electrical Systems and Information Technology*, 2016, vol. 3, no. 3, pp. 411-427. doi: <https://doi.org/10.1016/j.jesit.2016.07.002>.
11. Saidi L., Fnaiech F., Henao H., Capolino G.-A., Cirrincione G. Diagnosis of broken-bars fault in induction machines using higher order spectral analysis. *ISA Transactions*, 2013, vol. 52, no. 1, pp. 140-148. doi: <https://doi.org/10.1016/j.isatra.2012.08.003>.
12. Bouzida A., Touhami O., Abdelli R. Rotor Fault Diagnosis in Three Phase Induction Motors Using the Wavelet Transform. *International Conference on Control, Engineering & Information Technology (CEIT'13). Proceedings Engineering & Technology*, 2013, vol. 1, pp. 186-191. Available at: [http://ipco-co.com/PET\\_Journal/presented%20papers/095.pdf](http://ipco-co.com/PET_Journal/presented%20papers/095.pdf) (accessed 24 July 2022).
13. Dehina W., Boumehraz M., Kratz F. Diagnosis and Detection of Rotor Bars Faults in Induction Motor Using HT and DWT Techniques. *2021 18th International Multi-Conference on Systems, Signals & Devices (SSD)*, 2021, pp. 109-115. doi: <https://doi.org/10.1109/SSD52085.2021.9429381>.
14. Hussein A.M., Obed A.A., Zubo R.H.A., Al-Yasir Y.I.A., Saleh A.L., Fadhel H., Sheikh-Akbari A., Mokryani G., Abd-Alhameed R.A. Detection and Diagnosis of Stator and Rotor Electrical Faults for Three-Phase Induction Motor via Wavelet Energy Approach. *Electronics*, 2022, vol. 11, no. 8, art. no. 1253. doi: <https://doi.org/10.3390/electronics11081253>.

15. Cherif H., Menacer A., Bessam B., Kechida R. Stator inter turns fault detection using discrete wavelet transform. *2015 IEEE 10th International Symposium on Diagnostics for Electrical Machines, Power Electronics and Drives (SDEMPED)*, 2015, pp. 138-142. doi: <https://doi.org/10.1109/DEMPED.2015.7303681>.
16. Hassen K., Braham A., Zied L. Diagnosis of broken rotor bar in induction machines using pitch synchronous wavelet transform. *4th International Conference on Power Engineering, Energy and Electrical Drives*, 2013, pp. 896-901. doi: <https://doi.org/10.1109/PowerEng.2013.6635729>.
17. Eltabach M., Charara A., Zein I. A Comparison of External and Internal Methods of Signal Spectral Analysis for Broken Rotor Bars Detection in Induction Motors. *IEEE Transactions on Industrial Electronics*, 2004, vol. 51, no. 1, pp. 107-121. doi: <https://doi.org/10.1109/TIE.2003.822083>.
18. Didier G., Ternisien E., Caspary O., Razik H. Fault detection of broken rotor bars in induction motor using a global fault index. *IEEE Transactions on Industry Applications*, 2006, vol. 42, no. 1, pp. 79-88. doi: <https://doi.org/10.1109/TIA.2005.861368>.
19. Abu Ibaid O.Z.I., Belhamdi S., Abid M., Chakroune S. Diagnosis of rotor faults of asynchronous machine by spectral analysis of stator currents. *5<sup>th</sup> International Aegean Symposiums on Innovation Technologies & Engineering*, February 25-26, 2022, pp. 102-111. Available at: [https://www.aegeanconference.com/files/ugd/614b1f\\_1930a1802a034e389c403c987ca63644.pdf](https://www.aegeanconference.com/files/ugd/614b1f_1930a1802a034e389c403c987ca63644.pdf) (accessed 24 July 2022).
20. Choudira I., Khodja D., Chakroune S. Fuzzy Logic Based Broken Bar Fault Diagnosis and Behavior Study of Induction Machine. *Journal Européen Des Systèmes Automatisés*, 2020, vol. 53, no. 2, pp. 233-242. doi: <https://doi.org/10.18280/jesa.530210>.
21. Souad L., Bendiabdallah Youcef M., Samir M., Boukezata. Use of neuro-fuzzy technique in diagnosis of rotor faults of cage induction motor. *2017 5th International Conference on Electrical Engineering - Boumerdes (ICEE-B)*, 2017, pp. 1-4. doi: <https://doi.org/10.1109/ICEE-B.2017.8192148>.
22. Abdelhak G., Sid Ahmed B., Djekidel R. Fault diagnosis of induction motors rotor using current signature with different signal processing techniques. *Diagnostyka*, 2022, vol. 23, no. 2, pp. 1-9. doi: <https://doi.org/10.29354/diag/147462>.
23. Chow T.W.S., Hai S. Induction Machine Fault Diagnostic Analysis With Wavelet Technique. *IEEE Transactions on Industrial Electronics*, 2004, vol. 51, no. 3, pp. 558-565. doi: <https://doi.org/10.1109/TIE.2004.825325>.
24. Mohamed M.A., Hassan M.A.M., Albalawi F., Ghoneim S.S.M., Ali Z.M., Dardeer M. Diagnostic Modelling for Induction Motor Faults via ANFIS Algorithm and DWT-Based Feature Extraction. *Applied Sciences*, 2021, vol. 11, no. 19, art. no. 9115. doi: <https://doi.org/10.3390/app11199115>.
25. Kechida R., Menacer A. DWT wavelet transform for the rotor bars faults detection in induction motor. *2011 2nd International Conference on Electric Power and Energy Conversion Systems (EPECS)*, 2011, pp. 1-5. doi: <https://doi.org/10.1109/EPECS.2011.6126825>.
26. Kompella K.C.D., Mannam V.G.R., Rayapudi S.R. DWT based bearing fault detection in induction motor using noise cancellation. *Journal of Electrical Systems and Information Technology*, 2016, vol. 3, no. 3, pp. 411-427. doi: <https://doi.org/10.1016/j.jesit.2016.07.002>.
27. Behim M., Merabet L., Saad S. Detection and Classification of Induction Motor Faults Using DWPD and Artificial Neural Network: Case of Supply Voltage Unbalance and Broken Rotor Bars. *EasyChair Preprint no. 7756*. Available at: [https://easychair.org/publications/preprint\\_download/TrtH](https://easychair.org/publications/preprint_download/TrtH) (accessed 24 July 2022).
28. Mehrjou M.R., Mariun N., Karami M., Noor S.B.M., Zolfaghari S., Misron N., Kadir M.Z.A.A., Radzi M.A.M., Marhaban M.H. Wavelet-Based Analysis of MCSA for Fault Detection in Electrical Machine. In *Wavelet Transform and Some of Its Real-World Applications. InTech.*, 2015. doi: <https://doi.org/10.5772/61532>.
29. Cusido J., Romeral L., Ortega J.A., Rosero J.A., Espinosa A.G. Fault Detection in Induction Machines Using Power Spectral Density in Wavelet Decomposition. *IEEE Transactions on Industrial Electronics*, 2008, vol. 55, no. 2, pp. 633-643. doi: <https://doi.org/10.1109/TIE.2007.911960>.
30. Amanuel T., Ghirmay A., Ghebremeskel H., Ghebrehiwet R., Bahlubi W. Comparative Analysis of Signal Processing Techniques for Fault Detection in Three Phase Induction Motor. *Journal of Electronics and Informatics*, 2021, vol. 3, no. 1, pp. 61-76. doi: <https://doi.org/10.36548/jei.2021.1.006>.
31. Martinez-Herrera A.L., Ferrucho-Alvarez E.R., Ledesma-Carrillo L.M., Mata-Chavez R.I., Lopez-Ramirez M., Cabal-Yepez E. Multiple Fault Detection in Induction Motors through Homogeneity and Kurtosis Computation. *Energies*, 2022, vol. 15, no. 4, art. no. 1541. doi: <https://doi.org/10.3390/en15041541>.

Received 24.09.2022

Accepted 23.12.2022

Published 06.05.2023

Ossama Ziad Ibrahim Abu Ibaid<sup>1</sup>, PhD,

Saad Belhamdi<sup>1</sup>, Professor,

Mimouna Abid<sup>2</sup>, PhD,

Salim Chakroune<sup>1</sup>, Professor,

Souhil Mouassa<sup>3</sup>, Senior Lecturer,

Zuhair S. Al-Sagar<sup>4</sup>, Associate Professor,

<sup>1</sup> Department of Electrical Engineering,

Electrical Engineering Laboratory, University of M'Sila, Algeria,

e-mail: osama.abuibaid@univ-msila.dz;

saad.belhamdi@univ-msila.dz; salim.chakroun@univ-msila.dz

<sup>2</sup> Department of Electrical Engineering,

L2GEGI Laboratory, University of Tiaret, Algeria,

e-mail: mimouna.abid@univ-tiaret.dz (Corresponding Author)

<sup>3</sup> Department of Electrical Engineering,

University of Bouira, Algeria,

e-mail: souhil.mouassa@univ-bouira.dz

<sup>4</sup> Department of Renewable Energy,

Baqubah Technical Institute, Middle Technical University,

Baghdad, Iraq.

e-mail: Zuhairalsagar@mtu.edu.iq

#### How to cite this article:

Abu Ibaid O.Z.I., Belhamdi S., Abid M., Chakroune S., Mouassa S., Al-Sagar Z.S. Wavelet packet analysis for rotor bar breakage in an inverter induction motor. *Electrical Engineering & Electromechanics*, 2023, no. 3, pp. 3-11. doi: <https://doi.org/10.20998/2074-272X.2023.3.01>

V.I. Milykh, V.P. Shaïda, O.Yu. Yurieva

## Analysis of the thermal state of the electromagnetic mill inductor with oil cooling in stationary operation modes

**Introduction.** An electromagnetic mill (EMM) for the technological processing of various substances, which is based on the stator of a three-phase induction motor, is being studied. The stator winding has an increased current density, so the mill is provided with a system of forced cooling with transformer oil. **Problem.** Currently, there are no works on the thermal state calculation of the EMM with the given design and oil cooling. Therefore, the study of such EMMs thermal state is relevant, as it will contribute to increasing the reliability and efficiency of their work. **Goal.** Formation of a mathematical model of the thermal state of the electromagnetic mill inductor and the analysis of its heating in stationary modes of operation with cooling by transformer oil. **Methodology.** The problem of calculating the thermal state, namely the temperature distribution in the main parts of the electromagnetic mill, is solved by the equivalent thermal resistance circuit method. The design of the EMM is provided in a sufficiently complete volume, and on this basis, a corresponding equivalent thermal replacement circuit is formed, which is supplemented by an equivalent hydraulic circuit of oil passageways. An explanation is provided for the composition and solution of the equations algebraic system that describes the distribution of temperatures by the constituent elements of the EMM. **Results.** The thermal calculation results of the electromagnetic mill showed that the maximum heating temperature is much lower than the allowable one for the selected insulation class. According to the hydraulic scheme, the necessary oil consumption, its average speed and the corresponding pressure at the inlet of the intake pipe are determined, which are at an acceptable level. It is noted that the rather moderate temperature state of the inductor and the hydraulic parameters of the oil path are facilitated by such innovations in the design of the EMM as the loop double layer short chorded winding and axial ventilation channels in the stator core. **Originality.** Now EMM thermal equivalent circuits with air cooling only have been presented. Therefore, the developed thermal circuit of the oil-cooled inductor is new and makes it possible to evaluate the operating modes of the EMM. **Practical value.** The proposed technical solutions can be recommended for practical implementation in other EMMs. Taking into account the identified reserves of the EMM temperature state, a forecast was made regarding the transition from its oil cooling to air cooling. But the use of air cooling requires a change in the design of the EMM. References 34, tables 2, figures 5.

**Key words:** electromagnetic mill, forced cooling of the inductor with oil, analysis of the thermal state of the mill, method of equivalent thermal circuits, analysis of hydraulic parameters.

**Проблема.** Досліджується електромагнітний млин (ЕММ) для технологічної обробки різних речовин, який виконано на базі статора трифазного асинхронного двигуна. Обмотка статора має підвищену густину струму, тому для млина передбачена система примусового охолодження трансформаторною оливою. Наразі робіт з розрахунку теплового стану ЕММ з наданою конструкцією і охолодженням оливою не представлено. Тому дослідження теплового стану таких ЕММ є актуальним, бо сприятиме підвищенню надійності та ефективності їх роботи. **Метою** статті є формування математичної моделі теплового стану індуктора електромагнітного млина та аналіз його нагріву у стаціонарних режимах роботи з охолодженням трансформаторною оливою. **Задача** розрахунку теплового стану, а саме – розподілу температури в основних частинах індуктора електромагнітного млина, розв'язується методом еквівалентних теплових схем. Конструкція ЕММ надана у достатньо повному обсязі і на цій основі сформована відповідна еквівалентна холова схема заміщення, яка доповнена еквівалентною гідравлічною схемою шляхів проходження оливи. Надано пояснення щодо складання та розв'язання алгебраїчної системи рівнянь, які описують розподіл температур по складовим елементам індуктора ЕММ. **Результати** теплового розрахунку індуктора ЕММ показали, що максимальна температура нагріву значно менша за допустиму для обраного класу нагрівостійкості ізоляції. За гідравлічною схемою індуктора визначено необхідні витрати оливи, її середню швидкість і відповідний тиск на вході у впускний патрубков, які знаходяться на допустимому рівні. Зазначено, що досить помірного температурного стану індуктора і гідравлічним параметрам тракту оливи сприяють такі нововведення в конструкцію ЕММ, як двошарова скорочена петльова обмотка статора і аксіальні вентиляційні канали в осерді статора. Натепер були представлені теплові еквівалентні схеми ЕММ лише з повітряним охолодженням. Тому розроблена холова схема індуктора з охолодженням оливою є новою і дає можливість оцінки режимів роботи ЕММ. Бібл. 34, табл. 2, рис. 5.

**Ключові слова:** електромагнітний млин, примусове охолодження індуктора оливою, аналіз теплового стану млину, метод еквівалентних теплових схем, аналіз гідравлічних параметрів.

**Introduction.** Devices (apparatus) with a vortex layer of ferromagnetic elements or, abbreviated, vortex layer devices (VLDs), are quite well known and are used in various industries, agriculture and communal economy [1-5].

Despite the rather significant number of VLDs manufactured by the end of the last century, their introduction into industrial production was held back by a number of reasons. Among them is the lack of a clear methodology for designing VLDs [6, 7] and the need to take into account the purpose of a specific device, which forced each device to be designed separately. A significant obstacle is the cyclical mode of operation of

the equipment, which requires automation of the process of feeding and unloading the processed raw materials [3].

In the last two decades, the direction of development and implementation of VLDs received a powerful stimulus due to the relevance of global trends in the development of production. First of all, the increase in the cost of energy carriers, and the introduction of VLDs instead of traditional mills allows to reduce electricity costs [2, 6].

Secondly, the competition among global manufacturers has led to the demand to improve the quality of manufacture products and the efficiency of

© V.I. Milykh, V.P. Shaïda, O.Yu. Yurieva

existing technological processes. Here, too, VLDs came in handy [5, 8-11].

Thirdly, requirements for environmental protection in production and everyday life. The use of VLDs for the treatment of wastewater with organic or industrial pollution allows to significantly improve the quality of cleaning and reduce its cost.

At the present time, the most common are the VLDs for grinding substances, which due to their purpose have received the name of electromagnetic mills (EMMs), one of the options of which is considered in this work.

There are several large companies that manufacture VLDs for various purposes, and small enterprises that specialize in VLDs for only one purpose. An example of large enterprises is the well-known Globecore Company, Germany, one of whose branches is located in the city of Poltava, Ukraine. The most common product of this company is EMM type AVS-100 [12]. Also known is the EMM for crushing copper ore [13], created by Project SYSMEL, which has an automated loading/unloading system and a cooling system.

Depending on the purpose of EMM, there are peculiarities of the functioning of such devices, their construction and design methods. Therefore, the study of EMM, taking into account the specifics of their application, is an urgent issue.

**Analysis of previous studies.** The work [1], devoted to the theory of the functioning and structure of VLDs, is still considered basic for their design [4, 5].

Currently, there are several dozen scientific teams in different countries of the world conducting EMM research, the fields of which are different. In fact, most of these scientific groups go through the same stages of EMM research, starting with its design, manufacturing a sample, and ending with the improvement of its parameters. In this sense, a group of Polish scientists engaged in EMM research for crushing copper ore is quite indicative [10]. In their publications [3, 6, 13-15] over the last decade, they presented the results of EMM research, starting from the development of the mill design, the loading/unloading system, the raw material processing quality control system, and the installation control system.

The main part of the EMM is an inductor powered by a three-phase AC network and creates a rotating magnetic field [4, 7]. Under the action of this magnetic field, ferromagnetic elements located in the working chamber perform chaotic motion [1, 2, 7]. The inductor together with the working chamber and grinders (ferromagnetic) elements are active parts that ensure the processing. The structure of these parts directly affects the efficiency of the EMM [3, 7], therefore, the largest number of works is devoted to the study of their influence.

Currently, EMM manufacturers use two variants of the design of the inductor: the first variant, traditional, with clearly marked poles [3]; the second one – with ambiguous poles based on the stator of an induction motor [16].

Despite the different constructions of the inductor, most of them are made bipolar ( $2p = 2$ ) with a rotation frequency of the magnetic field of 3000 rpm. From the very beginning [1] and further, it is believed that a

homogeneous magnetic field in the working chamber is optimal for ensuring the uniformity of movement of mill elements. This is facilitated by the sinusoidal distribution of the magnetomotive force (MMF) by the boring of the stator core. This is quite close provided by a non-equal-pole structure with a three-phase winding, as in induction motors, which is adopted in a number of developments. An example of such a development is shown in [17], where a theoretical-experimental study of an inductor – a borrowed stator of a conventional induction motor – was performed.

The work [1] provides an analytical method for determining the dimensions and parameters of the EMM inductor, but it does not provide the necessary accuracy of calculations due to the accepted simplifications [6, 7]. In [4, 7], the problem of sufficiently accurate determination of the magnetic field and electromagnetic parameters of the EMM inductor is solved by their calculations by numerical methods using modern software complexes.

In [4], the numerical field analysis of the EMM inductor was performed using the FEMM software. Calculation interdependencies of electromagnetic quantities and the corresponding characteristics of the EMM inductor were obtained. But this is done on the assumption that the ferromagnetic elements are placed in the working chamber uniformly, as it was forced to do in [1].

In fact, the grinding elements in the working chamber move chaotically, because they constantly collide with each other and the inner surface of the working chamber. The development of a mathematical model of the trajectory of movement of grinding elements in the working chamber of the EMM was carried out in [7, 18], where it was established that the complex nature of the dependence of the electromagnetic force acting on the grinding elements on various factors precludes the possibility of obtaining an analytical solution.

A significant part of the works [4, 6-8] is devoted to determining the number and optimal size ratio of grinding elements, as well as the filling factor of the working chamber. The study of the influence of the dimensions of the working chamber on the efficiency of grinding of raw materials was carried out in [6].

Another area of EMM research is the assessment of the influence of the inductor operating mode and its control [4, 6, 7, 19] and the raw material processing time on the quality parameters of its processing [9, 14, 20, 21]. Studies of the efficiency of EMM were carried out in [7, 9, 10].

To ensure an effective grinding process, the EMM inductor must create a magnetic field with fairly high parameters in the working chamber. For example, in [9] it is indicated that the average value of magnetic flux density in the working chamber of the EMM prototype is 0.153 T, and in [4] the value of 0.2 T is considered. To ensure such parameters of the magnetic field in the working chamber, the inductor winding must have a high value of current density. Accordingly, for heat removal, it is necessary to create effective cooling of the inductor [6, 7].

In practice, three types of cooling are used: air, oil and water.

In EMM for grinding copper ore [3, 9], the inductor is cooled by air using fans. The work [16] also investigates EMM with traditional air cooling inherent in the stator of an induction motor.

But the most widespread is oil cooling, it is used in their EMMs by both the Globecore Company and a significant number of small manufacturers [4, 7, 10].

The issues of inductor cooling have received somewhat less attention compared to other studies, which is explained by the cyclical nature of the operation of a significant number of EMMs. That is, thanks to the short-term mode of its work, it had time to cool down.

The study of the thermal state of the EMM, created on the basis of the stator of an induction motor with air cooling, was carried out in [16, 22].

In [22], the results of calculating the temperature distribution, obtained by the method of equivalent thermal circuits, were compared with experimental data obtained earlier by EMM thermography [23].

But in general, unfortunately, works related to the study of the thermal state of oil-cooled EMMs are currently not presented. This may be due both to the increase in the complexity of thermal calculations, compared to air-cooled EMMs, and to significant time costs. Also, there is no clear criterion for choosing a cooling method for EMM, which would allow the designer to be clearly defined during its development.

Unlike EMM, the methods of thermal analysis of electric machines are well developed, and the choice of cooling system is structured [24]. Also, water cooling systems of electric machines for cars, based on the type of water «shirt» [25], are being researched and used quite intensively.

Therefore, it can be considered that the task of researching the thermal state of the EMM with forced oil cooling is relevant, as it will allow to increase the reliability and efficiency of the EMM.

For such research, there is already a promising improved design of EMM based on the stator of a three-phase induction motor, which was formed in the process of development evolution and provided in works [19, 26].

**The goal of the article** is the formation of a mathematical model of the thermal state of the inductor of an electromagnetic mill and the analysis of its heating in stationary modes of operation with cooling by transformer oil.

**Object of study.** The electromagnetic system of the improved EMM presented in [19, 26] is shown here in Fig. 1. The inductor is powered by a three-phase network with phase voltage of 100 V and frequency of 50 Hz.

The initial design parameter is the magnetic flux density of 0.12 T in the center of the empty working chamber. This state of the EMM is considered an ideal non-working course. In other modes, which are given in [19] and discussed later in the article, the chamber contains ferromagnetic elements, and the coefficient of its filling with them was considered to be equal to 0.1.

The electromagnetic calculation of the inductor is performed by analogy with the methods given in [4, 19, 26].

For reasons of the technological process, the radius of the inner surface of the chamber  $r_{ki} = 0.047$  m and the axial length of the stator core  $l_a = 0.25$  m are set. By

calculation, the radii of core boring  $r_{si} = 0.06$  m and its outer surface  $r_{se} = 0.109$  m are determined.

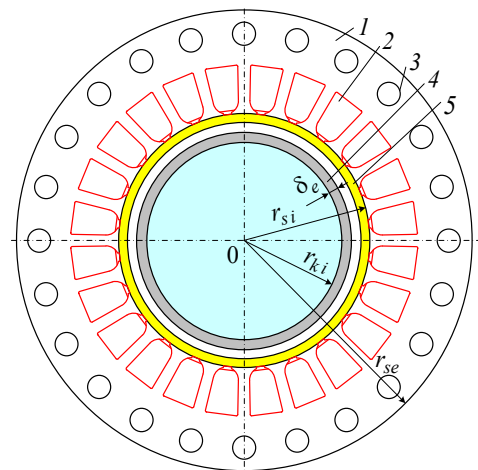


Fig. 1. Electromagnetic system of the rotating magnetic field inductor: 1 – laminated stator core; 2 – three-phase winding; 3 – ventilation channels; 4 – shell of the working chamber with thickness of  $\delta_e = 5$  mm; 5 – insulating pipe

The insulating pipe 5 (Fig. 1) is made of plastic, and through the air gap of 4 mm from it there is a shell of the working chamber 4 made of stainless steel. This tube holds and insulates the inductor winding in the slots and prevents oil from entering the gap. Also the pipe together with the air gap distance the working chamber from the zone of the teeth of the stator core with a nonuniform distribution of the magnetic field, which contributes to the uniform distribution of ferromagnetic elements in the chamber.

In a thermal sense, the insulating pipe and the air gap practically exclude heat transfer between the oil and the working chamber, so this path is not taken into account in the thermal calculation of the inductor.

To improve the operational properties of the inductor, two steps that have not yet been tested have been taken. Instead of the usual concentric diametral winding of the stator, a shortened loop winding is introduced, which allows to eliminate the asymmetry of the phase windings and to ensure an increase in the homogeneity of the magnetic field in the working chamber of the inductor – this is shown in [26]. In addition, axial ventilation channels are provided in the core of the stator, which is aimed at improving the cooling of the electromagnetic system of the inductor. At the same time, this is facilitated by a more «sparse» structure of the thinner frontal parts of the stator loop winding, which increases their cooling surface.

So, this is how the task of assessing the thermal state of the EMM inductor and the ability to ensure its acceptable level by cooling with transformer oil arose.

For a complete understanding of the operation of the EMM and an explanation of its electromagnetic component, Fig. 2 shows the structure of the inductor according to [19, 26], which actually ensures the operation of the mill, although this is not the main topic of the article. Here the instantaneous distribution of currents in the three-phase winding, the corresponding direction of action of its MMF  $F_s$  and the picture of the

2D magnetic field in the operating mode with the presence of ferromagnetic elements are shown.

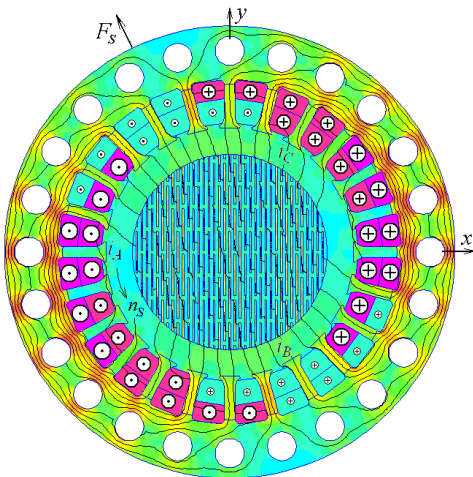


Fig. 2. Magnetic field in the cross section of the inductor at rated load

The well-known FEMM software based on the Finite Element Method was used to calculate the magnetic field, as indicated in [4, 19].

The magnetic field is rotating, and ferromagnetic elements move with it, ensuring the necessary processing of the substance in the working chamber.

It is known [4, 19, 26] that for electromagnetic calculations of the inductor, its electromagnetic system is enough, which is given in Fig. 2.

However, to calculate the thermal state of the inductor, it is necessary to take into account its entire 3D structure. The structure of the EMM along with the main dimensions is shown in Fig. 3 in its longitudinal section. Together with the cross section in Fig. 1, it provides a fairly complete picture of the entire structure of the inductor.

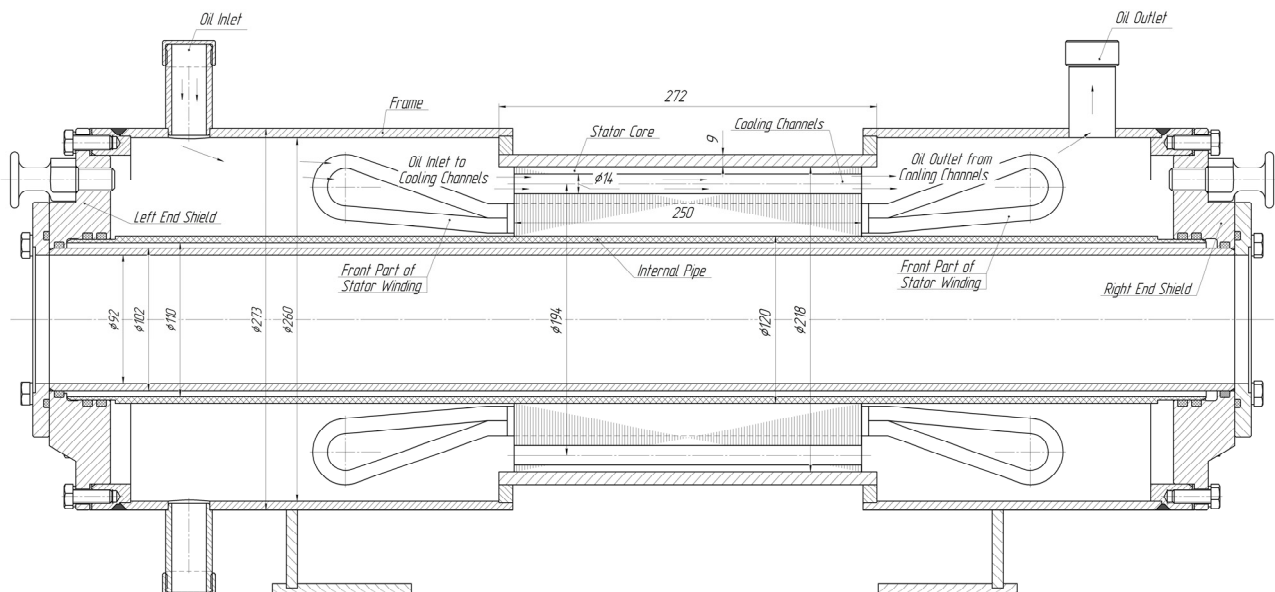


Fig. 3. Scheme of the design of the EMM with the main dimensions of the inductor and the working chamber

The thermal calculation of the inductor was performed for the temperature of the transformer oil at its inlet  $\theta_{oil} = 20 \text{ }^\circ\text{C}$ , the ambient temperature  $\theta_{ens} = 20 \text{ }^\circ\text{C}$ .

**Research methods and results.** The thermal calculation of the EMM inductor with forced cooling by the flow of transformer oil must take into account the heating of the oil along the length of the inductor. Therefore, it is desirable to use 3D modelling of the temperature field, for example, using the Finite Element Method. It is known that for this the calculation model is divided into separate elements in the form of tetrahedra. With the complex structure and rather large dimensions of the design of the EMM inductor, especially the frontal parts of its winding, the number of model elements must be very large. The experience of calculating even a 2D axisymmetric model of an electric machine [27] shows that the duration of the calculation will be excessive, as will the necessary computer resources.

In this case, the only possible solution for solving the formulated problem is the application of the method of equivalent thermal circuits (ETC).

Thermal calculation of electric machines using the ETC method ensures the reliability of the results with an error of up to 5-10 % [28, 29]. It allows to take into account the temperature change in the thin layer of insulation and to obtain the temperature distribution along the length of the inductor and in the entire volume of the EMM. This method was used to calculate the thermal state of a similar EMM, but with differences in design and at air cooling [22].

The necessary reference data for thermal calculation were obtained from modern reference books [30, 31]. Such data are the thermal conductivity  $\lambda$  of copper, electrical steel grade 2212, air, transformer oil, materials of the frame and end shields – steel St35, the inner tube of the stator – fiberglass, slot insulation of heat resistance class B; specific heat capacity  $c$  and mass density  $\rho$ ; kinematic viscosities  $\nu$  of air and transformer oil; dynamic viscosity  $\mu$  of the latter.

The movement of the heat flow for the proposed design of the inductor (Fig. 1, 3) is directed from the slot part of the winding to its frontal parts and to the teeth and

back of the inductor core. This heat from the core with the addition of magnetic losses in it is transferred to the frame, and from the ends of the core to the cooling transformer oil. Part of the heat from the core is transferred to the inner insulating pipe (Fig. 1), which is made of plastic. But heat is practically not transferred through it and the air gap, so the effect of heat from the grinding elements in the working chamber is not taken into account.

From the front parts of the winding, heat is transferred to the cooling oil, which enters from the inlet port, passes through the left front part of the winding, the

cooling channels inside the inductor core, through the right front part of the winding and exits through the outlet port. The heat from the transformer oil is transferred to the end shields, parts of the frame and the insulating pipe, free from the core. Due to the fact that the transformer oil is heated when passing through the inductor, the thermal system is asymmetrical. That is, the side of the inductor at the inlet of the transformer oil is colder than the side at the outlet.

On the basis of the scheme of the movement of the heat flow, the ETC of the EMM inductor is built (Fig. 4).

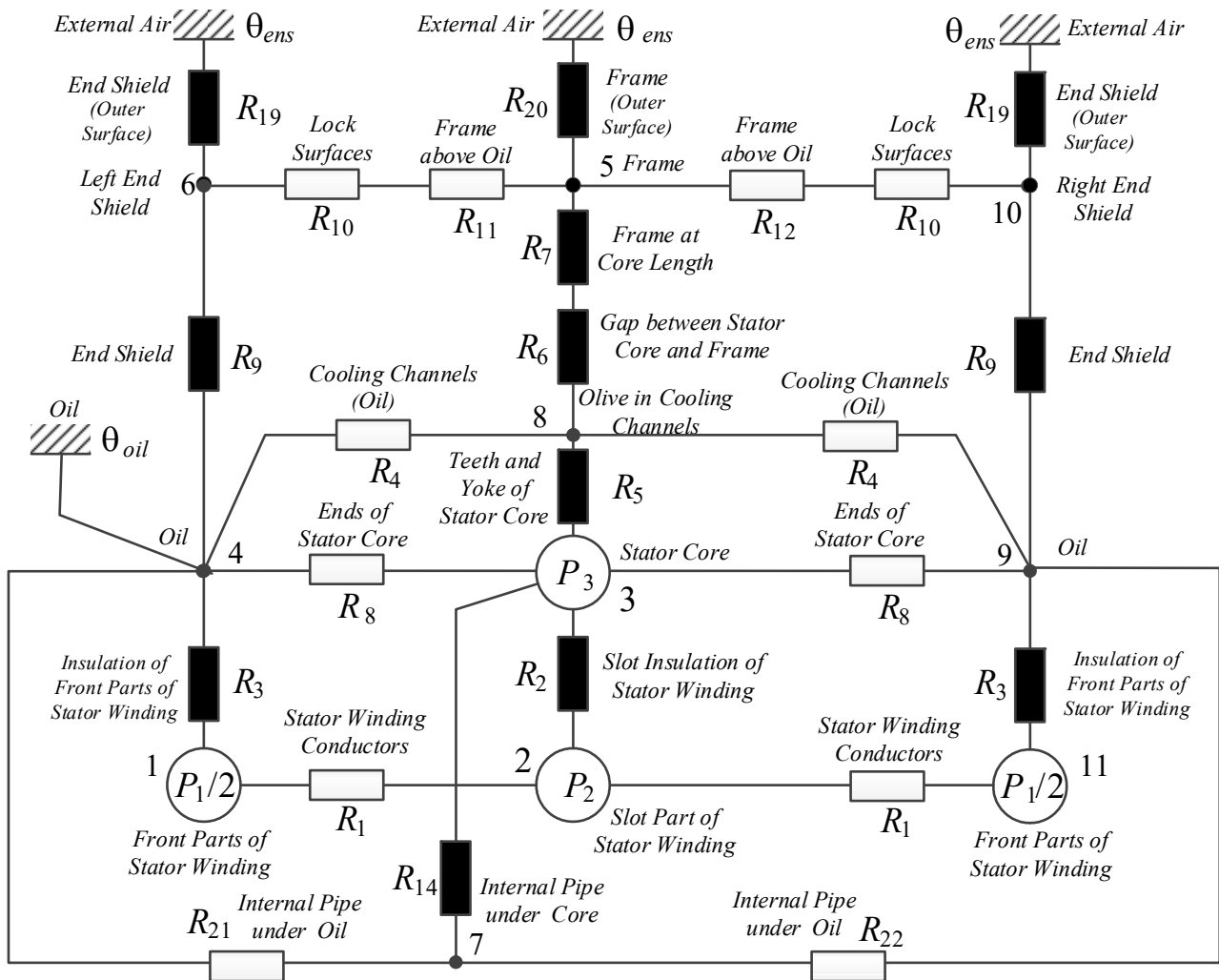


Fig. 4. Equivalent thermal circuit of the EMM inductor

In the inductor, separate homogeneous parts are distinguished, which in ETS are nodes 1–11: slot and two front parts of the winding, stator core, transformer oil in the space of the front parts and in the cooling channels of the inductor core, frame, end shields, internal insulating pipe. The sources of heat in the EMM inductor are its winding and core. Electric and magnetic losses in them were determined based on the results of electromagnetic calculation, as described in [4, 19].

Electrical losses are divided between the slot and front parts of the winding in proportion to the lengths of these parts and determine the power of the heat sources  $P_1$

and  $P_2$ . The power of the heat source of node 3 (teeth and back of the stator core)  $P_3$  is determined by magnetic and additional losses. The rest of the nodes do not have their own heat sources, so their power is zero. The principles of determining these losses are given in [4, 19, 26].

The equivalent thermal scheme has two reference nodes – nodes with defined temperature. These are the ambient air node with temperature  $\theta_{ens}$  and the inlet transformer oil node with temperature  $\theta_{oil}$ .

Thermal resistances of structural elements are determined according to generally accepted formulas, which depend on the structural element and its cooling

conditions [29]. The calculated expression for the thermal resistance is determined by the nature of the heat exchange.

Conductive thermal resistances were determined using reference thermal conductivities  $\lambda$  according to the general formula [29]:

$$R_{\lambda} = \frac{\delta}{\lambda \cdot S}, \quad (1)$$

where  $\delta$  is the thickness of the thermal wall of the EMM structural element;  $S$  is the surface area of the wall.

Convective thermal resistances were determined through heat transfer coefficients  $\alpha$ . Their values were chosen based on the experience of thermal calculations of structurally similar electric machines. The general formula for calculating convective thermal resistance [29]:

$$R_{\alpha} = \frac{1}{\alpha \cdot S}, \quad (2)$$

where  $S$  is the heat transfer surface area.

For example, the heat transfers from the surfaces of the end shields and the inductor frame were determined from [23] and were 124 W/(m<sup>2</sup>·°C) and 87 W/(m<sup>2</sup>·°C). The rest of the heat transfers were determined based on the experience of thermal calculations of induction motors [32, 33].

Thermal connections between nodes of the equivalent thermal circuit are determined by thermal resistances that do not depend on temperature. The determination of these resistances between the nodes of this scheme was carried out by analogy with the rules for solving the problems of calculating electric circuits.

For a simpler solution of the system of equations characterizing the thermal state of each node, thermal conductivities were used. The mutual thermal conductivities between the nodes are inverse values of the thermal resistances of the branches of the equivalent thermal circuit. The intrinsic thermal conductivities of the nodes are the sum of the conductivities of the branches entering the node. Thermal conductivities between nodes where there is no direct connection are zero.

In order to systematize the designations, the indices next to the letters correspond to the numbers of the circuit nodes.

Determination of the temperatures of equivalent nodes of the thermal circuit occurs with the help of the system of algebraic equations, which consists of heat balance equations of heat sources.

The system of equations in matrix symbols has the form:

$$A \times \theta + P = 0, \quad (3)$$

where  $A$  is the thermal conductivity matrix;  $\theta$  is the node temperature matrix;  $P$  is the power of heat sources matrix.

The equations are compiled for all nodes of the equivalent thermal scheme, except for reference nodes. For the nodes of the equivalent thermal circuit that have a thermal connection with the reference nodes, the combined losses are added to the power of the node – the product of the temperature of the reference node  $\theta_{oil}$  or  $\theta_{ens}$  and the thermal conductivity between the node and the reference point  $\Lambda_{4oil}$ ,  $\Lambda_{5ens}$ ,  $\Lambda_{6ens}$  or  $\Lambda_{10ens}$ .

$$P = \begin{bmatrix} P_1 \\ P_2 \\ P_3 \\ P_4 + \theta_{oil} \cdot \Lambda_{4oil} \\ P_5 + \theta_{ens} \cdot \Lambda_{5ens} \\ P_6 + \theta_{ens} \cdot \Lambda_{6ens} \\ P_7 \\ P_8 \\ P_9 \\ P_{10} + \theta_{ens} \cdot \Lambda_{10ens} \\ P_{11} \end{bmatrix}. \quad (4)$$

The solution of the system of equations is the temperature values of the elements of the inductor design – nodes of the equivalent thermal circuit (see Fig. 4): the frontal part on the side of the transformer oil inlet (node 1); slot part (node 2); stator core (node 3); transformer oil at the inlet (node 4); frame (node 5); end shield on the side of the transformer oil inlet (node 6); internal pipe (node 7); oil in the cooling channels (node 8); of transformer oil at the outlet (node 9); end shield on the side of the transformer oil outlet (node 10); front part of the winding on the side of the outlet of the transformer oil (node 11).

To perform the thermal calculation, the open access software SMATH Studio [34] was developed. The calculation was performed for four stationary modes of operation of the inductor: ideal non-working course (INW); «working» non-working course (WNW), when the ferromagnetic elements are loaded, and there is no processed raw material; nominal load mode (NLM), when there are both elements and raw materials; maximum load mode (MLM) [19]. The values of stator winding current  $I_s$ , input power  $P_{in}$ , output power  $P_{out}$ , electrical losses  $P_{els}$ , magnetic losses  $P_{mags}$ , required for thermal calculation, are summarized in Table 1.

Table 1  
The value of the quantities required for thermal calculation

Mode	$I_s$ , A	$P_{in}$ , W	$P_{out}$ , W	$P_{els}$ , W	$P_{mags}$ , W
INW	66,5	4142	–	4101	41
WNW	35,0	1190	0	1139	51
NLM	36,0	3074	1827	1206	47
MLM	46,0	5727	3715	1969	43

The results of the calculations are given in Table 2. Exceeding the temperature of the oil at the outlet above the temperature of the oil at the inlet in the modes is: INW – 22 °C, WNW – 6 °C, NLM – 7 °C, MLM – 11 °C.

As predicted in [19], the INW mode is the most stressful both from the point of view of the current load and the heating of the elements of the inductor structures. Therefore, it is very undesirable to have the inductor in this mode for a long time, that is, without ferromagnetic elements in the working chamber.

In other modes, and primarily in the nominal load mode, the temperature state of the inductor is quite moderate. The following factors contributed to this:

1) the reasonable selection of the stator winding voltage relative to the given level of magnetic flux density in the working chamber;

2) the use of a two-layer shortened stator loop winding with thinned and sparse frontal parts, which also ensures the symmetry of the three-phase inductor system and improved distribution of the magnetic field in the stator core and the working chamber;

3) the use of axial ventilation channels in the stator core.

Table 2  
Comparison of thermal calculation results for four oil-cooled inductor operating modes

Mode	Node numbers of the circuit and their temperature, °C					
	1	2	3	4	5	6
INW	62	71	44	31	30	30
WNW	32	34	27	23	23	23
NLM	32	35	27	23	23	23
MLM	40	45	31	26	25	25
	Node numbers of the circuit and their temperature, °C					
	7	8	9	10	11	
INW	41	36	53	46	77	
WNW	26	25	29	27	36	
NLM	26	25	30	28	37	
MLM	30	28	36	32	47	

Note that if we take the temperature of the environment and transformer oil at the level of 40 °C, as is done for electric machines, then all the temperatures in

Table 2 increase accordingly. The highest temperature of the frontal part then reaches almost 100 °C, and this already requires serious attention.

To complement the thermal calculation, hydraulic calculation is performed in parallel with it, of course, here too. The corresponding equivalent hydraulic circuit of the EMM inductor shown in Fig. 5 is linear and consists of serially connected sections. It contains sections with the following hydraulic resistances: inlet nozzle (path resistance  $Z_1$ ), exit to the space under the frame (sudden expansion of the channel  $Z_2$ ), space under the frame to the frontal parts (path resistance  $Z_3$ ), entrance to the space of the frontal parts (sudden narrowing of the channel  $Z_4$ ), space above the frontal parts (path resistance  $Z_5$ ), entrance under the core ring (sudden narrowing of the channel  $Z_6$ ), the core ring (path resistance  $Z_7$ ), entrance to the cooling holes (sudden narrowing of the channel  $Z_8$ ), cooling holes (path resistance  $Z_9$ ), exit from the cooling holes (sudden expansion of the channel  $Z_{10}$ ), core ring (path resistance  $Z_{11}$ ), exit from the core ring (sudden expansion of the channel  $Z_{12}$ ), space above the frontal parts (path resistance  $Z_{13}$ ), entrance to the space under the frame (sudden expansion of the channel  $Z_{14}$ ), space under the frame to the exhaust nozzle (path resistance  $Z_{15}$ ), inlet to the exhaust nozzle (sudden narrowing of the channel  $Z_{16}$ ), exhaust nozzle (path resistance  $Z_{17}$ ).

In the core, 24 cooling channels are placed parallel to each other. Their hydraulic resistances  $Z_8$ ,  $Z_9$  and  $Z_{10}$  make up the parallel branches of the hydraulic circuit with the number  $n_{ok} = 24$ .

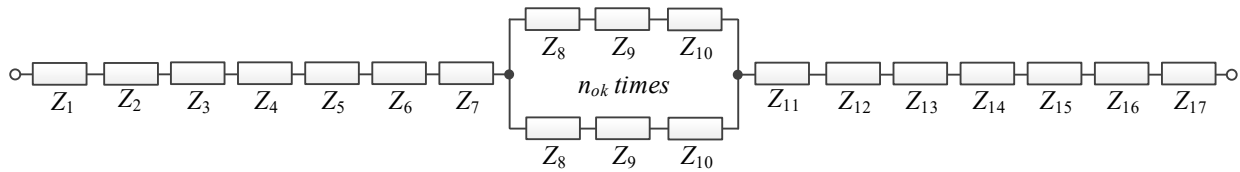


Fig. 5. Equivalent hydraulic circuit of the EMM inductor

Determination of the required oil consumption  $Q_v$  is required during the thermal calculation:

$$Q_v = \frac{k \cdot \Delta P}{C_{oil} \cdot \rho_{oil} \cdot \Delta \theta}, \quad (5)$$

where  $k$  is the coefficient that takes into account that not all heat is removed by oil,  $k = 0.8$ ;  $\Delta P$  is the total losses in the inductor (we assume the «most loaded» thermal mode),  $\Delta P = 4142$  W;  $C_{oil}$  is the specific heat capacity of transformer oil;  $C_{oil} = 1666$  J/(kg·K);  $\rho_{oil}$  is the mass density of transformer oil;  $\rho_{oil} = 880$  kg/m<sup>3</sup>;  $\Delta \theta$  is the permissible temperature excess of the oil during its movement along the hydraulic path,  $\Delta \theta = 22$  °C.

Substitute the value of  $\Delta \theta$  into (5) and we have oil consumption  $Q_v = 1.03 \cdot 10^{-4}$  m<sup>3</sup>/s.

The speed of oil movement depends on the oil consumption  $Q_v$  and the cross section of the corresponding section of the hydraulic path  $S_i$ . Let's determine the average speed of the oil at the entrance to the inlet pipe

$$V_{in} = \frac{Q_v}{S_{in p}}, \quad (6)$$

where  $S_{in p}$  is the cross-sectional area of the inlet pipe,  $S_{in p} = 491$  mm<sup>2</sup>.

Substitute the value of  $S_{in p}$  into (6) and we obtain the speed of oil movement  $V_{in} = 0.21$  m/s.

The hydraulic resistance of the  $i$ -th section of the hydraulic path is determined by the formula from [29]:

$$z_i = \xi_i \cdot \frac{\rho}{2 \cdot S_i^2}, \quad (7)$$

where  $\xi_i$  is the coefficient of hydraulic resistance of the  $i$ -th section of the hydraulic path;  $\rho$  is the mass density of the cooling medium;  $S_i$  is the cross-sectional area of the  $i$ -th section of the hydraulic tract.

After calculating the hydraulic resistances of individual sections, the total hydraulic resistance of the equivalent circuit  $z_\Sigma$  according to Fig. 5 is established, namely:

$$z_\Sigma = 5.46 \cdot 10^9 \text{ (N s}^2\text{)/m}^8.$$

The total pressure flow at such a hydraulic resistance is determined by the formula

$$\Delta P_{G\Sigma} = z_\Sigma \cdot Q_v^2, \quad (8)$$

and is equal to 57.9 Pa or 0.0006 atm.

Taking into account the identified reserves of the temperature state of the mill, as well as the hydraulic state of the oil path, it is possible to make a forecast regarding

the transition from oil cooling to air cooling. For this purpose, estimated thermal and hydraulic calculations were performed with air cooling according to the circuits shown in Fig. 4, 5. They showed that the use of air as a cooling medium while maintaining the structure of the EMM inductor and the close temperature level is technically very difficult, and therefore this option is impractical to implement.

As a result, by further developing the topic of switching to air cooling of the mill, it is possible to allow an increase in the temperature of its inductor elements within the permissible available reserve, as well as the use of a completely or partially open design of the inductor, that is, a significant change in the design of its frame.

### Conclusions.

1. Electromagnetic mills (EMMs) find new applications both in industry and agriculture. Thanks to the introduction of research by scientists, EMMs are increasingly moving from laboratory to industrial applications. But there are still insufficiently researched issues of creation and calculation of EMM inductor oil cooling systems.

2. A mathematical model of the thermal state of the EMM inductor in stationary operating modes with its cooling by transformer oil is formed. The model contains its equivalent thermal circuit and the corresponding system of heat balance equations, and is supplemented with an equivalent hydraulic circuit of oil movement paths along with the formulas of the corresponding parameters.

3. According to the formed model, the thermal calculation of the EMM inductor was performed for four modes of its operation. The obtained temperature data of the constituent elements of the inductor show that they are at a level far enough from the critical one for the applied insulation class B, and the adopted design of the EMM inductor ensures its reliable cooling.

4. According to the estimated calculation, a forecast was made that the use of air for cooling the EMM inductor requires the use of an open structure of its body, that is, a significant change in design.

5. Further work will be devoted both to the improvement of the EMM inductor cooling system with oil, and to the design and calculation studies of its air cooling system.

**Conflict of interest.** The authors of the article declare that there is no conflict of interest.

### REFERENCES

1. Logvinenko D.D., Sheljakov O.P. *Intensifikacija tehnologicheskikh processov v apparatah s vihrevym sloem* [Intensification of technological processes in apparatus with a vortex layer]. Kiev, Tehnika Publ., 1976. 144 p. (Rus).

2. Voitovich V.A., Kart M.A., Zakharychev E.A., Tarasov S.G. Vortex-layer devices as import-substituting equipment to produce paints and adhesives. *Polymer Science, Series D*, 2017, vol. 10, no. 2, pp. 153-155. doi: <https://doi.org/10.1134/S1995421217020253>.

3. Wołosiewicz-Głab M., Foszcz D., Gawenda T., Ogonowski S. Design of an electromagnetic mill. Its technological and control system structures for dry milling. *E3S Web of Conferences*, 2016, vol. 8, art. no. 01066. doi: <https://doi.org/10.1051/e3sconf/20160801066>.

4. Milykh V.I., Shilkova, L. V. Characteristics of a cylindrical inductor of a rotating magnetic field for technological purposes when it is powered from the mains at a given voltage. *Electrical Engineering & Electromechanics*, 2020, no. 2, pp. 13-19. doi: <https://doi.org/10.20998/2074-272X.2020.2.02>.

5. Ibragimov R.A., Korolev E.V., Kayumov R.A., Deberdeev T.R., Leksin V.V., Sprince A. Efficiency of activation of mineral binders in vortex-layer devices. *Magazine of Civil Engineering*, 2018, vol. 82, no. 6, pp. 191-198. doi: <https://doi.org/10.18720/MCE.82.17>.

6. Wołosiewicz-Głab M., Foszcz D., Saramak D., Gawenda T., Krawczykowski D. Analysis of a grinding efficiency in the electromagnetic mill for variable process and feed parameters. *E3S Web of Conferences*, 2017, vol. 18, art. no. 01012. doi: <https://doi.org/10.1051/e3sconf/20171801012>.

7. Całus D., Makarchuk O. Analysis of interaction of forces of working elements in electromagnetic mill. *Przegląd Elektrotechniczny*, 2019, vol. 95, no. 12, pp. 64-69. doi: <https://doi.org/10.15199/48.2019.12.12>.

8. Wołosiewicz-Głab M., Pięta P., Foszcz D., Niedoba T., Gawenda T. Adjustment of limestone grinding in an electromagnetic mill for use in production of sorbents for flue gas desulphurization. *Physicochemical Problems of Mineral Processing*, 2019, vol. 55, no. 3, pp. 779-791. doi: <https://doi.org/10.5277/ppmp19011>.

9. Ogonowski S., Wołosiewicz-Głab M., Ogonowski Z., Foszcz D., Pawełczyk M. Comparison of Wet and Dry Grinding in Electromagnetic Mill. *Minerals*, 2018, vol. 8, no. 4, art. no. 138. doi: <https://doi.org/10.3390/min8040138>.

10. Zhakirova N., Salakhov R., Sassykova L., Khamidullin R., Deberdeev T., Yalyshev U., Khamidi A., Seilkhanov T. Increasing the Yield of Light Distillates by Wave Action on Oil Raw Materials. *Eurasian Chemico-Technological Journal*, 2021, vol. 23, no. 2, pp. 125-132. doi: <https://doi.org/10.18321/ectj1083>.

11. Kovalev A.A., Kovalev D.A., Grigoriev V.S., Litt Y.V. The vortex layer apparatus as a source of low-grade heat in the process of pretreatment of the substrate before anaerobic digestion. *IOP Conference Series: Earth and Environmental Science*, 2021, vol. 938, no. 1, art. no. 012004. doi: <https://doi.org/10.1088/1755-1315/938/1/012004>.

12. *Mixing machine AVS-100. Electromagnetic mill.* Available at: <https://globecore.com/products/magnetic-mill/mixing-machine-avs-100/> (Accessed 20.02.2022).

13. Ogonowski S., Ogonowski Z., Pawełczyk M. Multi-Objective and Multi-Rate Control of the Grinding and Classification Circuit with Electromagnetic Mill. *Applied Sciences*, 2018, vol. 8, no. 4, art. no. 506. doi: <https://doi.org/10.3390/app8040506>.

14. Krawczykowski D., Foszcz D., Ogonowski S., Gawenda T., Wołosiewicz-Głab M. Analysis of the working chamber size influence on the effectiveness of grinding in electromagnetic mill. *IOP Conference Series: Materials Science and Engineering*, 2018, vol. 427, art. no. 012033. doi: <https://doi.org/10.1088/1757-899X/427/1/012033>.

15. Ogonowski S. On-Line Optimization of Energy Consumption in Electromagnetic Mill Installation. *Energies*, 2021, vol. 14, no. 9, art. no. 2380. doi: <https://doi.org/10.3390/en14092380>.

16. Styła S., Mańko M. A reluctance model of an electromagnetic mill using the stator of an asynchronous motor as an inductor. *Przegląd Elektrotechniczny*, 2020, vol. 96, no. 1, pp. 254-257. doi: <https://doi.org/10.15199/48.2020.01.58>.

17. Milykh V.I., Shilkova L.V. Numerical-experimental analysis of the magnetic field of a magnetic separator inductor on the basis of an asynchronous motor. *Bulletin of NTU «KhPI». Series: Electric machines and electromechanical energy conversion*, 2018, no. 5 (1281), pp. 104-109. (Ukr).

18. Makarchuk O., Calus D., Moroz V. Mathematical model to calculate the trajectories of electromagnetic mill operating elements. *Technical Electrodynamics*, 2021, no. 2, pp. 26-34. doi: <https://doi.org/10.15407/techmed2021.02.026>.
19. Milykh V.I., Shilkova L.V. Control current method of the concentration of ferromagnetic elements in the working chamber of the technological inductor of magnetic field during its operation. *Electrical Engineering & Electromechanics*, 2020, no. 5, pp. 12-17. doi: <https://doi.org/10.20998/2074-272X.2020.5.02>.
20. Shcherban' E.M., Stel'makh S.A., Beskopylny A., Mailyan L.R., Meskhi B., Shuyskiy A. Improvement of Strength and Strain Characteristics of Lightweight Fiber Concrete by Electromagnetic Activation in a Vortex Layer Apparatus. *Applied Sciences*, 2021, vol. 12, no. 1, art. no. 104. doi: <https://doi.org/10.3390/app12010104>.
21. Krauze O., Buchczik D., Budzan S. Measurement-Based Modelling of Material Moisture and Particle Classification for Control of Copper Ore Dry Grinding Process. *Sensors*, 2021, vol. 21, no. 2, art. no. 667. doi: <https://doi.org/10.3390/s21020667>.
22. Styła S. Analysis of temperature distribution in electromagnetic mill. *Przegląd Elektrotechniczny*, 2016, vol. 92, no. 3, pp. 103-106. doi: <https://doi.org/10.15199/48.2016.03.25>.
23. Vlasov A.B., Mukhin E.A. Methodology for calculating the temperature of the windings of an electric machine based on quantitative thermography. *Vestnik of MSTU*, 2011, vol. 14, no. 4, pp. 671-680. (Rus).
24. Yang Y., Bilgin B., Kasprzak M., Nalakath S., Sadek H., Preindl M., Cotton J., Schofield N., Emadi A. Thermal management of electric machines. *IET Electrical Systems in Transportation*, 2017, vol. 7, no. 2, pp. 104-116. doi: <https://doi.org/10.1049/iet-est.2015.0050>.
25. Lundmark S.T., Acquaviva A., Bergqvist A. Coupled 3-D Thermal and Electromagnetic Modelling of a Liquid-cooled Transverse Flux Traction Motor. *2018 XIII International Conference on Electrical Machines (ICEM)*, 2018, pp. 2640-2646. doi: <https://doi.org/10.1109/ICELMACH.2018.8506835>.
26. Milykh V.I., Tymin M.G. A comparative analysis of the parameters of a rotating magnetic field inductor when using concentric and loop windings. *Electrical Engineering & Electromechanics*, 2021, no. 4, pp. 12-18. doi: <https://doi.org/10.20998/2074-272X.2021.4.02>.
27. Ostashevskiy N.A., Shayda V.P., Petrenko A.N. Research into thermal state of a frequency-controlled asynchronous motor by means of a finite element method. *Electrical Engineering & Electromechanics*, 2011, no. 5, pp. 39-42. (Rus).
28. Kazi S.N. (Ed.) *Heat Transfer Phenomena and Applications*. London, United Kingdom, IntechOpen, 2012. doi: <https://doi.org/10.5772/3391>.
29. Ostashevskiy N.A., Petrenko A.N., Yurieva O.Yu. *Teplovi rozrakhunky elektrychnykh mashyn* [Thermal calculations of electric machines]. Kharkiv, O.M. Beketov NUUEKh Publ., 2020. 450 p. (Ukr).
30. *The Engineering Toolbox*. Available at: <https://www.engineeringtoolbox.com> (Accessed 20.02.2022).
31. *Materials Thermal Properties Database*. Available at: <https://thermtest.com/thermal-resources/materials-database> (Accessed 20.02.2022).
32. Duong M.T., Chun Y.-D., Park B.-G., Kim D.-J., Choi J.-H., Han P.-W. Thermal analysis of a high speed induction motor considering harmonic loss distribution. *Journal of Electrical Engineering and Technology*, 2017, vol. 12, pp. 1503-1510. doi: <https://doi.org/10.5370/JEET.2017.12.4.1503>.
33. Shams Ghahfarokhi P., Podgornovs A., Kallaste A., Cardoso A.J.M., Belahcen A., Vaimann T., Asad B., Tiismus H. Determination of Heat Transfer Coefficient from Housing Surface of a Totally Enclosed Fan-Cooled Machine during Passive Cooling. *Machines*, 2021, vol. 9, no. 6, art. no. 120. doi: <https://doi.org/10.3390/machines9060120>.
34. *SMATH Studio*. Available at: <https://smath.com> (Accessed 20.02.2022).

Received 11.08.2022

Accepted 25.10.2022

Published 06.05.2023

V.I. Milykh<sup>1</sup>, Doctor of Technical Science, Professor;  
V.P. Shaïda<sup>1</sup>, PhD, Associate Professor;  
O.Yu. Yurieva<sup>1</sup>, PhD, Associate Professor,  
<sup>1</sup>National Technical University «Kharkiv Polytechnic Institute»,  
2, Kyrpychova Str., Kharkiv, 61002, Ukraine,  
e-mail: mvikemkpi@gmail.com (Corresponding Author),  
vpsh1520@gmail.com; ele6780@gmail.com

#### How to cite this article:

Milykh V.I., Shaïda V.P., Yurieva O.Yu. Analysis of the thermal state of the electromagnetic mill inductor with oil cooling in stationary operation modes. *Electrical Engineering & Electromechanics*, 2023, no. 3, pp. 12-20. doi: <https://doi.org/10.20998/2074-272X.2023.3.02>



of dynamic systems. Recently, NNs have known large use in modeling, controlling and supervision of industrial systems. Using NN models for measuring, observing and diagnosis can solve many problems of classical modeling. These models allow global monitoring for complex systems, and offer the possibility of fault isolation with necessary decisions [15].

Following the obtained results given in [1] and taking into consideration the results of [2, 3, 16], it is possible to select as an input vector for the NN model the stored energy [17], the Kurtosis and the singular values decomposition (SVD) of each level ( $D_3, D_4, D_5, D_6, D_7$ ) and the resistant torque value. The designed NN model has three layers. Many tests of classification have been realized to determine the optimal structures of the NN model. The NN model used for discrimination of the stator fault is described as follow:

- 16 neural for the input layer;
- 10 neural for the hidden layer;
- 4 neural for the output layer.

The **main objective** of this research work is to present developments by applying NNs in fault diagnosis. Methods of diagnosis based on a black box model type (NNs with supervised learning) have been adopted. This research work is subdivided in two steps:

- The first step concerns a formulation of an input vector based on the Kurtosis values, SVD and the stored energy values in each level  $D_3, D_4, D_5, D_6, D_7$  with variations in short circuit percentage between 0 to 15 %. This formulation is applied for the phase A, B and C respectively in different operating regime from 0 to 7 N·m with a variation step of 0.25.

- The second step concerns the classifier conception to classify the operating modes of the induction machine. So, different classes are distinguished, three classes are used for fault cases and one class is used for normal case.

**Three-phase equivalent model of unbalanced asynchronous machine (X. Chang model).** The present paper shows an induction machine model taking into account a short circuit in the three-phases of the machine. To extract electrical faults signature, the stator currents of the phases are used. First, to detect effectively the presence of the signatures related to the stator currents of three-phase model, sophisticated techniques have been proposed. Furthermore, the obtained results using numerical simulation demonstrate that excellent performances have been obtained using the proposed method. Finally, in last section, many comments and explanations are highlighted. The model used in this work is the X. Chang model which equivalent three-phase model having the following properties:

- all parameters of the model are computable online;
- this model is derived directly from the equivalent three-phase model, no additional assumptions required;
- the mutual inductances no longer depend on the relative position between the stator and the rotor, the value of this position is unknown in practice;
- the model is verified by comparing the simulation data to the experimental data obtained on a test rig (Poitiers LAII Laboratory, France) in the time domain.

The motor model [6] in the presence of short circuit fault is obtained from electric and magnetic equations of

asynchronous machine. X. Chang et al, have proposed a transformation matrix  $T$  to transform the rotor variables into new variables having the same angular stator frequency. Equations (1) – (4) represent the new three-phase model in which all parameters can be computed on-line [8, 9]:

$$[U_s] = [R_s] \times [I_s] + [P \Psi_s]; \quad (1)$$

$$[0] = [R_r] \times [I_r^s] + (1-g)\Omega [K_{rs}^{sp}] [\Psi_r^s] + P [\Psi_r^s]; \quad (2)$$

$$[\Psi_s] = [M_s] \times [I_s] + [M_{sr}^s] \times [I_r^s]; \quad (3)$$

$$[\Psi_r^s] = [M_{sr}^s] \times [I_s] + [M_r^s] \times [I_r^s]; \quad (4)$$

where  $P$  is the differential operator  $d/dt$ .

- stator variables are:

$$[U_s] = [u_{sa} \quad u_{sb} \quad u_{sc}]^T; \quad (5)$$

$$[I_s] = [I_{sa} \quad I_{sb} \quad I_{sc}]^T; \quad (6)$$

$$[\Psi_s] = [\Psi_{sa} \quad \Psi_{sb} \quad \Psi_{sc}]^T; \quad (7)$$

$$[U_r] = [0 \quad 0 \quad 0]^T; \quad (8)$$

- rotor variables are:

$$[I_r] = [I_{ra} \quad I_{rb} \quad I_{rc}]^T; \quad (9)$$

$$[\Psi_r] = [\Psi_{ra} \quad \Psi_{rb} \quad \Psi_{rc}]^T; \quad (10)$$

$$[\Psi_r^s] = [T] \times [\Psi_r]; \quad (11)$$

$$[I_r^s] = [T] \times [I_r]; \quad (12)$$

$$[M_{rs}^s] = [T] \times [M_{rs}]; \quad (13)$$

$$[M_r^s] = [T] \times [M_r] \times [T]^{-1}; \quad (14)$$

It is important to note that the matrixes  $[R_s]$ ,  $[R_r]$ ,  $[L_{s\sigma}]$ ,  $[L_{r\sigma}]$ ,  $[M_{ss}]$ , and  $[M_{rr}]$  are constant matrixes. The parameters values depend on the number of considered coils turns. The matrixes  $[M_{sr}]$  and  $[M_{rs}]$  are with coefficients varying over time. Thus, the coefficients are in function of the relative position  $\theta$  between the stator and the rotor. This position is defined as follows:  $\theta$  is the angle between the stator phase A and the rotor phase A, thus the following expressions are obtained:

$$\begin{cases} \theta \cong \int \Omega' dt; \\ \Omega' \cong (1-g)\Omega; \\ g \cong (\Omega - \Omega') / \Omega, \end{cases}$$

where  $g$  is the slip coefficient;  $\Omega$  is the rotating field speed;  $\Omega'$  is the rotor mechanical speed.

If the rotor is balanced, the following equations are deduced:

$$[R_r] = \begin{bmatrix} R_r & 0 & 0 \\ 0 & R_r & 0 \\ 0 & 0 & R_r \end{bmatrix}; \quad (15)$$

$$[L_{r\sigma}] = \begin{bmatrix} L_{r\sigma} & 0 & 0 \\ 0 & L_{r\sigma} & 0 \\ 0 & 0 & L_{r\sigma} \end{bmatrix}; \quad (16)$$

$$[M_{rr}] = \begin{bmatrix} M_r & -M_r/2 & -M_r/2 \\ -M_r/2 & M_r & -M_r/2 \\ -M_r/2 & -M_r/2 & M_r \end{bmatrix}. \quad (17)$$

The following coefficients are defined as:

$$f_{sa}^* = 1 - f_{sa}; \quad f_{sb}^* = 1 - f_{sb}; \quad f_{sc}^* = 1 - f_{sc},$$

where  $f_{sa}$ ,  $f_{sb}$  and  $f_{sc}$  are the percentages of turns number reduction in stator 3 phases  $A$ ,  $B$  and  $C$ .

The matrixes  $[R_s]$ ,  $[L_{s\sigma}]$ ,  $[M_{ss}]$ ,  $[M_{sr}]$  and  $[M_{rs}]$  depend on 3 coefficients  $f_{sa}^*$ ,  $f_{sb}^*$  and  $f_{sc}^*$ :

$$[R_s] = R_s \begin{bmatrix} f_{sa}^* & 0 & 0 \\ 0 & f_{sb}^* & 0 \\ 0 & 0 & f_{sc}^* \end{bmatrix}; \quad (18)$$

$$[L_{s\sigma}] = R_s \begin{bmatrix} f_{sa}^{*2} L_{s\sigma} & L_0 & L_0 \\ L_0 & f_{sb}^{*2} L_{s\sigma} & L_0 \\ L_0 & L_0 & f_{sc}^{*2} L_{s\sigma} \end{bmatrix}; \quad (19)$$

$$[M_{ss}] = M_s \begin{bmatrix} f_{sa}^{*2} & \frac{-f_{sa}^* f_{sb}^*}{2} & \frac{-f_{sa}^* f_{sc}^*}{2} \\ \frac{-f_{sa}^* f_{sb}^*}{2} & f_{sb}^{*2} & \frac{-f_{sb}^* f_{sc}^*}{2} \\ \frac{-f_{sa}^* f_{sc}^*}{2} & \frac{-f_{sb}^* f_{sc}^*}{2} & f_{sc}^{*2} \end{bmatrix}; \quad (20)$$

$$[M_{sr}] = M \begin{bmatrix} f_{sa}^* \cos(\theta) & f_{sa}^* \cos(\theta + \frac{2\pi}{3}) & f_{sa}^* \cos(\theta - \frac{2\pi}{3}) \\ f_{sb}^* \cos(\theta - \frac{2\pi}{3}) & f_{sb}^* \cos(\theta) & f_{sb}^* \cos(\theta + \frac{2\pi}{3}) \\ f_{sc}^* \cos(\theta + \frac{2\pi}{3}) & f_{sc}^* \cos(\theta - \frac{2\pi}{3}) & f_{sc}^* \cos(\theta) \end{bmatrix}; \quad (21)$$

where:

$$[M_{sr}] = [M_{rs}]^T. \quad (22)$$

The transformation matrix  $T$ :

$$T = \frac{2}{3} \begin{bmatrix} \cos(\theta) + \frac{1}{2} & \cos(\theta + \frac{2\pi}{3}) + \frac{1}{2} & \cos(\theta - \frac{2\pi}{3}) + \frac{1}{2} \\ \cos(\theta - \frac{2\pi}{3}) + \frac{1}{2} & \cos(\theta) + \frac{1}{2} & \cos(\theta + \frac{2\pi}{3}) + \frac{1}{2} \\ \cos(\theta + \frac{2\pi}{3}) + \frac{1}{2} & \cos(\theta - \frac{2\pi}{3}) + \frac{1}{2} & \cos(\theta) + \frac{1}{2} \end{bmatrix}; \quad (23)$$

where:

$$[T]^{-1} = [T]^T. \quad (24)$$

From (1)–(4), the new model is rewritten in the following form:

$$P[\Psi_r^s] = [R_r] \times [M_r^s]^{-1} \times [M_{rs}^s] \times [I_s] - \left( [R_r] \times [M_r^s]^{-1} + (1-g)\mathcal{O}[K_{rs}^{sp}] \right) \times [\Psi_r^s] \quad (25)$$

$$P[I_s] = \Gamma^{-1} \left( [U_s] - \left( [R_s] + [M_{rs}^s] \times [M_r^s]^{-1} [R_r] [M_r^s]^{-1} [M_{rs}^s] \right) [I_s] \right) + \Gamma^{-1} [M_{rs}^s] [M_r^s]^{-1} \left( [R_r] \times [M_r^s]^{-1} + (1-g)\mathcal{O}[K_{rs}^{sp}] \right) [\Psi_r^s], \quad (26)$$

where:

$$\Gamma = \left( [M_s] - [M_{sr}] \times [M_r^s]^{-1} [M_{rs}^s] \right). \quad (27)$$

The obtained equations are nonlinear; thus, a numerical method must be implemented to reach a solution and the classical 4th order Runge Kutta method is chosen:

$$[K_{rs}^{sp}] = \begin{bmatrix} 0 & \sqrt{3}/3 & -\sqrt{3}/3 \\ -\sqrt{3}/3 & 0 & \sqrt{3}/3 \\ \sqrt{3}/3 & -\sqrt{3}/3 & 0 \end{bmatrix}. \quad (28)$$

**Mechanical equations.** According to [10] if we consider the current and flux in three-phase frame, the following expression is obtained:

$$C_{em} = \frac{P}{\sqrt{3}} \left( \Psi_{sb} I_{sa} - \Psi_{sc} I_{sa} - \Psi_{sa} I_{sb} + \Psi_{sc} I_{sb} - \Psi_{sa} I_{sc} - \Psi_{sb} I_{sc} \right). \quad (29)$$

In the case of three-phase source without neutral:

$$\begin{cases} I_{sa} = -I_{sb} - I_{sc}; \\ \Psi_{sa} = -\Psi_{sb} - \Psi_{sc}. \end{cases} \quad (30)$$

From this, the equation presented below is obtained:

$$C_{em} = \sqrt{3} P (\Psi_{sc} I_{sb} - \Psi_{sb} I_{sc}). \quad (31)$$

**Automatic detection steps of stator faults. DWT application for diagnosis.** The three-phase model of the synchronous machine is called X. Chang, which take into account a disequilibrium mode in the stator turns [1]. This model has ability to study many phenomena more than a short circuit fault in synchronous machines, which allows to select an efficient diagnosis method. For this reason, the DWT technique has been used [1]. This technique has proved significant results in terms of short circuit faults. In addition, it facilitates the X. Chang model use in real time to diagnosis and control of machines.

Analysis of wavelets is performed in order to study the spectral behavior, elaborate reliable spectral signatures, characterize short circuit fault between turns, and estimate in real time the phase currents ( $I_A$ ,  $I_B$  and  $I_C$ ).

In order to study the effect of turn number in short circuit ( $f_{sa}$ ,  $f_{sb}$  and  $f_{sc}$ ) on one of the three stators phase the nominal load  $C$  is fixed to 7 N·m, with variation in turn number between 0 % and 15 %. The experiment tests have been realized under variation of load between 0 and 7 N·m with a sampling step equals to 0.25. The obtained results in [1] show that the application of the wavelet technique is largely used for fault diagnosis. In fact, this technique allows decomposing the stator signal for a non-stationary current during a short circuit. The direct decomposition of the stator signal to multilevels generates a real image about the induction machine stator faults.

In the research work [1], it is also remarked that the coefficient amplitudes of signals which are obtained after decomposition are augmented comparing to healthy mode of the machine.

This augmentation is interpreted by the variation of the relative stored energy associated to each level of decomposition. It is observed that, the wavelet technique is used to extract and locate the no-stationary point in signals, which allows to select the stored energy as an important fault indicator. The fault indicator is considered as a parameter to formulate input vector of the artificial neural network (ANN). So, to detect automatically the differential state between the faulty and the healthy machine an ANN is designed.

In order to analyze the no-stationary generated in the stator current during a short-cut of a phase, or in transitional mode, the decomposition of the stator current signal of a specific phase has been performed (Table 1). The decomposition test is realized by using the DWT on the phase A «Daubechies (by 40 dB)». The decomposition level  $n$  depends on the sampling frequency  $f_e$  and the supply frequency  $f_s$  and can be calculated using the equation presented below [18]:

$$n > \frac{\log(f_e/f_s)}{\log 2} + 1, \quad (32)$$

where sampling frequency  $f_e = 2000$  samples/s; supply frequency  $f_s = 50$  Hz.

Table 1

Frequency bands for wavelet signal			
Levels	Approximations		Details
Level 1	A1	0-1000 Hz	1000-2000 Hz
Level 2	A2	0-500 Hz	500-1000 Hz
Level 3	A3	0.250 Hz	250-500 Hz
Level 4	A4	0-125 Hz	125-250 Hz
Level 5	A5	0-62.5 Hz	62.5-125 Hz
Level 6	A6	0-31.25 Hz	31.25-62.5 Hz
Level 7	A7	0-15.625 Hz	15.625-31.25 Hz

#### Architecture of the automatic diagnosis system.

By using the NN technique, it is possible to detect a short-cut in a stator phase during the operating of the induction machine. However, the localization of the fault represents a big problem. So, in this work the problem of localization is solved by considering specific indicators for the NN input. These indicators are used for classification and learning of the NN. The short circuit fault on the three stator phases is evident from the wavelet decomposition of stator current signal  $I_A$ , the results of the expertise carried out in our work showed that the best performance of the localization of the short circuit fault phase is the stored energy ( $E_j$ ), the Kurtosis value ( $KT$ ), the singular value decomposition (SVD) of each level  $D_3$ ,  $D_4$ ,  $D_5$ ,  $D_6$  and  $D_7$ :

- the proper value of the stored energy ( $E_j$ ) in each band of frequency is defined by the following formulation:

$$E_j = \sum_{k=1}^{k=n} D_{j,k}^2(n). \quad (33)$$

- Several facts on Kurtosis are transformed into the one for discrete time system as:

$$KT = \frac{\int_{-\infty}^{+\infty} x^4 p(x) dx}{\left[ \int_{-\infty}^{+\infty} x^2 p(x) dx \right]^2} = \lim_{N \rightarrow \infty} \frac{\frac{1}{N-1} \sum_{i=1}^N (x_i - x')^4}{\left\{ \frac{1}{N-1} \sum_{i=1}^N (x_i - x')^2 \right\}^2}, \quad (34)$$

where  $x_i$ ;  $i = 1, 2, \dots, N$  represents the discrete signal data;  $x'$  is an average of  $\{x_i\}$  and given as follow:

$$x' = \frac{1}{N} \sum_{i=1}^N x_i, \quad (35)$$

- the decomposition to singular values (SVD) allows to extract principal components of a matrix. In the case of signals, these principal components are linked to data which maximize the energy of signal. For example, the SVD of a matrix that composes of vibratory measures in different points allows under certain conditions to extract specific dominant proper modes [4].

In Tables 2–4 among 1334 experiments examples of experiences are presented. For each experiment, the value of load is fixed and the short-cut percentage varies between 0 % and 15 % in the phase A. So, an experiment is repeated for each value of load. The load values considered in the simulation are 0, 3.5 and 7 N·m.

Table 2

Stored energy evolution ( $E_j$ ) in levels  $D_3$ ,  $D_4$ ,  $D_5$ ,  $D_6$  and  $D_7$  in function to short circuit in phase A

Short circuit, %	$E_3$	$E_4$	$E_5$	$E_6$	$E_7$	Torque $C_r$ , N·m
0	0.00032867	0.13039	12.185	0.10273	0.090117	0
1	0.00033862	0.13235	12.846	0.10392	0.089307	
5	0.00039182	0.14131	16.095	0.10922	0.086439	
10	0.00049887	0.15584	21.936	0.11727	0.084027	
15	0.00067368	0.17576	30.673	0.12749	0.083692	
0	0.00052029	0.14211	18.863	0.11242	0.098359	3.5
1	0.00054522	0.14478	19.988	0.11424	0.098125	
5	0.00066619	0.15701	25.356	0.12237	0.097866	
10	0.00087918	0.17681	34.567	0.13490	0.099550	
15	0.00119040	0.20373	47.724	0.15096	0.104510	
0	0.00210290	0.30525	121.46	0.19438	0.196270	7
1	0.00218110	0.31311	126.18	0.19935	0.199820	
5	0.00253800	0.34828	147.43	0.22160	0.216480	
10	0.00310670	0.40248	180.55	0.25584	0.244090	
15	0.00385850	0.47173	223.27	0.29941	0.281750	

Table 3

SVD evolution in levels  $D_3$ ,  $D_4$ ,  $D_5$ ,  $D_6$  and  $D_7$  in function to short circuit in phase A

Short circuit, %	$SVD_3$	$SVD_4$	$SVD_5$	$SVD_6$	$SVD_7$	Torque $C_r$ , N·m
0	0.81076	16.149	156.11	14.334	13.425	0
1	0.82224	16.270	160.29	14.417	13.365	
5	0.88524	16.812	179.42	14.780	13.148	
10	0.99887	17.655	209.46	15.315	12.964	
15	1.16080	18.749	247.68	15.968	12.938	
0	1.02010	16.859	194.23	14.995	14.026	3.5
1	1.04420	17.016	199.94	15.116	14.009	
5	1.15430	17.720	225.19	15.644	13.990	
10	1.32600	18.805	262.93	16.426	14.110	
15	1.54300	20.186	308.95	17.376	14.457	
0	2.05080	24.708	492.88	19.717	19.813	7
1	2.08860	25.024	502.35	19.968	19.991	
5	2.25300	26.392	543.01	21.052	20.808	
10	2.49270	28.372	600.92	22.620	22.095	
15	2.77790	30.716	668.24	24.471	23.738	

Table 4

$KT$  evolution in levels  $D_3$ ,  $D_4$ ,  $D_5$ ,  $D_6$  and  $D_7$  in function to short circuit in phase A

Short circuit, %	$KT_3$	$KT_4$	$KT_5$	$KT_6$	$KT_7$	Torque $C_r$ , N·m
0	193.16	28.635	12.3050	63.194	71.722	0
1	188.78	27.614	11.9410	63.637	71.495	
5	169.47	23.783	10.391	64.755	69.782	
10	149.21	19.579	8.4478	64.377	65.305	
15	142.86	16.032	6.7193	61.632	57.558	
0	195.95	24.129	5.4852	53.033	60.318	3.5
1	199.08	23.101	5.2977	52.963	59.372	
5	214.10	19.302	4.6081	52.059	54.801	
10	236.47	15.270	3.8850	49.466	47.383	
15	259.73	12.022	3.3069	45.319	38.634	
0	449.87	6.6108	1.7489	25.888	22.014	7
1	455.70	6.3101	1.7480	25.802	21.521	
5	477.96	5.2501	1.7434	25.385	19.834	
10	503.00	4.2131	1.7362	24.768	18.421	
15	524.31	3.4466	1.7271	24.176	17.789	

Following Tables 2–4, the stored energy ( $E_j$ ), the Kurtosis value ( $KT$ ) and the singular value decomposition ( $SVD$ ) of different levels ( $D_3$ ,  $D_4$ ,  $D_5$ ,  $D_6$  and  $D_7$ ) are considered efficient indicators for diagnosis of the induction machine in terms of short-cut fault.

**ANN for diagnosis.** The present research work focuses on the use of an artificial NN model. This model allows to

estimate automatically the state of the induction machine in healthy and fault modes basing on the input indicators. Diagnosis using learning and recognition algorithms is considered as a powerful tool comparing to conventional techniques. However, training of an ANN requires a large database to attain high precision. In this sense, the three phases model of the induction machine is used (X. Chang). This model takes into account all possible situations of short circuit percentage for each stator phase.

**Stator fault diagnosis by NN.** The purpose of the proposed fault diagnosis system is to detect and locate short circuits on the stator windings of a three phase induction motor using ANN. The motor fault diagnosis process is shown in [1]. It is composed of four parts: data acquisition, feature extraction, fault detection and post-processing as shown in Fig. 1. The design of the ANN based fault diagnosis system can be decomposed in the following four steps [2]:

- preparation of a training data set for the ANN;
- selection of the ANN architecture;
- training of the ANN model;
- evaluation of the trained model on test dataset.

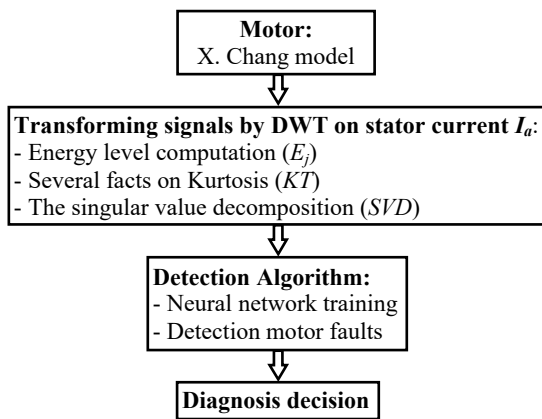


Fig. 1. Flowchart of proposed motor fault diagnosis

**Preparation of the training dataset for NN.** The dataset consists of examples where each example is couple of the input vector and the output default to train the classifier. Input data was collected through simulations using X. Chang's three-phase mathematical model. To locate the faulty phase of an induction motor very efficiently, since the model is practically validated in the NANTE Laboratory, the training data must cover the entire range of operating conditions, including all possible fault phenomena, even healthy cases.

The input matrix  $X_{train}$  and the output matrix  $Y_{train}$  have been used as database to train the ANN model. Equations (25), (26) and (29) are used to formulate the  $X_{train}$  matrix. The experiment tests have been realized under variation of load between 0 and 7 N·m with a sampling step equals to 0.25, which corresponds to the following different operating cases of the induction motor: healthy (29 samples) and fault of an odd number of shorted turns (with variation in turn number between 0 % and 15 %) on each stator phase [(435 = 29·15) samples]. Thus, a total of 1334 (1334 = 435·3 + 29) samples have been collected and applied as the inputs to the NNs for stator inter-turn fault diagnosis.

The desired outputs ( $S_i$ ) of the NN are chosen as follows:

- 1)  $S_1 = 1$  for a short circuit at phase As; otherwise,  $S_1 = 0$ ;
- 2)  $S_2 = 1$  for a short circuit at phase Bs; otherwise,  $S_2 = 0$ ;
- 3)  $S_3 = 1$  for a short circuit at phase Cs; otherwise,  $S_3 = 0$ .

Therefore, the output states of the NNs are set as the following (Table 5):

- [1; 0; 0; 0] – healthy mode;
- [0; 1; 0; 0] – a defect has occurred on phase A;
- [0; 0; 1; 0] – a defect has occurred on phase B;
- [0; 0; 0; 1] – a defect has occurred on phase C.

Table 5

The output states of the NNs

Type of fault	Symbol	S1	S2	S3	S4
Healthy mode	C1	1	0	0	0
Fault occurred on phase A	C2	0	1	0	0
Fault occurred on phase B	C3	0	0	1	0
Fault occurred on phase C	C4	0	0	0	1

The ANN paradigm used in the proposed fault diagnosis system is a feed forward multilayer perceptron NN trained by a back propagation and gradient descent algorithm. The number of input units of ANN is determined by the size of the input vector. However, the number of neurons in the output layer is determined by the number of faults to be diagnosed.

The input vector values are: the stored energy eigenvalues ( $E_j$ ), the Kurtosis value ( $KT$ ) and the singular value decomposition ( $SVD$ ) of each level  $D_3, D_4, D_5, D_6$  and  $D_7$ . The outputs of the ANN represent the fault classes, which are the 3 phases of the induction motor, respectively, and one hidden layer with 10 neurons. The activation functions of the hidden and output layers are «tansig» and «logsig», respectively.

**Training of the NN.** Multilayered perceptron NNs are trained using a supervised learning algorithm known as backpropagation. Backpropagation combined with descent gradient raining is the used training algorithm. It attempts to reduce global error by updating the weights in the direction of the gradient, thereby improving the performance of the ANN.

In this paper, the error is expressed as mean square error (MSE). The training performance is shown in Fig. 2, where a low training MSE is achieved after 334 epochs ( $2.6377 \cdot 10^{-7}$ ). The training output and error from the NN are shown in Fig. 3. From Fig. 4 it is clear that the NN is well trained and reproduces the desired output correctly with few errors.

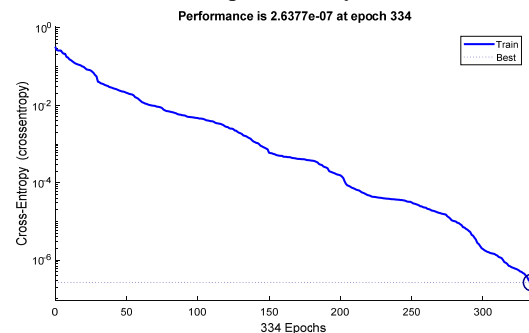


Fig. 2. Training performances of the NN

**Simulation results.** The performance of a NN on the test dataset is its capacity for generalization. This data set is divided into 2 parts. One set is used for training and the other set is used for testing. In fact, the trained ANN classifier performs well on both training and test data. The

test procedure is carried out on an independent test dataset from the training dataset to assess the generalizability of the trained model.

The test data set is presented to the NNs under 14 load torques (0.25, 0.75, 1.25, 1.75, 2.25, 2.75, 3.25, 3.75, 4.25, 4.75, 5.25, 5.75, 6.25, and 6.75 N·m) and corresponds to the

following different operating cases of the induction motor: healthy (14 samples) and fault of an even number of shorted turns (1, 2, 3, 4, 5, 6, 7, 8, 9, 10, 11, 12, 13, 14, and 15) on each stator phase [210 samples]. Thus, a total of 224 test samples were collected to test each phase stator inter-turn fault.

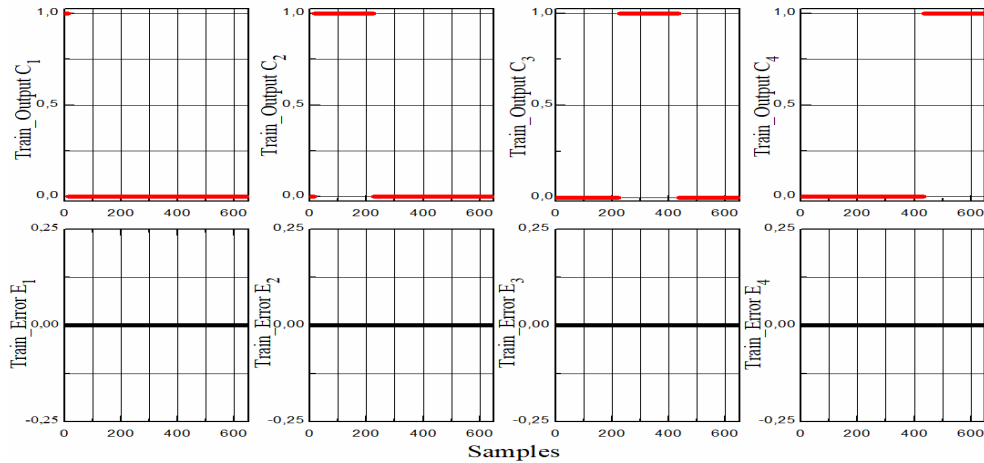


Fig. 3. Training outputs and errors of NN

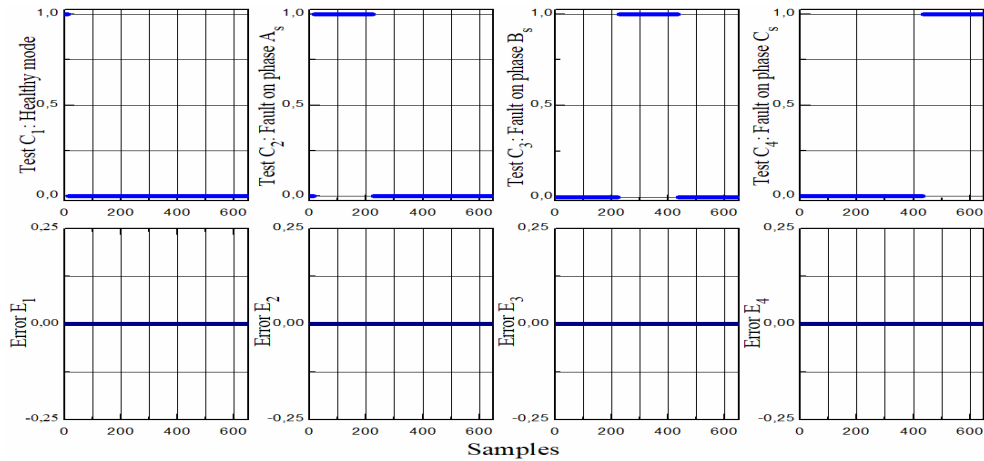


Fig. 4. Test outputs and errors for fault on phase As, Bs and Cs

Figure 4 shows the NN test outputs and their errors for faults on the As, Bs and Cs phases. The test output of the NN (C1, C2, C3, C4) is equal to (1, 0, 0, 0), (0, 1, 0, 0), (0, 0, 1, 0) and (0, 0, 0, 1) with good accuracy. This means that the NN is able to correctly locate the fault occurring on the faulty phase, As phase, Bs phase and Cs phase respectively. The test error for this case is very small. We conclude that the NN is able to correctly locate the stator inter turn short circuit fault occurring on one of the phases.

**Conclusions.** This article presents a technique of detection and localization of short circuit defects of turn-by-turn in induction motors, chosen as a condition model, the three-phase model of X. Chang because it takes into account the case of imbalance in the stator winding. This choice is based on the nature of the fault to be studied (short circuit) and in addition the ease of use of this model for diagnosis and monitoring. In this work, the use of two analytical methods for diagnosing and detecting defects in the machine is based on two techniques, one being discrete wavelet transform and the other on neural network fault classification techniques. The discrete wavelet transform application of the stator current in phase A is used to determine the three parameters that are

sensitive to the short circuit fault: energy, kurtosis and decomposition into singular values of each level  $D_3$ ,  $D_4$ ,  $D_5$ ,  $D_6$  and  $D_7$ . These values are then used as inputs for classifier neural network. The information provided by this input on the detection and localization of defects makes it a reliable indicator of the short circuit defects between coils in the stator windings of induction motors. The results obtained are outstanding, and the proposed technique is capable of automatically detecting and locating short circuit failures. As another area of this paper, we can expand our research to determine the number of short circuits on a faulty phase, allowing for a complete diagnostic procedure.

**Conflict of interest.** The authors declare no conflict of interest.

## REFERENCES

1. Wu Libo, Zhao Zhengming, Liu Jianzheng. A Single-Stage Three-Phase Grid-Connected Photovoltaic System With Modified MPPT Method and Reactive Power Compensation. *IEEE Transactions on Energy Conversion*, 2007, vol. 22, no. 4, pp. 881-886. doi: <https://doi.org/10.1109/TEC.2007.895461>.
2. Sakhara S., Saad S., Nacib L. Diagnosis and detection of short circuit in asynchronous motor using three-phase model.

*International Journal of System Assurance Engineering and Management*, 2017, vol. 8, no. 2, pp. 308-317. doi: <https://doi.org/10.1007/s13198-016-0435-1>.

3. Bessam B., Menacer A., Boumezhaz M., Cherif H. Wavelet transform and neural network techniques for inter-turn short circuit diagnosis and location in induction motor. *International Journal of System Assurance Engineering and Management*, 2017, vol. 8, no. S1, pp. 478-488. doi: <https://doi.org/10.1007/s13198-015-0400-4>.

4. Nacib L., Saad S., Sakhara S. A Comparative Study of Various Methods of Gear Faults Diagnosis. *Journal of Failure Analysis and Prevention*, 2014, vol. 14, no. 5, pp. 645-656. doi: <https://doi.org/10.1007/s11668-014-9860-0>.

5. Talhaoui H., Menacer A., Kessal A., Kechida R. Fast Fourier and discrete wavelet transforms applied to sensorless vector control induction motor for rotor bar faults diagnosis. *ISA Transactions*, 2014, vol. 53, no. 5, pp. 1639-1649. doi: <https://doi.org/10.1016/j.isatra.2014.06.003>.

6. Cherif H., Benakcha A., Khechekhouche A., Menacer A., Chehaidia S.E., Panchal H. Experimental diagnosis of inter-turns stator fault and unbalanced voltage supply in induction motor using MCSA and DWER. *Periodicals of Engineering and Natural Sciences*, 2020, vol. 8, no. 3, pp. 1202-1216. doi: <https://doi.org/10.21533/pen.v8i3.1058.g607>.

7. Xianrong Chang, Cocquemot V., Christophe C. A model of asynchronous machines for stator fault detection and isolation. *IEEE Transactions on Industrial Electronics*, 2003, vol. 50, no. 3, pp. 578-584. doi: <https://doi.org/10.1109/TIE.2003.812471>.

8. Filippetti F., Franceschini G., Tassoni C. Neural networks aided on-line diagnostics of induction motor rotor faults. *Conference Record of the 1993 IEEE Industry Applications Conference Twenty-Eighth IAS Annual Meeting*, 1993, pp. 316-323. doi: <https://doi.org/10.1109/IAS.1993.298942>.

9. Schoen R.R., Lin B.K., Habetler T.G., Schlag J.H., Farag S. An unsupervised, on-line system for induction motor fault detection using stator current monitoring. *IEEE Transactions on Industry Applications*, 1995, vol. 31, no. 6, pp. 1280-1286. doi: <https://doi.org/10.1109/28.475698>.

10. Said M.S.N., Benbouzid M.E.H., Benchaib A. Detection of broken bars in induction motors using an extended Kalman filter for rotor resistance sensorless estimation. *IEEE Transactions on Energy Conversion*, 2000, vol. 15, no. 1, pp. 66-70. doi: <https://doi.org/10.1109/60.849118>.

11. Shutenko O., Ponomarenko S. Analysis of distribution laws of transformer oil indicators in 110-330 kV transformers. *Electrical Engineering & Electromechanics*, 2021, no. 5, pp. 46-56. doi: <https://doi.org/10.20998/2074-272X.2021.5.07>.

12. Paranchuk Y.S., Shabatura Y.V., Kuznyetsov O.O. Electromechanical guidance system based on a fuzzy proportional-plus-differential position controller. *Electrical Engineering & Electromechanics*, 2021, no. 3, pp. 25-31. doi: <https://doi.org/10.20998/2074-272X.2021.3.04>.

13. Belbachir N., Zellagui M., Settoul S., El-Bayeh C.Z., Bekkouche B. Simultaneous optimal integration of photovoltaic distributed generation and battery energy storage system in active

distribution network using chaotic grey wolf optimization. *Electrical Engineering & Electromechanics*, 2021, no. 3, pp. 52-61. doi: <https://doi.org/10.20998/2074-272X.2021.3.09>.

14. Bengharbi A.A., Laribi S., Allaoui T., Mimouni A. Photovoltaic system faults diagnosis using discrete wavelet transform based artificial neural networks. *Electrical Engineering & Electromechanics*, 2022, no. 6, pp. 42-47. doi: <https://doi.org/10.20998/2074-272X.2022.6.07>.

15. Abid M., Laribi S., Larbi M., Allaoui T. Diagnosis and localization of fault for a neutral point clamped inverter in wind energy conversion system using artificial neural network technique. *Electrical Engineering & Electromechanics*, 2022, no. 5, pp. 55-59. doi: <https://doi.org/10.20998/2074-272X.2022.5.09>.

16. Bouchaoui L., Hemsas K.E., Mellah H., Benlahneche S. Power transformer faults diagnosis using undestructive methods (Roger and IEC) and artificial neural network for dissolved gas analysis applied on the functional transformer in the Algerian north-eastern: a comparative study. *Electrical Engineering & Electromechanics*, 2021, no. 4, pp. 3-11. doi: <https://doi.org/10.20998/2074-272X.2021.4.01>.

17. Bessous N., Zouzou S.E., Bentrah W., Sbaa S., Sahraoui M. Diagnosis of bearing defects in induction motors using discrete wavelet transform. *International Journal of System Assurance Engineering and Management*, 2018, vol. 9, no. 2, pp. 335-343. doi: <https://doi.org/10.1007/s13198-016-0459-6>.

18. Kechida R., Menacer A., Talhaoui H. Approach Signal for Rotor Fault Detection in Induction Motors. *Journal of Failure Analysis and Prevention*, 2013, vol. 13, no. 3, pp. 346-352. doi: <https://doi.org/10.1007/s11668-013-9681-6>.

Received 14.10.2022

Accepted 25.12.2022

Published 06.05.2023

Saadi Sakhara<sup>1,2</sup>, PhD, Associate Professor,

Mohamed Brahimi<sup>3</sup>, PhD, Associate Professor,

Leila Nacib<sup>1,2</sup>, PhD, Associate Professor,

Toufik Madani Layadi<sup>4</sup>, PhD, Associate Professor,

<sup>1</sup>Laboratory of Physics of Materials, Radiation and Nanostructures, University Mohamed El Bachir El Ibrahimi of Bordj Bou Arreridj, Algeria.

<sup>2</sup>Department of Electromechanical Engineering, University Mohamed El Bachir El Ibrahimi of Bordj Bou Arreridj, Algeria,

e-mail: saadi.sekhara@univ-bba.dz (Corresponding Author);  
leila.nacib@univ-bba.dz

<sup>3</sup>Physical Chemistry and Biology of Materials Laboratory, National Higher School of Artificial Intelligence, Algeria,  
e-mail: mohamed.brahimi@ensia.edu.dz

<sup>4</sup>Laboratory of Materials and Electronic Systems, Department of Electromechanical Engineering, University Mohamed El Bachir El Ibrahimi of Bordj Bou Arreridj, Algeria,

e-mail: toufikmadani.layadi@univ-bba.dz

#### How to cite this article:

Sakhara S., Brahimi M., Nacib L., Layadi T.M. Application of a wavelet neural network approach to detect stator winding short circuits in asynchronous machines. *Electrical Engineering & Electromechanics*, 2023, no. 3, pp. 21-27. doi: <https://doi.org/10.20998/2074-272X.2023.3.03>

A. Aib, D.E. Khodja, S. Chakroune

## Field programmable gate array hardware in the loop validation of fuzzy direct torque control for induction machine drive

**Introduction.** Currently, the direct torque control is very popular in industry and is of great interest to scientists in the variable speed drive of asynchronous machines. This technique provides decoupling between torque control and flux without the need to use pulse width modulation or coordinate transformation. Nevertheless, this command presents two major importunities: the switching frequency is highly variable on the one hand, and on the other hand, the amplitude of the torque and stator flux ripples remain poorly controlled throughout the considered operating speed range. The **novelty** of this article proposes improvements in performance of direct torque control of asynchronous machines by development of a fuzzy direct torque control algorithm. This latter makes it possible to provide solutions to the major problems of this control technique, namely: torque ripples, flux ripples, and failure to control switching frequency. **Purpose.** The emergence of this method has given rise to various works whose objective is to show its performance, or to provide solutions to its limitations. Indeed, this work consists in validation of a fuzzy direct torque control architecture implemented on the ML402 development kit (based on the Xilinx Virtex-4 type field programmable gate array circuit), through hardware description language (VHDL) and Xilinx generator system. The obtained **results** showed the robustness of the control and sensorless in front of load and parameters variation of induction motor control. The research directions of the model were determined for the subsequent implementation of results with simulation samples. References 19, tables 5, figures 26. **Key words:** fuzzy control, field programmable gate array, Xilinx system generator, direct torque control, power system.

**Вступ.** В даний час пряме управління моментом дуже популярне в промисловості і викликає великий інтерес у вчених у галузі частотно-регульованого приводу асинхронних машин. Цей метод забезпечує розв'язку між керуванням моментом, що крутить, і магнітним потоком без необхідності використання широтно-імпульсної модуляції або перетворення координат. Тим не менш, ця команда представляє дві основні незручності: з одного боку, частота комутації сильно варіюється, а з іншого боку, амплітуда пульсації моменту і потоку статора залишається погано контрольованою у всьому діапазоні робочих швидкостей. **Новизна** цієї статті пропонує поліпшення характеристик прямого керування моментом, що крутить, асинхронних машин шляхом розробки нечіткого алгоритму прямого управління моментом, що крутить. Останнє дозволяє вирішити основні проблеми цього методу управління, а саме: пульсації моменту, що крутить, пульсації потоку і нездатність контролювати частоту перемикання. **Мета.** Поява цього методу породило різні роботи, метою яких є показати його ефективність чи запропонувати рішення стосовно його обмежень. Дійсно, ця робота полягає у перевірці нечіткої архітектури прямого управління моментом, що крутить, реалізованої в наборі для розробки ML402 (на основі схеми Xilinx Virtex-4 з програмованою користувачем вентильною матрицею), за допомогою мови опису обладнання (VHDL) та генераторної системи Xilinx. **Отримані результати** показали робастність керування та безсенсорного керування при зміні навантаження та параметрів керування асинхронним двигуном. Визначено напрями дослідження моделі для подальшої реалізації результатів на імітаційних вибірках. Бібл. 19, табл. 5, рис. 26.

**Ключові слова:** нечітке управління, програмована користувачем вентильна матриця, генераторна система Xilinx, пряме управління моментом, що крутить, система живлення.

**Introduction.** Direct Torque Control (DTC) was realized by Takahashi and Depenbrock [1, 2] is more and more popular and it interests many scientists and industrialists in the field of variable speed applications [3, 4].

However, this strategy has two major drawbacks: on the one hand, the switching frequency is highly variable and on the other hand, the amplitude of the ripples of torque and of stator flux is poorly controlled over the entire speed range of the operation envisaged [5]. It should be noted that torque ripples generate additional noise and vibration and therefore cause fatigue in the rotating shaft [6].

To further reduce the impact of these phenomena on the service life of electric actuators, it is believed that intelligent techniques can provide an improvement. In terms of real-time management of managed applications based on intelligent techniques, there are new hardware design solutions such as Field Programmable Gate Array (FPGA) or application specific integrated circuit [7, 8]. These reconfigurable circuits are available and can be used as digital targets for implementation of control algorithms in a single component [9].

The advantages of such an implementation are multiple: reduction of execution time by adopting parallel processing, rapid prototyping of the numerical control on FPGA. The confidentiality of architecture and possibility

of application of intelligent controls make use of techniques which are more cumbersome in terms of computation time and the improvement of the quality of the control of electric machines [10, 11].

Evolution of micro computing, semiconductor technology and availability of rapid control means such as digital signal processor, reconfigurable circuits (FPGA). Today allows the scientific community to carry out very complex controls while taking into account the non-linearity of mathematical model of asynchronous machine [12, 13].

**The goal of the paper** is to evaluate the performance of the use of a fuzzy DTC inference system versus the classic DTC based on hysterized comparators, for the control of induction machines (IMs) based on a FPGA using available academic tools (MATLAB/Simulink, Xilinx system generator, Xilinx ISE, and ModelSim).

**Basic calculation relationships and assumptions.** The subject of DTC is controlling the torque and stator flux of asynchronous machine by applying several voltage vectors through a voltage inverter.

The control is generally carried out by a hysteresis controller. The purpose of control is to keep controlled variables within a specified hysteresis band [6]. The controller provides the necessary switching pulses to the inverter to generate the optimum voltage vector to supplies

the IM for a defined operating condition. The IM model is used with measured variables to estimate stator flux and electromagnetic torque required by control diagram (Fig. 1), where  $S_a, S_b, S_c$  are the Boolean switching commands;  $\omega$  is the speed for reference speed  $\omega_{ref}$ ;  $E_\phi, E_{T_e}$  are the flux and torque error respectively;  $T_e$  is the electromagnetic torque;  $T_{eref}$  is the reference electromagnetic torque;  $I_{sa}, I_{sb}$  are the stator currents in the  $abc$  reference frame;  $\phi_{sref}$  is the reference stator flux;  $|\phi_s|$  is the stator flux magnitude;  $\theta_{\phi_s}$  is the stator flux angle.

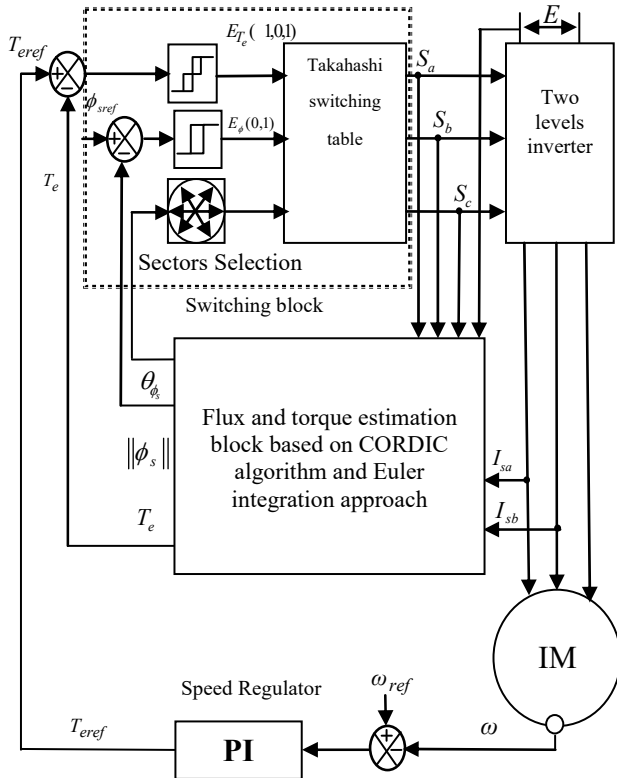


Fig. 1. DTC based IM control structure

The most significant element that can guarantee satisfactory DTC performance is stator flux estimator and torque estimator [12]. In this work we used optimized estimator developed in [14].

**Fuzzy DTC based IM control structure.** The research theme developed in this work mainly concerns the exploitation of new technological solutions to implement an intelligent control based on the DTC of an asynchronous machine around a hardware environment based on a FPGA.

This implementation is mainly aimed at reducing ripples at the level of electromagnetic torque and stator flux. In this part, two hysteresis regulators and Takahashi switching table (Table 1) will be replaced by a fuzzy controller. Figure 2 shows the control structure of fuzzy DTC based IM.

Table 1

		$V_i = (S_a, S_b, S_c)$					
$\phi, T_e, N$		$N=1$	$N=2$	$N=3$	$N=4$	$N=5$	$N=6$
$\phi=1$	$T_e=1$	(1,1,0)	(0,1,0)	(0,1,1)	(0,0,1)	(1,0,1)	(1,0,0)
	$T_e=0$	(1,1,1)	(0,0,0)	(1,1,1)	(0,0,0)	(1,1,1)	(0,0,0)
	$T_e=-1$	(1,0,1)	(1,0,0)	(1,1,0)	(0,1,0)	(0,1,1)	(0,0,1)
$\phi=0$	$T_e=1$	(0,1,0)	(0,1,1)	(0,0,1)	(1,0,1)	(1,0,0)	(1,1,0)
	$T_e=0$	(0,0,0)	(1,1,1)	(0,0,0)	(1,1,1)	(0,0,0)	(1,1,1)
	$T_e=-1$	(0,0,1)	(1,0,1)	(1,0,0)	(1,1,0)	(0,1,0)	(0,1,1)

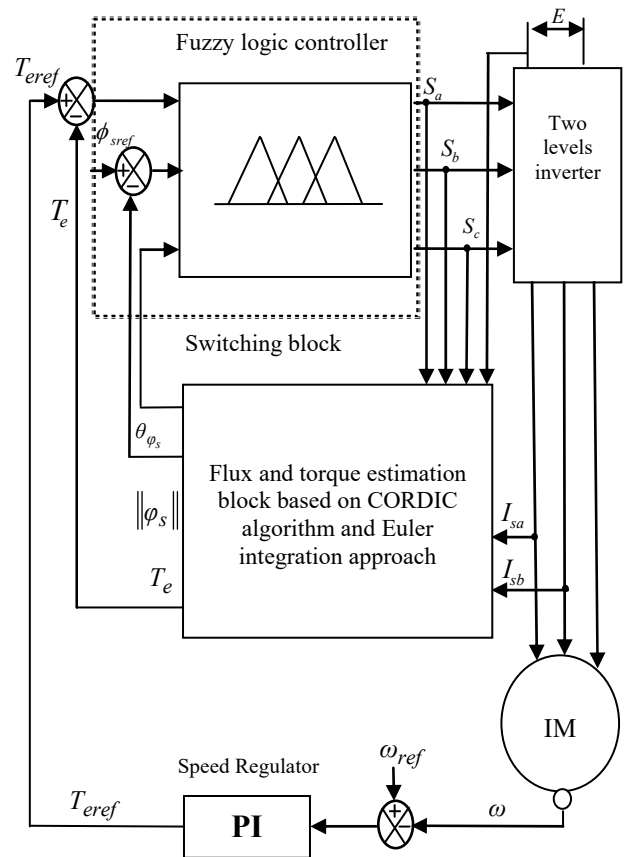


Fig. 2. Fuzzy DTC based IM control structure

**Fuzzy DTC control implementation.** The hardware implementation of a fuzzy inference system consists in implementing 3 phases of a fuzzy logic regulation: fuzzification, fuzzy inferences and defuzzification. This principle is represented by Fig. 3.

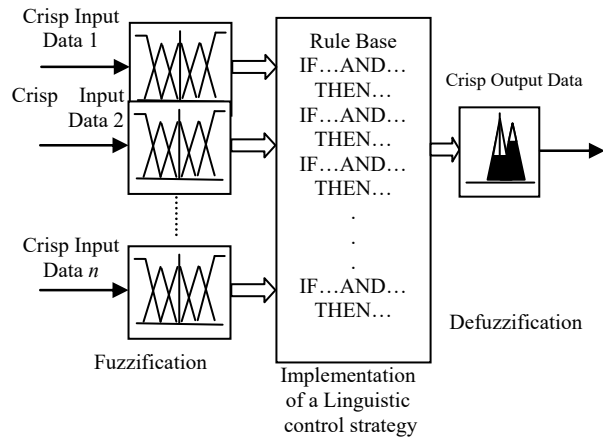


Fig. 3. Components of a fuzzy inference system

**Description of fuzzification module.** Fuzzification is the process of converting input data into fuzzy linguistic values. In literature, there are two material solutions to determine the degree of membership of a fuzzy set from a membership function.

The first solution is the memory-oriented approach, as the name suggests, for each finite number of inputs, the output values are calculated offline then they will be saved in memory. The advantage of this solution is that it is easy to change a membership function. The second solution is the calculation-oriented approach, only the

characteristics of the membership functions are saved in a memory in order to simplify the on-line calculation of output values of each membership function. For the case of triangular membership functions, their characteristics are: the center of the triangle «*c*» and the slope «*a*».

The hardware implementation of this solution is a combinatorial circuit which can include adders, subtractors, multiplexers, multipliers and most of the time a control unit.

In this study, we adopt the memory-oriented approach. Indeed, each linguistic input/output variable is represented by tables, a table for the degree of membership of each linguistic value. These tables are implemented in hardware by memory blocks ROMs addressable by a single input, such as the memory boxes which contain the degree of membership of linguistic value. However, the memory address space gives an image on the universe of discretized speech for example for a universe of normalized speech [0, 1] discretized in 64 points, we therefore use an address space [0: 63].

The membership functions of flux error, torque error, sectors and output vectors are illustrated by the following Fig. 4-7.

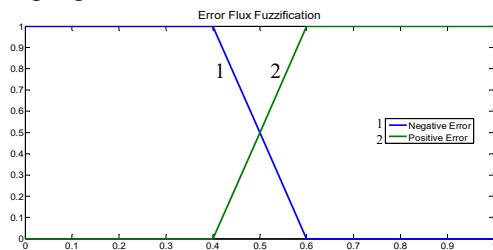


Fig. 4. The fuzzification membership functions of the flux error

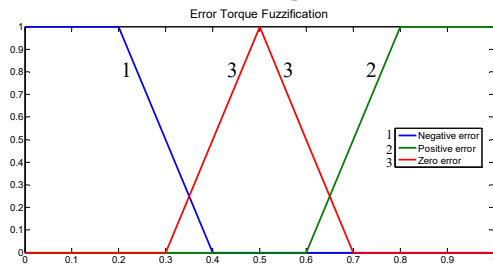


Fig. 5. Fuzzification membership functions of the torque error

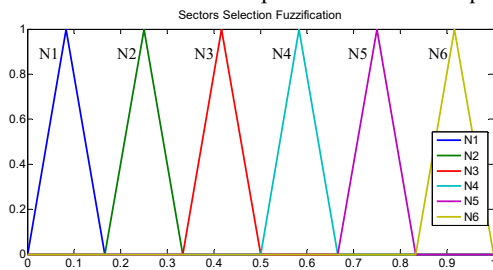


Fig. 6. Fuzzification membership functions of the angle

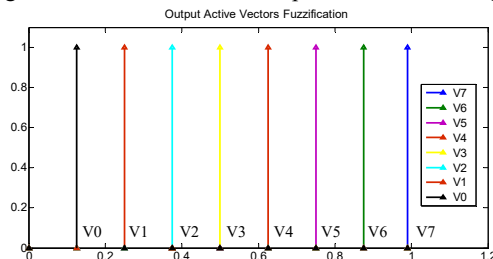


Fig. 7. Membership functions of the output

The hardware implementation of these functions is presented by hardware architectures in Fig. 8-11.

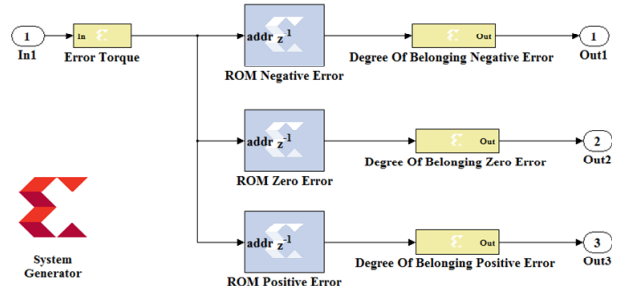


Fig. 8. Hardware architecture of the «Torque Error» linguistic variable

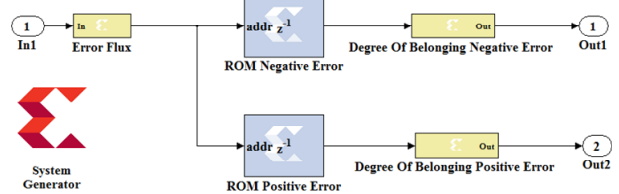


Fig. 9. Hardware architecture of the «Flux Error» linguistic variable

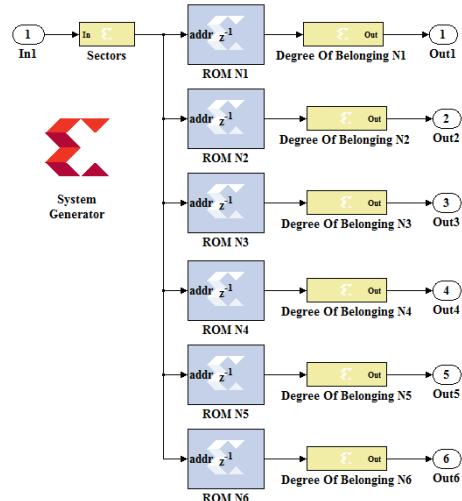


Fig. 10. Hardware architecture of the «Sectors» linguistic variable

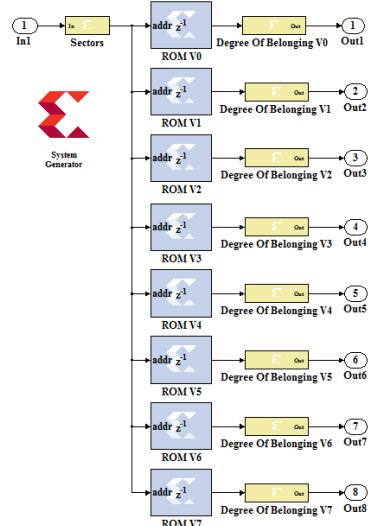


Fig. 11. Hardware architecture of the «Output vector» linguistic variable

The Xilinx resource estimator tool is used to estimate the hardware resources needed to implement each linguistic variable. Figure 12 shows the estimated resources for the linguistic variable «Torque Error».

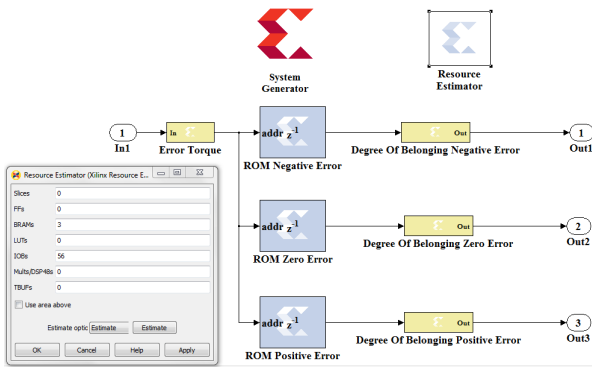


Fig. 12. Hardware resources consumed by the linguistic variable «Torque Error»

**Rule inference and rule evaluation.** Hardware description of fuzzy inference module is shown in Fig. 13. This module accepts as input three blocks of fuzzification module, the rule selector block allows building the rule base formed of 36 rules. This basis is obtained by making all the possible combinations between two fuzzy values of flux error, three fuzzy values of torque error and six fuzzy values of stator flux angle.

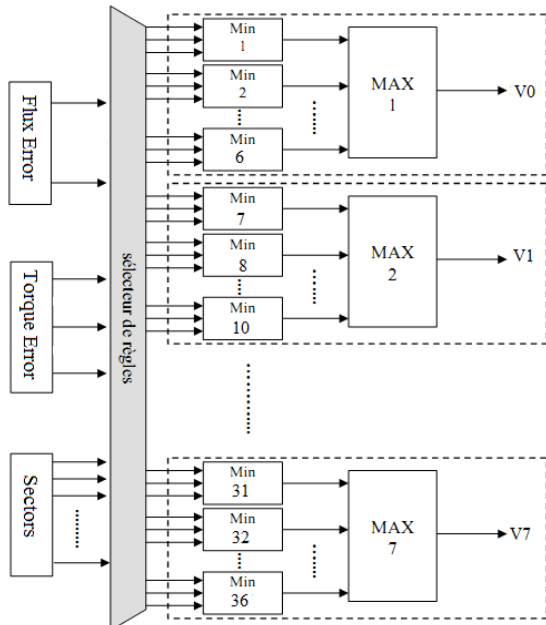


Fig. 13. Architecture of «fuzzy inference» module

The hardware implementation on «Xilinx System Generator» of operators (min/max) with 2 inputs is done by a comparator and a 2-1 multiplexer. Figure 14 shows the wiring of min/max functions.

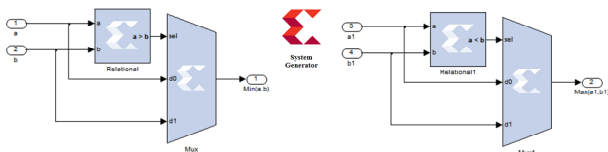


Fig. 14. Implementation of min/max functions on XSG

Using the resource estimator tool allows us to estimate the hardware resources consumed by a two-entry min operator (Fig. 15).

For operators (min/max) that have more than 2 inputs, 2 inputs (min/max) operators are used to implement these operators. For example, to implement an operator (min) with 3 inputs, we use 2 operators (min) with 2 inputs (Fig. 16).

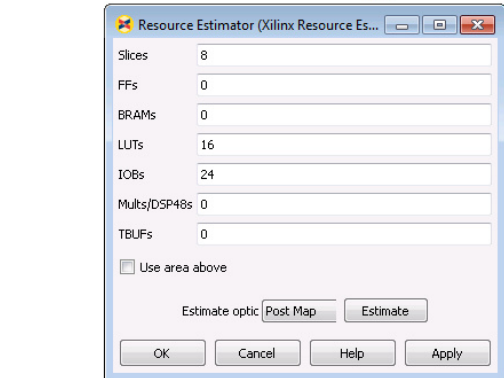
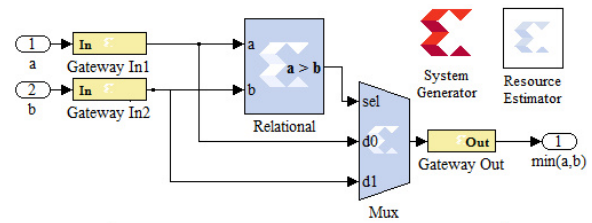


Fig. 15. Hardware resources consumed by a two-entry min operator

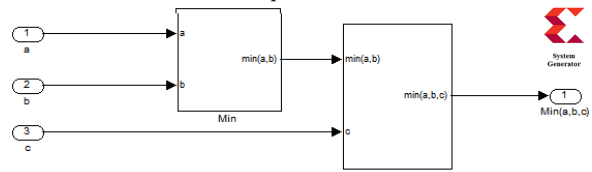


Fig. 16. Implementation of a 3-entry min function

**Composition of the rules.** If several rules can be activated simultaneously and recommend actions with different degrees of validity on same output, we consider that the rules which are linked by an operator OR (Fig. 17)  $\mu_{By} = \max[\mu_{Bi}(y)] i \in \{\text{indices of activated rules}\}$ .

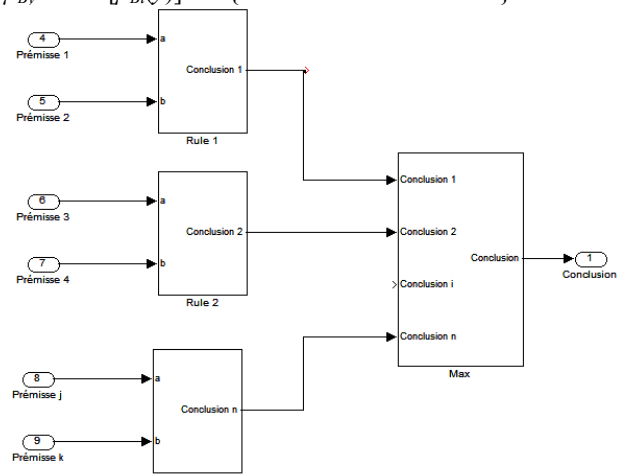


Fig. 17. Implementation of a composition of rules for an output

**Description of defuzzification module.** The hardware description of defuzzification module is carried out by a MAX operator as shown in Fig. 18. The inputs of this module are the outputs of the inference motor module. As it was specified in the preceding paragraph, the  $V_i$  ( $i = 0..7$ ) correspond to the degree of activation of voltages  $V$ . The output of this block, representing the output of the whole fuzzy block, corresponds to the voltage that it must be applied to the terminals of the machine through the inverter. The VHDL architecture of MAX defuzzification module is implemented by an assignment in the competitive mode:

$S_{135} \leq 001$  when  $V1 = \max$   
 else 010 when  $V2 = \max$   
 else 011 when  $V3 = \max$   
 else 100 when  $V4 = \max$   
 else 101 when  $V5 = \max$   
 else 110 when  $V6 = \max$   
 else 111 when  $V7 = \max$   
 else 000

Figure 18 shows a description of VHDL block used to implement the maximum defuzzification method.

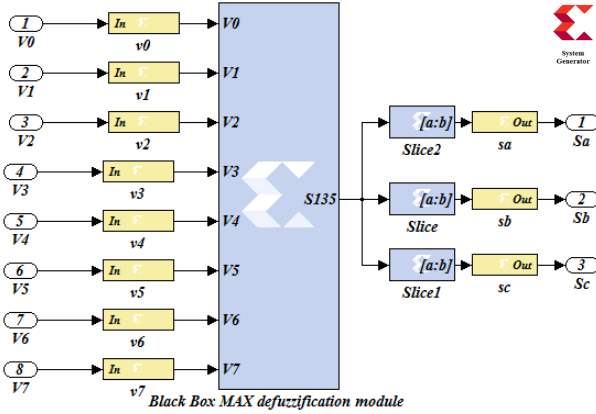


Fig. 18. VHDL MAX defuzzification module

**Simulation of fuzzy DTC control of asynchronous machine.** This phase involves the integration of a fuzzy inference system into DTC control algorithm. In this part, similarly to simulation with MATLAB, we will simulate using Xilinx generator system the architecture of the conventional DTC control and fuzzy DTC control. The fuzzy DTC control is applied to an IM whose specifications are given in Table 2.

Table 2

IM parameters	
Nominal voltage $U_n$ , V	220
Nominal current $I_n$ , A	2.35
Mechanical power $P_m$ , kW	1.08
Nominal speed $N$ , $\text{min}^{-1}$	1430
Supply frequency $f$ , Hz	50
Stator resistance $R_s$ , $\Omega$	10
Rotor resistance $R_r$ , $\Omega$	6.3
Stator self inductance $L_s$ , H	0.4642
Rotor self inductance $L_r$ , H	0.4612
Mutual inductance $L_m$ , H	0.4212
Moment of inertia $J$ , $\text{kg}\cdot\text{m}^2$	0.02
Pole pairs number $p$	2

The structure of conventional DTC control is illustrated in Fig. 1. Regarding fuzzy DTC control shown in Fig. 2, we will replace the blocks of hysteresis comparator modules and DTC control selection table by a fuzzy inference system that we have built and tested. To compare the both control approaches, we simulated these modules on MATLAB / Simulink with Xilinx generator system. The results are illustrated in Fig. 19.

Note that there is an improvement in the electromagnetic flux and torque obtained by the fuzzy DTC control compared to that obtained with the conventional DTC control with a significant reduction in ripples. Table 3 shows the performance in terms of resource consumption, obtained during the implementation of architecture of fuzzy DTC control on VIRTEX 4 FPGA given by architecture presented in Fig. 2.

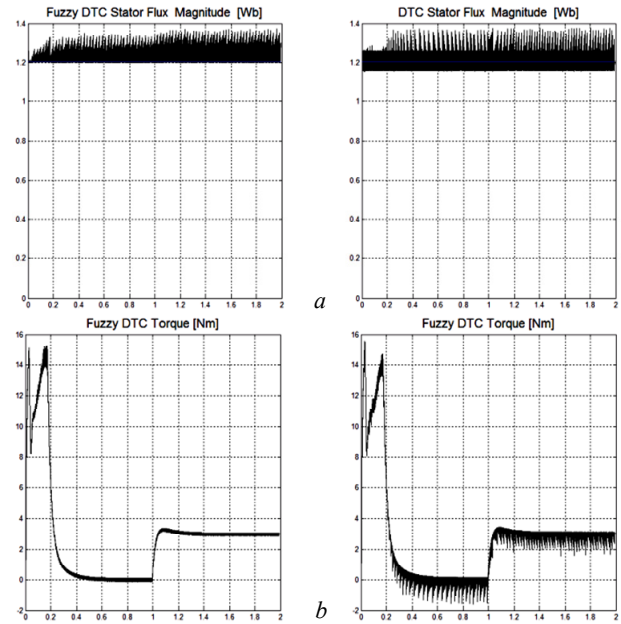


Fig. 19. Electromagnetic torque and stator flux obtained by XSG simulator for DTC (a) and fuzzy DTC (b)

Table 3

Resources used on FPGA circuit by fuzzy DTC control algorithm

Target device: ML402 Virtex-4 xc4vsx35-10ff668			
Logic utilization	Used	Available	Utilization
Number of Slice Flip Flops	1,365	30,72	4 %
Number of occupied Slices	1,620	15,36	10 %
Total Number of 4 input LUTs	2,453	30,72	7 %
Number of bonded IOBs	58	448	12 %
Number of FIFO16/RAMB16s	12	192	6 %
Number of BUFG/BUFGCTRLs	4	32	12 %

We note that the proposed architecture optimizes the use of the hardware resources of FPGA card (10 % of Slices and 7 % of LUTs), moreover this architecture considerably reduces the logical components used compared to architectures presented in [15, 16].

The maximum clock frequency is set by the synthesis tool equal to 231.64 MHz, which corresponds to a minimum period of 4.317 ns. In contrast, in [16] the maximum clock frequency is 54 MHz using DSPACE (Digital Signal Processing and Control Engineering). In [17] the minimum period is equal to 50 ns. We see that execution time is too long compared to FPGA due to sequential processing of DSPACE.

Table 4 presents the hardware resources consumed in this architecture compared to previous work in the same research axis.

Table 4

Comparison of the resources consumption

Logic utilization	References				
	[7]	[18]	[19]	[14]	Proposed
FPGA device family	Xilinx Virtex-4	Altera DE-115	Altera CYCLONE II	Xilinx Virtex-4	Xilinx Virtex-4
Embedded multiplier 9-bit elements	–	80	57	–	–
Total logic elements	10.346	6.931	3.256	2.909	2.836
Total combinational functions	18.594	6.491	2.549	7.411	7.686

**Validation of hardware architecture of proposed fuzzy controller.** After simulation step, the proposed hardware architecture of fuzzy controller was validated by co-simulation hardware on the ML402 target peripheral equipped with a VIRTEX4 FPGA circuit.

This step is dedicated to implement the control algorithms on a development board integrating an FPGA component. It is mainly intended for the verification and validation of digital implementation of control algorithms on FPGA targets in «Hardware in the loop» simulation environment as shown in Fig. 20.

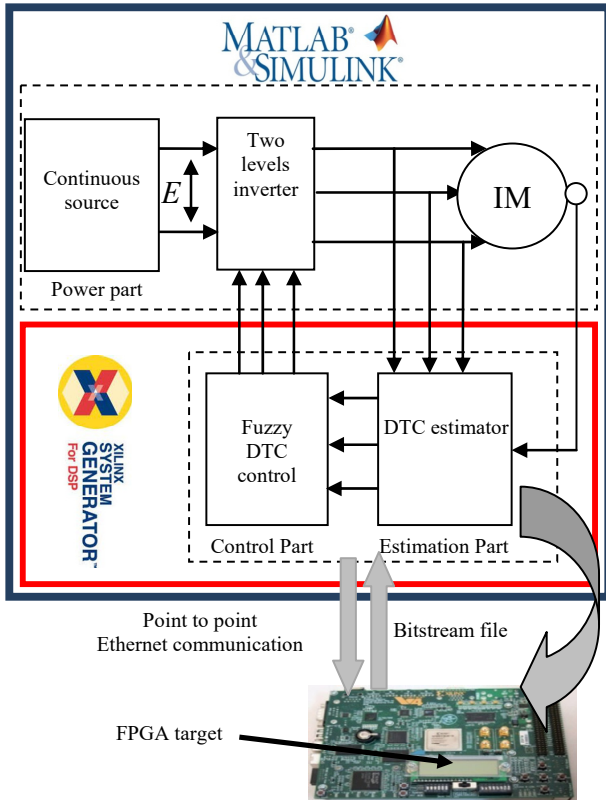


Fig. 20. Hardware in the loop validation of fuzzy DTC controller

Once simulation and timing analysis are done, the procedure of hardware co-simulation in XSG makes a bitstream file from the hardware prototype and a point to point Ethernet block for Hardware-In-the-Loop (HIL) procedure (Fig. 21).

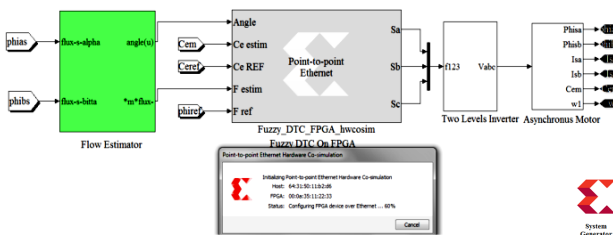


Fig. 21. Fuzzy DTC HIL point to point Ethernet block

The created block (Fig. 20) substitutes the architecture hardware that was constructed before (fuzzy DTC).

The point-to-point Ethernet blocks are linked to inverter and IM to run a HIL (Fig. 22). In this situation the models of motor and inverter are simulate in MATLAB/Simulink environment, and XSG architectures of Fuzzy DTC are achieved in the ML402 FPGA device. The HIL validation is executed by connecting the target device to PC via an Ethernet cable.



Fig. 22. Fuzzy DTC point to point Ethernet hardware in the loop process

Figure 23 show the waveforms of speed, torque and flux of IM controlled by fuzzy DTC control with co-simulation.

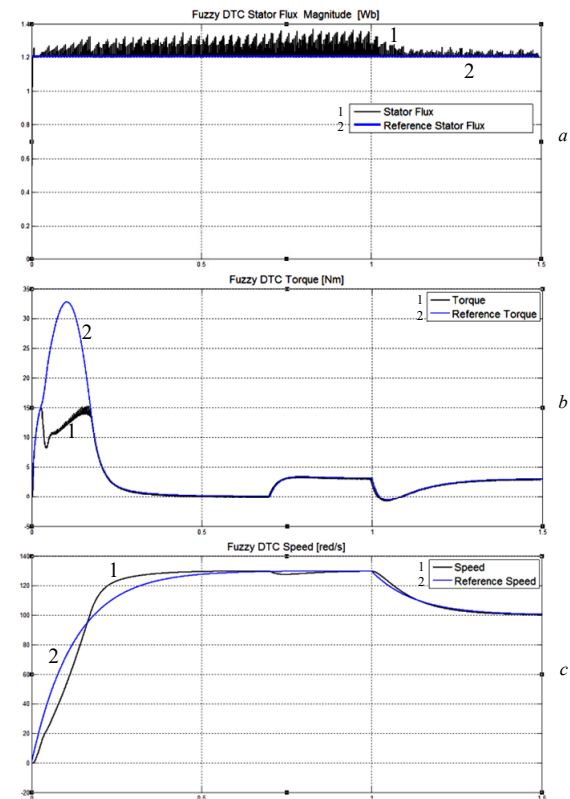


Fig. 23. Behavior of IM flux, torque and speed

The spectral analysis by MATLAB with Powergui FFT analysis tool of electromagnetic torque obtained by conventional DTC (Fig. 24) proposed in [14], the neuronal DTC (Fig. 25) proposed in [7] and by fuzzy DTC (Fig. 26) in steady state shows the existence of harmonics along the spectrum of electromagnetic torque obtained by conventional DTC unlike electromagnetic torque obtained by Fuzzy DTC. Table 5 shows the root mean square (RMS) error and the maximum ripple band of electromagnetic torque and stator flux for conventional DTC, the neuronal DTC and fuzzy DTC approaches.

The results of Table 5 show that DTC based on intelligent techniques considerably reduces the ripples of electromagnetic torque and stator flux compared to conventional DTC. Fuzzy DTC architecture gives the best results in terms of hardware resource consumption and in terms of electromagnetic torque ripple elimination.

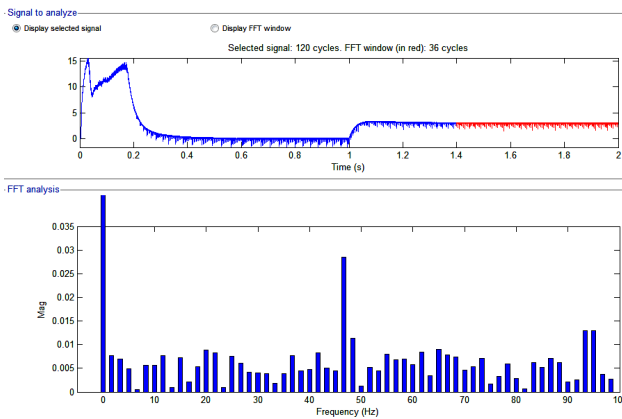


Fig. 24. Spectral analysis of electromagnetic torque obtained by conventional DTC

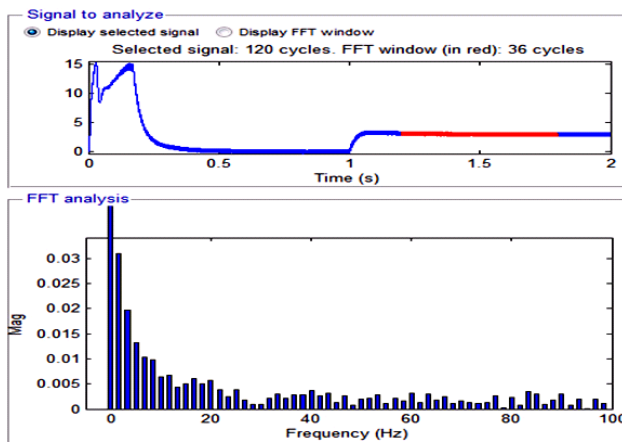


Fig. 25. Spectral analysis of electromagnetic torque obtained by neuronal DTC

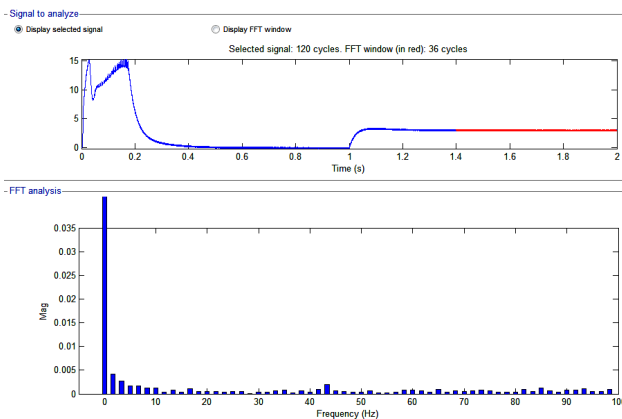


Fig. 26. Spectral analysis of electromagnetic torque obtained by fuzzy DTC

Table 5

Torque and flux ripples

		RMS error	max/min
Electromagnetic torque, N·m	Conventional DTC	0.0367	2.164
	Neuronal DTC	0.0314	0.955
	Fuzzy DTC	0.0096	0.827
Stator flux magnitude, Wb	Conventional DTC	0.0024	0.250
	Neuronal DTC	0.0011	0.090
	Fuzzy DTC	0.0017	0.171

### Conclusions.

1. The aim of this work was, first of all, to improve the dynamic performance of the direct torque control applied to induction motor supplied by a voltage inverter by introducing of a fuzzy inference system. Secondly, to

materialize the feasibility and to judge the quality of proposed control.

2. In this article, we mainly describe the development, implementation and validation of hardware architecture on field programmable gate array for fuzzy direct torque control of induction motor.

3. The originality of this work has been to combine the performance of artificial intelligence techniques and execution power of programmable logic circuits, for the definition of a control structure achieving the best simplicity / performance and speed / performance ratios.

4. We used unconventional control tools to implement a switching strategy without needing the switching table and hysteresis comparators used in conventional direct torque control.

5. Finally, we believe that the proposed solution improved the dynamic performance of induction motor and greatly reduced the disadvantages of conventional direct torque control such as torque ripples, flux ripples and switching frequency.

**Conflict of interest.** The authors declare that they have no conflicts of interest.

### REFERENCES

1. Takahashi I., Ohmori Y. High-performance direct torque control of an induction motor. *IEEE Transactions on Industry Applications*, 1989, vol. 25, no. 2, pp. 257-264. doi: <https://doi.org/10.1109/28.25540>.
2. Moussaoui L. Performance enhancement of direct torque control induction motor drive using space vector modulation strategy. *Electrical Engineering & Electromechanics*, 2022, no. 1, pp. 29-37. doi: <https://doi.org/10.20998/2074-272X.2022.1.04>.
3. Gdaim S., Mtibaa A., Mimouni M.F. Direct Torque Control of Induction Machine based on Intelligent Techniques. *International Journal of Computer Applications*, 2010, vol. 10, no. 8, pp. 29-35. doi: <https://doi.org/10.5120/1500-2017>.
4. Malyar V.S., Hamola O.Y., Maday V.S., Vasylychshyn I.I. Mathematical modelling of starting modes of induction motors with squirrel-cage rotor. *Electrical Engineering & Electromechanics*, 2021, no. 2, pp. 9-15. doi: <https://doi.org/10.20998/2074-272X.2021.2.02>.
5. Djamilia C., Yahia M. Direct Torque Control Strategies of Induction Machine: Comparative Studies. In *Direct Torque Control Strategies of Electrical Machines*. IntechOpen. 2021. doi: <https://doi.org/10.5772/intechopen.90199>.
6. Gdaim S., Mtibaa A., Mimouni M.F. Design and Experimental Implementation of DTC of an Induction Machine Based on Fuzzy Logic Control on FPGA. *IEEE Transactions on Fuzzy Systems*, 2015, vol. 23, no. 3, pp. 644-655. doi: <https://doi.org/10.1109/TFUZZ.2014.2321612>.
7. Eddine Khodja D., Simard S., Beguenan R. Implementation of optimized approximate sigmoid function on FPGA circuit to use in ANN for control and monitoring. *Control Engineering and Applied Informatics*, 2015, vol. 17, no. 2, pp. 64-72.
8. Da Costa C., Santin C.O. FPGA design approach of digital control of three-phase induction motor. *2017 Brazilian Power Electronics Conference (COBEP)*, 2017, pp. 1-6. doi: <https://doi.org/10.1109/COBEP.2017.8257221>.
9. Monmasson E., Cirstea M.N. FPGA Design Methodology for Industrial Control Systems – A Review. *IEEE Transactions on Industrial Electronics*, 2007, vol. 54, no. 4, pp. 1824-1842. doi: <https://doi.org/10.1109/TIE.2007.898281>.
10. Toh C.L., Idris N.R.N., Yatim A.H.M., Muhamad N.D., Elbuluk M. Implementation of a New Torque and Flux Controllers for Direct Torque Control (DTC) of Induction Machine Utilizing Digital Signal Processor (DSP) and Field

Programmable Gate Arrays (FPGA). *IEEE 36th Conference on Power Electronics Specialists*, 2005, pp. 1594-1599. doi: <https://doi.org/10.1109/PESC.2005.1581843>.

11. Lis J., Kowalski C.T., Orłowska-Kowalska T. Sensorless DTC control of the induction motor using FPGA. *2008 IEEE International Symposium on Industrial Electronics*, 2008, pp. 1914-1919. doi: <https://doi.org/10.1109/ISIE.2008.4677287>.

12. Sutikno T., Idris N.R.N., Jidin A.Z., Daud M.Z. FPGA based high precision torque and flux estimator of direct torque control drives. *2011 IEEE Applied Power Electronics Colloquium (IAPEC)*, 2011, pp. 122-127. doi: <https://doi.org/10.1109/IAPEC.2011.5779871>.

13. Monmasson E., Idkhajine L., Cirstea M.N., Bahri I., Tisan A., Naouar M.W. FPGAs in Industrial Control Applications. *IEEE Transactions on Industrial Informatics*, 2011, vol. 7, no. 2, pp. 224-243. doi: <https://doi.org/10.1109/TII.2011.2123908>.

14. Aib A. FPGA Hardware in the Loop Validation of Torque and Flux Estimators for Direct Torque Control (DTC) of an Induction Motor (IM). *International Journal of Intelligent Engineering and Systems*, 2021, vol. 14, no. 5, pp. 583-594. doi: <https://doi.org/10.22266/ijies2021.1031.51>.

15. Boukadida S., Gdaim S., Mtibaa A. Hardware Implementation of FTC of Induction Machine on FPGA. *Electronics ETF*, 2017, vol. 20, no. 2, pp. 76-84. doi: <https://doi.org/10.7251/ELS1620076B>.

16. Zare M.A., Kavasseri R.G., Ababei C. FPGA-based design and implementation of direct torque control for induction machines. *2014 International Conference on ReConFigurable Computing and FPGAs (ReConFig14)*, 2014, pp. 1-6. doi: <https://doi.org/10.1109/ReConFig.2014.7032520>.

17. Lee G.S., Lee D.H., Yoon T.W., Lee K.B., Song J.H., Choy I. Speed and flux estimation for an induction motor using a

parameter estimation technique. *International Journal of Control, Automation and Systems*, 2005, vol. 3, no. 1, pp. 79-86.

18. Sandre-Hernandez O., Rangel-Magdaleno J., Morales-Caporal R., Bonilla-Huerta E. HIL simulation of the DTC for a three-level inverter fed a PMSM with neutral-point balancing control based on FPGA. *Electrical Engineering*, 2018, vol. 100, no. 3, pp. 1441-1454. doi: <https://doi.org/10.1007/s00202-017-0597-0>.

19. Lotfi E., Elharoussi M., Abdelmounim E. VHDL design and FPGA implementation of direct torque control for induction machines. *Bulletin of Electrical Engineering and Informatics*, 2021, vol. 10, no. 3, pp. 1220-1231. doi: <https://doi.org/10.11591/eei.v10i3.2345>.

Received 25.07.2022

Accepted 15.11.2022

Published 06.05.2023

Abdelghani Aib<sup>1</sup>, Doctor of Electrotechnical,  
Djalal Eddine Khodja<sup>2</sup>, Doctor of Electrotechnical, Professor,  
Salim Chakroune<sup>1</sup>, Doctor of Electrotechnical, Professor,

<sup>1</sup> Research Laboratory on the Electrical Engineering,  
Faculty of Technology,

University of M'Sila, BP 166, Ichbilila 28000, Algeria,

e-mail: abdelghani.aib@univ-msila.dz,

salim.chakroune@univ-msila.dz (Corresponding Author).

<sup>2</sup> Signals & Systems Lab,

Institute of Electrical and Electronic Engineering,

Boumerdes, 35000, Algeria,

e-mail: djalaleddine.khodja@univ-msila.dz

#### How to cite this article:

Aib A., Khodja D.E., Chakroune S. Field programmable gate array hardware in the loop validation of fuzzy direct torque control for induction machine drive. *Electrical Engineering & Electromechanics*, 2023, no. 3, pp. 28-35. doi: <https://doi.org/10.20998/2074-272X.2023.3.04>

## Sensorless control of switched reluctance motor based on a simple flux linkage model

**Introduction.** The operation of switched reluctance motor requires prior knowledge of the rotor position, obtaining from either low resolution photocoupler based position sensor or high resolution shaft encoder, to control the on/off states of the power switches.

**Problem.** However, using physical position sensor in harsh environment will inevitably reduce the reliability of the motor drive, in which sensorless control comes into play. **Novelty.** In this paper, a sensorless control scheme of switched reluctance motor is proposed. **Methodology.** The method is based on a simple analytical model of the flux-linkage curves rather than the conventional approach that normally uses a look-up table to store all the data points of the flux-linkage curves. By measuring the phase current, rotor position can be deduced from the analytical model. **Practical value.** Simulation results are given and the proposed sensorless scheme is verified to provide a moderate position estimation accuracy in a wide speed range in both unsaturated and saturated conditions. References 9, figures 6.

**Key words:** analytical model, switched reluctance motor, sensorless control.

**Вступ.** Для роботи вентильного реактивного двигуна потрібне попереднє знання положення ротора, отримане або від датчика положення на основі оптичарі з низькою роздільною здатністю, або від енкодера з високою роздільною здатністю, щоб керувати станами вмикання/вимикання силових перемикачів. **Проблема.** Однак використання датчика фізичного положення в суворих умовах неминуче знижує надійність моторного приводу, в якому набуває чинності бездатчикове управління. **Новизна.** У цій роботі пропонується бездатчикова схема управління вентильним реактивним двигуном. **Методологія.** Цей метод заснований на простій аналітичній моделі кривих потокозчеплення, а не на традиційному підході, який зазвичай використовує довідкову таблицю для зберігання всіх точок даних кривих потокозчеплення. Вимірявши фазний струм, положення ротора можна вивести з аналітичної моделі. **Практична цінність.** Наведено результати моделювання та перевірено запропоновану бездатчикову схему для забезпечення помірної точності оцінки положення в широкому діапазоні швидкостей як у ненасичених, так і в насичених умовах. Бібл. 9, рис. 6.

**Ключові слова:** аналітична модель, вентильний реактивний двигун, бездатчикове керування.

**Introduction.** Switched reluctance motor (SRM) is an electric motor that has gained a lot of attention in recent decades due to its unique features such as rugged structure and cost effective [1, 2]. It has been widely adopted in industrial and home applications and shows superior performance. Unlike the induction motor and the synchronous motor that are able to run by just plugging in the phase terminal to the power grid, the operation of SRM cannot be separated from the dedicated controller and rotor position sensor, which is one of the main disadvantages of SRM [3].

The control of SRM always involves acquiring the rotor position as crucial information to determining the firing of switches. Due to the principle of the torque production in SRM, the magnetization of phases should synchronize with the rotor poles in order to maximize the efficiency of the torque production. Miss firing of the switches may heavily impact the performance of the SRM drives or even threaten its stable operation. A high-resolution optical encoder or a low-cost Hall effect sensor is therefore normally embedded in the SR motor.

SRM is quite suitable in the applications under harsh environment, the rotor position sensor may be impacted and malfunctioned however. In the applications with limited budget, the expensive encoder is usually not an option. Therefore, sensorless control is favorable in many cases.

The sensorless operation of SRM generally requires two kinds of rotor position information, continuous or discrete. The former one needs to resolve the rotor position uninterrupted while the latter one is simpler and only requires few points during an entire electrical cycle and the intermediate points can be interpolated [4].

Different types of position sensorless scheme have been reported in literatures, they can be broadly classified as active phase methods or inactive phase methods [5].

In [6], a sensorless method based on an analytical self-inductance model of SRM is introduced, the inductance curves at three crucial rotor positions are picked out to construct a complete inductance profile at all positions. The rotor position is then resolved from the transformed voltage equation. The method only measures the phase current and does not require additional hardware. Instead of using analytical model, look-up table is used in [7] to look up the rotor position if knowing the value of the current and the flux in real-time. Despite the advantage of high accuracy, the main drawback of the method is that large storage space is required to store the offline look-up table, which will add to the cost of the motor controller. By analyzing the inductance profile of SRM, a simple sensorless method that observes the current gradient is proposed in [8]. The current slope will suddenly change the sign at a specific location where the rotor position can be detected.

In this paper, a sensorless control scheme of SRM is proposed. It is based on a simple analytical model of the magnetization curves developed in [9] rather than using the look-up table in the conventional approach. The model only requires few parameters that are normally available or easily obtained to form the SRM magnetization curves. The rotor position is inherently a part of the model due to the nonlinear relationship among the flux-linkage, current and rotor position, thus it can be estimated from the flux-linkage model. The proposed sensorless control only requires the measurement of the current of the active phase in real-time, thus the hardware will be simple. Besides, there is no need to store the look-up table, so the memory size of the controller needed is reduced. Simulations under multiple operating conditions are carried out in MATLAB/Simulink to verify the correctness and effectiveness of the proposed sensorless control method.

**Proposed sensorless control method of SRM.** A sensorless method normally relies on the magnetization characteristics of the motor. Due to the nonlinear characteristics of SRM, the flux-linkage is a nonlinear function of the current and the rotor position, which implies that if the current and the flux-linkage are known, it is possible to deduce the rotor position. Therefore, having an accurate model of the magnetization characteristics of SRM makes it convenient to develop the sensorless control scheme, and the accuracy of the estimated position relies on the accuracy of the model.

The phase voltage equation of SRM can be written as

$$u = R \cdot i + \frac{d\psi(i, \theta)}{dt}, \quad (1)$$

where  $u$  is the phase voltage;  $R$  is the phase resistance;  $i$  is the phase current;  $\psi$  is the flux-linkage;  $\theta$  is the rotor position.

The flux-linkage can be rewritten in an integration manner as

$$\psi(i, \theta) = \int (u - R \cdot i) dt. \quad (2)$$

If it is not in low voltage application, the phase voltage can be assumed to be equal to the  $U_{DC}$ ,  $-U_{DC}$ , or 0 V, where  $U_{DC}$  is the DC link voltage, while only introducing minor error due to the comparatively small voltage drops across switches and diodes in the converter circuit. The phase resistance is measured one time when the motor stalls. The phase current is measured in real-time and by doing integration, the flux-linkage can be estimated.

Due to the doubly-salient structure of SRM, the flux-linkage characteristics vary with rotor position. Two typical positions are the unaligned position and aligned position. When the rotor pole is at unaligned position, the air gap dominates in the magnetic circuit, therefore the flux vs. current curve is a straight line, and the unaligned inductance is denoted as  $L_q$ , which is the slope of the flux-linkage curve. In aligned position, the flux-linkage curve is a straight line before knee point, and the inductance in this condition is  $L_d$ , which is notably larger than  $L_q$ . However, when the motor iron is saturated, the flux-linkage curves bends over and the slope is much smaller than unsaturated condition. The magnetization characteristics of the sample SRM is shown in Fig. 1. The results are obtained from FEM analysis. As can be seen from Fig. 1 that the flux-linkage is a nonlinear function of current and rotor position, which is a fundamental characteristic of any SR motor.

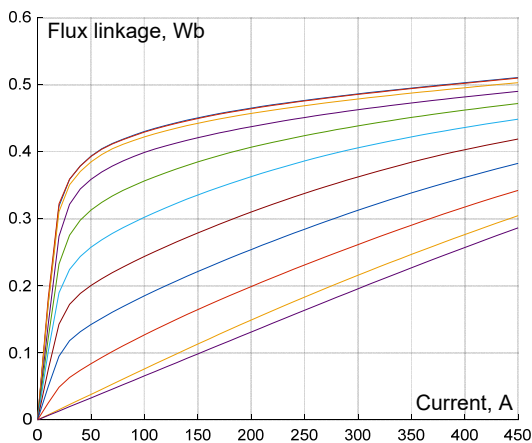


Fig. 1. Flux-linkage characteristics of the sample SRM obtained from FEM analysis

In order to model the nonlinear curves in Fig. 1, a simple analytical model is proposed in [1]. The curves at unaligned position can be simply represented by a straight line, and the slope is  $L_q$  in

$$\psi_q = L_q \cdot i, \quad (3)$$

where  $\psi_q$  is the unaligned flux-linkage.

The nonlinear curve at aligned position can be approximated by a function composed of exponential term, and written as

$$\psi_d = l_{dsat} \cdot i + A(1 - e^{-B \cdot i}), \quad (4)$$

where  $\psi_d$  is the aligned flux-linkage;  $l_{dsat}$  is the incremental inductance when the magnetic circuit is saturated at aligned position;  $A$  and  $B$  are the constant coefficients that can be determined in order the equation has a good approximation of the curve.

When the motor operates with maximum allowable current  $I_m$ , the motor is in deep saturation and the exponential term can be neglected, thus  $A$  can be deduced from (4) as

$$A = \psi_m - l_{dsat} \cdot I_m, \quad (5)$$

and  $B$  is calculated by

$$B = \frac{L_d - l_{dsat}}{\psi_m - l_{dsat} \cdot I_m}, \quad (6)$$

where  $\psi_m$  is the flux-linkage corresponds to  $I_m$ .

The magnetization curves of the intermediate positions between unaligned and aligned position can be deduced by using a nonlinear function as shown in (7), where  $N_r$  is the rotor pole number:

$$f(\theta) = \frac{2 \cdot N_r^3}{\pi^3} \cdot \theta^3 - \frac{2 \cdot N_r^2}{\pi^2} \cdot \theta^2 + 1. \quad (7)$$

Then the complete magnetization characteristics can be generalized as

$$\psi(i, \theta) = L_q \cdot i + [l_{dsat} \cdot i + A \cdot (1 - e^{-B \cdot i}) - L_q \cdot i] \cdot f(\theta). \quad (8)$$

The model in (8) makes it possible for the proposed sensorless scheme to preclude the use of the offline look-up table of the magnetization curves that takes up large amount of storage space in the controller.

Figure 2 shows the magnetization curves calculated from the aforementioned analytical model. As compared with the FEM result in Fig. 1, it can be said that the analytical model has good approximation. This is crucial in the sensorless control, otherwise the rotor position estimation will be erroneous due to a poor model.

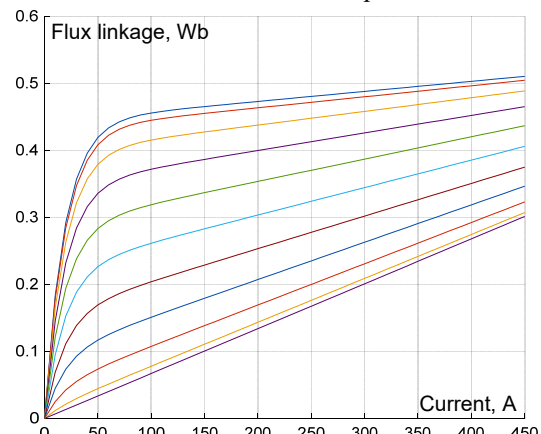


Fig. 2. Flux-linkage characteristics of the sample SRM calculated by the analytical model

From (8), the rotor position estimation can be deduced. The current  $i$  is measured in real-time, the flux-linkage  $\psi$  is then calculated by doing integration,  $L_q, I_{dsats}$ ,  $A$  and  $B$  are also known constants. Therefore, the rotor position  $\theta$  can be easily solved from (8), and sensorless operation is then possible by using this analytical model. In other words, if the current and the flux are known at the instant, the rotor position is solely determined in Fig. 1. This is the theoretical background of the rotor position estimation.

**Simulation results and discussion.** In order to verify the proposed sensorless control scheme, simulation is carried out in MATLAB/Simulink.

The simulation is at first evaluated at the speed of 1000 rpm. The speed is maintained constant by setting a high inertia value. The motor is operating under current

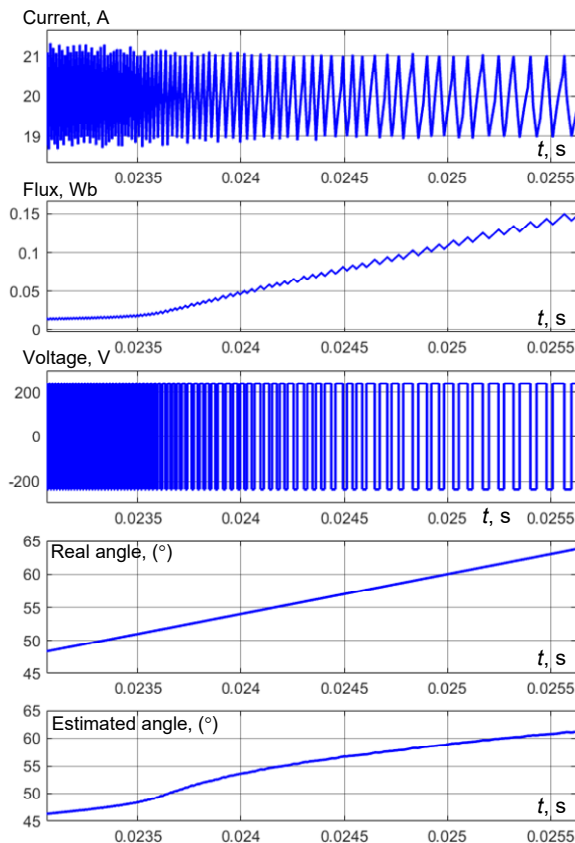


Fig. 3. Unsaturated operation at 1000 rpm

Then the simulation is carried out under different operation speeds in Fig. 5, 6. When operating in low speed, which is 50 rpm in Fig. 5, the current is kept in hysteresis manner at 200 A. It can be seen that the estimation error is below  $2^\circ$ . As in high speed operation in Fig. 6, the current can no longer maintained due to the significant back-EMF. Similar to the previous case, the maximum position estimation error is around  $2^\circ$ . Therefore, the proposed sensorless scheme is suitable in both low-speed and high-speed operation.

### Conclusions.

In this paper, a new sensorless control method for the switched reluctance motor is proposed. The method uses an analytical flux-linkage model such that the large look-up table used in conventional approaches is not needed. The proposed idea only needs to measure the

chopping control. In Fig. 3, the reference current is kept at 20 A, and the hysteresis bandwidth of the phase current is 2 A. As can be seen from the magnetization curves in Fig. 1, the motor is running under unsaturated condition with low current. By comparing estimated rotor position and the real rotor position measured in mechanical angle, it can be found that the maximum error is around  $2^\circ$ , which is an acceptable accordance.

In Fig. 4, the motor is running under saturated condition, where the reference current is raised to 300 A and the hysteresis band is 60 A. In this case, the maximum deviation of the estimated angle from the real angle is also around  $2^\circ$ . It can be concluded that the proposed position estimation works well in both unsaturated and saturated conditions.

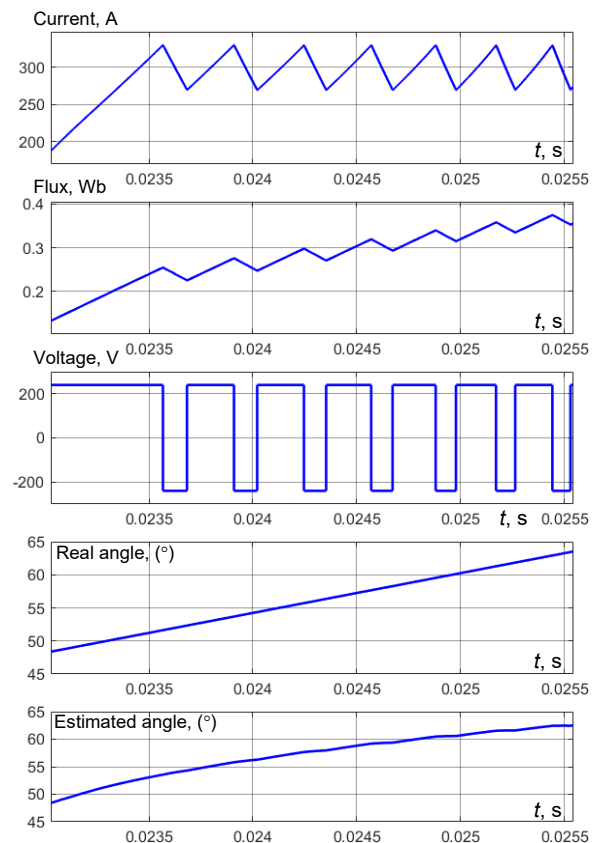


Fig. 4. Saturated operation at 1000 rpm

phase current in real-time, and the rotor position can be estimated continuously from solving a flux-linkage equation. The sensorless method has the merit of minimum data storage requirement since the large look-up table of the switched reluctance motor magnetization characteristics is replaced by the analytical model. Therefore, it is suitable to be used in low cost digital controllers. Simulation results have shown that the proposed sensorless control can acquire the rotor position continuously and the accuracy of the position estimation is small in low and high speed, unsaturated and saturated conditions.

**Acknowledgement.** This study was supported by Seoul National University of Science and Technology.

**Conflict of interest.** The authors declare that they have no conflicts of interest.

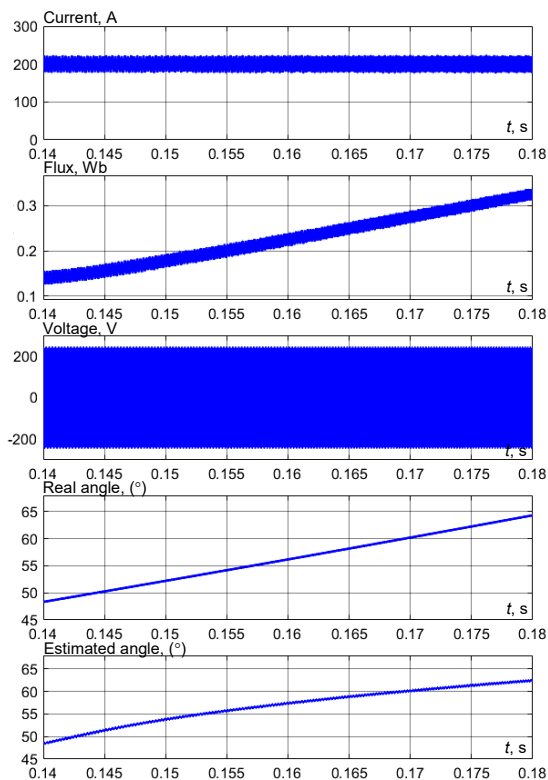


Fig. 5. Low-speed operation, 50 rpm

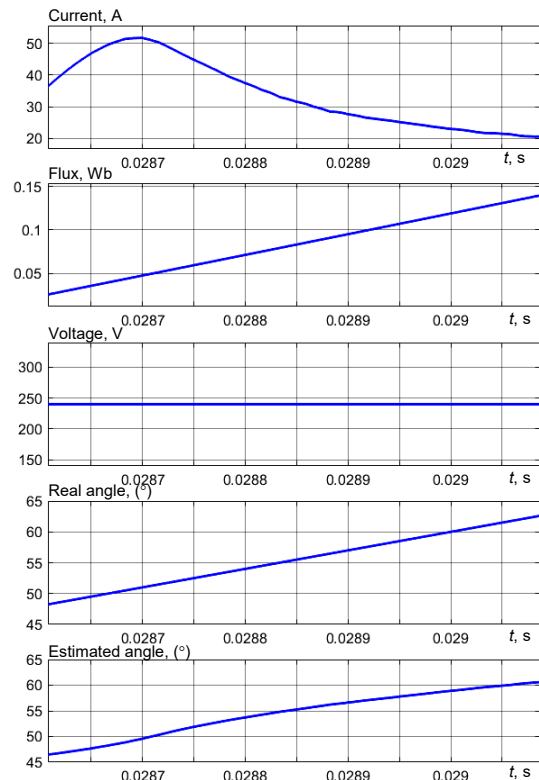


Fig. 6. High-speed operation, 5000 rpm

#### REFERENCES

- Xue X.D., Cheng K.W.E., Bao Y.J. Control and Integrated Half Bridge to Winding Circuit Development for Switched Reluctance Motors. *IEEE Transactions on Industrial Informatics*, 2014, vol. 10, no. 1, pp. 109-116. doi: <https://doi.org/10.1109/TII.2013.2251890>.
- Bostanci E., Moallem M., Parsapour A., Fahimi B. Opportunities and Challenges of Switched Reluctance Motor Drives for Electric Propulsion: A Comparative Study. *IEEE Transactions on Transportation Electrification*, 2017, vol. 3, no. 1, pp. 58-75. doi: <https://doi.org/10.1109/TTE.2017.2649883>.
- Cai J., Deng Z. Switched-Reluctance Position Sensor. *IEEE Transactions on Magnetics*, 2014, vol. 50, no. 11, pp. 1-4. doi: <https://doi.org/10.1109/TMAG.2014.2329957>.
- Tang Y., He Y., Wang F., Lee D., Ahn J., Kennel R. Back-EMF-based sensorless control system of hybrid SRM for high-speed operation. *IET Electric Power Applications*, 2018, vol. 12, no. 6, pp. 867-873. doi: <https://doi.org/10.1049/iet-epa.2017.0641>.
- Ehsani M., Fahimi B. Elimination of position sensors in switched reluctance motor drives: state of the art and future trends. *IEEE Transactions on Industrial Electronics*, 2002, vol. 49, no. 1, pp. 40-47. doi: <https://doi.org/10.1109/41.982246>.
- Suresh G., Fahimi B., Rahman K.M., Ehsani M. Inductance based position encoding for sensorless SRM drives. *30th Annual IEEE Power Electronics Specialists Conference. Record. (Cat. No.99CH36321)*, 1999, vol. 2, pp. 832-837. doi: <https://doi.org/10.1109/PESC.1999.785607>.
- Kaewpoo N., Ohshima K., Nakazawa Y., Fujii H., Uehara H., Hyakutake Y. Simulation of SRM Sensorless Control System for Electric Vehicle. *2018 International Conference on Engineering, Applied Sciences, and Technology (ICEAST)*, 2018, pp. 1-4. doi: <https://doi.org/10.1109/ICEAST.2018.8434508>.
- Gallegos-Lopez G., Kjaer P.C., Miller T.J.E. A new sensorless method for switched reluctance motor drives. *IEEE Transactions on Industry Applications*, 1998, vol. 34, no. 4, pp. 832-840. doi: <https://doi.org/10.1109/28.703987>.
- Le-Huy H., Brunelle P. A versatile nonlinear switched reluctance motor model in Simulink using realistic and analytical magnetization characteristics. *31st Annual Conference of IEEE Industrial Electronics Society*, 2005. IECON 2005, Raleigh, NC, USA, 2005, pp. 1-6. doi: <https://doi.org/10.1109/IECON.2005.1569136>.

Received 10.08.2022  
Accepted 30.11.2022  
Published 06.05.2023

Jiayi Fan<sup>1</sup>, Master's Degree,  
Yongkeun Lee<sup>1</sup>, PhD, Professor,  
<sup>1</sup>Seoul National University of Science and Technology,  
Seoul 01811, South Korea,  
e-mail: fjy1510780466@163.com,  
ykleee@seoultech.ac.kr (Corresponding Author)

#### How to cite this article:

Fan J., Lee Y. Sensorless control of switched reluctance motor based on a simple flux linkage model. *Electrical Engineering & Electromechanics*, 2023, no. 3, pp. 36-39. doi: <https://doi.org/10.20998/2074-272X.2023.3.05>

A. Boukadoum, A. Bouguerne, T. Bahi

## Direct power control using space vector modulation strategy control for wind energy conversion system using three-phase matrix converter

**Introduction.** Wind energy conversion system is getting a lot of attention since, they are provide several advantages, such as cost competitive, environmentally clean, and safe renewable power source as compared with the fossil fuel and nuclear power generation. A special type of induction generator, called a doubly fed induction generator is used extensively for high-power wind energy conversion system. They are used more and more in wind turbine applications due to the advantages of variable speed operation range and its four quadrants active and reactive power capabilities, high energy efficiency, and the improved power quality. Wind energy conversion systems require a good choice of power electronic converters for the improvement of the quality of the electrical energy produced at the generator terminals. There are several power electronics converters that are the most popular such as the two stage back-back converter. Because of the disadvantage of these converters to produce large harmonics distortions, we will choose using of three-phase matrix converter. **Purpose.** Work presents a direct power control using space vector modulation for a doubly fed induction generator based wind turbine. The main strategy control is to control the active and reactive powers and reduce the harmonic distortion of stator currents for variable wind speed. The **novelty** of the work is to use a doubly fed induction machine and a three pulses matrix converter to reduce the low cost, volume and the elimination of the grid side converter controller are very attractive aspects of the proposed topology compared to the conventional methods such as back-to-back converters. Simulation **results** are carried out on a 1.5 MW of wind energy conversion system connected to the grid. The efficiency of the proposed system has been simulated and high results performances are evaluated to show the validity of the proposed control strategy to decouple and control the active and reactive power for different values of wind speed. References 32, tables 2, figures 15. **Key words:** doubly fed induction generator, matrix converter, wind turbine, direct power control using space vector modulation strategy control, power quality.

**Вступ.** Системам перетворення енергії вітру приділяється велика увага, оскільки вони забезпечують низку переваг, таких як конкурентоспроможність за вартістю, екологічно чисте та безпечне відновлюване джерело енергії порівняно з викопним паливом та виробництвом ядерної енергії. Спеціальний тип асинхронного генератора, що називається асинхронним генератором з подвійним живленням, широко використовується в системах перетворення енергії вітру великої потужності. Вони все більше і більше використовуються у вітряних турбінах через переваги діапазону роботи зі змінною швидкістю та його чотириквadrантних можливостей активної та реактивної потужності, високої енергоефективності та покращеної якості електроенергії. Системи перетворення енергії вітру вимагають хорошого вибору силових електронних перетворювачів для покращення якості електроенергії, що виробляється на клеммах генератора. Існує кілька перетворювачів силової електроніки, які є найбільш популярними, наприклад двокаскадний зворотно-зворотний перетворювач. Через те, що ці перетворювачі не створюють великих гармонічних спотворень, ми виберемо використання трифазного матричного перетворювача. **Мета.** У роботі представлено пряме керування потужністю з використанням модуляції просторового вектора для вітряної турбіни на основі асинхронного генератора з подвійним живленням. Основною стратегією управління є управління активною та реактивною потужністю та зниження гармонічних спотворень струмів статора при змінній швидкості вітру. **Новизна** роботи полягає у використанні асинхронної машини з подвійним живленням і тріпульсного матричного перетворювача для зниження вартості, об'єму та усунення контролера перетворювача з боку мережі, що є дуже привабливими аспектами запропонованої топології у порівнянні зі звичайними методами, такими як зустрічно-зворотні перетворювачі. **Результати** моделювання отримані на системі перетворення енергії вітру потужністю 1,5 МВт, підключеної до мережі. Ефективність запропонованої системи була змодельована, а високі результати оцінені, щоб показати обґрунтованість запропонованої стратегії управління для поділу та управління активною та реактивною потужністю для різних значень швидкості вітру. Бібл. 32, табл. 2, рис. 15. **Ключові слова:** асинхронний генератор з подвійним живленням, матричний перетворювач, вітряна турбіна, пряме керування потужністю з використанням стратегії просторово-векторної модуляції, якість електроенергії.

**1. Introduction.** Nowadays, the use of renewable energy system in modern production of electrical energy has exponentially increased due to the increase in greenhouse gas concentrations in the atmosphere, which are extremely destructive to our planet [1]. Wind energy has grown faster than any other source of renewable energy [2]. Wind energy can help reduce total air pollution and carbon dioxide emissions, this generator is one of the rapidly expanding renewable energy sources with a 93 GW capacity addition in 2020 [3], it has become a suitable solution for producing clean energy and is currently the quickest developing source when correlated with other sustainable power sources [4]. Nonetheless, the use of available energy depends on weather conditions such as wind speed and its integration produces volatility in the power system. Integrating renewable energies with network connection, intelligent control, and storage systems could result in a change in generating electricity and reducing. Given current trends and the best available scientific evidence, mankind probably needs to reduce total emissions by at least 80 % since 2050 [5]. Yet each day

emissions continue to grow [6]. Wind energy conversion system (WECS) is getting a lot of attention since, they are provide several advantages, such as cost competitive, environmentally clean, and safe renewable power source as compared with the fossil fuel and nuclear power generation. A special type of induction generator, called a doubly fed induction generator (DFIG), is used extensively for high-power wind applications. They are used more and more in wind turbine applications due to the advantages of variable speed operation range and its four quadrants active and reactive power capabilities, high energy efficiency, and the improved power quality [7, 8]. WECSs require a good choice of power electronic converters for the improvement of the quality of the electrical energy produced at the generator terminals. There are several power electronics converters that are the most popular such as the two stage back-back converter and cycloconverter [9, 10]. Because of the disadvantage of these converters to produce large harmonics, we will choose using of direct matrix converter. The system under study is depicted in Fig. 1.

© A. Boukadoum, A. Bouguerne, T. Bahi

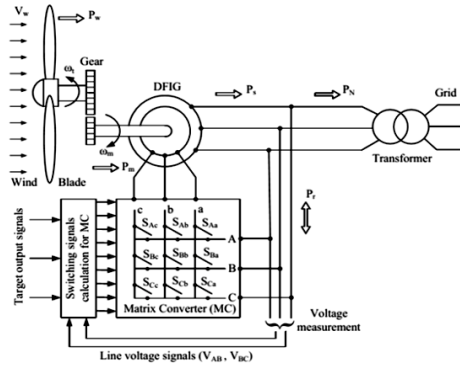


Fig. 1. WECS connected to the grid

It is composed of DFIG-wind turbine connected to the grid via a direct matrix converter (DMC). Wind turbines using a DFIG consist of a wound rotor induction generator and a three phase direct matrix converter. The stator winding is connected directly to the 50 Hz grid while the rotor is fed at variable frequency through the direct matrix converter [11, 12]. The DFIG technology allows extracting maximum energy from the wind for low wind speeds by optimizing the turbine speed, while minimizing mechanical stresses on the turbine during gusts of wind. In this study the variable wind speed is maintained at 9 m/s, 15 m/s and 11 m/s. Simulation results are carried out on a 1.5 MW DFIG WECS connected to the 575 V of voltage grid. The reactive power produced by the wind turbine is regulated at zero MVar. The paper is organized as follows: In section 2, the model of the wind turbine is presented. Next, the modeling of DFIG system is detailed in section 3. In section 4, mathematical modeling of a DMC is discussed. In section 5, the procedure of direct power control using space vector modulation (DPC-SVM) based direct matrix converter is explained. The simulation results are presented in section 6. Finally, section 7 concludes this study.

**2. Wind turbine model.** Wind energy can only extract a small part of the power from the wind, which is limited by the Betz limit to a maximum of 59 %. This quantity is described by the turbine power coefficient  $C_p$ , which is dependent on the blade pitch angle  $\beta$  and the peak speed ratio  $\lambda$ . The mechanical power of the wind turbine extracted from the wind is given by:

$$P_W = \frac{1}{2} \cdot \rho \cdot \pi \cdot R^2 \cdot C_p(\lambda, \beta) \cdot V^3, \quad (1)$$

where  $C_p$  is the power coefficient of the wind turbine;  $\beta$  is the blade pitch angle;  $\lambda$  is the tip speed ratio;  $\rho$  is the density of air;  $R$  is the rotor radius of wind, m;  $V$  is the wind speed, m/s.

The tip speed ratio  $\lambda$  is calculated from the actual values of rotor speed and wind speed  $V$  according to:

$$\lambda = \frac{R \cdot \Omega_W}{V}, \quad (2)$$

where  $\Omega_W$  is the angular velocity of rotor, rad/s.

From summaries achieved on a wind of 1.5 MW, the expression of the power coefficient for this type of turbine can be approximated by the following expression:

$$C_p(\lambda, \beta) = C_1 \cdot \left( \frac{C_2}{\lambda_i} - C_3 \cdot \beta - C_4 \right) \cdot e^{\left( \frac{C_5}{\lambda_i} \right)} + C_6 \cdot \lambda. \quad (3)$$

The parameter  $1/\lambda_i$  in (3) is defined as

$$\frac{1}{\lambda_i} = \frac{1}{\lambda + 0.008 \cdot \beta} - \frac{0.035}{1 + \beta^2}. \quad (4)$$

The proposed coefficients are equal to:

$$C_1 = 0.5176, C_2 = 116, C_3 = 0.4, C_4 = 5, C_5 = 2, C_6 = 0.0068.$$

The gearbox is installed between the turbine and the generator to transform slow speed wind turbine rotation to higher speed required by the generator [13]. Neglecting the gearbox losses, the mechanical torque and shaft speed of the wind turbine referred to the generator side of the gearbox are given by:

$$T_g = \frac{T_W}{G}; \quad \Omega_g = \Omega_W \cdot G, \quad (5)$$

where  $T_W$ ,  $T_g$  are the wind turbine aerodynamic and generator electromagnetic torques, N·m.

The resulting block diagram of the wind turbine model is presented in Fig. 2.

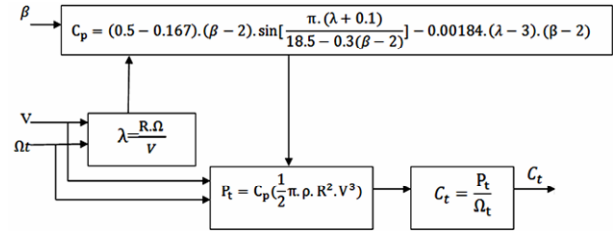


Fig. 2. Block diagram of the wind turbine model

Figure 3 illustrated the curves of power coefficient versus the tip-speed ratio for different values of the pitch angle. We can see in this figure that the optimal power coefficient of  $C_p$  is 0.48 for a speed ratio at 8 and  $\beta$  equal to  $0^\circ$ .

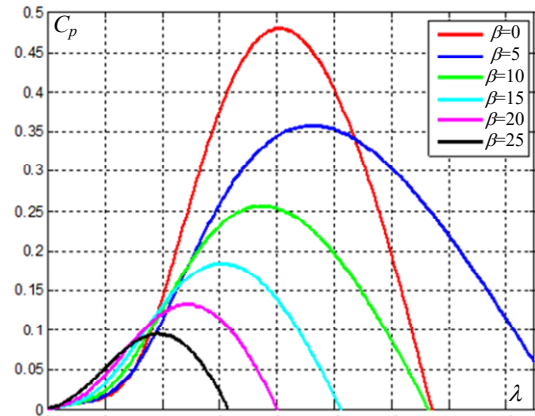


Fig. 3. Power coefficients for different values of  $\beta$

**3. DFIG model.** By choosing a  $d$ - $q$  reference frame synchronized with the stator flux, the electrical equations of the DFIG are written as follows:

$$\begin{cases} \frac{d}{dt} \varphi_{sd} = V_{sd} - R_s i_{sd} + \omega_s \varphi_{sq}; \\ \frac{d}{dt} \varphi_{sq} = V_{sq} - R_s i_{sq} + \omega_s \varphi_{sd}; \\ \frac{d}{dt} \varphi_{rd} = V_{rd} - R_r i_{rd} + (\omega_s - \omega) \cdot \varphi_{rq}; \\ \frac{d}{dt} \varphi_{rq} = V_{rq} - R_r i_{rq} - (\omega_s - \omega) \cdot \varphi_{rd}, \end{cases} \quad (6)$$

where  $V_{sd}$ ,  $V_{sq}$ ,  $i_{sd}$ ,  $i_{sq}$  are the stator voltages and currents in the synchronous reference frame, respectively;  $V_{rd}$ ,  $V_{rq}$ ,  $i_{rd}$ ,  $i_{rq}$  are the rotor voltages and currents in the synchronous reference frame, respectively;  $\omega_s$  is the stator

angular frequency;  $\omega$  is the slip angular speed;  $R_s$  is the stator resistance;  $\varphi_s, \varphi_r$  are the stator and rotor fluxes.

The stator and rotor flux can be expressed as

$$\begin{cases} \varphi_{sd} = L_s i_{sd} + M i_{rd}; \\ \varphi_{sq} = L_s i_{sq} + M i_{rq}; \\ \varphi_{rd} = L_r i_{rd} + M i_{sd}; \\ \varphi_{rq} = L_r i_{rq} + M i_{sq}. \end{cases} \quad (7)$$

The expressions of real and reactive power are given by:

$$\begin{cases} P_s = V_{sd} i_{sd} + V_{sq} i_{sq}; \\ Q_s = V_{sq} i_{sd} - V_{sd} i_{sq}; \\ P_r = V_{rd} i_{rd} + V_{rq} i_{rq}; \\ Q_r = V_{rq} i_{rd} - V_{rd} i_{rq}. \end{cases} \quad (8)$$

The control strategy, using the model of DFIG in ( $d$ - $q$ ) reference axis is the vector stator flux aligned with  $d$ -axis. So, by setting the quadratic component of the stator flux to the null value and by neglecting the stator resistance, the voltage equations of the stator windings can be simplified in steady state as:

$$\begin{cases} V_{sd} = \frac{d\varphi_{sd}}{dt} = 0; \\ V_{sq} = \omega_s \cdot \varphi_{sd} = V_s. \end{cases} \quad (9)$$

Hence, the relationship between the stator and rotor currents can be written as follows:

$$\begin{cases} i_{sd} = \frac{\varphi_s}{L_s} - \frac{L_m}{L_s} \cdot i_{rd}; \\ i_{sq} = -\frac{L_m}{L_s} \cdot i_{rq}. \end{cases} \quad (10)$$

From (8), (9), we can write:

$$\begin{cases} \varphi_{rd} = (L_r - \frac{M^2}{L_s}) \cdot i_{rd} + \frac{M V_s}{\omega_s L_s}; \\ \varphi_{rq} = (L_r - \frac{M^2}{L_s}) \cdot i_{rq}. \end{cases} \quad (11)$$

The expression of the stator and rotor voltage is given by:

$$\begin{cases} V_{sd} = \frac{R_s}{L_s} \varphi_{sd} - \frac{R_s}{L_s} M i_{rd}; \\ V_{sq} = -\frac{R_s}{L_s} \varphi_{rq} + \omega_s \varphi_{rd}; \\ V_{rd} = R_r i_{rd} + \sigma \cdot L_r \frac{di_{rd}}{dt} + e_{rd}; \\ V_{rq} = R_r i_{rq} + \sigma \cdot L_r \frac{di_{rq}}{dt} + e_{rd} + e_{\varphi}, \end{cases} \quad (12)$$

where:

$$\begin{cases} e_{rd} = \frac{R_s}{L_s} \varphi_{sd} - \frac{R_s}{L_s} M i_{rd}; \\ e_{rq} = -\frac{R_s}{L_s} \varphi_{rq} + \omega_s \varphi_{rd}; \\ e_{\varphi} = \omega_r \cdot \frac{M}{L_s} \cdot \varphi_{sd}; \\ \sigma = 1 - (\frac{M}{\sqrt{L_s L_r}})^2. \end{cases} \quad (13)$$

Stator real and reactive powers are described by:

$$P_s = g \cdot \frac{V_s M}{L_s} \cdot i_{rq}; \quad Q_s = g \cdot \frac{V_s M}{L_s} \cdot i_{rd}. \quad (14)$$

The electromagnetic torque is as follows:

$$T_{em} = -P \cdot \frac{M}{L_s} \cdot \varphi_{sd} \cdot i_{rq}. \quad (15)$$

**4. Matrix converter (MC)** is a DMC used to convert AC supply voltages into variable magnitude and frequency output voltages [14, 15] (Fig. 4). Three phases MC consists of array of nine IGBTs switches that are switched on and off in order to provide variable sinusoidal voltage and frequency to the load [8], in this type of converter there is no need to the intermediate DC link power circuit and this means no large energy storing capacitors [8-10]. This will increase the system reliability and reduce the weight and volume for such converters [16, 17]. This converter is proposed as an effective replacement for the WECS fed by back-to-back converter. The input voltages and currents can be given as:

$$V_i(t) = V_{i \max} \begin{bmatrix} \sin(\omega_i t) \\ \sin(\omega_i t - 2\pi/3) \\ \sin(\omega_i t - 4\pi/3) \end{bmatrix}. \quad (16)$$

$$i_i(t) = I_{i \max} \begin{bmatrix} \sin(\omega_i t + \varphi_i) \\ \sin(\omega_i t - 2\pi/3 + \varphi_i) \\ \sin(\omega_i t - 4\pi/3 + \varphi_i) \end{bmatrix}. \quad (17)$$

where  $i = \{A, B, C\}$  is the name of the input phase.

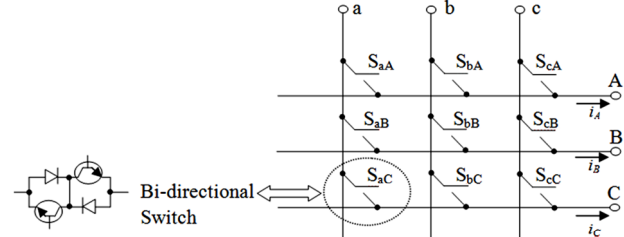


Fig. 4. Symbol of three phase matrix converter

The matrix converter will be designed and controlled in such a manner that the fundamental of the output voltages are:

$$V_j(t) = V_{j \max} \begin{bmatrix} \sin(\omega_j t) \\ \sin(\omega_j t - 2\pi/3) \\ \sin(\omega_j t - 4\pi/3) \end{bmatrix}. \quad (18)$$

$$i_j(t) = I_{j \max} \begin{bmatrix} \sin(\omega_j t + \varphi_j) \\ \sin(\omega_j t - 2\pi/3 + \varphi_j) \\ \sin(\omega_j t - 4\pi/3 + \varphi_j) \end{bmatrix}, \quad (19)$$

where  $j = \{a, b, c\}$  is the name of the output phase.

Ratio  $q$  is the ratio voltage between, its value cannot exceed 0.866 and cannot be negative [18, 19]:

$$q = V_{j \max} / V_{i \max}. \quad (20)$$

The switching function of a single switch is defined as follows:

$$S_{ij}(t) = \begin{cases} 0 & \text{if } S_{ij} \text{ is open;} \\ 1 & \text{if } S_{ij} \text{ is closed,} \end{cases} \quad (21)$$

where  $S_{ij}$  is the bi-directional power switch of matrix converter (see Fig. 4).

The input/output relationships of voltages and currents are related to the states of the nine switches, and can be written in matrix form as:

$$\begin{cases} \vec{V}_j(t) = M(t) \cdot V_i(t); \\ \vec{i}_i(t) = M(t)^t \cdot i_j(t). \end{cases} \quad (22)$$

The matrix  $M(t)^t$  is the transpose of the matrix  $M(t)$ ;

$$M(t) = \begin{bmatrix} m_{Aa}(t) & m_{Ba}(t) & m_{Ca}(t) \\ m_{Ab}(t) & m_{Bb}(t) & m_{Cb}(t) \\ m_{Ac}(t) & m_{Bc}(t) & m_{Cc}(t) \end{bmatrix}. \quad (23)$$

The variables  $m_{ij}(t)$  are the duty-cycles of the 9 switches and can be represented by:

$$m_{ij}(t) = \frac{1}{T} \int_0^T S_{ij}(t) dt, \quad (24)$$

where  $0 \leq m_{ij}(t) \leq 1$ ;  $T$  is the switching period.

**5. Control of matrix converter.** There are a number of possible modulation techniques that can be used for matrix converter control. The optimal modulation strategy should minimize the input current and output voltage harmonic distortion and device power losses. The most relevant control and modulation methods developed for the MCs are the Venturini method, the scalar method developed by Roy and the space-vector modulation (SVM) [20-24]. In this work the SVM method is preferred because it deals with scalar quantities rather than vectors, and this is important when controlling WECS. The SVM had previously been used for inverter control [25] proposed the use of SVM for matrix converters, this strategy control is based on the space vector representation of the input currents and output voltages at any time [26].

$$\vec{V}_j(t) = \frac{2}{3} (v_a + a \cdot v_b + a^2 \cdot v_c) = V_0 e^{j\alpha t}; \quad (25)$$

$$\vec{i}_i(t) = \frac{2}{3} (i_a + a \cdot i_b + a^2 \cdot i_c) = I_i e^{j\beta t}, \quad (26)$$

where  $a = e^{j\frac{2\pi}{3}}$ .

For the three-phase matrix converter, there are 27 possible switching configurations. The first 18 switching configurations determine an output voltage vector and an input current vector and will be named «active configurations». The last 3 switching configurations determine zero input current and output voltage vectors and will be named «zero configurations». The required modulation duty cycles for the switching configurations are giving by the following equation [21-23, 25]. These switching states and the output voltages and input current vectors are presented in Table 1. The sum of the absolute values of the four duty-cycles must be lower than unity.

In the control strategy of the WECS, the DPC-SVM uses 2 control loops with PI controllers, these inner control loops regulate the active and reactive power of AC grid. The estimated values of active and reactive AC grid power are compared with the real and reactive powers references [27-29]. To ensure a pure active power exchange from the wind generator and maintain the reactive power exchange to the grid.

The dynamic model of grid side electrical circuits is presented as [29-32]:

$$\begin{cases} V_{sd} = R_s i_{sd} + L_s \frac{di_{sd}}{dt} - \omega_s L_s i_{sq} + e_{csd}; \\ V_{sq} = R_s i_{sq} + L_s \frac{di_{sq}}{dt} - \omega_s L_s i_{sd} + e_{csq}. \end{cases} \quad (27)$$

The active and reactive power estimator as:

$$\begin{cases} P_{sd} = \frac{3}{2} (v_{sd} i_{sd} + v_{sq} i_{sq}); \\ Q_{sq} = \frac{3}{2} (v_{sq} i_{sd} - v_{sd} i_{sq}). \end{cases} \quad (28)$$

Table 1

Switching configurations			
N <sup>o</sup>	Combination	$\vec{V}_0(t)$	$\vec{i}_i(t)$
1	$S_{Aa}, S_{Bb}, S_{Cb}$	$(2/3) \cdot V_{ab} \cdot e^{j0}$	$(2/\sqrt{3}) \cdot i_A \cdot e^{-j\pi/6}$
2	$S_{Ab}, S_{Ba}, S_{Ca}$	$-(2/3) \cdot V_{ab} \cdot e^{j0}$	$-(2/\sqrt{3}) \cdot i_A \cdot e^{-j\pi/6}$
3	$S_{Ab}, S_{Bc}, S_{Cc}$	$(2/3) \cdot V_{bc} \cdot e^{j0}$	$(2/\sqrt{3}) \cdot i_A \cdot e^{j\pi/2}$
4	$S_{Ac}, S_{Bb}, S_{Cb}$	$-(2/3) \cdot V_{bc} \cdot e^{j0}$	$-(2/\sqrt{3}) \cdot i_A \cdot e^{j\pi/2}$
5	$S_{Ac}, S_{Ba}, S_{Ca}$	$(2/3) \cdot V_{ca} \cdot e^{j0}$	$(2/\sqrt{3}) \cdot i_A \cdot e^{j7\pi/6}$
6	$S_{Aa}, S_{Bc}, S_{Cc}$	$-(2/3) \cdot V_{ca} \cdot e^{j0}$	$-(2/\sqrt{3}) \cdot i_A \cdot e^{j7\pi/6}$
7	$S_{Ab}, S_{Ba}, S_{Cb}$	$(2/3) \cdot V_{ab} \cdot e^{j2\pi/3}$	$(2/\sqrt{3}) \cdot i_B \cdot e^{-j\pi/6}$
8	$S_{Aa}, S_{Bb}, S_{Ca}$	$-(2/3) \cdot V_{ab} \cdot e^{j2\pi/3}$	$-(2/\sqrt{3}) \cdot i_B \cdot e^{-j\pi/6}$
9	$S_{Ac}, S_{Bb}, S_{Cc}$	$(2/3) \cdot V_{bc} \cdot e^{j2\pi/3}$	$(2/\sqrt{3}) \cdot i_B \cdot e^{j\pi/2}$
10	$S_{Ab}, S_{Bc}, S_{Cb}$	$-(2/3) \cdot V_{bc} \cdot e^{j2\pi/3}$	$-(2/\sqrt{3}) \cdot i_B \cdot e^{j\pi/2}$
11	$S_{Aa}, S_{Bc}, S_{Ca}$	$(2/3) \cdot V_{ca} \cdot e^{j2\pi/3}$	$(2/\sqrt{3}) \cdot i_B \cdot e^{j7\pi/6}$
12	$S_{Ac}, S_{Ba}, S_{Cc}$	$-(2/3) \cdot V_{ca} \cdot e^{j2\pi/3}$	$-(2/\sqrt{3}) \cdot i_B \cdot e^{j7\pi/6}$
13	$S_{Ab}, S_{Bb}, S_{Ca}$	$(2/3) \cdot V_{ab} \cdot e^{j4\pi/3}$	$(2/\sqrt{3}) \cdot i_C \cdot e^{-j\pi/6}$
14	$S_{Aa}, S_{Ba}, S_{Cb}$	$-(2/3) \cdot V_{ab} \cdot e^{j4\pi/3}$	$-(2/\sqrt{3}) \cdot i_C \cdot e^{-j\pi/6}$
15	$S_{Ac}, S_{Bc}, S_{Cb}$	$(2/3) \cdot V_{bc} \cdot e^{j4\pi/3}$	$(2/\sqrt{3}) \cdot i_C \cdot e^{j\pi/2}$
16	$S_{Ab}, S_{Bb}, S_{Cc}$	$-(2/3) \cdot V_{bc} \cdot e^{j4\pi/3}$	$-(2/\sqrt{3}) \cdot i_C \cdot e^{j\pi/2}$
17	$S_{Aa}, S_{Ba}, S_{Cc}$	$(2/3) \cdot V_{ca} \cdot e^{j4\pi/3}$	$(2/\sqrt{3}) \cdot i_C \cdot e^{j7\pi/6}$
18	$S_{Ac}, S_{Bc}, S_{Ca}$	$-(2/3) \cdot V_{ca} \cdot e^{j4\pi/3}$	$-(2/\sqrt{3}) \cdot i_C \cdot e^{j7\pi/6}$
19	$S_{Aa}, S_{Ab}, S_{Ac}$	0	-
20	$S_{Ba}, S_{Bb}, S_{Bc}$	0	-
21	$S_{Ca}, S_{Cb}, S_{Cc}$	0	-

**6. Simulation results.** The simulation of wind system based on DFIG with the considered control systems 1 has been implemented using Simulink/MATLAB (Fig. 5).

The parameters of proposed conversion system are shown in Table 2.

Table 2

System parameters	
Parameters, units	Values
Grid frequency $f_s$ , Hz	50
Grid voltage $V_{srms}$ , V	575
Voltage $V_{rrms}$ , V	575
IGBTs switch frequency (SVM), kHz	6
Power $P_n$ , MW	1.5
Voltage (line-line) $V_{nrms}$ , V	575
Stator resistance $R_s$ , $\Omega$	0.01965
Stator Inductance $L_s$ , H	0.0397
Rotor resistance $R_r$ , $\Omega$	0.01909
Rotor Inductance $L_r$ , H	0.0397
Mutual inductance $L_m$ , H	1.354
Inertia $J$ , kg·m <sup>2</sup>	0.09526
Flux linkage $\Phi_f$ , Wb	0.05479

The obtained simulation results of considered WECS are presented in Fig. 6–8. The considered control of whole system has been tested for the wind speed during the period of the 3 s, while, the average wind speed has been adopted for different average values at 9 m/s, 11 m/s and 15 m/s (Fig. 6).

Figures 7, 8 present the responses of speed rotor and electromagnetic torque compared to the mechanical torque. It can be seen, that the electromagnetic torque  $T_{em}$  is accurately adjusted to the mechanical torque.

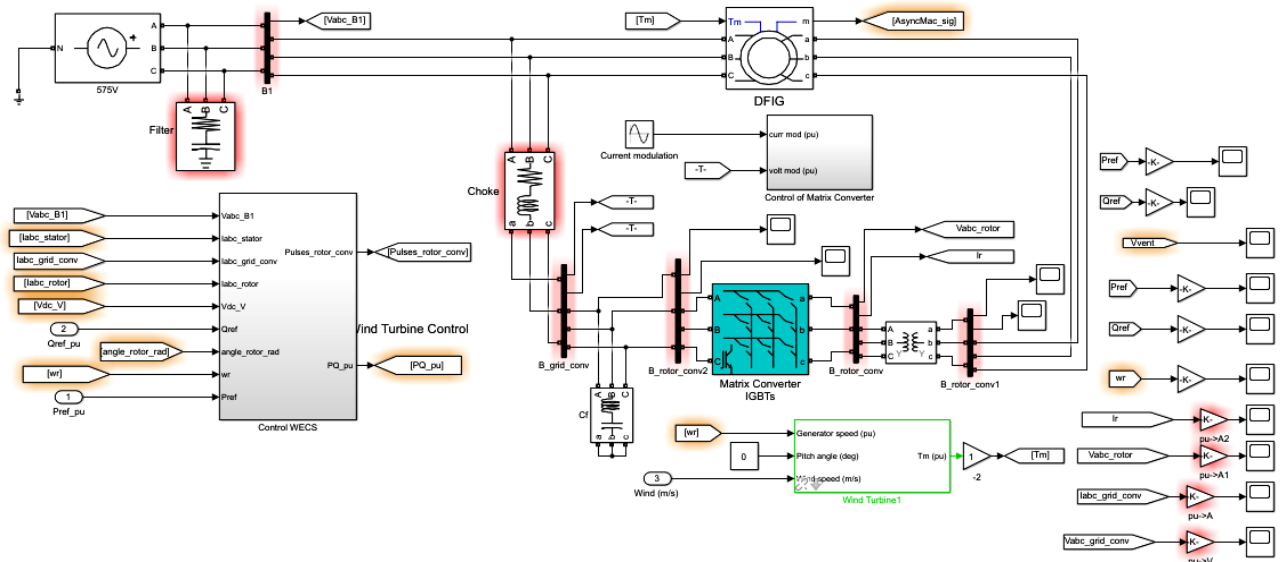


Fig. 5. Simulink model of WECS

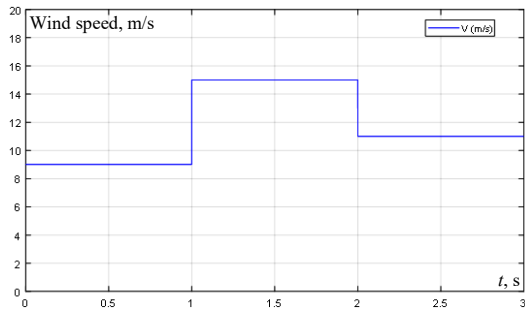


Fig. 6. Wind speed

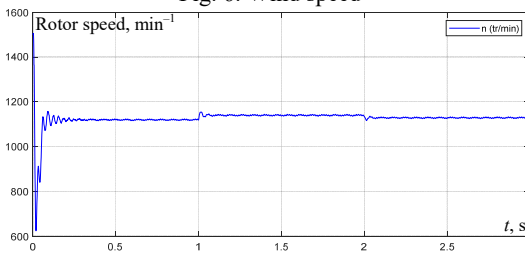


Fig. 7. Rotor speed of DFIG

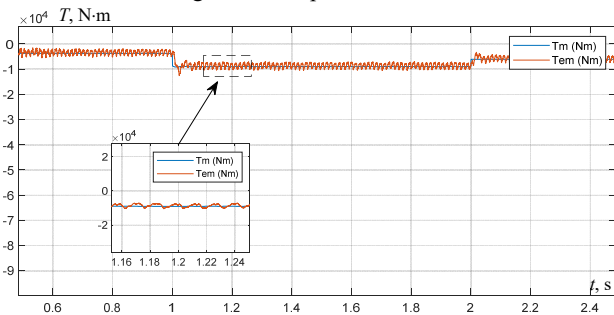


Fig. 8. Electromagnetic torque and its reference

So, the considered control system allows fast responses of the electromagnetic torque  $T_{em}$  of DFIG during temporary time variations of the wind speed.

The waveform of output currents (rotor currents of DFIG) and input currents of matrix converter are practically changing according to variations of wind speed (see Fig. 9, 10). We can see that these currents are sinusoidal. Figures 11, 12 display the three-phase voltages and current injected to the grid by the conversion system controlled by DPC-SVM strategy. It can be seen, that this current has a

sinusoidal form and changing according to the variations of wind speed.

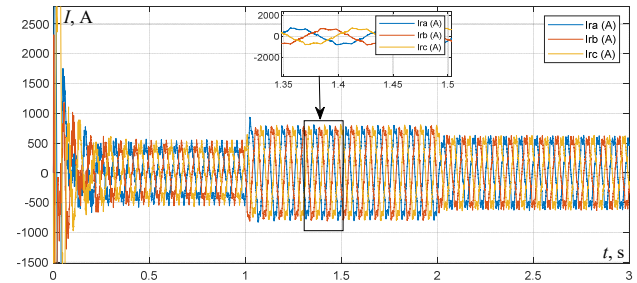


Fig. 9. Rotor currents (output currents of MC)

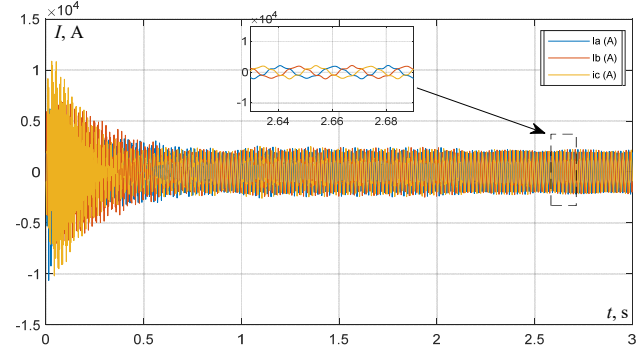


Fig. 10. Input currents of MC

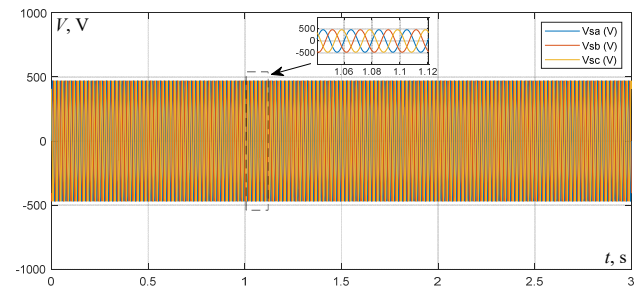


Fig. 11. Stator voltages connected to the grid

Figure 13 shows the grid voltage and current delivered by the generating system. It can be seen that the voltage is in phase opposition with the current, which proves that the proposed system drives with unitary factor power. Finally, Fig. 14, 15 present the active and reactive powers injected to the grid, controlled via the proposed DPC-SVM.

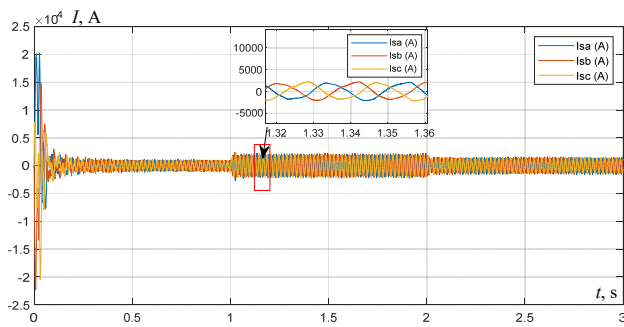


Fig. 12. Stator currents connected to the grid

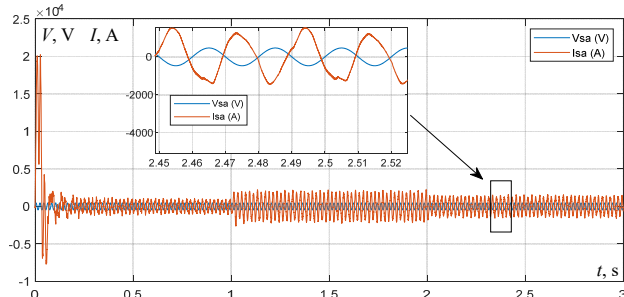


Fig. 13. Waveforms of grid phase voltage and current

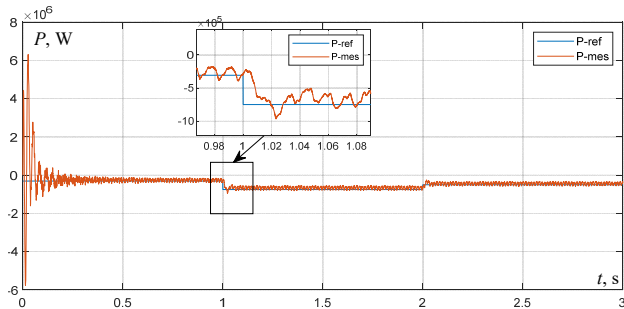


Fig. 14. Active power and its reference connected to the grid

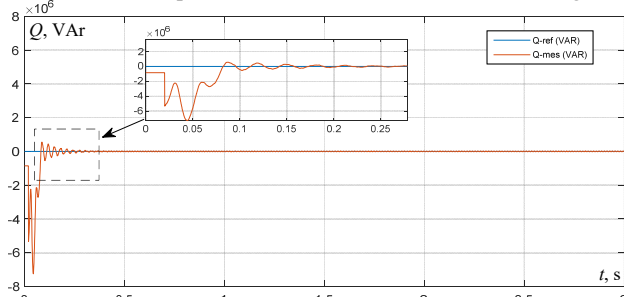


Fig. 15. Reactive power and its reference connected to the grid

We can conclude that, under the proposed control algorithm, the grid power amounts track their reference values with smooth profiles. Also, from these figures, it can be noticed, that only the active power generated by the proposed system is fully delivered to the AC grid, while the reactive power is controlled to be zero.

**7. Conclusions.** In this paper, a new proposed doubly fed induction generator of wind energy conversion system based direct matrix converter connected to the grid has been presented. In this study, the conventional back-to-back converters has been replaced by a direct matrix converter using direct power control using space vector modulation strategy control. The advantage in the proposed scheme is that the DC-link capacitors voltage and the grid side converter have been eliminated. In order to control the active and reactive power injected to the grid a direct power control using space vector modulation

strategy control have been explored. This technique eliminates the lookup table and reduces the grid powers and currents harmonics as well. In addition, the direct power control using space vector modulation strategy control guarantees good dynamic response and provides sinusoidal line currents. We can confirm that the direct matrix converter presents an interesting alternative for the variable wind speed. The simulation results are satisfactory, have a good performance and good control proprieties between measured and reference quantities. The results encourage a further development of this study to obtain clean energy.

**Conflict of interest.** The authors declare that they have no conflicts of interest.

## REFERENCES

1. Bistline J., Abhyankar N., Blanford G., Clarke L., Fakhry R., McJeon H., Reilly J., Roney C., Wilson T., Yuan M., Zhao A. Actions for reducing US emissions at least 50% by 2030. *Science*, 2022, vol. 376, no. 6596, pp. 922-924. doi: <https://doi.org/10.1126/science.abn0661>.
2. Williams J.H., DeBenedictis A., Ghanadan R., Mahone A., Moore J., Morrow W.R., Price S., Torn M.S. The Technology Path to Deep Greenhouse Gas Emissions Cuts by 2050: The Pivotal Role of Electricity. *Science*, 2012, vol. 335, no. 6064, pp. 53-59. doi: <https://doi.org/10.1126/science.1208365>.
3. Pfenninger S., Keirstead J. Comparing concentrating solar and nuclear power as baseload providers using the example of South Africa. *Energy*, 2015, vol. 87, pp. 303-314. doi: <https://doi.org/10.1016/j.energy.2015.04.077>.
4. Boopathi K., Ramaswamy S., Kirubakaran V., Uma K., Saravanan G., Thyagaraj S., Balaraman K. Economic investigation of repowering of the existing wind farms with hybrid wind and solar power plants: a case study. *International Journal of Energy and Environmental Engineering*, 2021, vol. 12, no. 4, pp. 855-871. doi: <https://doi.org/10.1007/s40095-021-00391-3>.
5. Staffell I., Pfenninger S. The increasing impact of weather on electricity supply and demand. *Energy*, 2018, vol. 145, pp. 65-78. doi: <https://doi.org/10.1016/j.energy.2017.12.051>.
6. Sureshkumar K., Ponnusamy V. Hybrid renewable energy systems for power flow management in smart grid using an efficient hybrid technique. *Transactions of the Institute of Measurement and Control*, 2020, vol. 42, no. 11, pp. 2068-2087. doi: <https://doi.org/10.1177/0142331220904818>.
7. Boumassata A., Kerdoun D., Oualah O. Maximum power control of a wind generator with an energy storage system to fix the delivered power. *Electrical Engineering & Electromechanics*, 2022, no. 2, pp. 41-46. doi: <https://doi.org/10.20998/2074-272X.2022.2.07>.
8. Boutoubat M., Mokrani L., Machmoum M. Control of a wind energy conversion system equipped by a DFIG for active power generation and power quality improvement. *Renewable Energy*, 2013, vol. 50, pp. 378-386. doi: <https://doi.org/10.1016/j.renene.2012.06.058>.
9. Tang C.Y., Guo Y., Jiang J.N. Nonlinear Dual-Mode Control of Variable-Speed Wind Turbines With Doubly Fed Induction Generators. *IEEE Transactions on Control Systems Technology*, 2011, vol. 19, no. 4, pp. 744-756. doi: <https://doi.org/10.1109/TCST.2010.2053931>.
10. El-Sattar A.A., Saad N.H., El-Dein M.Z.S. Dynamic response of doubly fed induction generator variable speed wind turbine under fault. *Electric Power Systems Research*, 2008, vol. 78, no. 7, pp. 1240-1246. doi: <https://doi.org/10.1016/j.epsr.2007.10.005>.
11. Kahla S., Bechouat M., Amieur T., Sedraoui M., Babes B., Hamouda N. Maximum power extraction framework using robust fractional-order feedback linearization control and GM-CPSO for PMSG-based WECS. *Wind Engineering*, 2021, vol. 45, no. 4, pp. 1040-1054. doi: <https://doi.org/10.1177/0309524X20948263>.

12. Sahri Y., Tamalouzt S., Hamoudi F., Belaid S.L., Bajaj M., Alharthi M.M., Alzaidi M.S., Ghoneim S.S.M. New intelligent direct power control of DFIG-based wind conversion system by using machine learning under variations of all operating and compensation modes. *Energy Reports*, 2021, vol. 7, pp. 6394-6412. doi: <https://doi.org/10.1016/j.egy.2021.09.075>.
13. Mazouz F., Belkacem S., Colak I., Drid S., Harbouche Y. Adaptive direct power control for double fed induction generator used in wind turbine. *International Journal of Electrical Power & Energy Systems*, 2020, vol. 114, art. no. 105395. doi: <https://doi.org/10.1016/j.ijepes.2019.105395>.
14. Zhi D., Xu L. Direct Power Control of DFIG With Constant Switching Frequency and Improved Transient Performance. *IEEE Transactions on Energy Conversion*, 2007, vol. 22, no. 1, pp. 110-118. doi: <https://doi.org/10.1109/TEC.2006.889549>.
15. Babes B., Hamouda N., Kahla S., Amar H., Ghoneim S.S.M. Fuzzy model based multivariable predictive control design for rapid and efficient speed-sensorless maximum power extraction of renewable wind generators. *Electrical Engineering & Electromechanics*, 2022, no. 3, pp. 51-62. doi: <https://doi.org/10.20998/2074-272X.2022.3.08>.
16. Wheeler P.W., Rodriguez J., Clare J.C., Empringham L., Weinstein A. Matrix converters: a technology review. *IEEE Transactions on Industrial Electronics*, 2002, vol. 49, no. 2, pp. 276-288. doi: <https://doi.org/10.1109/41.993260>.
17. Kolar J.W., Friedli T., Rodriguez J., Wheeler P.W. Review of Three-Phase PWM AC-AC Converter Topologies. *IEEE Transactions on Industrial Electronics*, 2011, vol. 58, no. 11, pp. 4988-5006. doi: <https://doi.org/10.1109/TIE.2011.2159353>.
18. Casadei D., Serra G., Tani A., Zarri L. Optimal Use of Zero Vectors for Minimizing the Output Current Distortion in Matrix Converters. *IEEE Transactions on Industrial Electronics*, 2009, vol. 56, no. 2, pp. 326-336. doi: <https://doi.org/10.1109/TIE.2008.2007557>.
19. Varajão D., Araújo R.E. Modulation Methods for Direct and Indirect Matrix Converters: A Review. *Electronics*, 2021, vol. 10, no. 7, art. no. 812. doi: <https://doi.org/10.3390/electronics10070812>.
20. Sayed M.A., Suzuki K., Takeshita T., Kitagawa W. PWM Switching Technique for Three-Phase Bidirectional Grid-Tie DC-AC-AC Converter With High-Frequency Isolation. *IEEE Transactions on Power Electronics*, 2018, vol. 33, no. 1, pp. 845-858. doi: <https://doi.org/10.1109/TPEL.2017.2668441>.
21. Shi T., Wu L., Yan Y., Xia C. Harmonic Spectrum of Output Voltage for Space Vector Pulse Width Modulated Ultra Sparse Matrix Converter. *Energies*, 2018, vol. 11, no. 2, art. no. 390. doi: <https://doi.org/10.3390/en11020390>.
22. Tuyen N., Dzung P. Space Vector Modulation for an Indirect Matrix Converter with Improved Input Power Factor. *Energies*, 2017, vol. 10, no. 5, art. no. 588. doi: <https://doi.org/10.3390/en10050588>.
23. Rodriguez J., Rivera M., Kolar J.W., Wheeler P.W. A Review of Control and Modulation Methods for Matrix Converters. *IEEE Transactions on Industrial Electronics*, 2012, vol. 59, no. 1, pp. 58-70. doi: <https://doi.org/10.1109/TIE.2011.2165310>.
24. Wang X., Lin H., She H., Feng B. A Research on Space Vector Modulation Strategy for Matrix Converter Under Abnormal Input-Voltage Conditions. *IEEE Transactions on Industrial Electronics*, 2012, vol. 59, no. 1, pp. 93-104. doi: <https://doi.org/10.1109/TIE.2011.2157288>.
25. Huber L., Borojevic D. Space vector modulation with unity input power factor for forced commutated cycloconverters. *Conference Record of the 1991 IEEE Industry Applications Society Annual Meeting*, 1991, pp. 1032-1041. doi: <https://doi.org/10.1109/IAS.1991.178363>.
26. Li D., Deng X., Li C., Zhang X., Fang E. Study on the space vector modulation strategy of matrix converter under abnormal input condition. *Alexandria Engineering Journal*, 2022, vol. 61, no. 6, pp. 4595-4605. doi: <https://doi.org/10.1016/j.aej.2021.10.020>.
27. Sellah M., Kouzou A., Mohamed-Seghir M., Rezaoui M.M., Kennel R., Abdelrahem M. Improved DTC-SVM Based on Input-Output Feedback Linearization Technique Applied on DOEWM Powered by Two Dual Indirect Matrix Converters. *Energies*, 2021, vol. 14, no. 18, art. no. 5625. doi: <https://doi.org/10.3390/en14185625>.
28. Sahri Y., Tamalouzt S., Hamoudi F., Belaid S.L., Bajaj M., Alharthi M.M., Alzaidi M.S., Ghoneim S.S.M. New intelligent direct power control of DFIG-based wind conversion system by using machine learning under variations of all operating and compensation modes. *Energy Reports*, 2021, vol. 7, pp. 6394-6412. doi: <https://doi.org/10.1016/j.egy.2021.09.075>.
29. Sun D., Wang X., Nian H., Zhu Z.Q. A Sliding-Mode Direct Power Control Strategy for DFIG Under Both Balanced and Unbalanced Grid Conditions Using Extended Active Power. *IEEE Transactions on Power Electronics*, 2018, vol. 33, no. 2, pp. 1313-1322. doi: <https://doi.org/10.1109/TPEL.2017.2686980>.
30. Chaudhuri A., Datta R., Kumar M.P., Davim J.P., Pramanik S. Energy Conversion Strategies for Wind Energy System: Electrical, Mechanical and Material Aspects. *Materials*, 2022, vol. 15, no. 3, art. no. 1232. doi: <https://doi.org/10.3390/ma15031232>.
31. Benbouhenni H., Lemdani S. Combining synergetic control and super twisting algorithm to reduce the active power undulations of doubly fed induction generator for dual-rotor wind turbine system. *Electrical Engineering & Electromechanics*, 2021, no. 3, pp. 8-17. doi: <https://doi.org/10.20998/2074-272X.2021.3.02>.
32. Benbouhenni H., Boudjema Z., Belaidi A. DPC Based on ANFIS Super-Twisting Sliding Mode Algorithm of a Doubly-Fed Induction Generator for Wind Energy System. *Journal Européen Des Systèmes Automatisés*, 2020, vol. 53, no. 1, pp. 69-80. doi: <https://doi.org/10.18280/jesa.530109>.

Received 22.08.2022

Accepted 10.11.2022

Published 06.05.2023

Aziz Boukadoum<sup>1</sup>, Associate Professor,

Abla Bouguerne<sup>1</sup>, Associate Professor,

Tahar Bahi<sup>2</sup>, Professor,

<sup>1</sup> Labget laboratory, Department of Electrical Engineering, Echahid Cheikh Larbi Tebessi University-Tebessa, Algeria, e-mail: azizboukadoum@yahoo.fr (Corresponding Author), bouguerneabla@yahoo.fr

<sup>2</sup> Department of Electrical Engineering, University Badji Mokhtar Annaba, Algeria, e-mail: tbahi@hotmail.fr

#### How to cite this article:

Boukadoum A., Bouguerne A., Bahi T. Direct power control using space vector modulation strategy control for wind energy conversion system using three-phase matrix converter. *Electrical Engineering & Electromechanics*, 2023, no. 3, pp. 40-46. doi: <https://doi.org/10.20998/2074-272X.2023.3.06>

V.G. Yagup, K.V. Yagup

## Acceleration of exit to steady-state mode when modeling semiconductor converters

The **purpose** of the article is to develop a method and algorithm for the accelerated calculation of steady states of thyristor converters using computer models of converters based on the use of the theory of difference equations in the form of recurrent linear relationships for state variables on the boundaries of the converter periods. **Methodology.** The article is devoted to the solution of the problem of reducing the cost of computer time to achieve the steady state of the thyristor converter. For this, it is proposed to use difference equations, for which the values of the state variables at the limits of the periods of the converter's operation are taken as variables. These values are accumulated during the initial periods of the transient process of the converter, after which the coefficients of the difference equations are calculated, and the following limit values of the state variables are found using the defined difference equations. A program in the algorithmic language of the MATLAB system is presented, which implements the proposed method and algorithm compatible with the visual model of the converter. **Results.** The theoretical foundations of the proposed method and the area of its applicability are substantiated. Recommendations are presented for determining the number of periods of the flow process that must be calculated for further implementation of the method. An algorithm for forming matrix relations for determining the coefficients of difference equations with respect to the values of state variables at the boundaries of periods is shown. Matrix equations are given that allow calculating the parameters of the steady state. All stages of the algorithm are illustrated with numerical examples. **Originality.** The method rationally combines all the advantages of visual modeling based on the numerical integration of equations using the method of state variables for the periods of operation of the converter with the analytical solution of the recurrence relations obtained on this basis for the values of state variables at the boundaries of adjacent periods. **Practical value.** The proposed method makes it possible to reduce by several orders of magnitude the computer time spent on calculating the parameters of the steady-state mode of the converter and, at the same time, to significantly improve the accuracy of these calculations. The practical application of the method is very effective in research and design of thyristor converters of electrical energy parameters. References 10, tables 2, figures 4.

**Key words:** thyristor converter, state variables, difference equations, steady state, visual model.

Стаття присвячена вирішенню проблеми зменшення витрат комп'ютерного часу для досягнення усталеного режиму тиристорного перетворювача. Для цього запропоновано використати різницеві рівняння, для яких в якості змінних приймаються значення змінних стану на межах періодів роботи перетворювача. Ці значення накопичуються на початкових періодах перехідного процесу перетворювача, після чого вираховуються коефіцієнти різницевого рівнянь, і наступні межові значення змінних стану знаходяться з використанням визначених різницевого рівнянь. Представлена програма на алгоритмічній мові системи MATLAB, яка реалізує запропоновані метод і алгоритм сумісно з візуальною моделлю перетворювача. Бібл. 10, табл. 2, рис. 4.

**Ключові слова:** тиристорний перетворювач, змінні стану, різницеві рівняння, усталений режим, візуальна модель.

**Introduction. Problem definition.** Research and design of thyristor converters at the current stage cannot be imagined without the use of computer models [1]. The functioning of such models is based on the piecewise linear approximation of the volt-ampere characteristics of the valve elements [2, 3]. Here, to simulate electromagnetic processes in the converter, the fitting method is used, in which the solution is stitched together from the links of solutions of linear differential equations describing the behavior of the converter in the interval of invariance of the state of the valve elements of the converter. Thus, the converter model spends computer time on analyzing the structure of the power part of the converter, forming graphs and topological matrices, finding the coefficients of linear differential equations by the method of, say, state variables, integrating the system of differential equations by a numerical method capable of overcoming the problem of system rigidity, and also for calculating valve switching moments and determining the next state of the valves [2]. Steady-state modes are usually in well-known programs for modeling converters by the setting method [4], which actually simulates the real start-up of the converter, usually from zero initial values for the state variables, which are capacitor voltages and inductance currents. To achieve a steady-state mode of the converter, it is necessary to calculate a large number of periods of the transient process. This process of reaching a steady-state mode, which in a real converter

takes a certain real time and is considered fundamentally inevitable and necessary, can take a significant amount of computer time in computer models. The problem deepens when the process of exiting to a stable mode is slowed down. This happens when there are reactive elements in the converter circuit which slowly accumulate large amounts of electromagnetic energy, as well as in cases of weakly damped converter circuits [5]. Added to this is the increase in simulation time when trying to increase the accuracy of calculations by reducing the step of integration of systems of differential equations of the converter during the periods of the transient process of setting the mode. When modeling converters in the MATLAB/Simulink/SimPowerSystem computer system, the factor that this system uses the interpreter mode, when the conversion of operators into machine command code is carried out at each call to the operator, is also involved, which is especially sensitive when implementing cyclic algorithms, so characteristic for modeling converters. Therefore, when the converter circuit is complicated, the simulation time increases significantly, as was observed, for example, when modeling steady-state modes in three-phase thyristor reactive power compensators. And therefore, the solution to the problem of speeding up calculations of steady-state modes of converters, and even just electrical systems, in computer modeling does not lose its **relevance** even at the present time

© V.G. Yagup, K.V. Yagup

In works [5, 6], the determination of steady-state parameters of a single-phase rectifier with a third-order smoothing filter based on Newton method is considered. Work [7] was carried out in the same direction. In these works, finding a solution is connected with the calculation of derivatives and carrying out an iterative process. In [8], the replacement of the integration of state equations by difference equations is considered, but not a DC converter is analyzed, but only a substitute circuit without semiconductor switches, which are necessarily included in the circuits of power parameter converters. It is also worth noting that the application of this method requires calculations using rather cumbersome analytical expressions. Steady-state processes in active converter systems are discussed in [9, 10]. The methods proposed in them are not of a general nature, but take into account the

peculiarities of pulse width modulation, which is used in power converters of this class only.

**The goal of the article** is to develop a method and algorithm for accelerated calculation of steady states of thyristor converters using computer models of converters based on the use of the theory of difference equations in the form of recurrent linear relationships for state variables on the boundaries of converter periods.

**The main part of the study.**

**1. Study of the transient process of starting the inverter.** We will consider the circuit of a single-phase autonomous current inverter on thyristors, which is used in practice for systems of high-frequency induction heating of metal [1, 2]. The structure of the circuit is clear from the converter model in the SimPowerSystem system [3], which is shown in Fig. 1.

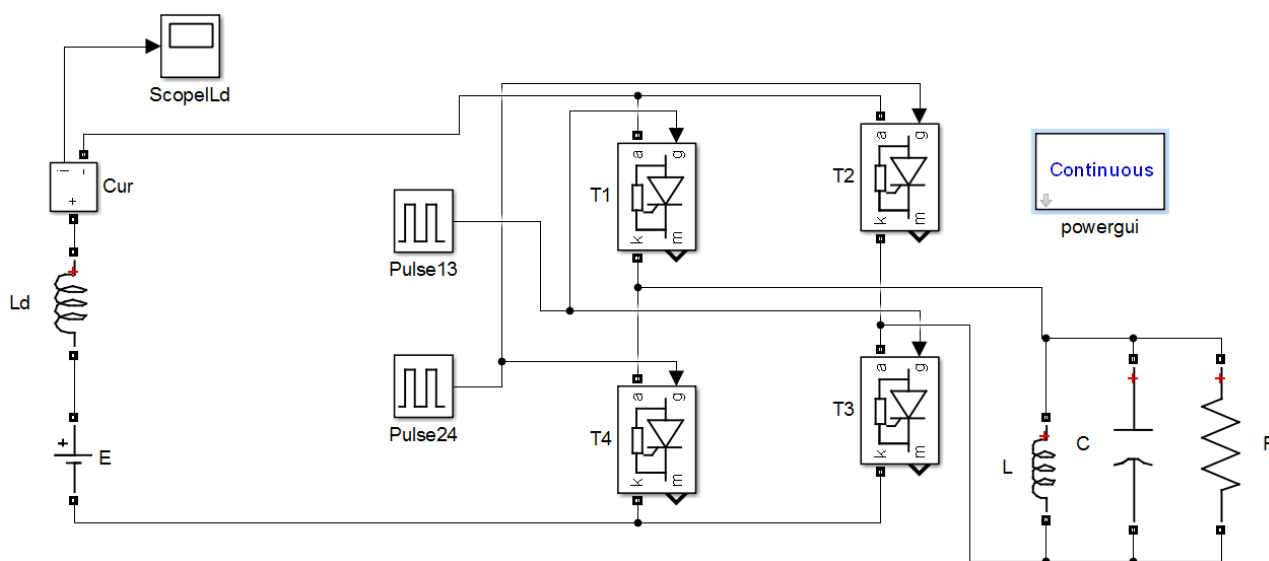


Fig. 1. The investigated model of the converter in SimPowerSystem

The inverter is fed from a constant voltage source  $E$  through a choke  $L_d$  with a large inductance. The voltage from the source is applied to the vertical diagonal of the semiconductor bridge consisting of thyristors T1–T4. An inverter load is connected to the horizontal diagonal, consisting of a switching capacitor  $C$  and active-inductive complex resistance  $R$  and  $L$ . Normalized circuit parameters:  $E = 100$  V,  $L_d = 40$  H,  $L = 1$  H,  $C = 0.111$  F,  $R = 50$   $\Omega$ . The control period of thyristors is taken as 2 s, it is specified in the property windows of the corresponding virtual thyristor control pulse generators. With zero initial conditions, the inverter start-up process was simulated. The simulation results are presented in the form of time diagrams in Fig. 2, namely:  $a$  – the voltage on the capacitor,  $b$  – the current in the load inductance,  $c$  – the current in the input chokes  $L_d$ .

From Fig. 2, it is especially clear that the start-up process is weakly damped, which entails the need to run a large number of periods to achieve a steady-state of the inverter.

**Difference equations for periods.** We will proceed from the fact that on the intervals of invariance of the state of the thyristors, the substitute circuits of the inverter are linear and are described by systems of linear differential equations. This, in turn, determines the linear

dependencies between the values of the variables of the state at the boundaries of the periods. We will use the following designations of state variables in the future: voltage on the switching capacitor  $v_C = x_1$ ; current in the load inductance  $i_{Ld} = x_3$ ; input choke current  $i_{Ld} = x_3$ . Then for the adjacent  $k$ -th and  $(k+1)$ -th boundaries of the periods, the following difference equations can be drawn up:

$$\begin{aligned} x_1^{k+1} &= a_{11}x_1^k + a_{12}x_2^k + a_{13}x_3^k + b_1E; \\ x_2^{k+1} &= a_{21}x_1^k + a_{22}x_2^k + a_{23}x_3^k + b_2E; \\ x_3^{k+1} &= a_{31}x_1^k + a_{32}x_2^k + a_{33}x_3^k + b_3E. \end{aligned} \quad (1)$$

In these equations, the superscripts mean the numbers of adjacent boundaries, on which the values of the inverter state variables are fixed. To determine the unknown coefficients of these equations, it is enough to have information about the values of the state variables at the boundaries of several initial periods of the starting transition process. The number of periods that must be calculated using the model should be equal to the sum of the number of reactive elements and power sources of the converter. For the inverter under consideration, taking  $k = 0, 1, 2, 3$  consecutively and using only the first equation of the system (1), we obtain the following system of equations:

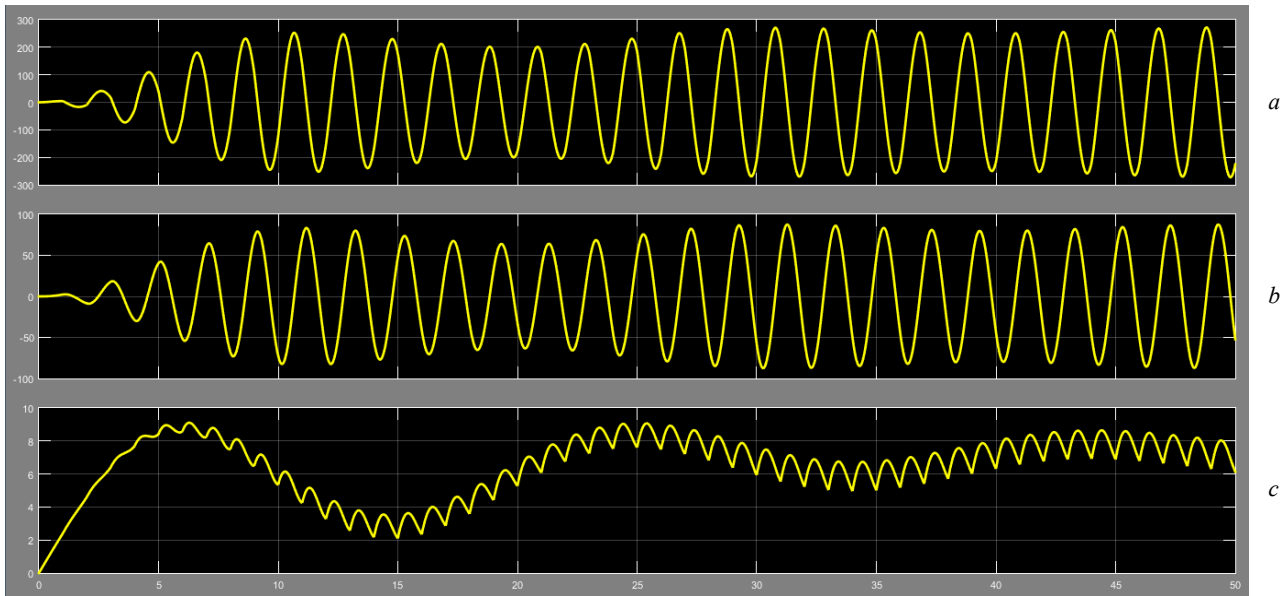


Fig. 2. Time diagrams:

*a* – the voltage on the capacitor, *b* – the current in the load inductance, *c* – the current in the input choke Ld

$$\begin{aligned}
 x_1^1 &= a_{11}x_1^0 + a_{12}x_2^0 + a_{13}x_3^0 + b_1E; \\
 x_1^2 &= a_{11}x_1^1 + a_{12}x_2^1 + a_{13}x_3^1 + b_1E; \\
 x_1^3 &= a_{11}x_1^2 + a_{12}x_2^2 + a_{13}x_3^2 + b_1E; \\
 x_1^4 &= a_{11}x_1^3 + a_{12}x_2^3 + a_{13}x_3^3 + b_1E.
 \end{aligned} \quad (2)$$

Considering the coefficients  $a_{11}$ ,  $a_{12}$ ,  $a_{13}$ ,  $b_1$  as unknown values, we rewrite the system of equations (2) in the following matrix form:

$$\begin{bmatrix} x_1^0 & x_2^0 & x_3^0 & E \\ x_1^1 & x_2^1 & x_3^1 & E \\ x_1^2 & x_2^2 & x_3^2 & E \\ x_1^3 & x_2^3 & x_3^3 & E \end{bmatrix} \times \begin{bmatrix} a_{11} \\ a_{12} \\ a_{13} \\ b_1 \end{bmatrix} = \begin{bmatrix} x_1^1 \\ x_1^2 \\ x_1^3 \\ x_1^4 \end{bmatrix}. \quad (3)$$

To solve the resulting system of linear algebraic equations, the inverse matrix method can be used, and then the solution with respect to unknown coefficients can be written in the form:

$$\begin{bmatrix} a_{11} \\ a_{12} \\ a_{13} \\ b_1 \end{bmatrix} = \begin{bmatrix} x_1^0 & x_2^0 & x_3^0 & E \\ x_1^1 & x_2^1 & x_3^1 & E \\ x_1^2 & x_2^2 & x_3^2 & E \\ x_1^3 & x_2^3 & x_3^3 & E \end{bmatrix}^{-1} \times \begin{bmatrix} x_1^1 \\ x_1^2 \\ x_1^3 \\ x_1^4 \end{bmatrix}. \quad (4)$$

Similarly, the coefficients of the remaining equations of the system (1) are found. It is worth noting that in this case the inverse square matrix does not change, and only the values of the elements of the column matrices in the left and right parts of the last matrix relation change.

After determining the coefficients, the system of equations (1) can be written in expanded matrix form:

$$\begin{bmatrix} x_1^{k+1} \\ x_2^{k+1} \\ x_3^{k+1} \end{bmatrix} = \begin{bmatrix} a_{11} & a_{12} & a_{13} \\ a_{21} & a_{22} & a_{23} \\ a_{31} & a_{32} & a_{33} \end{bmatrix} \times \begin{bmatrix} x_1^k \\ x_2^k \\ x_3^k \end{bmatrix} + \begin{bmatrix} b_1 \\ b_2 \\ b_3 \end{bmatrix} \times E. \quad (5)$$

In the shortened matrix form, the last system is written as follows:

$$\mathbf{X}_{k+1} = \mathbf{A} \times \mathbf{X}_k + \mathbf{B} \times E. \quad (6)$$

This matrix recurrent equation allows, by determining the vector  $\mathbf{X}^0$  of the initial values of the state variables, to calculate the next values of the state variables on the boundaries of the periods until reaching the steady-state, when these values on the adjacent boundaries will be repeated within the limits of the permissible error. Evidently, the expenses of computer time during such a steady-state mode will be several orders of magnitude smaller compared to the integration of differential equations with a fairly small step during the entire time the inverter model reaches steady-state modes. If it is still necessary to investigate the process during a certain period, it is enough to use the values of the state variables at the beginning of this period.

It is possible to speed up the acquisition of steady-state parameters, assuming that after endless use of (6) for  $k \rightarrow \infty$  we assume that  $\mathbf{X}^k = \mathbf{X}^{k+1} = \mathbf{X}^\infty$ , and then the last matrix equation takes the form:

$$\mathbf{X}^\infty = \mathbf{A} \times \mathbf{X}^\infty + \mathbf{B} \times E. \quad (7)$$

Solving this matrix equation with respect to the vector  $\mathbf{X}^\infty$ , we obtain the following matrix expression for finding the values of the state variables at the beginning of the steady-state period:

$$\mathbf{X}^\infty = (\mathbf{I} - \mathbf{A})^{-1} \times \mathbf{B} \times E. \quad (8)$$

The use of equation (8) makes it possible to speed up the calculation of the steady-state parameters of the converter even more.

**Results of numerical analysis.** With the specified parameters of the inverter, the visual model of the inverter (Fig. 1) was run during the first four periods of the start-up process. Here, the values of the state variables were fixed at the boundaries of the periods with their recording in the MATLAB workspace. The results obtained in this way are copied from the workspace and presented in Table 1.

Table 1  
Values of state variables at the boundaries of the start-up process

$k$	$x_1^k = v_c^k$	$x_2^k = i_L^k$	$x_3^k = i_{Ld}^k$
0	0	0	0
1	-10,050	-8,4836	4,595
2	-27,2585	-28,851	7,694
3	-54,555	-51,443	8,581
4	-88,909	-67,490	7,492

Now, to find the coefficients of the first equation of the system (1), we use the matrix relationship (4), in which we substitute the specific numerical values of the state variables of the converter on the boundaries of the periods, borrowed directly from the table:

$$\begin{bmatrix} v_C^\infty \\ i_L^\infty \\ i_{Ld}^\infty \end{bmatrix} = \begin{bmatrix} 1 & 0 & 0 \\ 0 & 1 & 0 \\ 0 & 0 & 1 \end{bmatrix} - \begin{bmatrix} 0,82234 & 0,48584 & -1,04908 \\ -0,053928 & 0,64337 & -3,36204 \\ -0,002911 & 0,084051 & 0,82288 \end{bmatrix} \times \begin{bmatrix} -0,10050 \\ -0,084836 \\ 0,045959 \end{bmatrix} \times 100 = \begin{bmatrix} -228,673 \\ -49,19248 \\ 6,36275 \end{bmatrix}.$$

The found values of the state variables were further used as the initial values of the capacitor voltage and inductance currents. In this case, the steady-state mode is immediately established in the inverter. This is evidenced by the time diagrams presented in Fig. 3, 4. Figure 3 shows the time diagrams of the voltage on the capacitor

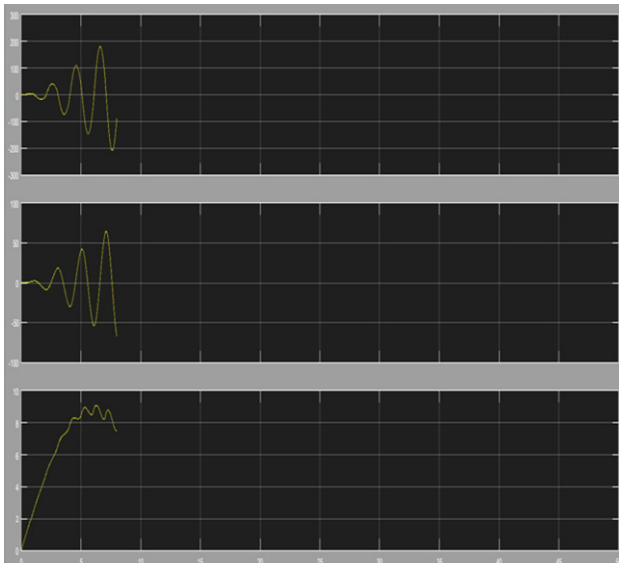


Fig. 3. Initial start-up periods of the inverter

Table 2 allows to quantitatively assess the accuracy of determining the initial values of the inverter state variables for the steady-state using the proposed method.

Table 2  
Values of state variables at the boundaries of the steady-state

$k$	$x_1 = v_c$	$x_2 = i_L$	$x_3 = i_{Ld}$
0	-228,673701	-49,192482	6,362751
1	-228,673719	-49,192489	6,362753
2	-228,673740	-49,192499	6,362754
3	-228,673765	-49,192509	6,362755
4	-228,673789	-49,192516	6,362754
5	-228,673812	-49,192518	6,362753

Here are the results of calculations of five periods of the steady-state of the inverter, represented by the values

$$\begin{bmatrix} a_{11} \\ a_{12} \\ a_{13} \\ b_1 \end{bmatrix} = \begin{bmatrix} 0 & 0 & 0 & 100 \\ -10,050 & -8,4836 & 4,595 & 100 \\ -27,2585 & -28,851 & 7,694 & 100 \\ -54,555 & -51,443 & 8,581 & 100 \end{bmatrix}^{-1} \times \begin{bmatrix} -10,050 \\ -27,2585 \\ -54,555 \\ -88,909 \end{bmatrix} = \begin{bmatrix} 0,82234 \\ 0,48584 \\ -1,04908 \\ -0,10050 \end{bmatrix}.$$

All coefficients of system equations (1) are calculated in a similar way. Taking into account these calculations, the matrix expression (8) takes the form:

and the currents of the load inductances and the input choke during the first four periods of the start-up process. Figure 4 shows the corresponding diagrams obtained as a result of the simulation of the steady-state process, obtained after running the model with the initial values of the state variables found using the proposed method.

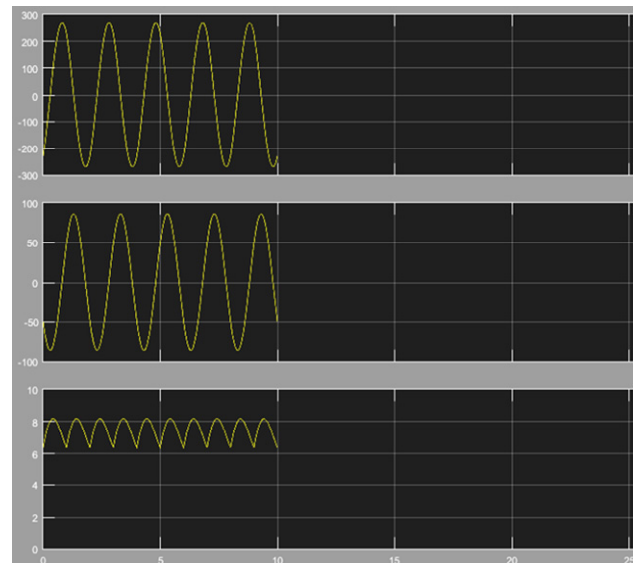


Fig. 4. Steady-state inverter mode

of the state variables at the boundaries of the periods of operation of the converter. As can be seen from Table 2, numerical values change from period to period only in 5-7 significant digits of the obtained results, which proves the high efficiency and accuracy of the proposed method. According to the described algorithm, a program was compiled in the algorithmic language of the MATLAB system. This program interacts with the converter visual model and the system workspace using built-in functions to implement matrix operations. The use of this program makes it possible to quickly determine the parameters of steady-state modes in the circuits of other converters with regular alternating states of semiconductor power devices.

**Conclusions.** A method of determining the steady-state mode parameters of semiconductor converters based

on the use of visual models of converters and the transition to recurrent formulas linking the values of state variables at the boundaries of periods is proposed. The method avoids the need to run the model for tens or hundreds of periods of the transient process before establishing a steady state. To implement the method, it is enough to calculate several periods of the transient process, which allows to find the coefficients of recurrence relationships using standard matrix functions. The use of these relationships makes it possible to run the process without integrating the differential equations by the method of state variables during each period, as well as to immediately find the values of the state variables at the beginning of the steady-state period. Numerical calculations carried out using the proposed method demonstrated high efficiency and accuracy of the results. Based on this algorithm, a MATLAB language program was compiled, which generalizes the proposed method for its application in the calculation of steady-state modes of converters with different circuit topology.

**Conflict of interest.** The authors of the article declare that there is no conflict of interest.

#### REFERENCES

1. Mohan N., Undeland T.M., Robbins W.P. *Power Electronics: Converters, Applications, and Design*. John Wiley & Sons, Inc., New York, 2002. 823 p.
2. Yagup V.G. *Automated calculation of thyristor circuits*. Kharkov, Vyshcha School Publishing House at KSU, 1986. 160 p. (Rus).
3. Rajagopalan V. *Computer-Aided Analysis of Power Electronic Systems*. Marcel Dekker, Inc., New York, 1987. 552 p.
4. Bakhvalov N.S., Zhidkov N.P., Kobel'kov G.M. *Numerical Methods*. Moscow, BINOM Publ., 2008. 636 p. (Rus).
5. Aprille T., Trick T. A computer algorithm to determine the steady-state response of nonlinear oscillators. *IEEE Transactions on Circuit Theory*, 1972, vol. 19, no. 4, pp. 354-360. doi: <https://doi.org/10.1109/TCT.1972.1083500>.
6. Aprille T.J., Trick T.N. Steady-state analysis of nonlinear circuits with periodic inputs. *Proceedings of the IEEE*, 1972, vol. 60, no. 1, pp. 108-114. doi: <https://doi.org/10.1109/PROC.1972.8563>.
7. Moskovko A., Vityaz O. Periodic steady-state analysis of relaxation oscillators using discrete singular convolution method. *2017 IEEE 37th International Conference on Electronics and Nanotechnology (ELNANO)*, 2017, pp. 506-510. doi: <https://doi.org/10.1109/ELNANO.2017.7939803>.
8. Verbizkij E.V., Romashko V.Y. Application of Difference Equations in Predictive Control Systems for DC-DC Converters. *Electronics and Communications*, 2012, vol. 17, no. 2, pp. 23-27. doi: <https://doi.org/10.20535/2312-1807.2012.17.2.220024>.
9. Mikhalchenko G.Ya., Mulikov D.S. Operation modes of frequency converter with active rectifier. *Proceedings of TUSUR University*, 2016, vol. 19, no. 2, p. 79-83. (Rus).
10. Cheng X., Chen Y., Chen X., Zhang B., Qiu D. An extended analytical approach for obtaining the steady-state periodic solutions of SPWM single-phase inverters. *2017 IEEE Energy Conversion Congress and Exposition (ECCE)*, 2017, pp. 1311-1316. doi: <https://doi.org/10.1109/ECCE.2017.8095941>.

Received 30.08.2022

Accepted 30.11.2022

Published 06.05.2023

V.G. Yagup<sup>1</sup>, Doctor of Technical Science, Professor,  
K.V. Yagup<sup>2</sup>, Doctor of Technical Science, Professor,  
<sup>1</sup> Kharkiv National Automobile and Highway University,  
25, Yaroslava Mudrogo Str., Kharkiv, 61002, Ukraine,  
e-mail: yagup.walery@gmail.com (Corresponding Author)  
<sup>2</sup> National Technical University «Kharkiv Polytechnic Institute»,  
2, Kyrpychova Str., Kharkiv, 61002, Ukraine.

#### How to cite this article:

Yagup V.G., Yagup K.V. Acceleration of exit to steady-state mode when modeling semiconductor converters. *Electrical Engineering & Electromechanics*, 2023, no. 3, pp. 47-51. doi: <https://doi.org/10.20998/2074-272X.2023.3.07>

V.O. Brzhezitsky, Y.O. Haran, Y.O. Trotsenko, O.R. Protsenko, A.O. Derzhuk, M.M. Dixit

## Ultimate effect of non-identity of resistive elements of high-voltage arm on frequency characteristics of broadband voltage divider (analytical research)

**Purpose.** Determination in the analytical form of the maximum limiting influence of the non-identity of the resistive elements of the high-voltage arm on the amplitude-frequency characteristic and phase-frequency characteristic of the voltage divider with parallel-series connection of R-, C-elements of the high-voltage arm. **Methodology.** Based on the previously developed theory of broadband voltage dividers with parallel-series connection of R-, C-elements, analytical expressions for amplitude-frequency and phase-frequency characteristics of the voltage divider are obtained and investigated taking into account the limit case of non-identical resistive elements of high-voltage arm. **Results.** The nature of the dependencies of the frequency characteristics of the broadband voltage divider on the value of the tolerance of the resistive elements of the high-voltage arm, the division factor of the voltage divider in a wide range of frequency changes are determined. Simplified approximating expressions for the maximum values of frequency characteristics of the voltage divider are proposed and their error is determined. **Originality.** For the first time in the analytical form the limiting influence of non-identity of resistive elements of a high-voltage arm of a voltage divider on its frequency characteristics is considered. A mathematical model of this influence is constructed and the limit values of frequency characteristics of the voltage divider are determined. **Practical value.** It is recommended to introduce into the normative documentation of broadband voltage dividers the corrected value of the division factor, which allows to significantly reduce the deviation of the actual value of the division factor of the voltage divider from the normalized value in a wide range of frequency changes. References 16, tables 3, figures 3.

**Key words:** high-voltage divider, frequency characteristics, analytical expressions, tolerance of resistive elements, parameters adjustment.

На основі раніше розвинутої теорії широкосмугових подільників напруги з паралельно-послідовним з'єднанням R-, C-елементів вперше одержані аналітичні вирази для амплітудно-частотної та фазо-частотної характеристик подільника напруги з урахуванням граничного випадку неідентичності резистивних елементів високовольтного плеча. Визначений загальний характер залежностей частотних характеристик від значення допуску резистивних елементів, коефіцієнта ділення подільника напруги в широкому діапазоні зміни частоти. Запропоновані спрощені апроксимуючі вирази для максимальних значень частотних характеристик та визначено їх похибки. Рекомендовано уведення в нормативно-технічну документацію широкосмугових подільників напруги відкорегованого значення коефіцієнта ділення. Бібл. 16, табл. 3, рис. 3.

**Ключові слова:** високовольтний подільник напруги, частотні характеристики, аналітичні вирази, допуск резистивних елементів, коригування параметрів.

**Introduction.** For the normal functioning of electric power systems, information about the instantaneous values of high voltage in certain areas is very important. Traditionally, for more than 100 years, electromagnetic voltage transformers have been used and continue to be used for this purpose [1]. The advantage of electromagnetic voltage transformers is high load capacity, which allows to complete various secondary circuits based on them, including of relay protection and control. There are even «DC voltage» transformers. This term refers to a converter consisting of a high-voltage DC resistor, a magnetic amplifier controlled by the DC of this resistor, and a rectifier for the output voltage of the magnetic amplifier. As a result, the output DC voltage of such a converter is proportional to its input voltage, and the converter is characterized by high load capacity. However, a significant disadvantage of voltage transformers is inertia. In this regard, they are not actually used to register fast-moving processes, when, on the contrary, a quick response of control systems is required. The situation improves significantly with the transition to the «digital substation» concept, when secondary circuits can be built on the basis of computer systems with minimal energy consumption. Here, high-voltage transformers can be replaced by broadband voltage dividers, which can be used to obtain information about instantaneous values of high voltage. This will allow, on the one hand, to significantly improve the management of power systems and, on the other hand,

to obtain complete information about the quality of electricity online.

**The goal of the work** is to continue previous research [2] and to study the ultimate impact of the non-identity of non-capacitive but resistive elements of the high-voltage arm on the amplitude-frequency and phase-frequency characteristics of the voltage divider.

It should be noted that in [2] the influence of the non-identity of only the capacitive elements of the high-voltage arm on the characteristics of the voltage divider was considered.

**General information about broadband voltage dividers.** It should be noted that the corresponding development of research on high-voltage broadband voltage dividers was realized mainly in the last 50 years. The processes that take place in high-voltage dividers are much more complicated than in voltage transformers. This is due to the variety of types of voltage dividers, ranges of their parameters and modes of use.

In research on high-voltage dividers in recent years [3–15], considerable attention is paid to increasing the accuracy of their mathematical models (up to the level of several ppm), stability of parameters, taking into account various factors, features of metrological calibration and normalization of characteristics. The considered substitution circuits of various types of high-voltage dividers are built on the use of shielded parallel-series connections of resistive and capacitive elements of the high-voltage arm, formed, as a rule, from the same

(identical) elements. As a rule, the selection of the nominal values of resistive and capacitive elements is performed based on approximately the same conductivity of the corresponding branches of the electric circuit at the main frequency of the voltage divider. Here, during high-frequency transients in the electric circuit of the voltage divider, the capacitive components of the branches of this circuit are more conductive (for example, the conductivity of the capacitive branch between two nodes of the electric circuit of the high-voltage arm of the voltage divider is 4-5 orders of magnitude greater than the parasitic capacitive conductivity between these nodes), therefore, they practically shunt the parasitic capacitive leakage of currents from the connection nodes of lumped circuit elements to grounded surfaces and circuit elements that are under a different potential. As a result, the design of a voltage divider with a series-parallel connection of resistive and capacitive lumped elements is the most effective in the development of broadband voltage dividers. In different operating modes of the voltage divider, the conductances of the resistive and capacitive branches of its substitution circuit change, so the influence on the error of the scale transformation coefficient of the voltage divider is a complex function of the dependence on the values of the resistances and capacities of the concentrated elements, as well as the current frequency. However, in reality, the used  $R_{RV}$ ,  $C_{RV}$  elements have a tolerance:

$$R_N(1 - \beta) \leq R_{RV} \leq R_N(1 + \beta),$$

$$C_N(1 - \Delta) \leq C_{RV} \leq C_N(1 + \Delta),$$

where  $R_N$ ,  $C_N$  are the nominal values of resistive and capacitive elements;  $\beta$ ,  $\Delta$  are the values of tolerances in relative units determined by the manufacturer. The influence of tolerances depends on their value, as well as the type of distribution of parameters within the tolerance. The latter is usually not normalized. Therefore, it is justified to consider (for the first time) the limit variant, when the capacitive elements of the high-voltage arm have equally probable values:

$$C'_{RV} = C_N(1 - \Delta), \quad C''_{RV} = C_N(1 + \Delta).$$

This case was considered in a previous work [2]. This article considers (for the first time) another limit variant, when the resistive elements have the value:

$$R'_{RV} = R_N(1 - \beta), \quad R''_{RV} = R_N(1 + \beta).$$

**Mathematical model of the voltage divider and study of the amplitude-frequency characteristic (frequency response).** According to [1], broadband voltage dividers consist of a large number of resistive and capacitive elements connected in parallel-series (see Fig. 1).

In Fig. 1:  $U_{in}$  – the input high voltage;  $U_{out}$  – the output low voltage;  $R_i$  and  $C_i$  – the elements of the high-voltage arm;  $r$  and  $c$  – the elements of the low-voltage arm.

The values of resistance and capacity, respectively, of resistors and capacitors included in the voltage divider can change under the influence of external conditions over time (temperature, humidity, etc.). In this regard, there is a need to study the frequency characteristics of the voltage divider in view of the non-identity of its components.

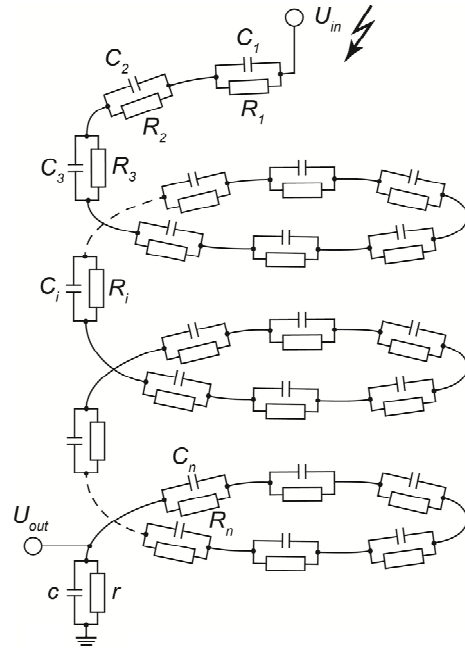


Fig. 1. Schematic diagram of a capacitive-ohmic voltage divider [1]

The schematic diagram of the voltage divider shown in Fig. 1 does not show parasitic capacitive branches, because, as was shown above, the influence of leakage of parasitic currents of a capacitive nature is significantly smaller (by 2-3 orders of magnitude) compared to the deviations of the actual parameters of the lumped elements from the nominal values.

The non-identity of the resistive and capacitive elements of the voltage divider affects the stability of its frequency characteristics, especially the pronounced nature of this effect on frequency response. Reducing frequency response changes in the operating frequency range is an important factor in improving the transmission characteristics of the measuring device. According to [1], the frequency response of the voltage divider is determined by (1), (2):

$$A = \frac{1}{K} A^*; \quad (1)$$

$$A^* = \frac{1 + \gamma^2}{\sqrt{\left(1 + \frac{K-1}{K} f\right)^2 + \gamma^2 \left(1 + \frac{K-1}{K} \delta\right)^2}}, \quad (2)$$

where  $A$  is the frequency response;  $A^*$  is the reduced frequency response;  $K$  is the nominal value of the division coefficient of the broadband voltage divider;  $f$  and  $\delta$  are the averaged parameters that take into account the non-identity of the elements of the parallel-series connection of resistive  $R_i$  and capacitive  $C_i$  elements of the high-voltage arm of the capacitive-ohmic voltage divider.

The dimensionless parameter  $\gamma$  depends on the angular frequency  $\omega$  and is defined as:

$$\gamma = \omega R_0 C_0; \quad (3)$$

$$R_0 = \frac{1}{n} \sum_{i=1}^n R_i; \quad (4)$$

$$C_0 = \frac{1}{n} \sum_{i=1}^n C_i, \quad (5)$$

where  $R_0$  and  $C_0$  are the average values of the elements of the high-voltage arm;  $n$  is the number of elements of the high-voltage arm.

The values of the parameters of the low-voltage arm are usually determined as follows:

$$r = \frac{nR_0}{K-1}, \quad c = \frac{C_0}{n}(K-1).$$

From a generalized consideration of the frequency characteristics of a broadband voltage divider with a parallel-serial connection of  $R$ -,  $C$ -elements of the high-voltage arm [1] for this case we have:  $R_0 = R_N$ ;  $C_1 = C_2 = \dots = C_N = C$ ;  $A = 0$ . Parameters  $f, \Delta$  are the non-identity functions of resistive elements  $\beta' = -\beta$  and  $\beta'' = +\beta$ , which are defined as:

$$f = \frac{1}{2}D(\beta') + \frac{1}{2}D(\beta''); \quad (6)$$

$$\delta = \frac{1}{2}G(\beta') + \frac{1}{2}G(\beta''), \quad (7)$$

where

$$D(\beta) = \frac{\gamma^2(-3\beta^2 - \beta^3 + \gamma^2(\beta^2 + \beta^3))}{(1 + \gamma^2)(1 + \gamma^2(1 + \beta^2))}; \quad (8)$$

$$G(\beta) = \frac{\beta^2 - \gamma^2(3\beta^2 + 2\beta^3)}{(1 + \gamma^2)(1 + \gamma^2(1 + \beta^2))}. \quad (9)$$

As a result, we obtain:

$$2f = \frac{\gamma^2(-3\beta^2 + \beta^3 + \gamma^2(\beta^2 - \beta^3))}{(1 + \gamma^2)(1 + \gamma^2(1 - \beta^2))} + \frac{\gamma^2(-3\beta^2 - \beta^3 + \gamma^2(\beta^2 + \beta^3))}{(1 + \gamma^2)(1 + \gamma^2(1 + \beta^2))}; \quad (10)$$

$$2\delta = \frac{\beta^2 - \gamma^2(3\beta^2 - 2\beta^3)}{(1 + \gamma^2)(1 + \gamma^2(1 - \beta^2))} + \frac{\beta^2 - \gamma^2(3\beta^2 + 2\beta^3)}{(1 + \gamma^2)(1 + \gamma^2(1 + \beta^2))}. \quad (11)$$

Below are the test checks of the resulting ratios that were performed:

1) if  $\beta = 0$ , then  $A^* \equiv 1$  for any values of  $\gamma, K$ ;

2) if  $\gamma = 0$ , then also  $A^* \equiv 1$  for any values of  $\beta, K$ ;

if  $\gamma \rightarrow \infty$ , similarly,  $A^* \equiv 1$  for any values of  $\beta, K$ .

The results of the conducted tests confirm the adequacy of the used mathematical model to the physical object under study.

To study the dependence, similarly to [2], we apply the approach when it is possible to find the limiting expressions under the conditions  $\gamma \rightarrow 0$  and  $\gamma \rightarrow \infty$ . Substituting  $\gamma \rightarrow 0$  into expressions (10), (11) gives the dependencies:

$$f_{\gamma \rightarrow 0} = -3\beta^2\gamma^2; \quad \delta_{\gamma \rightarrow 0} = \beta^2 - \gamma^2(5\beta^2 + \beta^4). \quad (12)$$

In turn, using (12) under the condition  $\gamma \rightarrow 0$  allows (2) to obtain the limiting expression:

$$A_{\gamma \rightarrow 0}^* = 1 + \frac{K-1}{K}\beta^2\gamma^2\left(2 - \frac{K-1}{2K}\beta^2\right). \quad (13)$$

That is,  $A^*$  grows from  $\gamma$  in a parabolic dependence with the coefficient  $\frac{K-1}{K}$  and  $\beta^2$ . The expression in parentheses (13) is a small variable value and in the range  $0 \leq \beta \leq 0.2$  is 2...1.98 (for  $K \rightarrow \infty$ ).

Substituting  $\gamma \rightarrow \infty$  into expressions (10), (11) provides:

$$f_{\gamma \rightarrow \infty} = \frac{\beta^2 - \beta^4}{(1 - \beta^2)^2}; \quad \delta_{\gamma \rightarrow \infty} = \frac{1}{\gamma^2} \frac{3\beta^2 - \beta^4}{(1 - \beta^2)^2},$$

and, finally:

$$A_{\gamma \rightarrow \infty}^* = 1 + \frac{K-1}{K}\beta^2 \frac{1}{\gamma^2} \left( \frac{3 - \beta^2}{2(1 - \beta^2)^2} \right). \quad (14)$$

The expression in parentheses (14) in the range  $0 \leq \beta \leq 0.2$  is 1.5...1.6, i.e. it is a slightly variable quantity.

The results obtained in (13), (14) allow a purposeful approach to further research of the frequency response of the voltage divider based on computerized calculations.

Further calculations were made of the dependencies of  $A^*(\gamma)$  for different values of  $\beta$  and  $K$ . In Fig. 2 the resulting graphs of  $A^*(\gamma)$  at  $\beta = 0.05$  and  $\beta = 0.2$  for  $K = 10$  and  $K = 10^6$  in the range of  $\gamma$  change from 0.001 to 1000 are plotted. Dependencies of  $A^*(\gamma)$  have a typical maximum in the region  $\gamma \approx 1$ . The influence of the maximum in the regions of  $\lg \gamma \leq -1.5$  and  $\lg \gamma \geq +1.5$  is negligible.

Figure 2 shows: curve 1 – the dependence  $A^*(\gamma)$  at  $\beta = 0.05$  and  $K = 10$ ; curve 2 – the dependence  $A^*(\gamma)$  at  $\beta = 0.05$  and  $K = 10^6$ ; curve 3 – the dependence  $A^*(\gamma)$  at  $\beta = 0.2$  and  $K = 10$ ; curve 4 – the dependence  $A^*(\gamma)$  at  $\beta = 0.2$  and  $K = 10^6$ .

To find the maximum  $A_{\max}^*$ , it is necessary to equate the derivative  $\frac{dA^*}{d\gamma}$  to zero and to determine the value of

$\gamma_{\max}$  from this condition. By substituting this value in (2), using (10), (11), it is possible to obtain the desired value of  $A_{\max}^*$ . In connection with the complex dependence of  $A^*$  on the initial values, which practically makes it impossible to carry out these operations in an analytical form, software tools were used to find  $A_{\max}^*(\gamma_{\max})$ .

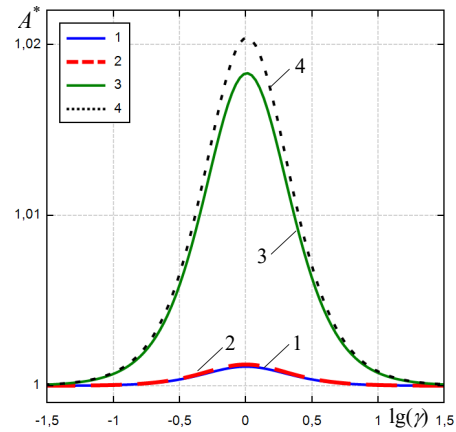


Fig. 2. Graph of the reduced frequency response depending on the dimensionless frequency parameter  $\gamma$  in a semi-logarithmic scale

In the program package SMATH Solver [16], the functional dependence  $A^*(\gamma)$  was deduced, after which, with the help of mathematical modules of this program package,  $\gamma_{\max}$  was found for the extremum point and the value of the extremum  $A_{\max}^*$  of this function at different  $\beta$  and  $K$  (through iterative calculations in the program cycle). Data arrays of various combinations of parameters were obtained.

Table 1 shows examples of the obtained results of the calculation of  $A_{\max}^*$ ,  $\gamma_{\max}$  for values of  $\beta = 0.01; 0.02; \dots 0.2$

and the value of  $K = 10^1; 10^2; 10^3; 10^4; 10^6$ . The analysis of the obtained data is given in the next section.

Table 1

Results of calculations of  $A_{\max}^*(\gamma_{\max})$  for  $K = 10^1; 10^2; 10^3; 10^4; 10^6$

K	10		100		1000		10000		100000	
	$\gamma_{\max}$	$A_{\max}$								
0,01	1,000068779	1,000045002	1,000068779	1,000049502	1,000068779	1,000049952	1,000068779	1,000049997	1,000068779	1,000050002
0,02	1,000210615	1,000180032	1,000210615	1,000198039	1,000210615	1,00019984	1,000210615	1,00020002	1,000210615	1,00020004
0,03	1,000473922	1,000405164	1,000473923	1,000445699	1,000473923	1,000449752	1,000473923	1,000450158	1,000473923	1,000450202
0,04	1,000785403	1,000720519	1,000785401	1,000792628	1,000785401	1,000799839	1,000785401	1,000800056	1,000785401	1,000800064
0,05	1,001228359	1,001126267	1,001228355	1,001239033	1,001228355	1,001250311	1,001228355	1,001251439	1,001228355	1,001251563
0,06	1,00181747	1,001622629	1,001817473	1,001785181	1,001817474	1,001801439	1,001817474	1,001803065	1,001817474	1,001803244
0,07	1,002475774	1,002209873	1,00247578	1,002431397	1,002475781	1,002453555	1,002475781	1,002455771	1,002475781	1,002456015
0,08	1,003236693	1,002888318	1,003236703	1,003178068	1,003236705	1,003207052	1,003236705	1,003209951	1,003236705	1,00321027
0,09	1,00410082	1,003658335	1,004100836	1,004025641	1,004100838	1,004062386	1,004100838	1,004066061	1,004100838	1,004066465
0,1	1,005026594	1,004520342	1,005026583	1,004974624	1,005026582	1,005020075	1,005026582	1,005024621	1,005026582	1,005025121
0,11	1,006092522	1,00547481	1,006092507	1,00602559	1,006092506	1,006080701	1,006092506	1,006086213	1,006092506	1,006086819
0,12	1,007264098	1,006522264	1,007264079	1,007179173	1,007264077	1,007244911	1,007264076	1,007251485	1,007264076	1,007252209
0,13	1,008542457	1,007663279	1,008542432	1,008436072	1,00854243	1,008513416	1,008542429	1,008521152	1,008542429	1,008522002
0,14	1,00992884	1,008898485	1,009928808	1,009797051	1,009928805	1,009886996	1,009928805	1,009895991	1,009928805	1,009896981
0,15	1,011424591	1,010228564	1,011424552	1,011262941	1,011424548	1,011366495	1,011424548	1,011376852	1,011424548	1,011377991
0,16	1,013031165	1,011654257	1,013031119	1,012834641	1,013031115	1,01295283	1,013031114	1,012964651	1,013031114	1,012965951
0,17	1,014750131	1,013176359	1,014750077	1,014513117	1,014750072	1,014646987	1,014750071	1,014660376	1,014750071	1,014661849
0,18	1,01658317	1,014795722	1,016583109	1,01629941	1,016583103	1,016450024	1,016583102	1,016465088	1,016583102	1,016466745
0,19	1,018532086	1,016513258	1,018532017	1,018194629	1,01853201	1,018363072	1,01853201	1,018379919	1,01853201	1,018381773
0,2	1,020598807	1,018329939	1,020598732	1,020199959	1,020598724	1,020387339	1,020598723	1,020406081	1,020598723	1,020408142

**Analysis of frequency response results.** Processing of the obtained data array allows us to propose a simplified expression for  $A_{\max}^*$  in the form:

$$A_{\max}^* = 1 + 0,505113 \frac{K-1}{K} \beta^2. \quad (15)$$

Formula (15) is applicable for any values  $\beta \leq 0.2$  and  $K \geq 10$ . Here, the error of only the additional term in the right-hand side of (15) in relation to the exact data does not exceed  $\pm 1\%$  in absolute value, which can be considered quite acceptable.

Analyzing the obtained data, it can be noted that the non-identity of the resistive elements of the high-voltage arm of the voltage divider can lead to a significant increase in its error (up to 2% or more). It is possible to halve this error value by using a corrected frequency response value:

$$A_{cor}^* = 1 + 0,25256 \frac{K-1}{K} \beta^2. \quad (16)$$

Expression (16) can be entered in the technical documentation (passport) of the voltage divider.

The development of the use of high-voltage broadband voltage dividers, including commercial implementation, requires the possibility of «quick assessment» of the quality of their frequency characteristics based on the initial data on the elemental «base», which can be determined using formula (15).

Just as for capacitive elements [2], the influence of the non-identity of resistive elements (15) is proportional to the multiplier  $\frac{K-1}{K}$ , thus, it is maximal for high-voltage dividers.

For values  $1 < K < 10$ , additional research is required.

The considered theory of voltage dividers with a parallel-series connection of resistive and capacitive elements can be successfully applied to the study of the so-called «capacitor» high-voltage insulation, when each layer of insulation can be represented by a parallel connection of resistive and capacitive elements. As a rule, for such insulation, the condition  $C_1 = C_2 = \dots = C_i = \dots = C_n = C$  is used, while the non-identity of  $R$ -elements may be related to the wetting of individual layers of insulation or the deterioration of their properties over time. With regard to this option of using the considered theory, it should be emphasized that expressions (1)–(11) do not assume a small value of the parameter  $\beta$ , that is, they can be applied in the general case when  $\beta$ , for example, reaches values of 0.9; 0.99, etc., and any layer of «capacitor» insulation can be considered as the low-voltage arm of the voltage divider.

**Study of the phase-frequency characteristic (PFC).** According to [1], PFC of a voltage divider with a parallel-serial connection of  $R$ -,  $C$ -elements of the high-voltage arm is described by the expression:

$$\varphi = \arctg \left( \frac{(\delta - f)\gamma}{f + \frac{K}{K-1} + \gamma^2 \left( \delta + \frac{K}{K-1} \right)} \right), \quad (17)$$

where  $f, \delta, \gamma, K$  have the same values as in (3) – (11).

Similarly (12) – (14), we can use the approach of determining the limit values in the approximations  $\gamma \rightarrow 0$  and  $\gamma \rightarrow \infty$ . Here, we obtain:

$$\varphi_{\gamma \rightarrow 0} = \frac{K-1}{K} \beta^2 \gamma, \quad (18)$$

$$\varphi_{\gamma \rightarrow \infty} = -\frac{K-1}{K} \beta^2 \frac{1}{\gamma} (1-\beta^2)^{-1}. \quad (19)$$

Expression (19) has a factor  $(1-\beta^2)^{-1}$ , which under the conditions  $0 \leq \beta \leq 0.2$  is an invariant value of 1...1.04.

Since the deviations from zero under the conditions  $\gamma \rightarrow 0$  and  $\gamma \rightarrow \infty$  are multipolar, it will be useful to determine  $\varphi$  at an intermediate point, for example, at  $\gamma = 1$ . The corresponding transformations according to (17) give the expression:

$$\varphi_{\gamma=1} = \arctg \left( \frac{2\beta^4(K-1)}{K(8+2\beta^4-4\beta^2)+4\beta^2} \right). \quad (20)$$

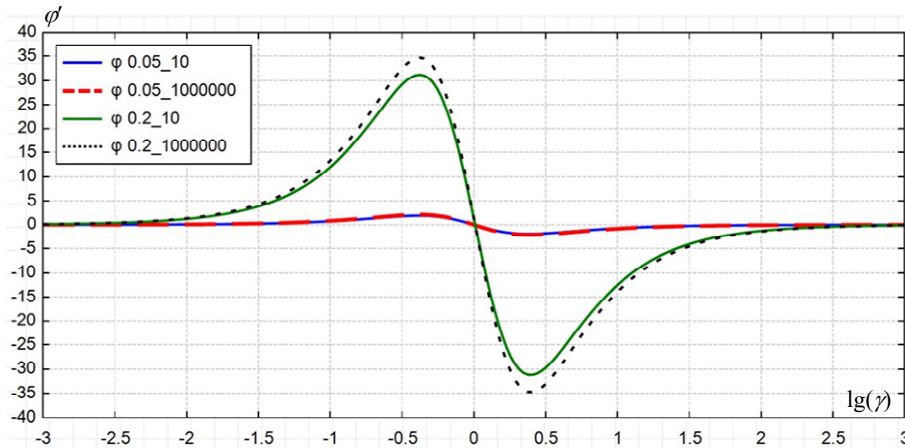


Fig. 3. Graph of PFC depending on the dimensionless frequency parameter  $\gamma$  in the semi-logarithmic scale

Next, similarly to the previous section, computerized calculations were performed for the two extrema of the dependence  $\varphi(\gamma)$ , and for the region  $\gamma < 1$  it was data  $\varphi_{\max}(\gamma'_{\max})$ , and for the region  $\gamma > 1$ , respectively,  $\varphi_{\min}(\gamma'_{\min})$ .

Table 2 shows the results of the performed

Estimation of the right-hand side of (20) at  $\beta = 0.2$  and  $K \rightarrow \infty$  gives  $\varphi_{\gamma=1} = \arctg(0.000407)$ , which corresponds to  $\varphi = 1.4'$ . Thus, all investigated dependencies of  $\varphi(\gamma)$  will, in fact, pass at  $\gamma = 1$  in the range  $0 \dots 1.4'$ .

Figure 3 shows the curves of changes in the frequency response of the voltage divider  $\varphi$  (in arc minutes) on the dimensionless frequency parameter  $\gamma$  (when it changes from 0.001 to 1000) for values of  $\beta = 0.05$ ;  $\beta = 0.2$  and  $K = 10$ ;  $K = 10^6$ . For clarity, the scale on the abscissa is shown on a logarithmic scale (from  $\lg \gamma = -3$  to  $\lg \gamma = +3$ ). The deviation of PFC from the zero value is negligible for  $\lg \gamma \leq -2.5$  and  $\lg \gamma \geq 2.5$ .

calculations of  $\varphi_{\max}(\gamma'_{\max})$  for the values  $\beta = 0.01$ ;  $0.02$ ; ...  $0.20$  and  $K = 10^1$ ;  $10^2$ ;  $10^3$ ;  $10^4$ ;  $10^6$ .

Table 3 shows the results of the performed calculations of  $\varphi_{\min}(\gamma'_{\min})$  for the values  $\beta = 0.01$ ;  $0.02$ ; ...  $0.20$  and  $K = 10^1$ ;  $10^2$ ;  $10^3$ ;  $10^4$ ;  $10^6$ .

Table 2

Results of calculations of  $\varphi_{\max}(\gamma'_{\max})$  for  $K = 10^1$ ;  $10^2$ ;  $10^3$ ;  $10^4$ ;  $10^6$

K	10		100		1000		10000		1000000	
	$\gamma'_{\max}$	$\varphi_{\max}, '$								
0.01	0,414210916	0,077351043	0,414211575	0,085086338	0,414211641	0,08585987	0,414211648	0,085937223	0,414211648	0,085945732
0.02	0,414248876	0,309425058	0,414251515	0,340370627	0,414251779	0,343465215	0,414251805	0,343774674	0,414251808	0,343808714
0.03	0,414312168	0,696284723	0,414318108	0,765928709	0,414318702	0,772893263	0,414318761	0,77358972	0,414318768	0,77366633
0.04	0,414400826	1,238034555	0,414411392	1,361887062	0,414412449	1,374272804	0,414412555	1,375511383	0,414412566	1,375647627
0.05	0,414514901	1,934820995	0,414531425	2,128422909	0,414533077	2,147784299	0,414533243	2,149720451	0,414533261	2,149933427
0.06	0,414654456	2,78683252	0,414678276	3,065764371	0,414680658	3,093660044	0,414680896	3,096449636	0,414680922	3,096756492
0.07	0,414819573	3,794299795	0,414852033	4,174190665	0,414855279	4,212184367	0,414855604	4,215983784	0,414855639	4,21640172
0.08	0,415010343	4,957495853	0,415052799	5,454032349	0,415057045	5,503693882	0,41505747	5,508660114	0,415057517	5,509206401
0.09	0,415226875	6,276736314	0,415280694	6,905671609	0,415286077	6,968577785	0,415286615	6,974868529	0,415286675	6,975560512
0,1	0,415469294	7,752379633	0,415535855	8,529542593	0,415542513	8,607278195	0,415543178	8,615051949	0,415543252	8,615907064
0,11	0,415737737	9,384827387	0,415818434	10,32613179	0,415826506	10,42029055	0,415827313	10,42970671	0,415827402	10,43074249
0,12	0,416032358	11,1745246	0,416128601	12,29597846	0,416138229	12,40816403	0,416139192	12,41938299	0,416139298	12,42061708
0,13	0,416353328	13,12196007	0,416466545	14,43967512	0,416477872	14,57150209	0,416479004	14,58468534	0,416479129	14,5861355
0,14	0,416700831	15,22766682	0,416832469	16,75786802	0,41684564	16,91096292	0,416846957	16,92627315	0,416847102	16,92795729
0,15	0,41707507	17,49222248	0,417226597	19,2512578	0,417241759	19,42726011	0,417243275	19,44486133	0,417243442	19,44679748
0,16	0,417476262	19,91624974	0,417649169	21,92060003	0,417666472	22,12116327	0,417668203	22,14122088	0,417668393	22,14342723
0,17	0,417904643	22,50041691	0,418100447	24,76670594	0,418120043	24,9934987	0,418122003	25,01617962	0,418122218	25,01867454
0,18	0,418360464	25,24543842	0,418580708	27,79044313	0,418602752	28,04515017	0,418604957	28,07062294	0,4186052	28,07342497
0,19	0,418843996	28,15207543	0,419090252	30,99273635	0,419114902	31,27705969	0,419117367	31,3054946	0,419117639	31,30862247
0,2	0,419355527	31,22113644	0,419629397	34,37456834	0,419656814	34,69022842	0,419659556	34,7217976	0,419659858	34,72527025

Table 3

Results of calculations of  $\varphi_{\min}(\gamma'_{\min})$  for  $K = 10^1; 10^2; 10^3; 10^4; 10^6$ 

K	10		100		1000		10000		100000	
	$\beta$	$\gamma'_{\min}$	$\varphi_{\min}$	$\gamma'_{\min}$	$\varphi_{\min}$	$\gamma'_{\min}$	$\varphi_{\min}$	$\gamma'_{\min}$	$\varphi_{\min}$	$\gamma'_{\min}$
0,01	2,414387533	-0,077351043	2,414383691	-0,085086338	2,414383307	-0,08585987	2,414383268	-0,085937223	2,414383264	-0,085945732
0,02	2,414890851	-0,309425058	2,414875476	-0,340370628	2,414873938	-0,343465215	2,414873784	-0,343774674	2,414873768	-0,343808715
0,03	2,415730325	-0,696284723	2,41569571	-0,76592871	2,415692248	-0,772893264	2,415691902	-0,773589721	2,415691864	-0,773666331
0,04	2,416906878	-1,238034557	2,416845284	-1,361887064	2,416839125	-1,374272806	2,416838509	-1,375511385	2,416838441	-1,375647628
0,05	2,418421802	-1,934820997	2,418325453	-2,128422912	2,418315818	-2,147784302	2,418314854	-2,149720453	2,418314748	-2,149933343
0,06	2,420276774	-2,786832524	2,420137838	-3,065764375	2,420123944	-3,093660049	2,420122554	-3,096449641	2,420122401	-3,096756496
0,07	2,422473853	-3,7942998	2,422284433	-4,17419067	2,42226549	-4,212184373	2,422263596	-4,215983789	2,422263387	-4,216401726
0,08	2,425015494	-4,95749586	2,424767616	-5,454032356	2,424742827	-5,50369389	2,424740348	-5,508660122	2,424740075	-5,509206409
0,09	2,427904558	-6,276736323	2,427590154	-6,905671619	2,427558711	-6,968577795	2,427555567	-6,974868539	2,427555221	-6,975560522
0,1	2,431144318	-7,752379644	2,430755217	-8,529542605	2,430716303	-8,607278208	2,430712412	-8,615051961	2,430711984	-8,615907076
0,11	2,434738475	-9,384827401	2,434266386	-10,32613181	2,434219171	-10,42029056	2,43421445	-10,42970672	2,43421393	-10,4307425
0,12	2,438691168	-11,17452461	2,438127666	-12,29597848	2,438071308	-12,40816405	2,438065672	-12,41938301	2,438065052	-12,4206171
0,13	2,443006988	-13,12196009	2,4423435	-14,43967514	2,44227714	-14,57150211	2,442270504	-14,58468536	2,442269774	-14,58613552
0,14	2,447690993	-15,22766685	2,446918783	-16,75786805	2,446841547	-16,91096294	2,446833823	-16,92627318	2,446832973	-16,92795731
0,15	2,452748722	-17,4922225	2,451858873	-19,25125783	2,451769868	-19,42726014	2,451760968	-19,44486136	2,451759989	-19,44679751
0,16	2,458186212	-19,91624977	2,457169613	-21,92060007	2,457067928	-22,12116331	2,457057759	-22,14122091	2,45705664	-22,14342727
0,17	2,464010018	-22,50041694	2,462857344	-24,76670598	2,462742044	-24,99349874	2,462730514	-25,01617966	2,462729245	-25,01867458
0,18	2,470227226	-25,24543846	2,468928924	-27,79044317	2,468799052	-28,04515021	2,468786065	-28,07062298	2,468784636	-28,07342501
0,19	2,476845481	-28,15207548	2,475391749	-30,9927364	2,475246324	-31,27705974	2,475231781	-31,30549465	2,475230181	-31,30862251
0,2	2,483873006	-31,22113649	2,482253776	-34,3745684	2,482091788	-34,69022848	2,482075589	-34,72179766	2,482073807	-34,7252703

**Analysis of PFC results.** The «impressive» factor is the practical coincidence of the absolute values of  $\varphi_{\max}$  and  $\varphi_{\min}$  (up to 8 significant figures, that is, up to the error of the calculations) at the same values of  $\beta$  and  $K$ .

The region of PFC deviation from zero is more «stretched» in  $\gamma$  ( $-2.5 < \lg \gamma < 2.5$ ) compared to frequency response ( $-1.5 < \lg \gamma < 1.5$ ), which is explained by the degree of dependence on  $\gamma$  in the corresponding expressions (18), (19), compared to (13), (14).

Processing of the received array of calculation data given in Table 2, 3, allows us to propose the following simplified expressions:

$$\varphi'_{\max} = 863,8 \frac{K-1}{K} \beta^2, \text{ arc minutes}, \quad (21)$$

$$\varphi'_{\min} = -863,8 \frac{K-1}{K} \beta^2, \text{ arc minutes}. \quad (22)$$

Formulas (21), (22) are applicable for any values of  $\beta \leq 0.2$  and  $K \geq 10$ . Here, the error (21), (22) in relation to the exact calculated values according to (17) does not exceed  $\pm 0.5\%$ , which is quite acceptable.

If the ranges  $\gamma \leq 1$  or, conversely,  $\gamma \geq 1$  are used in certain studies, correction values for  $\varphi$  can be introduced, which are 50% of the values given in (21), (22).

A comparison of the obtained results with the data of publications [2–15] shows that the effect of the non-identity of the resistive elements of the high-voltage arm of the voltage divider is significant compared to such factors of parameter instability as temperature change, shielding imperfection, the influence of external electric fields, frequency change and should be taken into account in the theory and the practice of voltage dividers, especially for reference measurements.

**Conclusions.** The ultimate influence of the non-identity of the resistive elements of the high-voltage arm of the voltage divider on its amplitude-frequency and phase-frequency characteristics is quantitatively determined.

It is shown that this influence is proportional to the factor  $\frac{K-1}{K}$ , where  $K$  is the nominal value of the division coefficient of the voltage divider.

It is proposed to introduce the corrected value of the amplitude-frequency characteristic into the technical documentation of the voltage dividers, which makes it possible to reduce their error by a factor of two.

The carried out development of the theory of voltage dividers can be successfully applied to the study of processes in «capacitor» high-voltage insulation.

The materials of the article can be used for an express assessment of the quality of broadband high-voltage dividers, based on data on their element base.

A comparison of the obtained results with materials [2] shows that the ultimate effect of the non-identity of the resistive elements of the high-voltage arm gives fundamentally different results compared to the ultimate effect of the non-identity of the capacitive elements of the high-voltage arm of the voltage divider.

**Conflict of interest.** The authors of the article declare that there is no conflict of interest.

#### REFERENCES

1. Anokhin Y.L., Brzhezitskyi V.O., Haran Ya.O., Masliuchenko I.M., Protsenko O.P., Trotsenko Ye.O. Application of high voltage dividers for power quality indices measurement. *Electrical Engineering & Electromechanics*, 2017, no. 6, pp. 53–59. doi: <https://doi.org/10.20998/2074-272x.2017.6.08>.
2. Brzhezitskyi V.O., Haran Y.O., Derzhuk A.O., Protsenko O.R., Trotsenko Y.O., Dixit M.M. Ultimate effect of non-identity of capacitive elements of high-voltage arm on frequency characteristics of voltage divider (analytical research). *Electrical Engineering & Electromechanics*, 2021, no. 4, pp. 46–52. doi: <https://doi.org/10.20998/2074-272X.2021.4.06>.
3. Li D., Liu K., Lei M., Zhou F., Yue C., Yu J. Study on the ratio change measurement of 1000 kV HVDC divider based on improved DC voltage summation method. *High Voltage*, 2020, vol. 5, no. 2, pp. 202–208. doi: <https://doi.org/10.1049/hve.2019.0127>.

4. Havunen J., Hällström J. Reference switching impulse voltage measuring system based on correcting the voltage divider response with software. *IEEE Transactions on Instrumentation and Measurement*, 2021, vol. 70, pp. 1-8. art. no. 1006008. doi: <https://doi.org/10.1109/tim.2021.3063753>.
5. Hrbac R., Kolar V., Bartłomiejczyk M., Mleak T., Orsag P., Vanc J. A development of a capacitive voltage divider for high voltage measurement as part of a combined current and voltage sensor. *Elektronika ir Elektrotechnika*, 2020, vol. 26, no. 4, pp. 25-31. doi: <https://doi.org/10.5755/j01.eie.26.4.25888>.
6. Alf-Peter E., Hällström J., Bergman A. Optimization of the design of a wideband 1000 kV resistive reference divider. *XVII International Symposium on High Voltage Engineering*, Hannover, Germany, August 22-26, 2011.
7. Kovacevic U.D., Stankovic K.D., Kartalovic N.M., Loncar B.B. Design of capacitive voltage divider for measuring ultrafast voltages. *International Journal of Electrical Power & Energy Systems*, 2018, vol. 99, pp. 426-433. doi: <https://doi.org/10.1016/j.ijepes.2018.01.030>.
8. Thümmler T., Marx R., Weinheimer C. Precision high voltage divider for the KATRIN experiment. *New Journal of Physics*, 2009, vol. 11, no. 10, art. no. 103007. doi: <https://doi.org/10.1088/1367-2630/11/10/103007>.
9. Panko V., Banas S., Burton R., Ptacek K., Divin J., Dobes J. Enhanced Model of Nonlinear Spiral High Voltage Divider. *Radioengineering*, 2015, vol. 24, no. 1, pp. 130-136. doi: <https://doi.org/10.13164/re.2015.0130>.
10. Abdel Mageed H.M., El-Rifaie A.M., Aladdin O.M. Traceability of DC high voltage measurements using the Josephson voltage standard. *Measurement*, 2014, vol. 58, pp. 269-273. doi: <https://doi.org/10.1016/j.measurement.2014.08.029>.
11. Abdel Mageed H.M., Salah Eldeen R.S. Adapted Technique for Calibrating Voltage Dividers of AC High-Voltage Measuring Systems. *MAPAN*, 2020, vol. 35, no. 1, pp. 11-17. doi: <https://doi.org/10.1007/s12647-019-00334-8>.
12. Lee S.H., Yu K.M., Choi J.Y., Jang S.M. Low-Uncertainty Equality Between the Voltage-Dividing and Resistance Ratio of a DC Resistive High Voltage Divider. *Journal of Electrical Engineering & Technology*, 2019, vol. 14, no. 4, pp. 1789-1795. doi: <https://doi.org/10.1007/s42835-019-00157-2>.
13. Li Q., Wang L., Zhang S., Tang Y., Xu Y. Method to Determine the Ratio Error of DC High-Voltage Dividers. *IEEE Transactions on Instrumentation and Measurement*, 2012, vol. 61, no. 4, pp. 1072-1078. doi: <https://doi.org/10.1109/TIM.2011.2178672>.
14. Pan Feng, Xiao Yong, Lin Guoying, Xiao Xia, Shuai Hang. Analysis of the influencing factors for the 500 kV DC voltage reference divider used for on-site calibration. *2015 12th IEEE International Conference on Electronic Measurement & Instruments (ICEMI)*, 2015, pp. 25-29. doi: <https://doi.org/10.1109/ICEMI.2015.7494180>.
15. Boyko M.I., Syomkin S.O. Investigation of amplitude-temporal characteristics of a high-voltage resistive voltage divider. *Electrical Engineering & Electromechanics*, 2019, no. 4, pp. 59-68. doi: <https://doi.org/10.20998/2074-272X.2019.4.09>.
16. *MathStudio Manual*. Available at: <http://mathstud.io/manual/> (accessed 22 May 2022).

Received 28.07.2022

Accepted 22.10.2022

Published 06.05.2023

V.O. Brzhezitsky<sup>1</sup>, Doctor of Technical Science, Professor,

Y.O. Haran<sup>1</sup>, PhD,

Y.O. Trotsenko<sup>1</sup>, PhD, Associate Professor,

O.R. Protsenko<sup>1</sup>, PhD, Associate Professor,

A.O. Derzhuk<sup>1</sup>, Postgraduate Student,

M.M. Dixit<sup>2</sup>, Postgraduate Student,

<sup>1</sup>National Technical University of Ukraine «Igor Sikorsky Kyiv Polytechnic Institute»,

37, Prospect Peremohy, Kyiv-56, 03056, Ukraine,

e-mail: y.garan@kpi.ua (Corresponding Author)

<sup>2</sup>Vishwaniketan Institute of Management Entrepreneurship and Engineering Technology,

Survey No. 52, Kumbhivali, Tal, Khalapur, Maharashtra, 410202, India,

e-mail: mandardixit78@gmail.com

#### How to cite this article:

Brzhezitsky V.O., Haran Y.O., Trotsenko Y.O., Protsenko O.R., Derzhuk A.O., Dixit M.M. Ultimate effect of non-identity of resistive elements of high-voltage arm on frequency characteristics of broadband voltage divider (analytical research). *Electrical Engineering & Electromechanics*, 2023, no. 3, pp. 52-58. doi: <https://doi.org/10.20998/2074-272X.2023.3.08>

O.I. Khrysto

## Energy characteristics for nanosecond current interrupter of semiconductor-magnetic pulse generator's terminal stage

**Introduction.** A semiconductor diode based on reverse current interruption is used to increase a pulse amplitude and peak power delivered on the process load. Usually, a current interrupter is located in the last stage of semiconductor-magnetic pulse generator (SMPG) and is connected in parallel to the load. **Problem.** Most of publications on this topic mostly concern with analysis of physical processes in the diode structure itself within its oscillating circuit, which is separated from previous SMPG's pulse compression stages under condition of unidirectional energy transfer from the generator to the load. In this sense, the efficiency of conversion should be determined by the joint of electromagnetic interaction between non-linear compression stages, current interrupter and process load. **Goal.** Develop a mathematical model of nanosecond current interrupter to determine its electrical and energy characteristics as a part of high-voltage parallel circuit with magnetic pulse compression, depending on the duration and moment of current interruption, the equivalent circuit for load resistance, and to set the most optimal modes of its operation. **Methodology.** In this work, it is proposed to use a comprehensive approach aimed at the study of electromagnetic processes in the SMPG's circuits with a nanosecond current interrupter, which takes into account the topology of circuit, the design parameters of saturable reactor, the magnetization curve, the equivalent load's resistance, as well as the time parameters of power switches. **Results.** Analytical expressions describing the electrical and energy characteristics of the interrupter when it operating on the active load are obtained. A numerical simulation of interrupter in the SMPG's double-loop pumping circuit is carried out, taking into account a nonlinearity of SR's magnetization curve. Three operation modes of interrupter is described, depending on the initial moment of reverse conduction current interruption. The analysis of interrupter operation on the load with an active-capacitive component is carried out. **Practical meaning.** The results of research can be applied in development of high-voltage SMPG scheme with improved energy-dynamic parameters. References 20, figures 10.

**Key words:** semiconductor-magnetic pulse generator, nanosecond current interrupter, saturable reactor, magnetization curve, numerical simulation.

У даній роботі використовується комплексний підхід, спрямований на дослідження електромагнітних процесів у схемі магнітно-напівпровідникового генератора імпульсів з наносекундним переривником струму, який враховує топологію схеми, конструктивні параметри комутуючого дроселя, криву намагнічування його осердя, еквівалентний опір навантаження, а також часові параметри періодичної комутації силових ключів. Запропоновано модель наносекундного переривника струму паралельної ланки магнітного стиснення на основі експоненційного зростання його активного опору. Отримано аналітичні вирази, що описують електричні та енергетичні характеристики переривника струму при роботі на активне навантаження. Виконане числове модулювання переривника струму у двухконтурній схемі магнітного генератора імпульсів з урахуванням нелінійності кривої намагнічування комутуючих дроселів. Розглянуто три режими його роботи в залежності від моменту початку обриву струму зворотної провідності. Проведено аналіз роботи переривника струму на навантаження з активно-ємнісною складовою. Результати досліджень можуть бути застосовано при розробці високовольтних магнітно-напівпровідникових генераторів імпульсів з поліпшеними енергодинамічними параметрами. Бібл. 20, рис. 10.

**Ключові слова:** магнітно - напівпровідниковий генератор імпульсів, переривник струму, комутуючий дросель, крива намагнічування, числове моделювання.

**Problem.** In present, one of the promising areas of nanosecond pulse technology is the use of combination of an inductive storage and a semiconductor current interrupter in the terminate compression stage of semiconductor-magnetic pulse generator (SMPG) circuit, that allows to enhance a voltage amplitude and pulse power on the load. The majority of publications on this topic mostly concern with analysis of physical processes in the semiconductor diode structure, rather than the efficiency of energy conversion. For this reason, electrical and energy characteristics of the SMPG's terminal stage should be determined due to the compatible electromagnetic interaction between non-linear compression stages, current interrupter and electrical load. In addition, the unidirectional energy transfer from generator to the load is a separate case from the entire set of energy modes of SMPG oscillations.

**Analysis of recent research and publications.** SMPGs [1, 2] are a class of convertor technology, that were originally developed for powering microwave emitters and pumping gas lasers [3], where the sharpness of the pulse front plays a primary role. Over the last

decade, SMPG has become more and more widely used in electric discharge technologies for water purification and disinfection [4, 5], for air ionization by streamer discharge to remove toxic impurities [6, 7], as well as for agricultural processing [8] or food pasteurization [9]. A low-temperature plasma of barrier or corona discharges of specified technologies is a main tool for processing the primary medium (material) to eliminate harmful substances in it. Usually, the plasma of these discharges is maintained due to the release of energy from a capacitive storage, but the need to increase the peak power of pulse and energy conversion efficiency led to development of SMPG with inductive energy storage. This became possible thanks to the use, along with traditional magnetic compression stages, of semiconductor current interrupters, which are highly alloyed diodes with the effect of a sharp interruption of the reverse conduction current (SOS-diodes) [10, 11].

The traditional model of a semiconductor diode [12-14] considers a system of differential equations of the electron-hole plasma for a continuity of charged particles,

© O.I. Khrysto

the equation of an electrostatic field and thermal conductivity, which have nonlinear coefficients (mobility, ionization, and recombination) that, in turn, depend on intensity of electric field strength and temperature. At the same time, the differential equations of electric circuits do not take into account the nonlinearity of saturable reactor's (SR) magnetization curve and are considered with fixed parameters. A simultaneous solution of the hyperbolic equation for charged particles with the Poisson equation of the elliptic type can cause numerical instability, especially in the case of the sharp change in the potential between a neighboring mesh points, which exceeds 2 kT/q ratio. This circumstance requires the use of special calculation algorithms [15] (Gummel-Scharfetter difference scheme) aimed at smoothing the calculation grid. Another disadvantage of this model is that the forward and reverse conduction phases of the diode are considered from two independent circuits, provided that the SR's magnetization currents of compression stage are neglected.

A more simplified version is proposed in [16], where a high-voltage converter is modeled using an ideal current source, which changes its current through the inductance of a saturated SR according to an exponential dependence. As a result, an analytical expression was obtained that describes the pulse character on the active-capacitive load, which makes it possible to determine the energy and power released on the load. At the same time, the model does not allow to calculate the energy dissipated on the diode itself during the conversion. It is clear that energy losses in the nanosecond current interrupter (hereinafter NCI) will be determined both by the duration of the reverse current interruption and by the load parameters. In addition, for a more accurate calculation, the model should also take into account the inductive component of the electric discharge load, since the length of connecting wires can significantly affect the nature of nanosecond pulses formation.

#### Separation of previously unsolved part of tasks.

The experience of modeling various variants of SMPG and the analysis of existing ones, including the ones given above, shows that there are a number of issues that cannot be solved effectively, relying only on known knowledge in this area. First, when simulating a compression stage with NCI, one must take into account the nonlinear nature of the SR's magnetization curve. This is explained by the fact that in the reverse conduction circuit of diode, the discharge current of compression stage's capacitor has a complex character, consisting of two harmonic components. The first harmonic reflects the process of magnetization of the SR's core, and the second the process of its saturation. If there is no second harmonic in the reverse conduction current of the diode, it means that the SR is not saturated until the moment of interruption and the compression stage does not function properly. By changing the harmonic composition of the reverse current accordingly, it is possible to influence the current magnitude in which its interruption is realized. Secondly, it should be noted that the real technological load has a non-linear nature with a reactive component and an active resistance that can vary from units of mΩ to tens of kΩ.

**Purpose of the article** is to develop a mathematical model of nanosecond current interrupter to determine its electrical and energy characteristics as a part of high-voltage magnetic pulse compression parallel stage, depending on the duration and the moment of current interruption, the equivalent circuit for load resistance, and to set the most optimal modes of its operation.

**Research methods:** mathematical modeling of converter devices, numerical analysis for solving systems of nonlinear integro-differential equations, and approximate analytical expression of nonlinear characteristics of converter devices.

**Main content of work.** The operating principle of SOS diodes can be divided into two phases: in the first phase, when direct current flows, a charge accumulates in highly doped regions of the semiconductor structure; in the second phase, during the passage of the reverse current, a reverse voltage is applied to the diode, which ensures the removal of the accumulated charge from the highly doped regions with the subsequent formation of a volume charge region near the p-n junction, which leads to a sharp interruption of the current through the diode and an increase of field strength in it.

The interruption of inductive current occurs as a result of a sharp increase in the internal resistance of semiconductor NCI at the stage of reverse current conduction. The most physically close to describing a sharp current interruption is the NCI's model based on the time-dependent exponential resistance growth

$$R = R_0 \cdot \exp(\alpha \cdot t), \quad (1)$$

where  $\alpha$  characterizes the growth rate of the interrupter resistance.

Suppose that the current break occurs at the moment of reaching the maximum of the reverse current through the NCI, when the maximum energy is stored in the inductance of SR. Then a replacement circuit will look like a parallel connection of the SR's inductance, the NCI's time-dependent active resistance and the load.

Circuit parameters are chosen as follows: the inductance of the magnetic energy storage device is  $L_{sr} = 1 \mu\text{H}$ , the initial current that breaks the NCI is  $I_0 = 100 \text{ A}$ , the initial resistance of the one is  $R_0 = 0,1 \Omega$ , the load resistance  $R_L = 150 \Omega$ .

Differential equations for an inductive circuit with a NCI:

$$L_{sr} \frac{di_0}{dt} + \frac{R_L \cdot R_0 e^{\alpha t}}{R_L + R_0 e^{\alpha t}} \cdot i_0 = 0 \quad (2)$$

is a first-order homogeneous differential equation whose solution is a function of the form:

$$i_0(t) = A \cdot \exp \left[ - \int \frac{R_L \cdot R_0 e^{\alpha t}}{L_{sr} (R_L + R_0 e^{\alpha t})} dt \right], \quad (3)$$

where  $A = \frac{I_0}{\exp \left[ - \frac{R_L}{\alpha \cdot L_{sr}} \ln(R_L + R_0) \right]}$  – the constant,

which is determined under zero initial conditions.

The general solution of equation (3):

$$i_0(t) = \frac{I_0}{\exp\left[-\frac{R_L}{\alpha \cdot L_{sr}} \ln(R_L + R_0)\right]} \times \exp\left[-\frac{R_L}{\alpha \cdot L_{sr}} \ln(R_L + R_0 \cdot \exp(\alpha \cdot t))\right]. \quad (4)$$

Current through the NCI:

$$i_1(t) = \frac{i_0(t)}{\frac{R_0}{R_L} \exp(\alpha \cdot t) + 1}. \quad (5)$$

Current through the load:

$$i_2(t) = \frac{i_0(t) \cdot R_0 \exp(\alpha \cdot t)}{R_0 \cdot \exp(\alpha \cdot t) + R_L}. \quad (6)$$

The energy dissipated on the load:

$$E_{RL} = \int_0^{\infty} i_2^2(t) \cdot R_L dt. \quad (7)$$

$$E_{RL} = \int_0^{\infty} \frac{i_0^2(t) \cdot R_0^2 \exp(2\alpha \cdot t)}{(R_0 \cdot \exp(\alpha \cdot t) + R_L)^2} R_L dt =$$

$$= -\frac{0.5 \cdot A^2 \cdot L_{sr}}{(R_L + R_0 \cdot \exp(\alpha \cdot t))^{\frac{2R_L}{\alpha L_{sr}} + 1}} \times$$

$$\times \left( R_0 \exp(\alpha \cdot t) + L_{sr} \cdot \alpha \cdot \frac{R_L}{\alpha L_{sr} + 2R_L} \right) \Big|_0^{\infty}.$$

Since,  $\lim_{t \rightarrow \infty} \frac{1}{(R_L + R_0 \exp(\alpha \cdot t))^{\frac{2R_L}{\alpha L_{sr}} + 1}} = 0$ , then we

have:

$$E_{RL} = \frac{0.5 \cdot A^2 \cdot L_{sr}}{(R_L + R_0) \alpha L_{sr}} \left( R_0 + \frac{L_{sr} \cdot \alpha \cdot R_L}{\alpha L_{sr} + 2R_L} \right). \quad (8)$$

Energy dissipated on the converter:

$$E_d = \int_0^{\infty} i_1^2(t) \cdot R_0 \exp(\alpha \cdot t) dt. \quad (9)$$

$$E_d = \int_0^{\infty} \frac{i_0^2(t) \cdot R_0 \exp(\alpha \cdot t)}{(R_0 \cdot \exp(\alpha \cdot t) + R_L)^2} R_L^2 dt =$$

$$= -\frac{A^2 \cdot L_{sr} \cdot R_L^2}{(\alpha L_{sr} + 2R_L)(R_L + R_0 \exp(\alpha \cdot t))^{\frac{2R_L}{\alpha L_{sr}} + 1}} \Big|_0^{\infty}.$$

$$E_d = \frac{A^2 \cdot L_{sr} \cdot R_L^2}{(\alpha L_{sr} + 2R_L)(R_L + R_0) \alpha L_{sr}}. \quad (10)$$

The conversion efficiency is estimated as the ratio of the energy dissipated on the load, to the energy stored in the inductance  $L_{sr}$

$$K_{eff} = \frac{\exp\left(\frac{2R_L}{\alpha L_{sr}} \ln(R_L + R_0)\right)}{(R_L + R_0) \alpha L_{sr}} \cdot \left( R_0 + \frac{L_{sr} \cdot \alpha \cdot R_L}{\alpha L_{sr} + 2R_L} \right). \quad (11)$$

Figures 1,a,c show characteristics of the instantaneous power dissipated on the load and the NCI depending on the rate of current interruption with constant load resistance  $R_L = 150 \Omega$ , and the Fig. 1,b,d show the corresponding characteristics of dissipated energy on the load and on the switch in the same dependence. The coefficient of exponential function for the corresponding graph: 1 –  $10^{9.2}$ , 2 –  $10^{9.5}$ , 3 –  $10^{9.8}$ . The quantitative value of these coefficients was chosen exactly such to provide mathematical calculations that would satisfy the nanosecond range of the interrupter's switching process duration. The time to reach a maximum power of each characteristics in Fig. 1,a respectively, is: 1 – 9,4 ns, 2 – 6,4 ns, 3 – 3,4 ns. At the same time, for maximum and minimum time of current interruption, the voltage amplitude on the load is 6 kV and 12,2 kV, respectively.

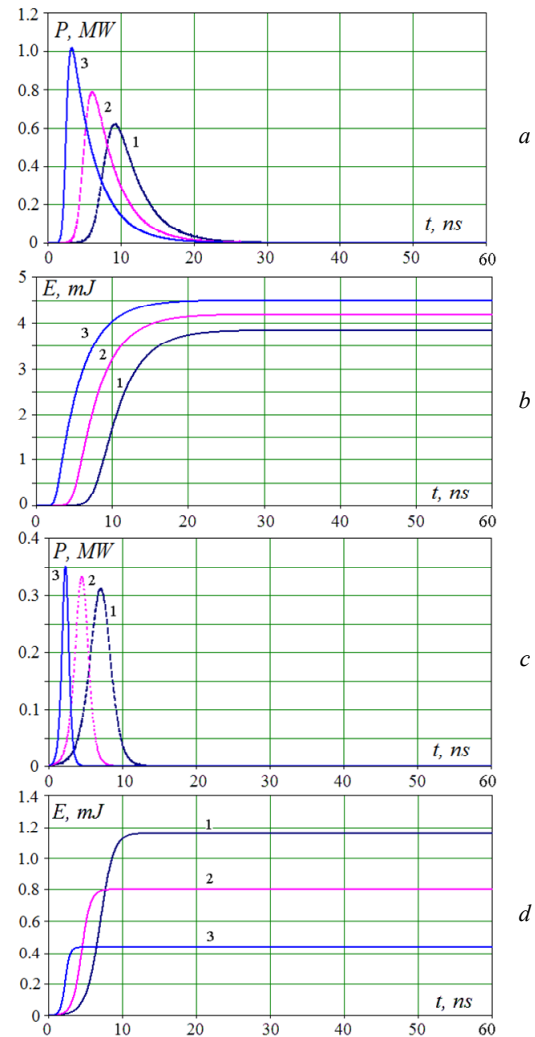


Fig. 1. Characteristics of dissipated power and energy: a) dissipated power on the load; b) dissipated energy on the load; c) dissipated power on the NCI; d) dissipated energy on the NCI

It can be seen from Fig. 1 that the peak value of the power released on the load and on the NCI are separated in time, while the characteristics have different areas, and accordingly, different dissipated energy. The energy dissipated on the load and on the NCI in the order of increasing exponential coefficient are respectively equal:  $E_{RL} = 3,8 \text{ mJ}$ ,  $4,2 \text{ mJ}$ ,  $4,5 \text{ mJ}$ ;  $E_d = 1,1 \text{ mJ}$ ,  $0,8 \text{ mJ}$ ,  $0,4 \text{ mJ}$ .

Thus, as the breaking rate of current increases, the energy dissipated in the NCI decreases, and therefore the energy dissipated in the load increases.

Figure 2 shows the characteristics of energy dissipated on the load and energy dissipated on the NCI, depending on the load resistance at the fixed value of coefficient  $\alpha$ . According to the characteristics it is clear that as the load resistance increases, the energy dissipated on the switch also increases. So for the value of the coefficient  $\alpha = 10^9$ , the energy dissipated on the load becomes equal to the energy dissipated on the load with the load resistance  $R_L = 500 \Omega$ . The real technological load, like a laser tube or a barrier discharge, is a complex parametric load, in which the discharge loop inductance and the capacitance of the electrode system are present.

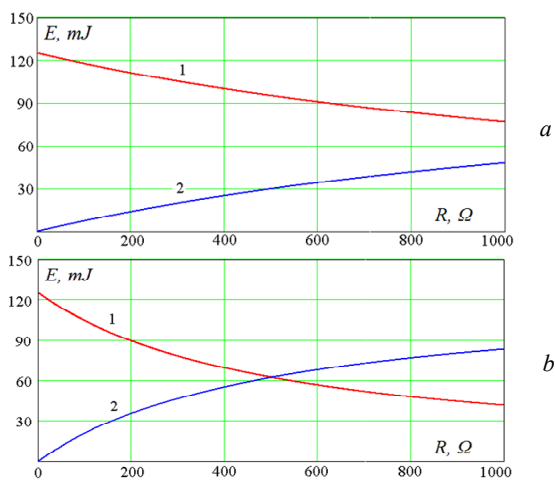


Fig. 2. Characteristic of energy dissipated on the load (1), characteristic of energy dissipated on the NCI (2), depending on the load resistance: a)  $\alpha = 10^{9.5}$ , b)  $\alpha = 10^9$

Now consider the mutual operation of NCI with a parallel pulse compression stage. The circuit of a two-circuit pumping of a semiconductor current interrupter is shown in Fig. 3.

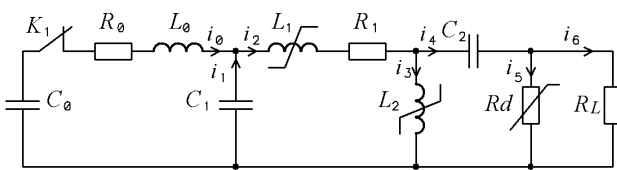


Fig. 3. The equivalent circuit for diode NCI with a terminal series-parallel compression stage

When the SR  $L_1$  is saturated, the diode is pumped by direct current, when the SR  $L_2$  is saturated, a reverse current of larger amplitude and shorter duration passes through the diode. Let us consider the operating regimes of the parallel compression stage when the reverse half-wave of the current is broken off with a diode at different instants of time. The SR model based on the arctangent function of the core magnetization and its provisions is described in [17]. Based on Kirchhoff's laws, a system of integro-differential equations was compiled. To determine the currents and voltages in the generator circuits, a system of algebraic equations with nonlinear coefficients was obtained using the finite-difference approximation by Euler's method [18]. Integral sums of voltages on

capacitors  $C_0 - C_2$  from currents were calculated using the trapezoidal method.

Parameters of the circuit: the capacitance  $C_0 = C_1 = C_2 = 2,4 \text{ nF}$ , the inductance of the charging circuit is  $L_0 = 120 \mu\text{H}$ , the resistance of the first circuit is  $R_0 = 1 \Omega$ , the resistance of the second circuit is  $R_1 = 0,1 \Omega$ , the load resistance is  $R_L = 150 \Omega$ , the cores volumes of the SR's  $L_1$  and  $L_2$  are  $V_{m1} = V_{m2} = 31,7 \cdot 10^{-6} \text{ m}^3$ , the number of windings turns of the SR's  $L_1$  and  $L_2$  is  $w_1 = 35$  and  $w_2 = 10$ , respectively. The step of time sampling before the current breakage was chosen equal to 2 ns, after breakage - 0.005 ns. Figure 4 shows the combined energies characteristics on the capacitors  $C_1$  and  $C_2$  at different moments of current interruption.

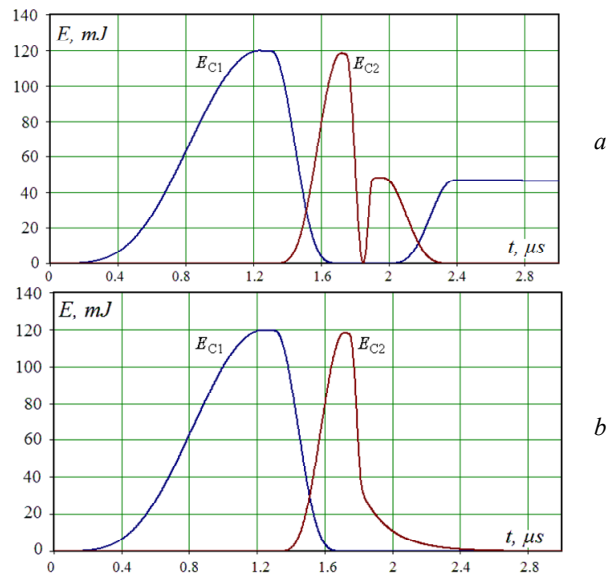


Fig. 4. Energy characteristics of pulse compression stages at different moments of the reverse current breakage through the NCI: a) when the reverse current through NCI drops; b) when the reverse current through NCI increases

Based on the simulation results, it is possible to distinguish three operation regimes of the NCI together with a series-parallel pulse compression stage. The regime when the current flowing through the inductance of the SR  $L_2$  occurs at the half-wave current drop, is energetically inefficient, since the SR  $L_1$  is saturated repeatedly and some of energy is returned to the capacitor of the previous compression stage (Fig. 4,a). The regime with the maximum power release occurs when the current is broken off at its maximum, when all energy is concentrated at the magnetic field of the SR  $L_2$  inductance. The regime when the current is broken off in the first half-wave is also effective and has the advantage that it makes it possible to form a pulse on the load with a sharper leading front and a longer trailing edge. In this case, the energy is introduced into the load both from the inductive storage device  $L_2$  and from the capacitor  $C_2$  (Fig. 4,b). When the pulse front is formed, energy is put into the load from the inductive storage, and during the pulse trailing edge, the energy on the load is put from the capacitive storage.

The next part of the research to consider the operation of NCI diode in the composition of a parallel

stage for active-inductive and active-inductive-capacitive loads. Variants of loads are shown in Fig. 5.

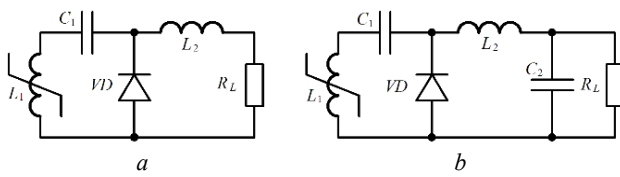


Fig. 5. The NCI load's options:  
a) active-inductive; b) active-inductive-capacitive

**Modeling the NCI operation on the active-inductive load.** According to Fig. 6,*a,b*, when the NCI operates on the active-inductive load, the characteristic of the peak power dissipated on the load is described second-order polynomial dependence on the load resistance, and the same characteristic for the NCI has a linear increasing dependence within the active load resistance from 10 to 500  $\Omega$ . At the same time, the characteristic of energy dissipated on the load has a maximum in the range from 120 to 150  $\Omega$ , the characteristic of energy dissipated on the NCI also has an increasing linear character as the characteristic of the peak power on it.

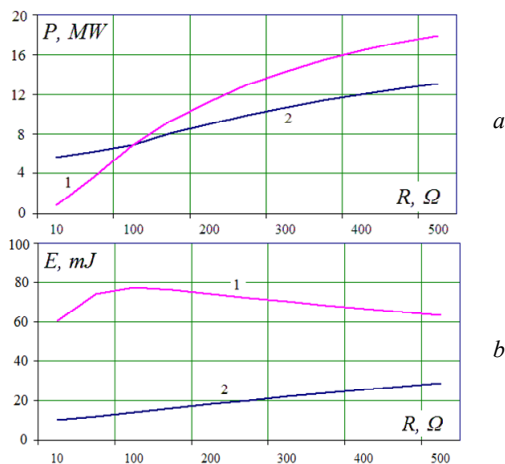


Fig. 6. Characteristics of the peak power (*a*) and energy (*b*) dissipated on the load (1) and on the NCI (2), depending on the active load resistance

**Modeling the NCI operation on the active-inductive-capacitive load.** Figure 7 shows the characteristics for the two load inductance values.

It is determined that if the load has a capacitive component, then maxima will appear in the characteristics of the peak power dissipated on the load. At the same time, the characteristics of the dissipated power and energy on the NCI become a linear character. It turns out that the capacitance makes it possible to stabilize the energy losses in the NCI when the active resistance of the load changes. Also, the peak power on the NCI depends on the inductive component of the load and increases with increasing it value. A sharp decrease in the characteristic in the range from 100 to 10  $\Omega$  is due to incomplete transfer of energy from the inductance of the saturated SR to the load and for a longer period of current oscillations, some of the energy from the SR inductance returns back to the longitudinal capacitor. A smooth reduction of

characteristic in the range from 200 to 500  $\Omega$  is due to a decrease in the peak current through the load.

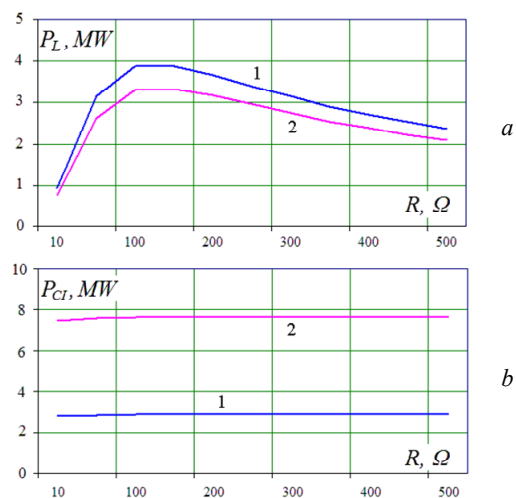


Fig. 7. Characteristics of the peak power dissipated on the load (*a*) and on the NCI (*b*) for two values of the load inductance:  
1 – 100 nH; 2 – 300 nH

When the capacitance varies from 10 to 200 pF, the peak power characteristics have a decreasing nature, as shown in Fig. 8,*a*. At the same time, the characteristic falls faster on the load than on the NCI. That is, the energy losses to the NCI also stabilize when the capacitive component of the load changes. But for the characteristics of current trough the load with an increase in its capacity, there is a decrease in the sharpness of the pulse leading edge and an increase in its duration. The noted results are shown in Fig. 8,*b*.

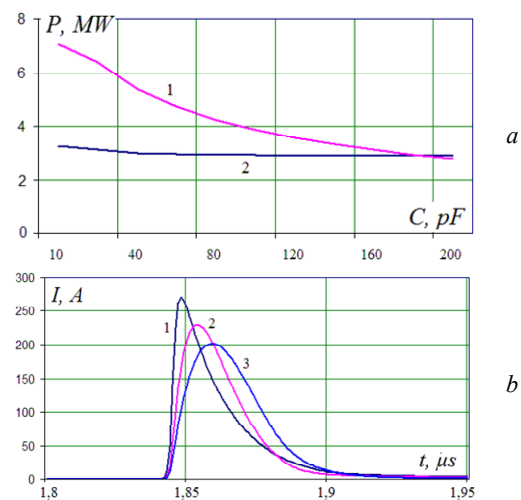


Fig. 8. Characteristics of peak power (*a*) and current characteristics in the load (*b*): a) 1 – on the load, 2 – on the NCI;  
b) 1 –  $C = 10$  pF, 2 – 50 pF, 3 – 100 pF

Thus, the capacitive load component allows to stabilize the energy losses in the NCI current when the resistance of the active component of the load changes.

**Physical modeling of a semiconductor current interrupter.** To implement inductive current interruption and confirm mathematical calculations, a two-switch SMPG scheme with a parallel-serial stage in the charging circuit was used, the scheme of which is shown in Fig. 9.

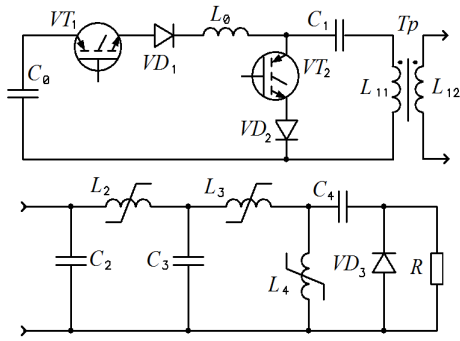


Fig. 9. A schematic diagram of two-switch SMPG with output pulse compression stage and semiconductor current interrupter

Two series-connected high-voltage diodes of the KC201E type were used as a semiconductor current interrupter. The design of these diodes is a series connection of many avalanche p-n junctions, which allows to increase the maximum allowable reverse voltage, which is proportional to the number of diodes inside the column. The maximum reverse voltage for this diode assembly is 15 kV. Electrical and structural parameters of SR  $L_2 - L_4$  and capacitors  $C_2 - C_4$  of the high-voltage part of the SMPG are implemented the same as in the calculation model. The load was assembled from two series power resistors, each with an active resistance of 24  $\Omega$ . A capacitive voltage divider [19] with a division ratio of 1:11000 and a low-inductive current shunt [20] with a resistance of 0,16  $\Omega$  were used to measure electrical signals on the current interrupter.

Figure 10 shows the recorded current and voltage waveforms of the semiconductor interrupter, which can be explained as follows.

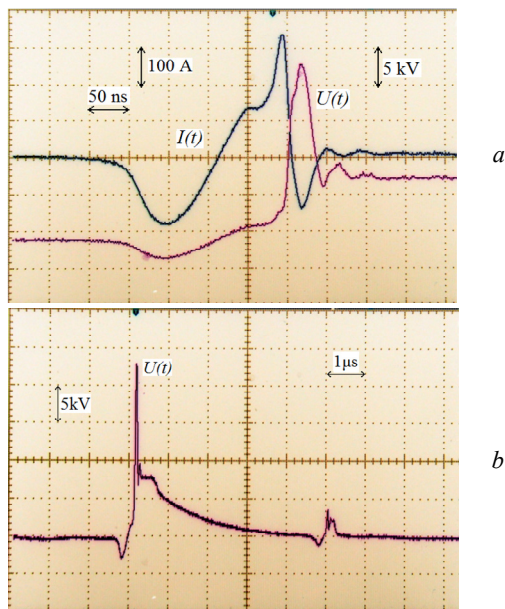


Fig. 10. Waveforms of the SMPG: a) current  $I(t)$  and voltage  $U(t)$  of the semiconductor interrupter  $VD_3$ , 50 ns/div; b) voltage on the semiconductor interrupter  $VD_3$ , 1  $\mu$ s/div

The negative half-wave of the current is caused by its flowing through the stage  $VD_3 - C_3 - L_3 - C_4$  due to the turning on of the diode  $VD_3$  in the forward direction and characterizes the process of charging the capacitor  $C_4$ . The accumulated charge of capacitor  $C_4$  tends to be

released through the stage  $VD_3 - C_4 - L_4$ , at the same time, the reverse half-wave of the current consists of two harmonic components. The first harmonic of the current has a longer period of oscillation and reflects the process of magnetization of the core of the SR  $L_4$ , the second harmonic occurs when it is saturated and has a much shorter period of oscillation. In addition, the boundary between two states of the core has a region lasting 10 ns, for which the differential permeability of the core increases, which is reflected on the waveform as the termination of current growth. Reverse current is turned off by the diode  $VD_3$  in approximately 25 ns. The inductive current interrupted before reaching its maximum. Therefore, the pulse on the load will have a sharp front and a long decline, which is supported by the discharge of the capacitor  $C_4$ . At the same time, the reverse voltage developing on the diode does not exceed the allowable breakdown value for this assembly. This mode of operation of the interrupter is fully consistent with mathematical modeling and corresponds to the results indicated above.

The obtained research results were used at the Institute of Impulse Processes and Technologies of the National Academy of Sciences of Ukraine in the development of a laboratory variant of a high-voltage semiconductor-magnetic pulse generator, forming pulses with an amplitude of 30 kV, an energy of 0.2 J, a pulse repetition rate of up to 10 kHz and a duration of 80 ns, which was applied for electro-filtration of gas emissions.

**Conclusions.** The conducted studies show that the use of semiconductor current interrupter as part of a serial-parallel compression stage allows a radically to influence not only on the generated pulse front but also on its decline. A model of a nanosecond current interrupter based on the time-dependent exponential nature of the internal resistance growth is proposed. Analytical expressions that describe the electrical and energy characteristics of the current interrupter for a parallel circuit of its connection with an inductive storage and active load are obtained. It is shown that the dissipated energy in the load and the energy losses in the current interrupter are described by mirror functions with asymptotic behavior. Numerical modeling of a current interrupter as part of a serial-parallel circuit of magnetic pulse compression stage made it possible to distinguish three modes of its operation, the most effective of which is the current interruption mode at the maximum of stored energy in the saturable reactor inductance and the current interruption mode during its increase. In the latter case, energy is delivered in the load in two stages: during the formation of the pulse front, it is released from the inductive storage, and during the formation of the pulse decline, it is released from the capacitive one. It was found that if the load has a capacitive component, then the optimum in the peak power characteristic of the load appears in the range  $R_L = 120-150 \Omega$ . At the same time, the capacitive component leads to the suppression of dissipated energy on the current interrupter, so that the energy losses on it remain practically constant, independent of the load's active resistance.

**Conflict of interest.** The author declares no conflict of interest.

## REFERENCES

1. Khrysto O. Energy transfer processes in high-voltage circuits based on magnetic pulse compression. *Acta Electrotechnica et Informatica*, 2020, vol. 20, no. 3, pp. 3-10. doi: <https://doi.org/10.15546/aei-2020-0013>.
2. Li S., Gao J., Yang H., Zhu D., Qian B., Cui Y., Wu Q., Zhang J. Investigation on Adjustable Magnetic Pulse Compressor in Power Supply System. *IEEE Transactions on Power Electronics*, 2019, vol. 34, no. 2, pp. 1540-1547. doi: <https://doi.org/10.1109/TPEL.2018.2830106>.
3. Choi J. Introduction of the magnetic pulse compressor (MPC) – fundamental review and practical application. *Journal of Electrical Engineering and Technology*, 2010, vol. 5, no. 3, pp. 484-492. doi: <https://doi.org/10.5370/JEET.2010.5.3.484>.
4. Guo X., Zheng D., Blaabjerg F. Power Electronic Pulse Generators for Water Treatment Application: A Review. *IEEE Transactions on Power Electronics*, 2020, vol. 35, no. 10, pp. 10285-10305. doi: <https://doi.org/10.1109/TPEL.2020.2976145>.
5. Boyko N.I., Makogon A.V. The micro- and nanosecond discharges in gas bubbles for water disinfection and purification. *Electrical Engineering & Electromechanics*, 2019, no. 3, pp. 50-54. doi: <https://doi.org/10.20998/2074-272X.2019.3.08>.
6. Bozhko I.V., Zozulev V.I., Kobylchak V.V. SOS-generator for the electric discharge technology used pulse barrier discharge. *Technical Electrodynamics*, 2016, no. 2, pp. 63-67. doi: <https://doi.org/10.15407/techned2016.02.063>.
7. Pokryvailo A., Yankelevich Y., Wolf M. A High-Power Pulsed Corona Source for Pollution Control Applications. *IEEE Transactions on Plasma Science*, 2004, vol. 32, no. 5, pp. 2045-2054. doi: <https://doi.org/10.1109/tps.2004.835952>.
8. Takaki K., Takahashi K., Hayashi N., Wang D., Ohshima T. Pulsed power applications for agriculture and food processing. *Reviews of Modern Plasma Physics*, 2021, vol. 5, no. 12. doi: <https://doi.org/10.1007/s41614-021-00059-9>.
9. Tamborrino A., Urbani S., Servili M., Romaniello R., Perone C., Leone A. Pulsed Electric Fields for the Treatment of Olive Pastes in the Oil Extraction Process. *Applied Sciences*, 2019, vol. 10, no. 1, art. no. 114. doi: <https://doi.org/10.3390/app10010114>.
10. Boyko N.I. Powerful generators of high-voltage pulses with nanosecond fronts. *Electrical Engineering & Electromechanics*, 2018, no. 1, pp. 59-61. doi: <https://doi.org/10.20998/2074-272X.2018.1.09>.
11. Weihua Jiang, Yatsui K., Takayama K., Akemoto M., Nakamura E., Shimizu N., Tokuchi A., Rukin S., Tarasenko V., Panchenko A. Compact solid-State switched pulsed power and its applications. *Proceedings of the IEEE*, 2004, vol. 92, no. 7, pp. 1180-1196. doi: <https://doi.org/10.1109/JPROC.2004.829003>.
12. Rukin S.N. Pulsed power technology based on semiconductor opening switches: A review. *Review of Scientific Instruments*, 2020, vol. 91, no. 1, art. no. 011501. doi: <https://doi.org/10.1063/1.5128297>.
13. Fardi H. Numerical Analysis of Semiconductor PN Junctions Using MATLABM. *Journal of Scientific Research and Reports*, 2015, vol. 6, no. 2, pp. 84-98. doi: <https://doi.org/10.9734/JSRR/2015/14434>.
14. Sharabani Y., Rosenwaks Y., Eger D. Mechanism of fast current interruption in p- $\pi$ -p diodes for nanosecond opening switches in high-voltage-pulse applications. *Physical Review Applied*, 2015, vol. 4, no. 1, art. no. 014015. doi: <https://doi.org/10.1103/PhysRevApplied.4.014015>.
15. Scharfetter D.L., Gummel H.K. Large-signal analysis of a silicon Read diode oscillator. *IEEE Transactions on Electron Devices*, 1969, vol. 16, no. 1, pp. 64-77. doi: <https://doi.org/10.1109/T-ED.1969.16566>.
16. Pereverzev A.V., Litvinenko T.M. High-voltage converter for electrodischarge neutralization of sulfur dioxide. *Technical Electrodynamics*, 2015, no. 6, pp. 84-89.
17. Khrysto O.I., Zozulev V.I., Sholokh D.O. Numerical simulation of electromagnetic processes in the scheme of magnetic pulse generator. *Technical Electrodynamics*, 2014, no. 2, pp. 22-28.
18. Nurujjaman Md. Enhanced Euler's method to solve first order ordinary differential equations with better accuracy. *Journal of Engineering Mathematics and Statistics*, 2020, vol. 4, no. 1, pp. 1-13. doi: <https://doi.org/10.5281/zenodo.3731020>.
19. Anokhin Y.L., Brzhezitsky V.O., Haran Y.O., Masliuchenko I.M., Protsenko O.P., Trotsenko Y.O. Application of high voltage dividers for power quality indices measurement. *Electrical Engineering & Electromechanics*, 2017, no. 6, pp. 53-59. doi: <https://doi.org/10.20998/2074-272X.2017.6.08>.
20. Baranov M.I., Kniaziev V.V., Rudakov S.V. Coaxial disk shunt for measuring in the heavy-current chain of high-voltage generator of storm discharges of impulses of current of artificial lightning with the integral of action to  $15 \cdot 10^6$  J/Ohm. *Electrical Engineering & Electromechanics*, 2017, no. 5, pp. 45-50. doi: <https://doi.org/10.20998/2074-272X.2017.5.07>.

Received 01.08.2022

Accepted 22.11.2022

Published 06.05.2023

O.I. Khrysto<sup>1</sup>, PhD, Senior Researcher,

<sup>1</sup>Institute of Pulse Processes and Technologies of NAS of Ukraine, 43-A, Bogoyavlenskij Avenue, Mykolayiv, 54018, Ukraine. e-mail: alexander.khristo@gmail.com

*How to cite this article:*

Khrysto O.I. Energy characteristics for nanosecond current interrupter of semiconductor-magnetic pulse generator's terminal stage. *Electrical Engineering & Electromechanics*, 2023, no. 3, pp. 59-65. doi: <https://doi.org/10.20998/2074-272X.2023.3.09>

Y. Ayat, A.E. Badoud, S. Mekhilef, S. Gassab

## Energy management based on a fuzzy controller of a photovoltaic/fuel cell/Li-ion battery/supercapacitor for unpredictable, fluctuating, high-dynamic three-phase AC load

**Introduction.** Nowadays, environmental pollution becomes an urgent issue that undoubtedly influences the health of humans and other creatures living in the world. The growth of hydrogen energy increased 97.3 % and was forecast to remain the world's largest source of green energy. It can be seen that hydrogen is one of the essential elements in the energy structure as well as has great potential to be widely used in the 21st century. **Purpose.** This paper aims to propose an energy management strategy based a fuzzy logic control, which includes a hybrid renewable energy sources system dedicated to the power supply of a three-phase AC variable load (unpredictable high dynamic). Photovoltaic (PV), fuel cell (FC), Li-ion battery, and supercapacitor (SC) are the four sources that make up the renewable hybrid power system; all these sources are coupled in the DC-link bus. Unlike usual the SC was connected to the DC-link bus directly in this research work in order to ensure the dominant advantage which is a speedy response during load fast change and loads transient. **Novelty.** The power sources (PV/FC/Battery/SC) are coordinated based on their dynamics in order to keep the DC voltage around its reference. Among the main goals achieved by the fuzzy control strategy in this work are to reduce hydrogen consumption and increase battery lifetime. **Methods.** This is done by controlling the FC current and by state of charge (SOC) of the battery and SC. To verify the fuzzy control strategy, the simulation was carried out with the same system and compared with the management flowchart strategy. The results obtained confirmed that the hydrogen consumption decreased to 26.5 g and the SOC for the battery was around 62.2-65 and this proves the desired goal. References 47, tables 7, figures 19.

**Key words:** energy management strategy, fuzzy logic control, hybrid renewable energy source.

**Вступ.** В даний час забруднення навколишнього середовища стає актуальною проблемою, яка, безперечно, впливає на здоров'я людини та інших істот, які живуть у світі. Зростання водневої енергетики збільшилося на 97,3 %, і прогнозувалося, що вона залишиться найбільшим у світі джерелом зеленої енергії. Видно, що водень є одним із найважливіших елементів у структурі енергетики, а також має великий потенціал для широкого використання у 21 столітті. **Мета.** У цій статті пропонується стратегія управління енергоспоживанням, заснована на нечіткому логічному управлінні, яка включає гібридну систему відновлюваних джерел енергії, призначену для живлення трифазного змінного навантаження змінного струму (непередбачувана висока динаміка). Фотоелектричні (PV), паливні елементи (FC), літій-іонні батареї та суперконденсатори (SC) – це чотири джерела, з яких складається відновлювана гібридна енергосистема; всі ці джерела підключені до шини постійного струму. На відміну від звичайних застосувань, у цій дослідницькій роботі SC був підключений до шини постійного струму безпосередньо, щоб забезпечити домінуючу перевагу, що полягає в швидкому реагуванні при швидкій зміні навантаження та перехідних режимах навантаження. **Новизна.** Джерела живлення (PV/FC/батареї/SC) координуються на основі їхньої динаміки, щоб підтримувати напругу постійного струму біля свого еталонного значення. Серед основних цілей, досягнутих стратегією нечіткого управління у цій роботі, - зниження споживання водню та збільшення терміну служби батареї. **Методи.** Це робиться шляхом керування струмом FC та станом заряду (SOC) батареї та SC. Для перевірки стратегії нечіткого управління було проведено моделювання з тією самою системою та порівняння зі стратегією блок-схеми керування. Отримані результати підтвердили, що споживання водню знизилося до 26,5 г, а SOC для батареї становило близько 62,2-65, що доводить досягнення бажаної мети. Бібл. 47, табл. 7, рис. 19.

**Ключові слова:** стратегія енергоменеджменту, нечітке логічне управління, гібридне відновлюване джерело енергії.

**Introduction.** The expansion of conventional power networks has led to the instability of the power network due to its inability to meet various energy requirements, especially in rural areas with difficult terrain and very low population density, where the decentralized supply of energy to remote areas has become necessary. The Renewable energy systems like a solar, wind, and hydrogen, to name a few, contribute effectively in global energy balance, These sources are sustainable and have zero emission compared to systems that rely on traditional fuels such heavy oil, natural gas, and coal [1], The system can reach optimal efficiency by combining these sources with energy storage elements [2, 3]. Although these resources are primarily weather-dependent, any significant changes in the weather can drastically affect power generation [4]. This hasn't stopped governments from increasing the percentage of renewable energy in their energy mix, which is predicted to reach 23 % by 2035 [5]. A hybrid power system (HPS) can alleviate the problem of energy demand, especially in distant places, when a self-contained renewable resource is unable to offer reliable and sufficient electricity. HPS is made up of a variety of non-renewable and renewable energy sources, as well as converters and energy storage system devices. It also has a number of advantages, including great

flexibility and power management capabilities [6]. In [7] authors explained that hydrogen is the energy source of the future; he noted that the cost of hydrogen (CH) will decrease as its use grows and production and storage methods improve; he also discussed the necessity of producing hydrogen using electrical energy generated from renewable energy sources. Hydrogen energy has the biggest benefit over other sources of energy in that it can be stored and delivered. Solar energy, wind turbines, and hydroelectric power plants can all provide excess electricity that can be stored as hydrogen energy for later use. Energy can be continuously produced and stored in this manner. As a result, numerous researches have been conducted [8]. The polymer electrolyte membrane fuel cell (PEMFC) systems, according to [9], are one of the efficient energy conversion devices utilized for the direct conversion of hydrogen energy received from diverse RES into electrical energy. In [10] authors shows the impacts of lithium-ion batteries for renewable energy (wind and solar) storage for grid applications are assessed through a life cycle assessment covering the batteries supply phase, their end-of-life, and use. Results show that the new lithium-ion battery cathode chemistry has 41.7 % more particulate matter and 52.2 % more acidification.

© Y. Ayat, A.E. Badoud, S. Mekhilef, S. Gassab

Because of the growing demand for efficient, high-power energy storage, the development of supercapacitors (SCs) has gotten a lot of attention in recent years. Authors in [11] investigated how to improve the energy density of SCs for renewable energy generation applications. This potential was assessed by calculating the performance (energy and power) of a series of SCs that use advanced materials that electrochemists have been studying for the past 10-15 years. In [12] were considered that the SC is one of the greatest energy storage elements for hybrid electric power systems. Many studies have looked into HPS, which combine fuel cells (FCs) with batteries and SCs, In [13, 14] authors improved the energy management in hybrid FC/battery/SC for electric vehicle applications (FC as the primary source, and battery with the SCs as backup source). Authors provide a combination of artificial neural network and primary biliary cirrhosis in this article to control and manage the energy of this multisource system, the stability of the hybrid system while providing an acceptable solution for transferring energy between sources. In order to get greater dynamic performance, the system still need several advanced control approaches. Photovoltaic (PV) wind battery is another type of hybrid renewable energy systems used in energy systems to assess the charging and discharging capabilities of the system, for the energy management of this hybrid energy sources. In [15] displays an intelligent fractional order PID controller. Through a DC-link voltage, PV-wind-battery is connected to a smart grid. To extract the maximum power point (MPP) from the wind and PV, the converters are controlled by an intelligent fractional order PID method, despite the fact that this research gives predictions using the proposed technique while taking local uncertainty into account, the impact of climate conditions on the generated energy still standing. Authors in [16] present an optimized energy management strategy (EMS) for PV/FC/battery DC microgrid based on salp swarm algorithm (SSA), the proposed SSA-based EMS is evaluated and compared to the existing particle swarm optimization (PSO)-based EMS. The SSA provides a more stable working environment for the power system (FC and battery) than the PSO, because the planned EMS is dependent on a central controller, any failure of this controller could have significant implications for the power system, this can be avoided for decentralized control systems. Because of the advantages of using a SC during a load change that is transitory, surprising and quick. In [17] authors included the SC to the renewable hybrid power system (REHPS), which includes PV, PEMFC, battery, and SC. To achieve the maximum value of state of charge (SOC) and the lowest value of hydrogen consumption, the suggested energy management system employs a hybrid method that includes fuzzy logic, frequency decoupling, and state machine control strategies. The adaptive fractional fuzzy sliding mode control (AFFSMC) technique is provided for power management in a PV/FC/SC/battery hybrid system in grid-connected microgrid applications [18]. In operating settings, the AFFSMC outperforms the traditional PI controller, according to research. For the proposed system, a REHPS, a PV array serves as the major power source in this arrangement during day light

when it is available and a FC (PEMFC) as a secondary power source during the night or in the shading time, battery and SC as storage elements and to provide transient load demand.

**The goal of the paper** is to try to improve some of the weaknesses and results of previous research, and that is by connecting the SC directly to DC voltage bus in order to ensure a speedy response during load fast change and load transient, also, in this work, hydrogen consumption and battery SOC were taken into account and optimized (for cost and lifetime cycle) in addition to combining all DC/DC converters into a single unit. This study describes energy management strategies for a fuzzy logic control approach for a REHPS (PV/FC/Battery/SC), The system's performance is simulated using the MATLAB/Simulink software, the results were compared to the control approach for management flowcharts, the system was also tested on a three-phase AC variable load, demonstrating its efficiency.

**System description.** REHPS investigated in this research is designed to provide power to a specific load, four sources make up the REHPS: a PV generator as a renewable energy source that serves as the primary source during daytime hours. The FC intervenes as a supplementary source at night or during shade period. When the load power is high, batteries serve as an energy storage element for the FC, ultracapacitors can be used as a transient power compensator or when changing loads quickly. To controlling the power of each source and maintaining a constant voltage level as much as feasible DC-DC converters regulate all energy sources and storage systems. Boost converter for PV and PEMFC power sources, as well as a bidirectional converter (buck and boost) to manage the charging and discharging of batteries, a three-phase DC-AC converter is used to provide the load with a three-phase regulated current source in this study. In order to expose the system's responsiveness under various scenarios, we assumed the load is a random variable load (Fig. 1).

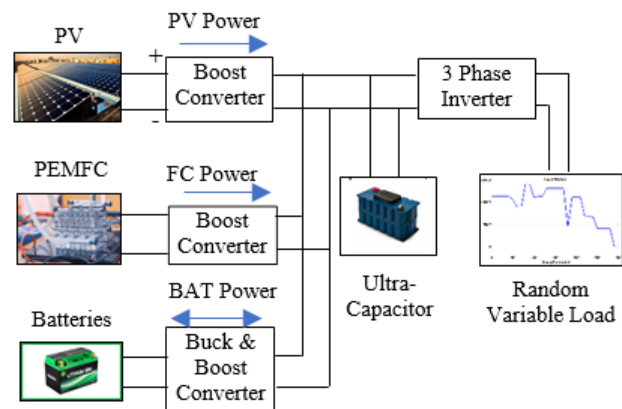


Fig. 1. Structure of the studied REHPS

The suggested energy management system uses the rule based fuzzy logics strategy. In Fig. 2 the hierarchical management and control system is illustrated as a block diagram with its inputs and outputs. The management method presented in this study is based on the following key criteria: lowest hydrogen use while maintaining maximum SOC, extended life cycle, and high overall system efficiency.

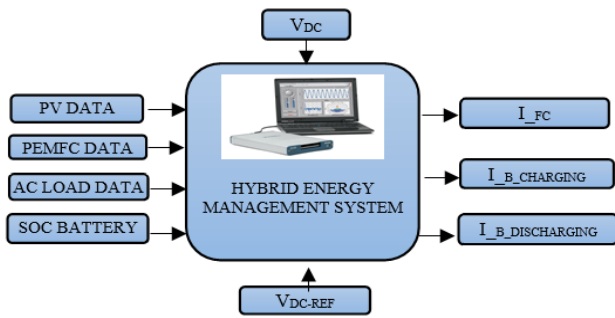


Fig. 2. Block diagram of the energy management system

### Modeling and sizing of electrical system parameters.

**1. PV source.** A solar generator is made up of a group of basic PV cells that are linked in series and/or parallel to generate the necessary electrical characteristic, where their common model is depicted in Fig. 3.

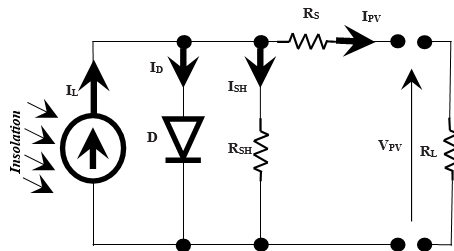


Fig. 3. Single diode PV cell model

The photocurrent is  $I_{ph}$ , and the diode current is  $I_d$ .  $R_{sh}$  is connected to the non-ideal feature of the  $p-n$  junction and the presence of flaws along the cell's borders that favor a short-circuit path around the junction.  $R_s$  indicates the totality of the resistances confronted with the electrons' trajectory [19, 20].

The PV panel used in simulation in this work is referenced by: ASMS-180M from Aavid Solar Company (exists in MATLAB. According to our rated power (10 kW), we have used  $M_s \cdot M_p = 6 \cdot 10 = 60$  – PV panels to achieve this power value (Table 1).

Table 1

Simulation parameters of the used PV field

$P_{MPP}$ – MPP power value, kW (180×6×10)	10.8
$V_{MPP}$ – MPP voltage value, V (36×10)	360
$I_{MPP}$ – MPP current value, A (5×6)	30
$I_{SCS}$ – short circuit current value, A (5.5×6)	33
$V_{OCS}$ – open circuit voltage value, V (45×12)	540

**2. PEMFC generation system.** PEMFC is a popular renewable energy source that has been recommended as preferred because to its benefits such as high efficiency (up to 45 %), high energy density (up to 2 W/cm<sup>2</sup>), silent operation, low-temperature operation, quick start-up, and system resilience [21, 22]. It was frequently used for this purpose used in a number of applications for this reason, including vehicle propulsion, small-dispersed generation, and portable applications [23]. However, it has some disadvantages, including an inconsistent output voltage, a poor reaction to load fluctuations, and a high price [24]. Through electrochemical reactions of oxygen and hydrogen, PEMFC generates electricity-using hydrogen as a fuel, and because the PEMFC's only by-product is water, no emissions are produced. The FC's equivalent circuit is shown in Fig. 4 [25]. The parameters of the PEMFC used

in simulation in this work are detailed in Table 2 (exists in MATLAB). DC/DC boost converter is attached to the PEMFC's output, the converter receives the reference FC current and uses it to adjust the amount of output power it sends to the system, the  $I-V$  curve for the FC employed in the proposed system is shown in Fig. 5 [26].

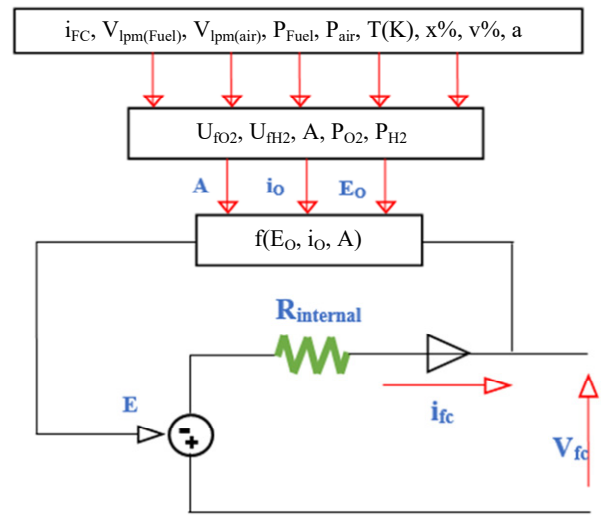


Fig. 4. FC equivalent circuit

Table 2

Parameters of the PEMFC data sheet

FC nominal parameters Stack Power Nominal	10287.5
FC nominal parameters Stack Power Maximal	12544
Nominal utilization hydrogen	98.98
Nominal utilization oxident	42.88
Nominal consumption fuel	113.2
Nominal consumption air	269.5
Temperature system, T	318

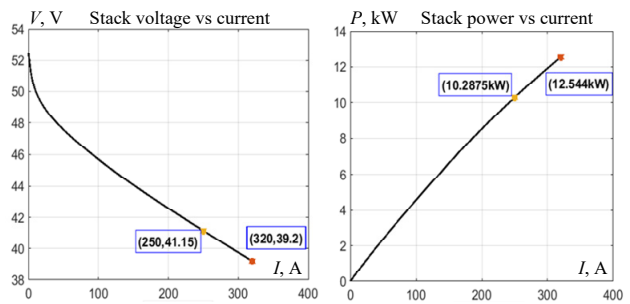


Fig. 5. The suggested system's  $I-V$  curve for the FC

**3. Li-ion battery.** Li-ion batteries were utilized for this research work, because, when compared to other battery types, they have shown to offer a high energy density and efficiency (such as lead-acid, NiCd or NiMH) [27]. When considering lithium batteries, the SOC %, remaining usable life, and deterioration are the most significant characteristics to consider as well as various other factors such as detection of battery parameters, charge control, as well as battery protection and alarm [28, 29]. The updated model of the battery as a function of open cell ohmic resistance, cell circuit, cell inductance, capacitance, long/short time resistance, and the load current is represented by the equivalent battery circuit in Fig. 6.

Table 3 displays the battery parameters, to manage the battery's charging and discharging procedures, the battery's output is coupled to a buck/boost DC/DC converter.

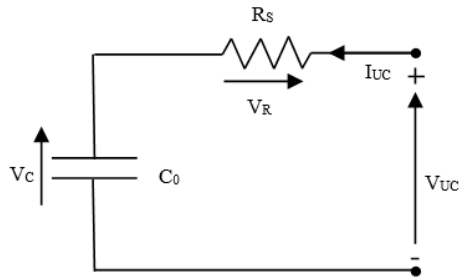


Fig. 6. Battery equivalent circuit

Table 3  
Parameters of the Li-ion battery data sheet

Voltage nominal, V	48
Capacity rated, Ah	40
Initial SOC, %	65
Capacity maximum, Ah	40
Cut-off voltage, V	36
Voltage fully charged voltage, V	55.8714
Discharge current nominal, A	17.3913

**4. Ultracapacitor.** An ultracapacitor (UC), also known as an electrochemical double layer capacitor, is a type of capacitor that has a very high capacitance, is a low-voltage energy storage device that functions similarly to a battery but has a very high capacitance value. High power density, low series resistance, high efficiency, huge charge/discharge capacity, and reduced heating losses are all features of UCs [30]. These fast-response deep-discharge capacitors are suited for use across a broader temperature range. The terminal voltage of a UC, on the other hand, declines when the SOC diminishes, and the rate of reduction is dependent on the load current [31]. The basic UC model is given in Fig. 7.

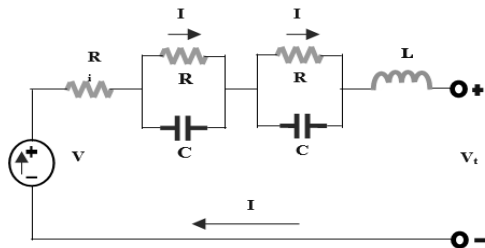


Fig. 7. Basic UC model

Table 4 shows the specifications of the UC that was employed.

Capacitance rated, F	15.6
Equivalent DC series resistance, mΩ	150
Voltage rated voltage, V	291.6
Number of series capacitors	108
Number of parallel capacitors	1
Voltage initial, V	270

**The energy management system** is a computerized software that regulates the power response of each energy source in relation to load demand via the converters that are connected to it. The EMS has a significant impact on system overall performance and efficiency, fuel economy, and distributed generation service life, as well as managing the SOC and avoiding deep discharging, and maintaining DC voltage stability [32]. When discharging, the energy storage element was employed as a source of energy in this study, because the proposed system includes many electrical power sources such as PV and FC, an energy management approach was required to regulate, monitor, and enhance the system's operation in order to achieve the system's maximum performance [33, 34]. With REHPSs, a wide range of EMSs and control techniques are employed, In this research, the fuzzy logic control (FLC) was employed as a control strategy for calculating and setting the reference values of FC power, as well as the PI cascaded control for calculating and setting the reference values of battery charge and discharge currents.

**Control of the active PV generator.** The controller of the PV generator must manage PV voltage in order to adopt a maximum power point tracking (MPPT) approach in order to harvest the maximum power from the PV system. The PV generator's reference voltage is established using a basic perturbation and observation (P&O) based MPPT algorithm. The control unit from the duty cycle (u) to the PV voltage ( $V_{pv}$ ) is shown in Fig. 8, two cascaded PI controllers complete this process, restoring  $V_{pv}$  to its reference [35, 36].

Table 5

PV converter	
Topology converter	Boost converter
Technic control	Two cascade PI controllers
Parameters control (kp, ki)	Voltage: (0,1131, 32) Current: (14,1421, 20000)

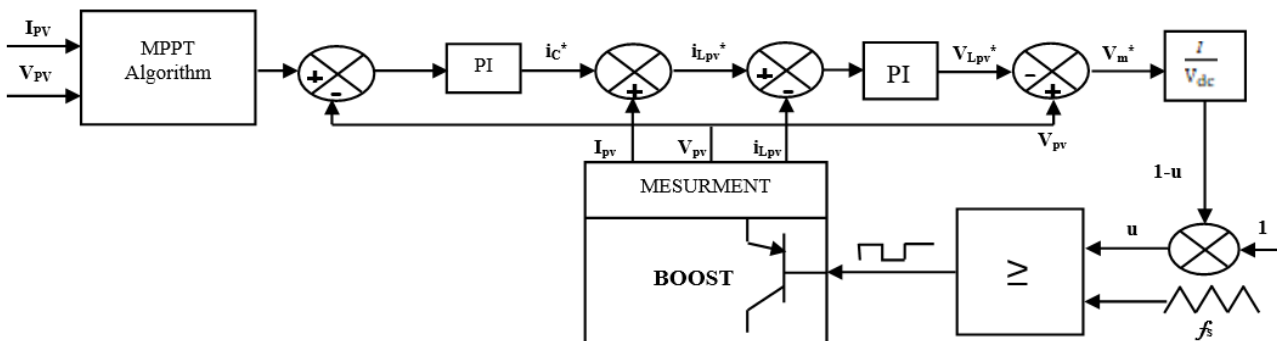


Fig. 8. CU from the duty cycle (u) to the voltage PV

**Battery charging/discharging current control.** For balancing power and regulating DC bus voltage, the battery pack is critical, the charging/discharging battery current is controlled in this study using a PI control

method. It is determined by the difference between the DC voltage's real and reference values [37-41]. The PI control technique for the battery charge/discharge operation is shown in Fig. 9.

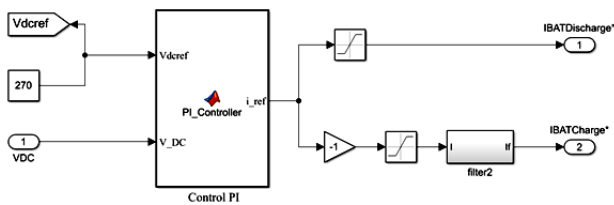


Fig. 9. Battery charge/discharge control approach based on PI

**Fuzzy logic controller for PEMFC system.** Instead of the usual true or false Boolean logic, the FLC is a control technique based on the level of truth (one or zero), fuzzification, fuzzy interface, and defuzzification are the basic control phases in fuzzy control [42-44]. The fuzzy IF/THEN rules are triggered to use the fuzzy interface for mapping the fuzzy values after the fuzzification technique changes the input values to fuzzy values, the defuzzification technique provides output values at the conclusion. As a control approach and in the application of systems optimization, fuzzy logic control is employed in hybrid power systems. The fuzzy logical control in this study contains two input variables and one output variable, where the input variables are excess demand power  $\Delta_d$  and SOC, and the output variable is the FC system reference power  $P_{fc\_ref}$ . The  $\Delta_d$  is divided into four zones to provide this fuzzy control: very small (VS), small (S), medium (M), and big (B). Similarly, the battery SOC is divided into 3 categories: low (L), when SOC is less than  $SOC_{min}$ ; good (G), when SOC is between 65 and 85; high (H), when SOC is greater than  $SOC_{max}$ .  $P_{fc\_ref}$ , like  $\Delta_d$ , is specified in 4 states, including VS, S, M, and B for the fuzzy output. Table 6 shows the rule foundation for the fuzzy logical control algorithm, which has 12 rules. Figures 10, *a-c* show the membership functions of the SOC,  $\Delta_d$ , and  $P_{fc\_ref}$ , respectively. The centroid method is used with Mamdani's fuzzy inference methodology for defuzzification.

The  $P_{fc\_ref}$  is the output of the system control level in the PEMFC generating system. FC system reference output current  $I_{fc\_ref}$  is then calculated by dividing the  $P_{fc\_ref}$  by the FC voltage, through Fig. 11, the FC current reference value based on the reference power. Finally, the output current of the DC/DC converter is adjusted to this value by a

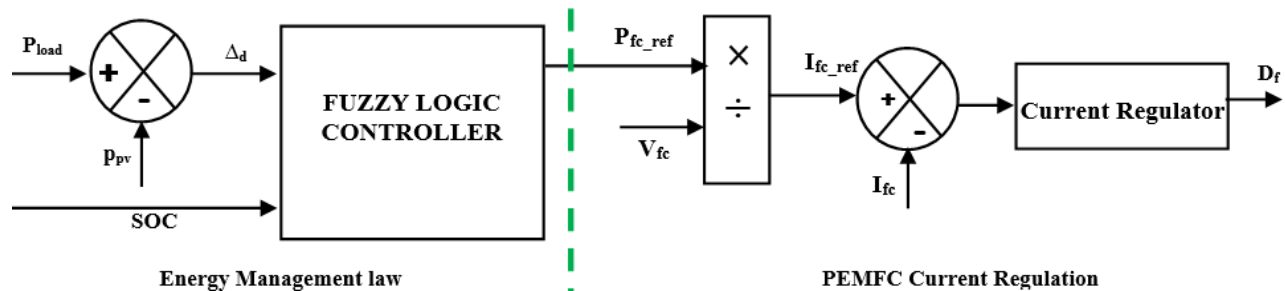


Fig. 11. PEMFC generating DC/DC converter control structure

**Results and discussion.** Throughout the simulation, in order to monitor and manage the operation of the proposed system at varying load values (ranging from around 0 to 14 kW) as shown in Fig. 12 the system is intended to provide sufficient power to a random three-phase dump load. In MATLAB/Simulink the suggested configuration and hybrid energy management system are developed and simulated for a total simulation period of 300 s.

current regulator [44-47]. Figure 12 depicts the control structure of the PEMFC generating DC/DC converter.

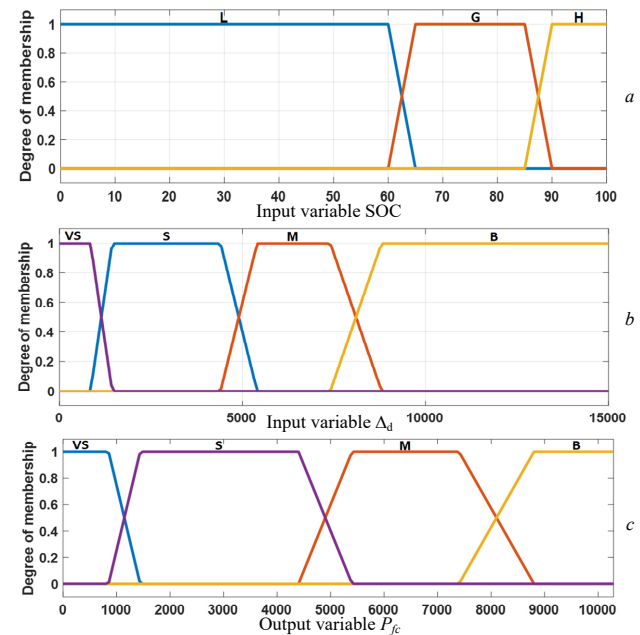


Fig. 10. *a* – battery SOC membership functions; *b* – surplus demand power membership functions  $\Delta_d$ ; *c* – FC power membership functions

Table 6  
Fuzzy logical control's rule basis

FL rules			
1	If SOC is H	And $\Delta_d$ is VS	Then $P_{fc\_ref}$ is VS
2	If SOC is H	And $\Delta_d$ is S	Then $P_{fc\_ref}$ is S
3	If SOC is H	And $\Delta_d$ is M	Then $P_{fc\_ref}$ is M
4	If SOC is H	And $\Delta_d$ is B	Then $P_{fc\_ref}$ is B
5	If SOC is G	And $\Delta_d$ is VS	Then $P_{fc\_ref}$ is VS
6	If SOC is G	And $\Delta_d$ is S	Then $P_{fc\_ref}$ is S
7	If SOC is G	And $\Delta_d$ is M	Then $P_{fc\_ref}$ is M
8	If SOC is G	And $\Delta_d$ is B	Then $P_{fc\_ref}$ is B
9	If SOC is L	And $\Delta_d$ is VS	Then $P_{fc\_ref}$ is S
10	If SOC is L	And $\Delta_d$ is S	Then $P_{fc\_ref}$ is M
11	If SOC is L	And $\Delta_d$ is M	Then $P_{fc\_ref}$ is B
12	If SOC is L	And $\Delta_d$ is B	Then $P_{fc\_ref}$ is B

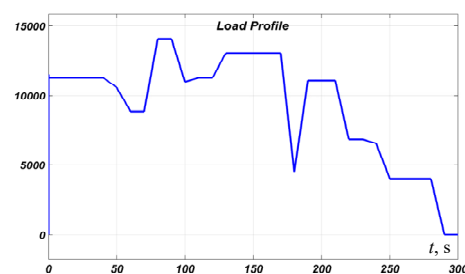


Fig. 12. Load profile

Figures 13-15 show the irradiation profile, PV current, and PV power consumed, respectively. The PV is assumed to be operating at a constant temperature of 25 °C, and about the irradiance value is designed to indicate meteorological conditions, solar intensity, nighttime, and whether or not shade is present.

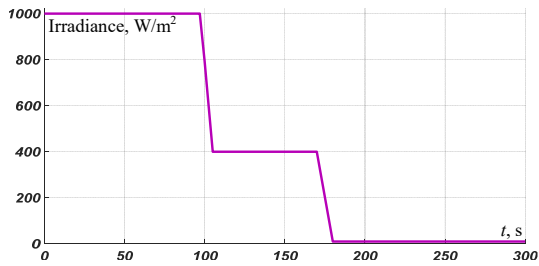


Fig. 13. Irradiation profile used throughout the simulation

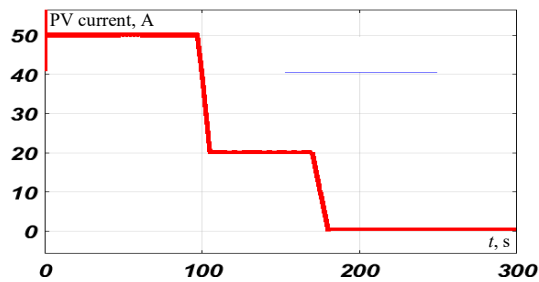


Fig. 14. PV current

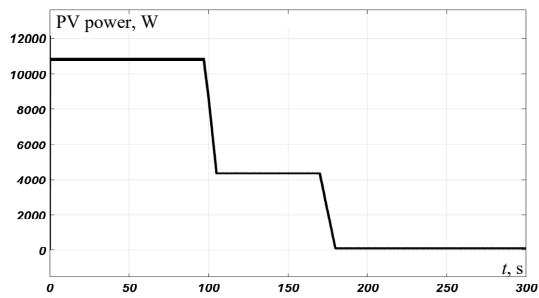


Fig. 15. PV power

The irradiance value is 1000 W/m<sup>2</sup> according to day light at the start (at 0 s) of the simulation period, with solar panels producing a maximum power of 10.8 kW, because the temperature  $T = 25$  °C is expected to be constant, during this time, the solar panels cover the load requirement of 11.08 kW with the aid of the FC's low power, and the battery maintains its initial SOC, which is 65 %. At 40 s, the PV power generated surpasses the load requirement, since the irradiance value remained constant at 1000 W/m<sup>2</sup> when the load power decreased, the excess PV power production is utilized to charge the battery and SC, in this instance, the PV power interferes in regulating and controlling of charging/discharging of the batteries, and also the regulation and controlling of the FC current, at the same time, the FC's power consumption is reduced. At 70 s, (there is no excess power since the load demand exceeds the PV power generated), the load power began to rise and the solar panels continue to produce the greatest amount of energy possible, it is insufficient to meet the load demand of 14 kW, because of its sluggish response of the FC and battery, the SC begins to supply the load with the required power (for its quick response).

At 98 s, and when the irradiance value falls to 400 W/m<sup>2</sup>, the amount of power generated by the PV

panels is decreasing, in this situation, the EMS calculates the difference between the load power and the PV power. And then the updated values of the FC current and battery charge/discharge current are determined. As both the PV, FC, and battery begin to provide power to the system based on the FC reference current and battery discharge current, the SC power is reduced, and the load power is provided mostly by the PV, FC, and battery, with the SC providing a small portion of the load power. The irradiance value drops to 0 W/m<sup>2</sup> after 180 s (the PV power is 0 W) and the load power began to decline once more, because of the charge/discharge responsiveness of the SC, the SC begins to give power to the load sooner than the FC and battery, the SC power is reduced once again, with the FC and battery providing the majority of the load power. At 220 s the load continues to decrease as the FC alone becomes sufficient to meet its demand. At 270 s, as the load continues to decrease, the FC covers the load requirement, in this situation the extra power is used to charge the battery once more. When this time period comes to a close, the load power is zero, and the FC provides power to charge the battery and the SC. Figure 16 depicts the performance of all power sources during the course of the simulation, from 0 to 300 s.

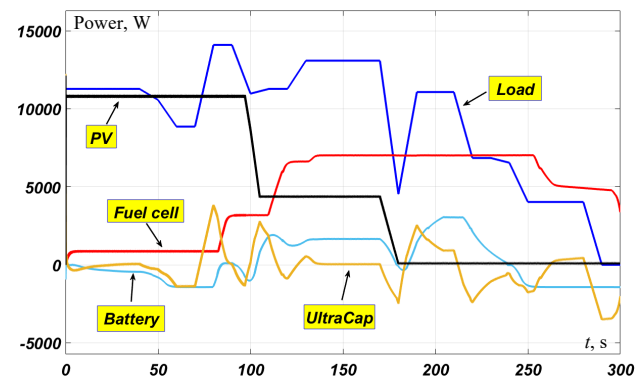


Fig. 16. Performance of all power sources

Figure 17,a depicts the battery's SOC percentage, which at the beginning of the simulation maintains its initial value of 65 %, and in the 40 s, through the lack of power demand for the load, through the lack of power demand for the load, the battery is charged through the excess solar panels power 65.5 %, and by raising the load's demand power, the battery is drained to support other power sources through the specified strategy of supplying the load with its required power until it reaches a value of 63.6 % at 170 s. The load increases again and the battery is discharged until it reaches its minimum value of 62.7 % at 280 s. At the end of the simulation, SOC % is increased to 63.5 % with decreasing load (300 s).

Figure 17,b depicts the battery's output power, battery power is represented negatively owing to the charging mode, then it becomes positive when the load rises and the battery begins to give power to the system. Figure 17,c depicts the battery voltage, whereas Fig. 17,d depicts the battery current. These 2 graphs illustrate that at maximum battery output power and maximum discharging current, the lowest battery voltage exists, and when the battery's output power and discharge current are at their lowest, the maximum battery voltage value exists.

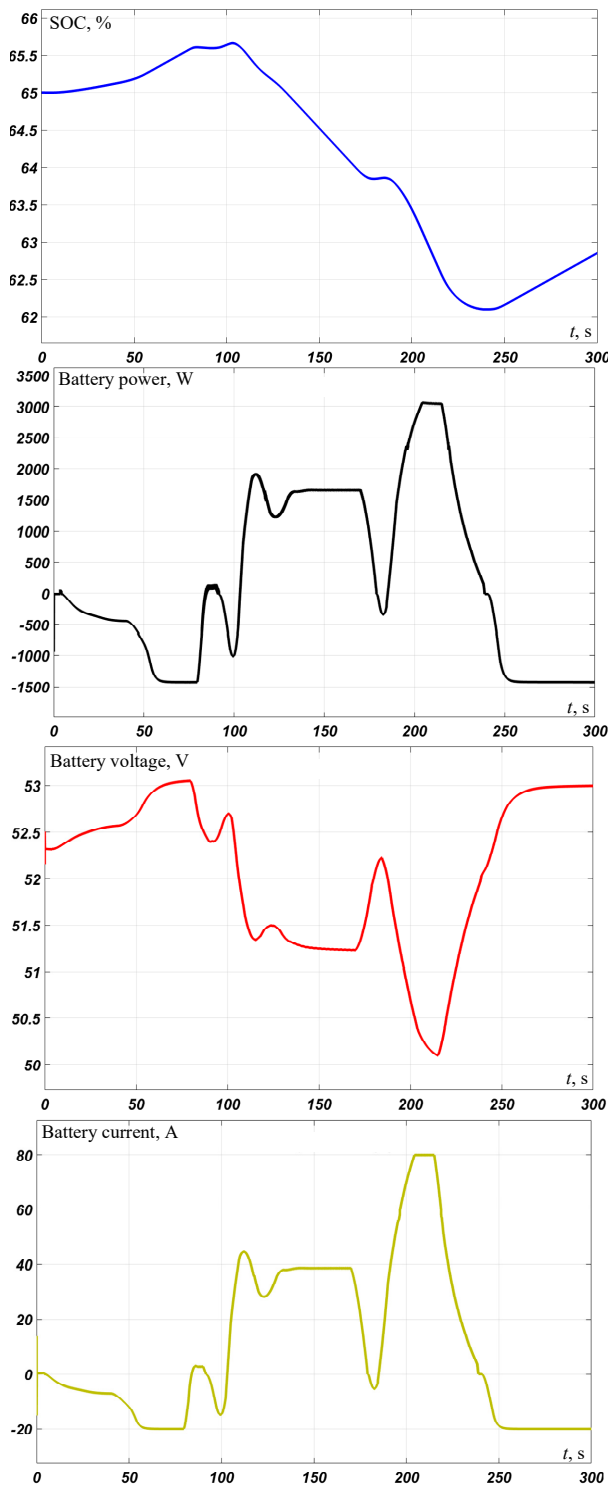


Fig. 17. a – battery SOC; b – battery power; c – battery voltage; d – battery current

Figure 18 depicts the FC values over 300 s (the simulation period). Figure 18,a illustrates the hydrogen fuel consumption, which reaches 27 g at the completion of the simulation. The fuel flow rate is shown in Fig. 18,b. The FC voltage and current are depicted in Fig. 18,c,d. The highest current FC is obtained at maximum load power, lowest SOC value, and minimal PV power (Fig. 18,e,f,g).

The findings of the rule-based fuzzy logics technique needed to be validated, for that we checked the H<sub>2</sub> consumption results and the battery's ultimate SOC from the energy management system, which is used to

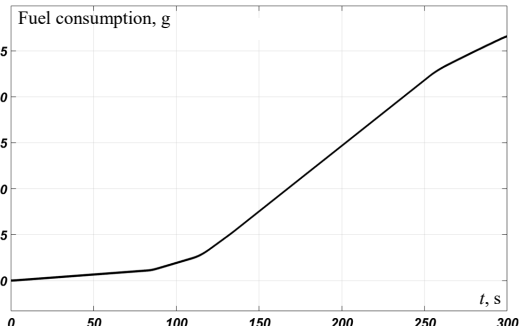
govern hybrid energy sources, this is accomplished by comparing these findings to the same results obtained in the same scenario but with the management flowchart of the REHPS. According to the current study, the flowchart of management in MATLAB function was set up with three inputs, which were  $P_{load}$ ,  $P_{PV}$ , and battery SOC, while the output was set to be the FC reference current.

a

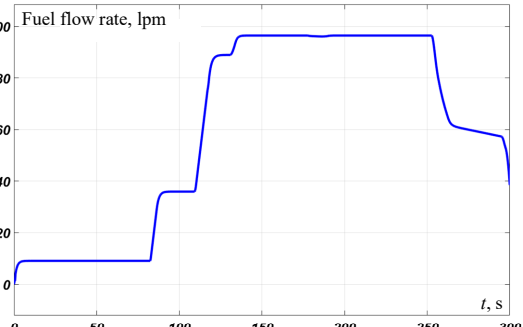
b

c

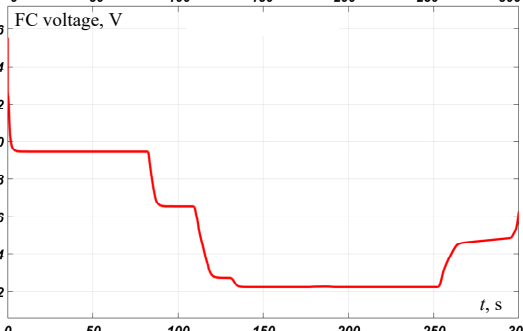
d



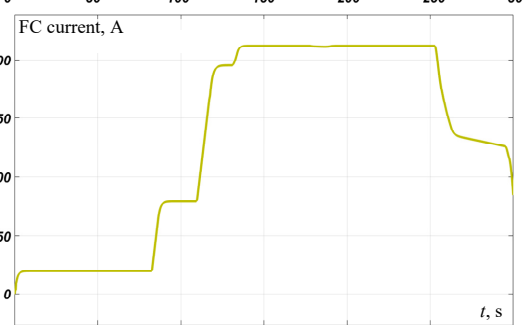
a



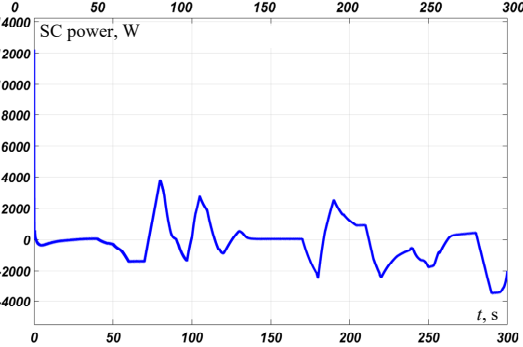
b



c



d



e

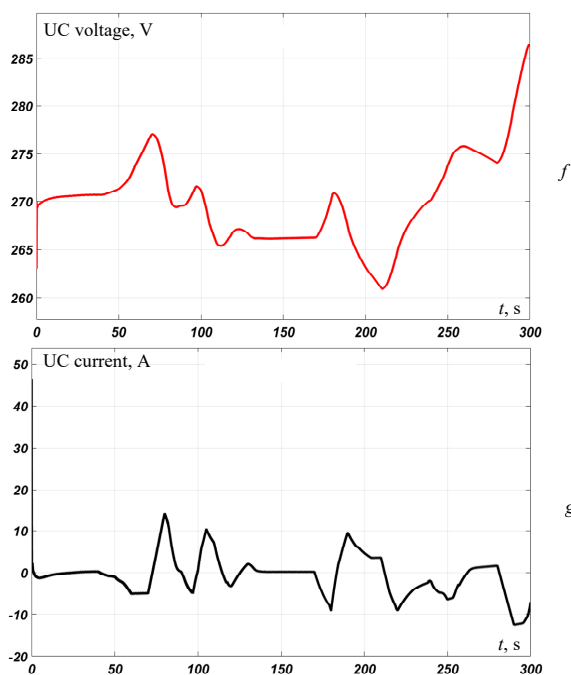


Fig. 18. *a* – hydrogen fuel consumption; *b* – fuel flow rate; *c* – FC voltage; *d* – FC current; *e* – SC power; *f* – UC voltage; *g* – UC current

Figures 19,*a,b* depict a comparison of 2 control techniques for SOC and hydrogen consumption. Table 7 shows the results of the comparison.

Table 7

Comparison among considered control strategies

Method	Fuzzy logic strategy	Management flowchart
Hydrogen consumption, g	26.5	29.1
SOC, %	[62.2-65]	[59.2-65]

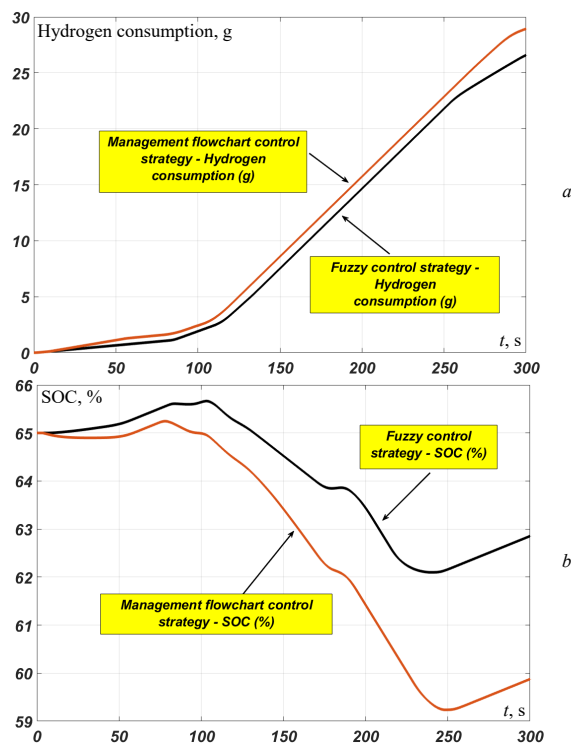


Fig. 19. *a* – comparison results H2 consumption; *b* – comparison results battery SOC

According to this study, the management flowchart control approach is the most hydrogen-consuming, while the fuzzy control strategy consumes the least. The fuzzy logic technique achieves low hydrogen consumption and a high SOC value at the same time, as well as a long life cycle and good overall system efficiency.

When compared to the management flowchart, which takes longer to charge, the fuzzy control method has a faster charge time. When it comes to discharging, fuzzy has a favorable outcome with less discharge time. On the other hand, management is quick to discharge.

**Conclusions.** It has become necessary to have an energy management system through the use of effective strategies to control and monitor the behavior and dynamics of hybrid energy sources. This paper presents the fuzzy control strategy for the power management of the hybrid renewable energy systems (photovoltaic/fuel cell/supercapacitor/battery), this hybrid power system is able to solve the lone source problem in addition to providing the load with the energy it needs with continuity and stability, PV provides the main power to the load and in case of shading and night, the fuel cell intervenes to meet the power shortage, and to solve the problem of slow response to fuel cell during the rapid change of load power we added the battery and supercapacitor to the system, which also maintains the stability of DC voltage at its reference value. The proposed strategy worked to reduce hydrogen consumption and improve the battery state of charge, proving the feasibility of the management technique proposed in this study, fair, and effective. Simulation results are developed in MATLAB/Simulink environment to demonstrate the effectiveness of the fuzzy control strategy performance in different loading conditions; the results prove that the fuzzy control strategy performs better than the management flowchart control strategy under the same operating conditions in terms of hydrogen consumption and battery state of charge. In this work, the values of simulation parameters were carefully selected for future practical investigation. In order to improve the system in future research, it is suggested to focus on exploiting the excess energy by using it in the production of hydrogen by connecting an electrolyzer, and there is always room to improve energy management strategies for more efficient performance.

**Conflict of interest.** The authors declare no conflict of interest.

#### REFERENCES

1. Abdelkareem M.A., El Haj Assad M., Sayed E.T., Soudan B. Recent progress in the use of renewable energy sources to power water desalination plants. *Desalination*, 2018, vol. 435, pp. 97-113. doi: <https://doi.org/10.1016/j.desal.2017.11.018>.
2. Rezk H., Sayed E.T., Al-Dhaifallah M., Obaid M., El-Sayed A.H.M., Abdelkareem M.A., Olabi A.G. Fuel cell as an effective energy storage in reverse osmosis desalination plant powered by photovoltaic system. *Energy*, 2019, vol. 175, pp. 423-433. doi: <https://doi.org/10.1016/j.energy.2019.02.167>.
3. Pelegov D., Pontes J. Main Drivers of Battery Industry Changes: Electric Vehicles – A Market Overview. *Batteries*, 2018, vol. 4, no. 4, art. no. 65. doi: <https://doi.org/10.3390/batteries4040065>.
4. Chmutina K., Wiersma B., Goodier C.I., Devine-Wright P. Concern or compliance? Drivers of urban decentralised energy initiatives. *Sustainable Cities and Society*, 2014, vol. 10, pp. 122-129. doi: <https://doi.org/10.1016/j.scs.2013.07.001>.

5. Apergis N., Payne J.E. Renewable and non-renewable energy consumption-growth nexus: Evidence from a panel error correction model. *Energy Economics*, 2012, vol. 34, no. 3, pp. 733-738. doi: <https://doi.org/10.1016/j.eneco.2011.04.007>.
6. Louarem S., Kebbab F.Z., Salhi H., Nouri H. A comparative study of maximum power point tracking techniques for a photovoltaic grid-connected system. *Electrical Engineering & Electromechanics*, 2022, no. 4, pp. 27-33. doi: <https://doi.org/10.20998/2074-272X.2022.4.04>.
7. Tarhan C., Çil M.A. A study on hydrogen, the clean energy of the future: Hydrogen storage methods. *Journal of Energy Storage*, 2021, vol. 40, art. no. 102676. doi: <https://doi.org/10.1016/j.est.2021.102676>.
8. Kong L., Yu J., Cai G. Modeling, control and simulation of a photovoltaic /hydrogen/ supercapacitor hybrid power generation system for grid-connected applications. *International Journal of Hydrogen Energy*, 2019, vol. 44, no. 46, pp. 25129-25144. doi: <https://doi.org/10.1016/j.ijhydene.2019.05.097>.
9. Abdelkareem M.A., Sayed E.T., Mohamed H.O., Obaid M., Rezk H., Chae K.-J. Nonprecious anodic catalysts for low-molecular-hydrocarbon fuel cells: Theoretical consideration and current progress. *Progress in Energy and Combustion Science*, 2020, vol. 77, art. no. 100805. doi: <https://doi.org/10.1016/j.pecs.2019.100805>.
10. da Silva Lima L., Quartier M., Buchmayr A., Sanjuan-Delmás D., Laget H., Corbisier-D., Mertens J., Dewulf J. Life cycle assessment of lithium-ion batteries and vanadium redox flow batteries-based renewable energy storage systems. *Sustainable Energy Technologies and Assessments*, 2021, vol. 46, art. no. 101286. doi: <https://doi.org/10.1016/j.seta.2021.101286>.
11. Zhao J., Burke A.F. Review on supercapacitors: Technologies and performance evaluation. *Journal of Energy Chemistry*, 2021, vol. 59, pp. 276-291. doi: <https://doi.org/10.1016/j.jechem.2020.11.013>.
12. Poonam, Sharma K., Arora A., Tripathi S.K. Review of supercapacitors: Materials and devices. *Journal of Energy Storage*, 2019, vol. 21, pp. 801-825. doi: <https://doi.org/10.1016/j.est.2019.01.010>.
13. Ferahtia S., Djeroui A., Mesbahi T., Houari A., Zeglache S., Rezk H., Paul T. Optimal Adaptive Gain LQR-Based Energy Management Strategy for Battery-Supercapacitor Hybrid Power System. *Energies*, 2021, vol. 14, no. 6, art. no. 1660. doi: <https://doi.org/10.3390/en14061660>.
14. Benmouna A., Becherif M., Boulon L., Dépature C., Ramadan H.S. Efficient experimental energy management operating for FC/battery/SC vehicles via hybrid Artificial Neural Networks-Passivity Based Control. *Renewable Energy*, 2021, vol. 178, pp. 1291-1302. doi: <https://doi.org/10.1016/j.renene.2021.06.038>.
15. Majumder I., Dash P.K., Dhar S. Real-time Energy Management for PV-battery-wind based microgrid using on-line sequential Kernel Based Robust Random Vector Functional Link Network. *Applied Soft Computing*, 2021, vol. 101, art. no. 107059. doi: <https://doi.org/10.1016/j.asoc.2020.107059>.
16. Ferahtia S., Djeroui A., Rezk H., Houari A., Zeglache S., Machmoum M. Optimal control and implementation of energy management strategy for a DC microgrid. *Energy*, 2022, vol. 238, art. no. 121777. doi: <https://doi.org/10.1016/j.energy.2021.121777>.
17. Kamel A.A., Rezk H., Abdelkareem M.A. Enhancing the operation of fuel cell-photovoltaic-battery-supercapacitor renewable system through a hybrid energy management strategy. *International Journal of Hydrogen Energy*, 2021, vol. 46, no. 8, pp. 6061-6075. doi: <https://doi.org/10.1016/j.ijhydene.2020.06.052>.
18. Sedaghati R., Shakarami M.R. A novel control strategy and power management of hybrid PV/FC/SC/battery renewable power system-based grid-connected microgrid. *Sustainable Cities and Society*, 2019, vol. 44, pp. 830-843. doi: <https://doi.org/10.1016/j.scs.2018.11.014>.
19. Paul A.L. *Electricity from Sunlight: An Introduction to Photovoltaics*. John Wiley & Sons, Ltd, 2010. 238 p.
20. Choudar A. *Gestion Locale de l'Energie et Commande Coordonnée d'un Générateur PV Actif Connecté à un Micro-Réseau Electrique Intelligent*. PhD Thesis, ENP Algiers, Algeria (2017). (Fra).
21. Larminie J., Dicks A. *Fuel Cell Systems Explained, 2nd ed.* John Wiley & Sons Ltd., Hoboken, NJ, USA, 2003. 418 p.
22. Gebregergis A., Pillay P., Rengaswamy R. PEMFC Fault Diagnosis, Modeling, and Mitigation. *IEEE Transactions on Industry Applications*, 2010, vol. 46, no. 1, pp. 295-303. doi: <https://doi.org/10.1109/TIA.2009.2036677>.
23. Maiti T.K., Singh J., Dixit P., Majhi J., Bhushan S., Bandyopadhyay A., Chattopadhyay S. Advances in perfluorosulfonic acid-based proton exchange membranes for fuel cell applications: A review. *Chemical Engineering Journal Advances*, 2022, vol. 12, art. no. 100372. doi: <https://doi.org/10.1016/j.cej.2022.100372>.
24. Bendjedja B., Rizoug N., Boukhnifer M., Bouchafaa F., Benbouzid M. Influence of secondary source technologies and energy management strategies on Energy Storage System sizing for fuel cell electric vehicles. *International Journal of Hydrogen Energy*, 2018, vol. 43, no. 25, pp. 11614-11628. doi: <https://doi.org/10.1016/j.ijhydene.2017.03.166>.
25. Wang N., Qu Z., Zhang G. Modeling analysis of polymer electrolyte membrane fuel cell with regard to oxygen and charge transport under operating conditions and hydrophobic porous electrode designs. *ETransportation*, 2022, vol. 14, art. no. 100191. doi: <https://doi.org/10.1016/j.etrans.2022.100191>.
26. Wilson D., Bousbaine A., Andrade J. Simulink model for a hydrogen pem fuel cell for automotive applications. *The 10th International Conference on Power Electronics, Machines and Drives (PEMD 2020)*, 2021, pp. 146-151. doi: <https://doi.org/10.1049/icp.2021.1176>.
27. Fernandez L.M., Garcia P., Garcia C.A., Torreglosa J.P., Jurado F. Comparison of control schemes for a fuel cell hybrid tramway integrating two DC/DC converters. *International Journal of Hydrogen Energy*, 2010, vol. 35, no. 11, pp. 5731-5744. doi: <https://doi.org/10.1016/j.ijhydene.2010.02.132>.
28. Chen W., Liang J., Yang Z., Li G. A Review of Lithium-Ion Battery for Electric Vehicle Applications and Beyond. *Energy Procedia*, 2019, vol. 158, pp. 4363-4368. doi: <https://doi.org/10.1016/j.egypro.2019.01.783>.
29. Lu L., Han X., Li J., Hua J., Ouyang M. A review on the key issues for lithium-ion battery management in electric vehicles. *Journal of Power Sources*, 2013, vol. 226, pp. 272-288. doi: <https://doi.org/10.1016/j.jpowsour.2012.10.060>.
30. Saw L.H., Somasundaram K., Ye Y., Tay A.A.O. Electro-thermal analysis of Lithium Iron Phosphate battery for electric vehicles. *Journal of Power Sources*, 2014, vol. 249, pp. 231-238. doi: <https://doi.org/10.1016/j.jpowsour.2013.10.052>.
31. Hassan Q., Jaszczur M., Al-Jiboory A.K., Hasan A., Mohamad A. Optimizing of hybrid renewable photovoltaic/wind turbine/super capacitor for improving self-sustainability. *Energy Harvesting and Systems*, 2022, vol. 9, no. 2, pp. 151-164. doi: <https://doi.org/10.1515/ehs-2021-0095>.
32. Hassan Q., Jaszczur M., Abdulateef A.M., Abdulateef J., Hasan A., Mohamad A. An analysis of photovoltaic/supercapacitor energy system for improving self-consumption and self-sufficiency. *Energy Reports*, 2022, vol. 8, pp. 680-695. doi: <https://doi.org/10.1016/j.egyvr.2021.12.021>.
33. Ren H., Wu Q., Gao W., Zhou W. Optimal operation of a grid-connected hybrid PV/fuel cell/battery energy system for residential applications. *Energy*, 2016, vol. 113, pp. 702-712. doi: <https://doi.org/10.1016/j.energy.2016.07.091>.
34. Ali Moussa M., Derrouazin A., Latroch M., Aillerie M. A hybrid renewable energy production system using a smart controller based on fuzzy logic. *Electrical Engineering & Electromechanics*, 2022, no. 3, pp. 46-50. doi: <https://doi.org/10.20998/2074-272X.2022.3.07>.
35. Guichi A., Mekhilef S., Berkouk E.M., Talha A. Optimal control of grid-connected microgrid PV-based source under partially shaded conditions. *Energy*, 2021, vol. 230, art. no. 120649. doi: <https://doi.org/10.1016/j.energy.2021.120649>.

36. Stroe D.-I., Zaharof A., Iov F. Power and Energy Management with Battery Storage for a Hybrid Residential PV-Wind System – A Case Study for Denmark. *Energy Procedia*, 2018, vol. 155, pp. 464-477. doi: <https://doi.org/10.1016/j.egypro.2018.11.033>.
37. Behrooz F., Mariun N., Marhaban M., Mohd Radzi M., Ramli A. Review of Control Techniques for HVAC Systems – Nonlinearity Approaches Based on Fuzzy Cognitive Maps. *Energies*, 2018, vol. 11, no. 3, art. no. 495. doi: <https://doi.org/10.3390/en11030495>.
38. Gassab S., Radjeai H., Mekhilef S., Choudar A. Power management and coordinated control of standalone active PV generator for isolated agriculture area-case study in the South of Algeria. *Journal of Renewable and Sustainable Energy*, 2019, vol. 11, no. 1, art. no. 015305. doi: <https://doi.org/10.1063/1.5064444>.
39. Han Y., Chen W., Li Q., Yang H., Zare F., Zheng Y. Two-level energy management strategy for PV-Fuel cell-battery-based DC microgrid. *International Journal of Hydrogen Energy*, 2019, vol. 44, no. 35, pp. 19395-19404. doi: <https://doi.org/10.1016/j.ijhydene.2018.04.013>.
40. Kadri A., Marzougui H., Aouiti A., Bacha F. Energy management and control strategy for a DFIG wind turbine/fuel cell hybrid system with super capacitor storage system. *Energy*, 2020, vol. 192, art. no. 116518. doi: <https://doi.org/10.1016/j.energy.2019.116518>.
41. Rezaei H., Abdollahi S.E., Abdollahi S., Filizadeh S. Energy management strategies of battery-ultracapacitor hybrid storage systems for electric vehicles: Review, challenges, and future trends. *Journal of Energy Storage*, 2022, vol. 53, art. no. 105045. doi: <https://doi.org/10.1016/j.est.2022.105045>.
42. Zhang Y., Wei W. Model construction and energy management system of lithium battery, PV generator, hydrogen production unit and fuel cell in islanded AC microgrid. *International Journal of Hydrogen Energy*, 2020, vol. 45, no. 33, pp. 16381-16397. doi: <https://doi.org/10.1016/j.ijhydene.2020.04.155>.
43. Zhang X., Liu L., Dai Y. Fuzzy State Machine Energy Management Strategy for Hybrid Electric UAVs with PV/Fuel Cell/Battery Power System. *International Journal of Aerospace Engineering*, 2018, pp. 1-16. doi: <https://doi.org/10.1155/2018/2852941>.
44. Tang D., Wang H. Energy Management Strategies for Hybrid Power Systems Considering Dynamic Characteristics of Power Sources. *IEEE Access*, 2021, vol. 9, pp. 158796-158807. doi: <https://doi.org/10.1109/ACCESS.2021.3131168>.
45. Shavelkin A.A., Gerlici J., Shvedchikova I.O., Kravchenko K., Kruhliak H.V. Management of power consumption in a photovoltaic system with a storage battery connected to the network with multi-zone electricity pricing to supply the local facility own needs. *Electrical Engineering & Electromechanics*, 2021, no. 2, pp. 36-42. doi: <https://doi.org/10.20998/2074-272X.2021.2.06>.
46. Choudar A., Boukhetala D., Barkat S., Brucker J.-M. A local energy management of a hybrid PV-storage based distributed generation for microgrids. *Energy Conversion and Management*, 2015, vol. 90, pp. 21-33. doi: <https://doi.org/10.1016/j.enconman.2014.10.067>.
47. Liao J., Jiang Y., Li J., Liao Y., Du H., Zhu W., Zhang L. An improved energy management strategy of hybrid photovoltaic/battery/fuel cell system for stratospheric airship. *Acta Astronautica*, 2018, vol. 152, pp. 727-739. doi: <https://doi.org/10.1016/j.actaastro.2018.09.007>.

Received 30.08.2022

Accepted 03.11.2022

Published 06.05.2023

Yahia Ayat<sup>1</sup>, PhD,

Abd Essalam Badoud<sup>1</sup>, Professor,

Saad Mekhilef<sup>2</sup>, Professor,

Samir Gassab<sup>1</sup>, Doctor of Electrical Engineering,

<sup>1</sup> Automatic Laboratory of Setif, Electrical Engineering Department, University of Ferhat Abbas Setif 1, Setif, 19000, Algeria,

e-mail: ayat.yahia@yahoo.com;

badoudabde@univ-setif.dz (Corresponding Author);

guessab.s@gmail.com

<sup>2</sup> School of Software and Electrical Engineering,

Department of Telecommunications, Electrical, Robotics and Biomedical Engineering,

Swinburne University of Technology, Melbourne, Australia,

e-mail: saad@um.edu.my

#### How to cite this article:

Ayat Y., Badoud A.E., Mekhilef S., Gassab S. Energy management based on a fuzzy controller of a photovoltaic/fuel cell/Li-ion battery/supercapacitor for unpredictable, fluctuating, high-dynamic three-phase AC load. *Electrical Engineering & Electromechanics*, 2023, no. 3, pp. 66-75. doi: <https://doi.org/10.20998/2074-272X.2023.3.10>

## Efficient method for transformer models implementation in distribution load flow matrix

**Introduction.** Most distribution networks are unbalanced and therefore require a specific solution for load flow. There are many works on the subject in the literature, but they mainly focus on simple network configurations. Among the methods dedicated to this problem, one can refer to the load flow method based on the bus injection to branch current and branch current to bus voltage matrices. **Problem.** Although this method is regarded as simple and complete, its drawback is the difficulty in supporting the transformer model as well as its winding connection types. Nevertheless, the method requires the system per unit to derive the load flow solution. **Goal.** In the present paper, our concern is the implementation of distribution transformers in the modeling and calculation of load flow in unbalanced networks. **Methodology.** Unlike previous method, distribution transformer model is introduced in the topology matrices without simplifying assumptions. Particularly, topology matrices were modified to take into account all winding types of both primary and secondary sides of transformer that conserve the equivalent scheme of an ideal transformer in series with an impedance. In addition, the adopted transformer models overcome the singularity problem that can be encountered when switching from the primary to the secondary side of transformer and inversely. **Practical value.** The proposed approach was applied to various distribution networks such as IEEE 4-nodes, IEEE 13-nodes and IEEE 37-nodes. The obtained results validate the method and show its effectiveness. References 24, tables 4, figures 9.

**Key words:** distribution systems, unbalanced load flow, distribution transformer models, topology network matrix.

**Вступ.** Більшість розподільчих мереж незбалансовані і тому потребують спеціального рішення для потоку навантаження. У літературі є багато робіт на цю тему, але переважно вони присвячені простим мережевим конфігураціям. Серед методів, присвячених цій проблемі, можна назвати метод потоку навантаження, заснований на введенні шини в матрицю струму відгалуження і відгалуження струму в матрицю напруги шини. **Проблема.** Хоча цей метод вважається простим та повним, його недоліком є складність підтримки моделі трансформатора, а також типів з'єднання його обмоток. Проте метод вимагає системи на одиницю для отримання рішення про потік навантаження. **Мета.** У цій статті нас цікавить застосування розподільних трансформаторів для моделювання та розрахунку потоку навантаження у незбалансованих мережах. **Методологія.** На відміну від попереднього методу, модель розподільного трансформатора вводиться в матриці топології без спрощення припущень. Зокрема, матриці топології були змінені, щоб врахувати всі типи обмоток як первинної, так і вторинної сторін трансформатора, які зберігають еквівалентну схему послідовно ідеально включеного трансформатора з імпедансом. Крім того, прийняті моделі трансформаторів долають проблему сингулярності, з якою можна зіткнутися при перемиканні з первинної на вторинну обмотку трансформатора і навпаки. **Практична цінність.** Пропонований підхід був застосований до різних розподільних мереж, таких як IEEE з 4 вузлами, IEEE з 13 вузлами та IEEE з 37 вузлами. Отримані результати підтверджують метод та показують його ефективність. Бібл. 24, табл. 4, рис. 9.

**Ключові слова:** розподільні системи, незбалансований потік навантаження, моделі розподільних трансформаторів, матриця топології мережі.

**Introduction.** Electrical distribution systems are generally unbalanced and therefore require special attention when solving the load flow problem for planning, operation and design studies [1, 2]. The power flow solution method must be robust and efficient to account for the characteristics of distribution systems, i.e., radial or weakly meshed configuration, unbalanced multi-phases, large number of branches and nodes, high R/X ratio. Such load flow method must be able to handle different distribution components with sufficient details, especially the distribution transformer (DT) models whatever its winding connections. Load flow algorithms in distribution networks can be classified into two types: The first class of methods is based on Newton-Raphson algorithms [3, 4]. This well-known approach uses three-phase current injection method in rectangular coordinates [5, 6]. In [7] the author presents a modified version of current injection method. Other linear forms are presented in [8, 9]. However, their application is far from being adapted in unbalanced networks and the incorporation of distribution transformer models in nodal admittance matrices has revealed their difficult application and inefficiency to converge due to the singularity problem [10]. Methods of the second type use the forward and backward sweeping (FBS) algorithms [11, 12]. They are based on Kirchhoff's laws. In this class of methods, branch numbering scheme is required for computing currents and node voltages that makes DT modelling, with various winding connection is difficult.

Beside the above mentioned load flow methods, other methods may also be used, such those based on special topological characteristics of distribution networks [13]. The work [14] introduced a new contribution to power flow solution, using the node incidence matrix and a complex vector based model in  $\alpha\beta 0$  stationary reference frame. The formulation of the admittance matrix in the  $\alpha\beta 0$  reference and the estimation of the initial network voltage profile complicate the calculation, especially for large networks. The most cited algorithms were referred to in [15-18]. They are based on three matrices namely, bus injection to branch current matrix (BIBC), branch current to bus voltage (BCBV) matrix and distribution load flow matrix (DLF). However, in the latter, DT models and other distribution components cannot be directly incorporated.

**The goal.** In this paper one proposes a method for unbalanced three-phase power flow solution which can handle DT regardless the type of its windings connection. DT models given by [19], which overcome the singularity problem, have been used. In the proposed load flow method, the BIBC and BCBV network topology matrices have been modified to incorporate DT whose equivalent scheme is branch impedance in series with ideal transformer taking into account the connection type of primary and secondary windings.

**The model of components. Distribution line.** Typical branch model of distribution lines is shown in Fig. 1, where the line to ground charging capacitance is

ignored. The self and mutual elements of the 3×3 phase-impedance matrix are determined by Carson's equations. For neutral distribution line, Kron reduction is used [19].

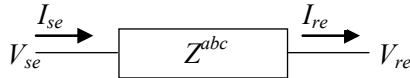


Fig. 1. Typical distribution line branch

From the line model given by Fig. 1, we can write:

$$V_{re} = V_{se} - \Delta V^{sr}; \quad (1)$$

$$\Delta V^{sr} = Z^{abc} I_{se}; \quad (2)$$

$$I_{re} = I_{se}, \quad (3)$$

where  $I_{se} = [I_{se}^a \ I_{se}^b \ I_{se}^c]^T$  and  $I_{re} = [I_{re}^a \ I_{re}^b \ I_{re}^c]^T$  are respectively the line current vectors at sending and receiving ends;  $V_{se} = [V_{se}^a \ V_{se}^b \ V_{se}^c]^T$  and  $V_{re} = [V_{re}^a \ V_{re}^b \ V_{re}^c]^T$  are respectively the line to ground voltage vectors at sending and receiving ends;  $\Delta V^{sr} = [\Delta V^{sa} \ \Delta V^{sb} \ \Delta V^{sc}]^T$  is the line voltages drop vector.

If there are no full phase components in the distribution system, the elements corresponding to the missed phases in the impedance matrix are set to zero.

**Load model.** In unbalanced three-phase distribution systems, the loads are specified by the power complex form. All the loads are assumed to be Wye or Delta connected and can be modeled as, constant power, constant current, constant impedance or any combination of the above cited models. Then, for a specified power  $S^{\varphi(sp)}$  and voltage  $V^\varphi$ , the equivalent load current injected into phase  $\varphi$  can be calculated by (4):

$$I_L^\varphi = \left( \frac{S^{\varphi(sp)}}{V^\varphi} \right)^*, \quad (4)$$

where  $\varphi = \{\varphi_1 \ \varphi_2 \ \varphi_3\}$  refers to phases  $\{a \ b \ c\}$  for Wye load or  $\{ab \ bc \ ca\}$  for Delta load. The load currents injected into the  $i^{\text{th}}$  bus are given by (5):

$$I_L^{\varphi_1\varphi_2\varphi_3} = \mathbf{D} \cdot \begin{bmatrix} I_L^{\varphi_1} \\ I_L^{\varphi_2} \\ I_L^{\varphi_3} \end{bmatrix}. \quad (5)$$

Depending on the load connection, Wye or Delta, the matrix  $\mathbf{D}$  is given by (6):

$$\mathbf{D} = \begin{cases} \mathbf{I} \text{ (identite matrix) for Wye load;} \\ \begin{bmatrix} 1 & 0 & -1 \\ -1 & 1 & 0 \\ 0 & -1 & 1 \end{bmatrix} \text{ for Delta load.} \end{cases} \quad (6)$$

For single phase and two phase-loads, the currents in the missed phases are set to zero.

**Distribution transformer.** Three-phase transformer is modeled by connecting three single-phase transformers, in which the transformer magnetizing currents are neglected. To convert the line-to-neutral voltages to phases voltages and the line currents to phases currents, the Wye or Delta windings connection shown in Fig. 2 [20, 21].

The branch equivalent model of a distribution transformer is as shown in Fig. 3.

On Fig. 3:  $I_s = [I_s^a \ I_s^b \ I_s^c]^T$  and  $I_p = [I_p^a \ I_p^b \ I_p^c]^T$  are respectively the secondary and primary line currents;  $V_s = [V_s^a \ V_s^b \ V_s^c]^T$  and  $V_p = [V_p^a \ V_p^b \ V_p^c]^T$  are respectively

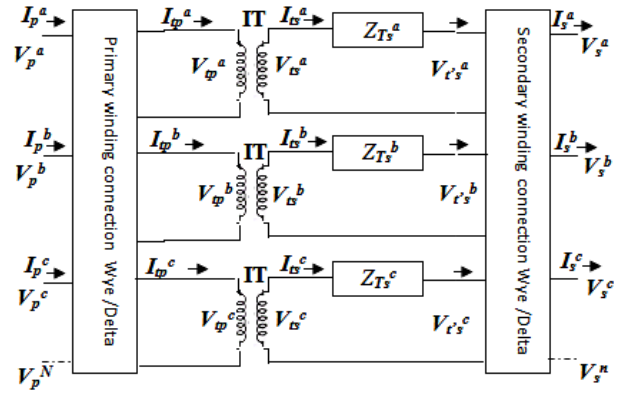


Fig. 2. Three-phase transformer scheme

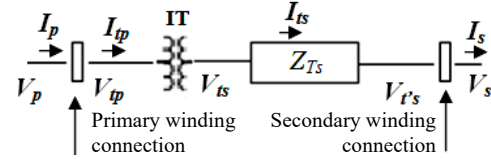


Fig. 3. Transformer simplified branch model

secondary and primary line-to-neutral voltages;  $I_{ts} = [I_{ts}^a \ I_{ts}^b \ I_{ts}^c]^T$  and  $V_{ts} = [V_{ts}^a \ V_{ts}^b \ V_{ts}^c]^T$  are the transformer secondary phase currents and voltages;  $V_{t's} = [V_{t's}^a \ V_{t's}^b \ V_{t's}^c]^T$  are the transformer secondary phase voltages without voltages drop;  $I_{tp} = [I_{tp}^a \ I_{tp}^b \ I_{tp}^c]^T$  and  $V_{tp} = [V_{tp}^a \ V_{tp}^b \ V_{tp}^c]^T$  are respectively the transformer primary phase currents and voltages;  $IT$  is the ideal transformer;  $Z_{T_s}$  is the secondary transformer impedance matrix given by:

$$\mathbf{Z}_{T_s} = \begin{bmatrix} Z_{T_s}^a & 0 & 0 \\ 0 & Z_{T_s}^b & 0 \\ 0 & 0 & Z_{T_s}^c \end{bmatrix}. \quad (7)$$

Using the DT equivalent branch shown in Fig. 3 and rearranging the accurate transformer equations given by [19], one can write the following equations.

**Current equations.** For the secondary and primary line currents, one can write the following relationships:

$$I_p = \mathbf{K}_I I_{ts}; \quad (8)$$

$$I_{ts} = \mathbf{K}_L I_s. \quad (9)$$

Substituting  $I_{ts}$  by its expression (9) into (8) leads to:

$$I_p = \mathbf{K}_I \mathbf{K}_L I_s, \quad (10)$$

where  $\mathbf{K}_I$  is the current transformation matrix. This matrix also takes into account the transition from  $I_{tp}$  to  $I_p$ . It is as given by Table 1.  $\mathbf{K}_L$  is the matrix transforming the secondary line currents into phase delta currents. It is equal to:

$$\mathbf{K}_L = \begin{cases} \mathbf{I} \text{ (identite matrix) for Wye connection;} \\ \frac{1}{3} \begin{bmatrix} 1 & -1 & 0 \\ 1 & 2 & 0 \\ -2 & -1 & 0 \end{bmatrix} \text{ for Delta connection.} \end{cases} \quad (11)$$

**Voltage equations.** The relations between secondary and primary line-to-neutral voltages can be obtained as:

$$V_{ts} = \mathbf{K}_v V_p; \quad (12)$$

$$V_{t's} = V_{ts} - \mathbf{Z}_{T_s} I_{ts}; \quad (13)$$

$$V_s = \mathbf{K}_w V_{t's}. \quad (14)$$

Table 1.  $K_I, K_L, K_v, K_w$  for some common industrial distribution transformers

Connection	Coefficients				
	$K_I$	$K_L$	$K_v$	$K_w$	$n_T$
YG-yg	$\frac{1}{n_T} \begin{bmatrix} 1 & 0 & 0 \\ 0 & 1 & 0 \\ 0 & 0 & 1 \end{bmatrix}$	$\begin{bmatrix} 1 & 0 & 0 \\ 0 & 1 & 0 \\ 0 & 0 & 1 \end{bmatrix}$	$\frac{1}{n_T} \begin{bmatrix} 1 & 0 & 0 \\ 0 & 1 & 0 \\ 0 & 0 & 1 \end{bmatrix}$	$\begin{bmatrix} 1 & 0 & 0 \\ 0 & 1 & 0 \\ 0 & 0 & 1 \end{bmatrix}$	$\frac{V_{LN}^{High Side}}{V_{LN}^{Low Side}}$
D-yg	$\frac{1}{n_T} \begin{bmatrix} 1 & -1 & 0 \\ 0 & 1 & -1 \\ -1 & 0 & 1 \end{bmatrix}$	$\begin{bmatrix} 1 & 0 & 0 \\ 0 & 1 & 0 \\ 0 & 0 & 1 \end{bmatrix}$	$\frac{1}{n_T} \begin{bmatrix} 1 & 0 & -1 \\ -1 & 1 & 0 \\ 0 & -1 & 1 \end{bmatrix}$	$\begin{bmatrix} 1 & 0 & 0 \\ 0 & 1 & 0 \\ 0 & 0 & 1 \end{bmatrix}$	$\frac{V_{LL}^{High Side}}{V_{LN}^{Low Side}}$
Y-d	$\frac{1}{n_T} \begin{bmatrix} 1 & 0 & 0 \\ 0 & 1 & 0 \\ 0 & 0 & 1 \end{bmatrix}$	$\frac{1}{2} \begin{bmatrix} 1 & -1 & 0 \\ 1 & 2 & 0 \\ -2 & -1 & 0 \end{bmatrix}$	$\frac{1}{n_T} \begin{bmatrix} 1 & 0 & 0 \\ 0 & 1 & 0 \\ 0 & 0 & 1 \end{bmatrix}$	$\frac{1}{2} \begin{bmatrix} 2 & 1 & 0 \\ 0 & 2 & 1 \\ 1 & 0 & 2 \end{bmatrix}$	$\frac{V_{LN}^{High Side}}{V_{LL}^{Low Side}}$
gY-d	$\frac{1}{n_T} \begin{bmatrix} 1 & 0 & 0 \\ 0 & 1 & 0 \\ 0 & 0 & 1 \end{bmatrix}$	$\frac{1}{2} \begin{bmatrix} 1 & -1 & 0 \\ 1 & 2 & 0 \\ -2 & -1 & 0 \end{bmatrix}$	$\frac{1}{n_T} \begin{bmatrix} 1 & 0 & 0 \\ 0 & 1 & 0 \\ 0 & 0 & 1 \end{bmatrix}$	$\frac{1}{2} \begin{bmatrix} 2 & 1 & 0 \\ 0 & 2 & 1 \\ 1 & 0 & 2 \end{bmatrix}$	$\frac{V_{LN}^{High Side}}{V_{LL}^{Low Side}}$
D-d	$\frac{1}{n_T} \begin{bmatrix} 1 & 0 & -1 \\ -1 & 1 & 0 \\ 0 & -1 & 1 \end{bmatrix}$	$\frac{1}{2} \begin{bmatrix} 1 & -1 & 0 \\ 1 & 2 & 0 \\ -2 & -1 & 0 \end{bmatrix}$	$\frac{1}{n_T} \begin{bmatrix} 1 & -1 & 0 \\ 0 & 1 & -1 \\ -1 & 0 & 1 \end{bmatrix}$	$\frac{1}{2} \begin{bmatrix} 2 & 1 & 0 \\ 0 & 2 & 1 \\ 1 & 0 & 2 \end{bmatrix}$	$\frac{V_{LL}^{High Side}}{V_{LL}^{Low Side}}$

Here  $V_{LN}$  is the rated-to-neutral voltage;  $V_{LL}$  is the rated line-to-line voltage.

Combining (12), (13) and (14), one can write:

$$V_s = K_w K_v V_p - K_w Z_{T3} K_L I_s, \quad (15)$$

where  $K_v$  is the voltage transformation matrix given in Table 1. It takes into account the primary winding connection type i.e. transition from  $V_p$  to  $V_p$ .  $K_w$  is the matrix which transforms the phase delta voltages to secondary line-to-neutral voltages. Like  $K_L, K_w$  matrix is given by:

$$K_w = \begin{cases} \mathbf{I} \text{ (identite matrix) for Wye connection;} \\ \frac{1}{3} \begin{bmatrix} 2 & 1 & 0 \\ 0 & 2 & 1 \\ 1 & 0 & 2 \end{bmatrix} \text{ for Delta connection.} \end{cases} \quad (16)$$

The relations (10) and (15) remain applicable regardless the transformer configuration even for those having voltage or current zero-sequence component interrupted like Wye-Delta and ground Wye-Delta.

**Proposed method.** Two basic topology matrices are required for solving three-phase power flow problem namely, bus injection currents to branch currents matrix  $B_I$  and the matrix  $B_v$  that links branch voltage drops to bus voltages mismatch. The currents and voltages relations are as given below:

$$I = B_I I_{bus}; \quad (17)$$

$$\Delta V_{bus} = B_v \Delta V. \quad (18)$$

To update bus voltages, the following equation, where  $V_{bus}^{nl}$  is the no-load bus voltage vector, is used:

$$V_{bus} = V_{bus}^{nl} - \Delta V_{bus}. \quad (19)$$

Combining (17) and (18) with Ohm's law given by (20), bus voltages mismatch  $\Delta V_{bus}$  given by (21) is derived.

$$\Delta V = ZI; \quad (20)$$

$$\begin{cases} \Delta V_{bus} = mDLF \cdot I_{bus}; \\ mDLF = B_v Z B_I. \end{cases} \quad (21)$$

Equations (21) are similar to those given in literature by the following equations [10, 18]:

$$\begin{cases} \Delta V_{bus} = DLF \cdot I_{bus}; \\ DLF = BCBV \cdot BIBC. \end{cases} \quad (22)$$

In the method given by [16], BCBV and BIBC matrices are built based on DT equivalent scheme given in Fig. 3. To simplify the modeling of the network and after decoupling the phases of the DT, one substituted the mutual impedances by injecting currents in the nodes. This leaves, in the model, only the DTs whose equivalent scheme is an ideal transformer in series with impedance. The trick used to rule out the ideal transformer is the per-unit system, which makes the ratio of the transformer equal to 1. Then, only the series impedance remains in the DT model. Unlike the method described above and governed by (22), in the proposed method whose mathematical model is given by (21), DTs are also substituted by their equivalent scheme of Fig. 3 without any simplifications. Matrices named  $B_I$  and  $B_v$ , the details of which are developed in the following sections, are then constructed. Thus, in (21), the mDLF matrix is the modified of version of the DLF matrix that appears in (22).

**$B_I$  and  $B_v$  matrices building.** The construction of  $B_I$  and  $B_v$  matrices is illustrated using the one-line diagram of the radial distribution system shown in Fig. 4 and where  $V_j$  is the substation voltage.

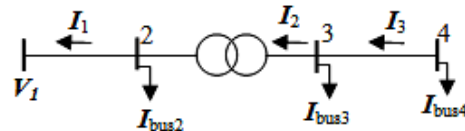


Fig. 4. Radial distribution network

**$B_I$  matrix building.** The  $B_I$  matrix building begin by calculating the bus injected currents  $I_{bus2}^{abc}$ ,  $I_{bus3}^{abc}$  and  $I_{bus4}^{abc}$  using (4) and (5) and integrating them in bus current vector  $I_{bus}$  as it is shown below:

$$I_{bus} = \begin{bmatrix} I_{bus2}^{abc} & I_{bus3}^{abc} & I_{bus4}^{abc} \end{bmatrix}. \quad (23)$$

Then, the relationships between bus currents and branch currents are determined using (3) and (10). They are as given below:

$$\begin{cases} \mathbf{I}_3^{abc} = \mathbf{I}_{bus4}^{abc}; \\ \mathbf{I}_2^{abc} = \mathbf{I}_{bus3}^{abc} + \mathbf{I}_{bus4}^{abc}; \\ \mathbf{I}_1^{abc} = \mathbf{I}_{bus2}^{abc} + \mathbf{K}_I \mathbf{K}_L \mathbf{I}_2^{abc}. \end{cases} \quad (24)$$

One can also write  $\mathbf{I}_I^{abc}$  in the following form:

$$\mathbf{I}_1^{abc} = \mathbf{I}_{bus2}^{abc} + \mathbf{K}_I \mathbf{K}_L \mathbf{I}_{bus3}^{abc} + \mathbf{K}_I \mathbf{K}_L \mathbf{I}_{bus4}^{abc}. \quad (25)$$

Equations (24) can also be rewritten in the following matrix form:

$$\begin{bmatrix} \mathbf{I}_1^{abc} \\ \mathbf{I}_2^{abc} \\ \mathbf{I}_3^{abc} \end{bmatrix} = \begin{bmatrix} \mathbf{I} & \mathbf{K}_I \mathbf{K}_L & \mathbf{K}_I \mathbf{K}_L \\ 0 & \mathbf{I} & \mathbf{I} \\ 0 & 0 & \mathbf{I} \end{bmatrix} \begin{bmatrix} \mathbf{I}_{bus2}^{abc} \\ \mathbf{I}_{bus3}^{abc} \\ \mathbf{I}_{bus4}^{abc} \end{bmatrix}. \quad (26)$$

This matrix form brings us to the relationship given by (17) and thereby one can deduce  $\mathbf{B}_I$  by identification:

$$\mathbf{B}_I = \begin{bmatrix} \mathbf{I} & \mathbf{K}_I \mathbf{K}_L & \mathbf{K}_I \mathbf{K}_L \\ 0 & \mathbf{I} & \mathbf{I} \\ 0 & 0 & \mathbf{I} \end{bmatrix}. \quad (27)$$

It is worth noting that 0 and  $\mathbf{I}$  in (27) are  $3 \times 3$  matrices.

**$\mathbf{B}_V$  matrix building.** To build  $\mathbf{B}_V$  matrix, one calculates first branch voltage drops. For the considered example (Fig. 4), the branch voltage drops are given as:

$$\begin{cases} \Delta V_1^{abc} = \mathbf{Z}_1^{abc} \mathbf{I}_1^{abc}; \\ \Delta V_2^{abc} = \mathbf{Z}_{Ts}^{abc} \mathbf{I}_2^{abc}; \\ \Delta V_3^{abc} = \mathbf{Z}_3^{abc} \mathbf{I}_3^{abc}, \end{cases} \quad (28)$$

where  $\mathbf{Z}_1^{abc}$ ,  $\mathbf{Z}_3^{abc}$  are the 1<sup>st</sup> and 3<sup>rd</sup> branch impedance matrices;  $\mathbf{Z}_{Ts}^{abc}$  is the 2<sup>nd</sup> branch impedance matrix transformer included.

In a matrix form, the (28) becomes:

$$\begin{bmatrix} \Delta V_1^{abc} \\ \Delta V_2^{abc} \\ \Delta V_3^{abc} \end{bmatrix} = \begin{bmatrix} \mathbf{Z}_1^{abc} & 0 & 0 \\ 0 & \mathbf{Z}_{Ts}^{abc} & 0 \\ 0 & 0 & \mathbf{Z}_3^{abc} \end{bmatrix} \begin{bmatrix} \mathbf{I}_1^{abc} \\ \mathbf{I}_2^{abc} \\ \mathbf{I}_3^{abc} \end{bmatrix}. \quad (29)$$

The identification of the matrix form (29) to that given by (20) allows us deducing the  $\mathbf{Z}$  matrix. As shown in (29), it should be pointed out that the full matrix  $\mathbf{Z}$  is built by gathering, on its diagonal, all branch impedance matrices.

After which, the branch to bus voltages are calculated according to (1) and (15). One can write in this case:

$$\begin{cases} \mathbf{V}_2^{abc} = \mathbf{V}_1^{abc} - \Delta V_1^{abc}; \\ \mathbf{V}_3^{abc} = \mathbf{K}_w \mathbf{K}_v \mathbf{V}_2^{abc} - \Delta V_2^{Tr(abc)}; \\ \mathbf{V}_4^{abc} = \mathbf{V}_3^{abc} - \Delta V_3^{abc}. \end{cases} \quad (30)$$

Combining the (30) gives:

$$\begin{bmatrix} \mathbf{V}_2^{abc} \\ \mathbf{V}_3^{abc} \\ \mathbf{V}_4^{abc} \end{bmatrix} = \begin{bmatrix} \mathbf{I} \\ \mathbf{K}_w \mathbf{K}_v \\ \mathbf{K}_w \mathbf{K}_v \end{bmatrix} \mathbf{V}_1^{abc} - \begin{bmatrix} \mathbf{I} & 0 & 0 \\ \mathbf{K}_w \mathbf{K}_v & \mathbf{I} & 0 \\ \mathbf{K}_w \mathbf{K}_v & \mathbf{I} & \mathbf{I} \end{bmatrix} \begin{bmatrix} \Delta V_1^{abc} \\ \Delta V_2^{Tr(abc)} \\ \Delta V_3^{abc} \end{bmatrix}. \quad (31)$$

Equation (31) can be stated in the following contracted form:

$$\mathbf{V}_{bus} = \mathbf{B}_{1v} \mathbf{V}_1 - \mathbf{B}_v \Delta V. \quad (32)$$

It is useful to note that  $\mathbf{B}_{1v}$  is the first column of  $\mathbf{B}_v$ . For the bus voltages initialization,  $\mathbf{V}_{bus}^{nl}$  is obtained by equalizing the (32) and (19). Its equation is below given:

$$\mathbf{V}_{bus}^{nl} = \mathbf{B}_{1v} \mathbf{V}_1. \quad (33)$$

**$\mathbf{B}_I$  and  $\mathbf{B}_V$  flowchart.** For large distribution networks with  $n$  buses and  $m$  branches the flowchart for matrices  $\mathbf{B}_V$  and  $\mathbf{B}_I$  building is presented in Fig. 5. Branch data are stored in four vectors,  $\mathbf{A}_s$  for sending-end buses,  $\mathbf{A}_r$  for the receiving-end buses,  $\mathbf{A}_I$  and  $\mathbf{A}_v$  for current and voltage transformation coefficients  $k_I$  and  $k_v$  respectively if the branches contains transformer. It can be seen that if the branch type (h) to be added in  $\mathbf{B}_I$  matrix is a line section, then, the column vector  $\mathbf{B}_I(:,s)$  is stored directly in  $\mathbf{B}_I(:,r)$ . But in the case of transformer the  $\mathbf{B}_I(:,s)$  need to be multiplied by the current transformation coefficient  $k_I$  before to be stored in  $\mathbf{B}_I(:,r)$ . In both cases  $\mathbf{B}_I(h,r)$  is set to 1. A similar procedure can be used for building  $\mathbf{B}_V$  but, by changing columns to rows and taking voltage transformation coefficient  $k_v$  for branch containing transformer.

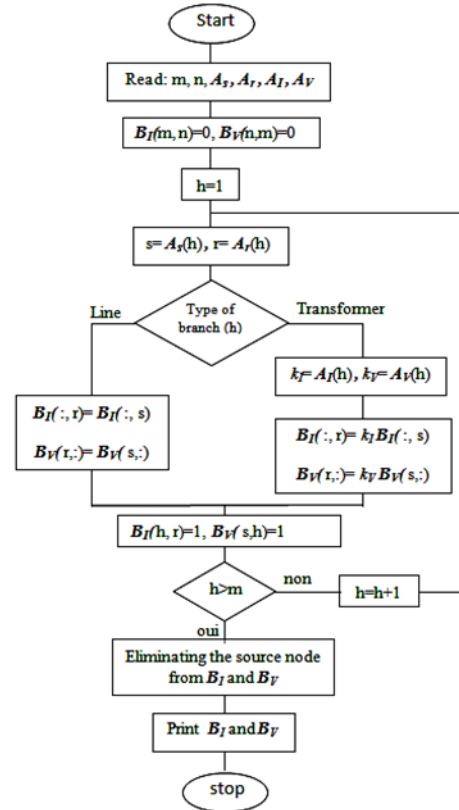


Fig. 5. Flowchart for  $\mathbf{B}_I$  and  $\mathbf{B}_V$  building for large distribution network

The proposed algorithm can easily be extended to a multiphase or multi-buses systems by expending the bus index  $i$  to vector  $(1 \times 3)$ . The corresponding 1 in  $\mathbf{B}_I$  or in  $\mathbf{B}_V$  matrices will be a  $3 \times 3$  identity matrix and the corresponding  $k_I$  and  $k_v$  are respectively substituted by  $\mathbf{K}_I$ ,  $\mathbf{K}_L$  and  $\mathbf{K}_v$ ,  $\mathbf{K}_w$  matrices. If there are non-full phase components in the distribution system, the matrix columns and rows corresponding to missed phase will be eliminated.

**Load flow algorithm.** The proposed algorithm can be summarized in the following steps:

- Step 1: Check the data and component modelling.
- Step 2: Form  $\mathbf{B}_I$  and  $\mathbf{B}_V$  matrices built using procedures described in previous section.
- Step 3: Assemble all branch impedance matrices in the full matrix  $\mathbf{Z}$  as in (29).
- Step 4: Determine the mDLF =  $\mathbf{B}_v \mathbf{Z} \mathbf{B}_I$  matrix using (21).
- Step 5: Initialize bus voltages using  $\mathbf{V}_{bus}^{nl} = \mathbf{B}_{1v} \mathbf{V}_1$  given by (33).

Step 6: while the convergence rate is not reached. Solve iteratively the following equations, which, at  $(k)^{\text{th}}$  iteration, are given by:

- Compute  $I_{Li}^{\varphi_1\varphi_2\varphi_3(k)}$  by (4) and (5) for a specified load and  $V_i^{(k)}$  at bus  $i$ ;
- assemble all  $I_{Li}^{\varphi_1\varphi_2\varphi_3(k)}$  in a vector  $I_{bus}^{(k)}$  as in (23);
- calculate  $\Delta V_{bus}^{(k)} = \text{mDLF } I_{bus}^{(k)}$  given by (21);
- determine  $V_{bus}^{(k+1)} = V_{bus}^{nl} - \Delta V_{bus}^{(k)}$  using (19).

Step 7: End while.

Step 8: Write the results.

Step 9: End.

As convergence criterion at  $(k+1)^{\text{th}}$  iteration, the following inequality, where  $\varepsilon$  is the convergence rate, fixed by user, is considered:

$$\max \left( \left| \Delta V_{bus}^{(k+1)} - \Delta V_{bus}^{(k)} \right| \right) \leq \varepsilon. \quad (34)$$

**Test results.** The load flow program was implemented using MATLAB. To validate the proposed method, the IEEE test networks stated by the Distribution Test Feeders Working Group, have been considered. Three test systems have been used in this work, it's about respectively the IEEE 4-bus, the IEEE 13-bus and the IEEE 37-bus networks.

The validation is first done for the IEEE 4-bus network the results of which are given in [23]. The obtained results

have also been compared to those given by GridLAB-D for the 4-nodes, 13-nodes and 37-nodes IEEE power systems. GridLAB-D is a distribution software based on FBS method, well explained in [22, 24], using line and transformer models available in [19] and which are the same as those we had considered.

**First test network.** The proposed method has first been applied to the IEEE 4-bus test feeder shown by Fig. 6. Four practice winding connections of a step-down transformer with unbalanced loads were considered. Standard  $30^\circ$  connections are assumed for Wye-Delta and Delta-Wye banks. The line-to-line infinite bus-source voltages are equal to  $[12.47\angle 0^\circ \ 12.47\angle -120^\circ \ 12.47\angle 120^\circ]^T$  kV. The obtained voltages for each phase of buses 2, 3 and 4 are as given by Table 2 and Table 3 which show that our results are in agreement with those given by both IEEE [23] and GridLAB-D. It is to be noted that this version of GridLAB-D doesn't support the Wye-Delta and ground Wye-Delta configurations. As shown by (19) and (33), the voltages of the various nodes are calculated with respect to that of the ground taken as reference. Thereby one don't need to update the transformer primary voltage when there is a zero-sequence components.

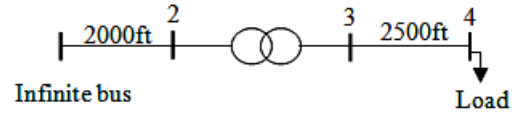


Fig. 6. IEEE4 bus test feeder

Table 2. IEEE 4-bus test feeder voltages comparison (IEEE results)

Connection	Node ID	$V^{\varphi_1}$ [Volt/°deg]		$V^{\varphi_2}$ [Volt/°deg]		$V^{\varphi_3}$ [Volt/°deg]	
		IEEE	Proposed method	IEEE	Proposed method	IEEE	Proposed method
gY-gY	2	7164/-0.1	7163.72/-0.14	7110/-120.2	7110.47/-120.18	7082/119.3	7082.05/119.26
	3	2305/-2.3	2305.53/-2.26	2255/-123.6	2254.71/-123.62	2203/114.18	2202.91/114.79
	4	2175/-4.1	2175.02/-4.12	1930/-126.8	1929.82/-126.79	1833/102.8	1832.86/102.85
D-gY	2	12350/29.6	12350.22/29.60	12314/-90.4	12313.83/-90.39	12333/149.8	12332.68/149.75
	3	2290/-32.4	2290.34/-32.39	2261/-153.8	2261.65/-153.81	2214/85.2	2214.05/85.18
	4	2157/-34.2	2156.90/-34.24	1936/-157.0	1936.16/-157.03	1849/73.4	1849.59/73.39
Y-D	2	7112/-0.2	7111.14/-0.20	7144/-120.4	7143.62/-120.43	7112/119.5	7111.11/119.54
	3	3896/-2.8	3896.39/-2.82	3972/-123.8	3972.17/123.82	3874/115.7	3875.16/115.70
	4	3425/-5.8	3425.54/-5.76	3646/-130.3	3646.38/-130.27	3298/108.6	3297.76/108.58
gY-D	2	7113/-0.2	7111.1/-0.2	3896/-2.8	3896.4/-2.82	3425/-5.8	3425.5/-5.76
	3	7144/-120.4	7143.6/-120.4	3972/-123.8	3972.2/-123.82	3646/-130.3	3646.4/-130.28
	4	7111/119.5	7111.1/119.54	3875/115.7	3875.2/115.7	3298/108.6	3297.8/108.58
D-D	2	12341/29.8	12341.02/29.81	12370/-90.5	12370.28/-90.48	12302/149.5	12301.78/149.55
	3	3902/27.2	3901.86/27.20	3972/-93.9	3972.54/-93.91	3871/145.7	3871.49/145.74
	4	3431/24.3	3430.79/24.28	3647/-100.4	3647.53/-100.36	3294/138.6	3293.82/138.62

$\varphi = \{\varphi_1 \ \varphi_2 \ \varphi_3\} = \{\{ag, bg, cg\} \text{ or } \{ab, bc, ca\}\}; a, b, c: \text{phases, g: ground}$

Table 3. IEEE 4-bus test feeder voltages comparison (GridLAB-D results)

Connection	Node ID	$V^{\varphi_1}$ [Volt/°deg]		$V^{\varphi_2}$ [Volt/°deg]		$V^{\varphi_3}$ [Volt/°deg]	
		Proposed method	GridLab-D	Proposed method	GridLab-D	Proposed method	GridLab-D
gY-gY	2	7163.72/-0.14	7163.7/-0.14	7110.47/-120.18	7110.5/-120.18	7082.05/119.26	7082/119.26
	3	2305.53/-2.26	2305.5/-2.26	2254.71/-123.62	2254.7/-123.62	2202.91/114.79	2202.8/114.79
	4	2175.02/-4.12	2175/-4.12	1929.82/-126.79	1929.8/-126.8	1832.86/102.85	1832.7/102.85
D-gY	2	12350.22/29.60	12350/29.6	12313.83/-90.39	12314/-90.4	12332.68/149.75	12333/149.8
	3	2290.34/-32.39	2290.3/-32.39	2261.65/-153.81	2261.65/-135.8	2214.05/85.18	2213.9/85.2
	4	2156.90/-34.24	2156.9/-34.24	1936.16/-157.03	1936.1/-157.0	1849.59/73.39	1849.4/73.4
Y-D	2	7111.14/-0.20	CHTC	7143.62/-120.43	CHTC	7111.11/119.54	CHTC
	3	3896.39/-2.82	CHTC	3972.17/123.82	CHTC	3875.16/115.70	CHTC
	4	3425.54/-5.76	CHTC	3646.38/-130.27	CHTC	3297.76/108.58	CHTC
gY-D	2	7111.1/-0.2	CHTC	3896.4/-2.82	CHTC	3425.5/-5.76	CHTC
	3	7143.6/-120.4	CHTC	3972.2/-123.82	CHTC	3646.4/-130.28	CHTC
	4	7111.1/119.54	CHTC	3875.2/115.7	CHTC	3297.8/108.58	CHTC
D-D	2	12341.02/29.81	12341/29.8	12370.28/-90.48	12370.3/-90.5	12301.78/149.55	12301.7/149.5
	3	3901.86/27.20	3901.8/27.2	3972.54/-93.91	3972.5/-93.9	3871.49/145.74	3871.5/145.7
	4	3430.79/24.28	3430.7/24.3	3647.53/-100.36	3647.5/-100.4	3293.82/138.62	3293.8/138.6

$\varphi = \{\varphi_1 \ \varphi_2 \ \varphi_3\} = \{\{ag, bg, cg\} \text{ or } \{ab, bc, ca\}\}; a, b, c: \text{phases, g: ground; CHTC - cannot handle this configuration}$

**Second test network.** The second network considered is the IEEE 13-bus test system which originally contains variety of components such as cables and lines with various configurations and only one transformer at node 633. As shown by Fig. 7, this test system has been modified by excluding the regulator at substation and the distributed load on line 632-671. A second transformer has been added to the line 671-680. The results given by the proposed method have been compared to those obtained using GridLAB-D program. The results in Table 4 validate the proposed method and demonstrate its good level of accuracy.

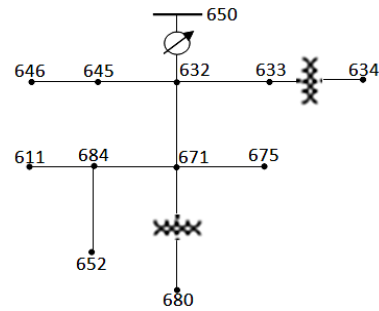


Fig. 7. IEEE 13-bus test feeders

Table 4. Voltages results of IEEE 13-bus test feeder

Node ID	$V^{\varphi_1}$ [Volt/°deg]		$V^{\varphi_2}$ [Volt/°deg]		$V^{\varphi_3}$ [Volt/°deg]	
	Proposed method	GridLab-D	Proposed method	GridLab-D	Proposed method	GridLab-D
650	2401.8/0.0	2401.8/0.0	2401.8/-120	2401.8/-120	2401.8/120	2401.8/120
632	2286.2/-2.06	2286.2/-2.06	2335.7/-122.09	2335.7/-122.09	2306.9/118.29	2306.9/118.29
671	2201.5/-4.98	2201.6/-4.98	2341.7/-122.68	2341.7/-122.68	2200.6/116.91	2200.6/116.91
680	256.36/-34.02	256.36/-34.02	259.07/-152.76	259.07/-152.76	262.62/86.09	262.62/86.09
633	2277.8/-2.15	2278.4/-2.14	2330.2/-122.13	2330.8/-122.14	2301.3/118.27	2300.2/118.29
634	255.67/-2.93	255.73/-2.92	263.4/-122.65	263.48/-122.67	260/117.74	259.86/117.75
645	-	-	2301.3/-122.28	2301.2/-122.28	2315.2/118.18	2315.1/118.18
646	-	-	2290.4/-122.35	2290.3/-122.36	2318/118.15	2317.8/118.15
675	2181.6/-5.15	2181.6/-5.15	2344.4/-122.78	2344.4/-122.78	2191.7/117.02	2191.7/117.02
684	2197.4/-4.99	2197.5/-4.99	-	-	2195.7/116.8	2195.7/116.8
611	-	-	-	-	2190.9/116.64	2190.9/116.63
652	2180.5/-4.99	2180.3/-5.01	-	-	-	-

- missed phases

**Third test network.** The third test feeder is the IEEE 37-bus network where voltage regulator and distributed load are discarded. As shown by Fig. 8, this network includes four down-step transformers located at nodes 702, 703, 709 and 737.

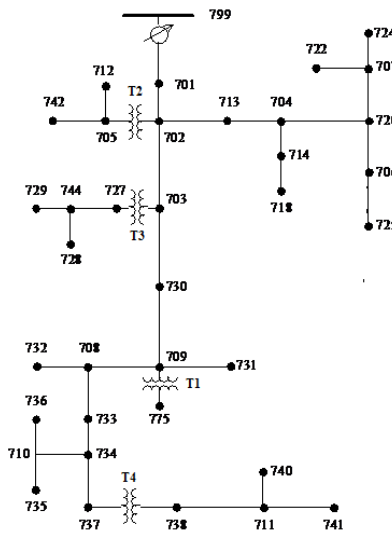


Fig. 8. IEEE 37-bus test feeders

Voltage profiles given by both proposed method and GridLAB-D are shown by Fig. 9,a,b. Figure 9,a shows voltage-profiles for nodes located at transformers primary-sides, the line-to-line voltage magnitudes of which is between 4.55 kV and 4.58 kV. Figure 9,b, on the other hand, gives voltage-profiles for nodes located at transformers secondary-sides whose line-to-line voltage magnitudes are between 360 V and 480 V. These figures show that the voltage profile obtained by the proposed method agree with that given by GridLAB-D.

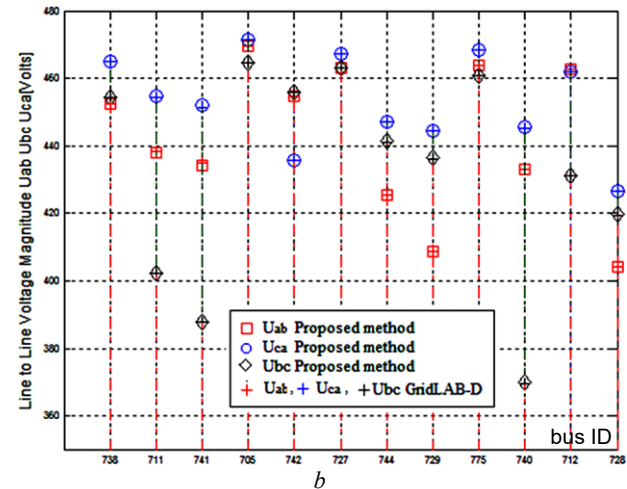
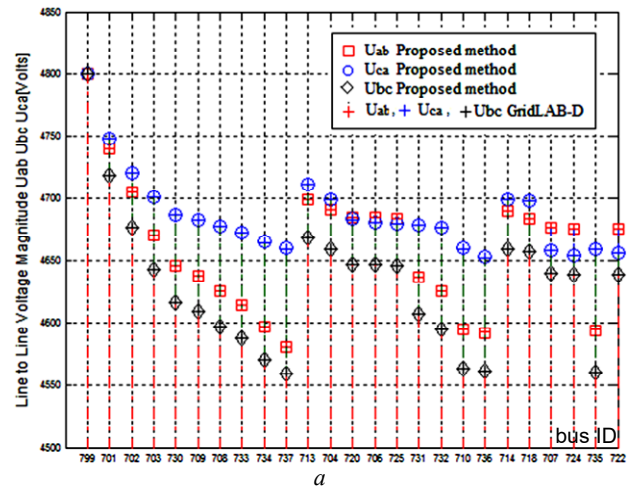


Fig. 9. Proposed method and GridLAB-D voltage profiles for IEEE 37-bus: a – voltages of nodes situated before transformers; b – voltages of nodes situated at transformers secondary side

**Conclusions.** In this paper, the well-known matrices bus injection to branch current and branch current to bus voltage have been modified and led to new matrices. The latter support all practical transformer models and configuration types. No assumptions are made using these new matrices. One can use either real values or per-unit system for the network parameters. Based on an elaborate flowchart of topological matrix construction, the proposed power flow method is validated by comparing the results obtained with those given by the GridLAB-D program for three IEEE test systems. It has been shown that the proposed method is efficient, can handle different distribution components and can be extended to large and complex balanced and unbalanced distribution networks.

**Conflict of interest.** The authors declare no conflict of interest.

#### REFERENCES

- Rahmani A., Slimani L., Bouktir T. Unbalanced load flow with hybrid wavelet transform and support vector machine based error-correcting output codes for power quality disturbances classification including wind energy. *Electrical Engineering & Electromechanics*, 2019, no. 6, pp. 62-69. doi: <https://doi.org/10.20998/2074-272X.2019.6.09>.
- Djabali C., Bouktir T. Simultaneous allocation of multiple distributed generation and capacitors in radial network using genetic-salp swarm algorithm. *Electrical Engineering & Electromechanics*, 2020, no. 4, pp. 59-66. doi: <https://doi.org/10.20998/2074-272X.2020.4.08>.
- Jangra J., Vadhera S. Load flow analysis for three phase unbalanced distribution feeders using Matlab. *2017 2nd International Conference for Convergence in Technology (I2CT)*, 2017, pp. 862-866. doi: <https://doi.org/10.1109/I2CT.2017.8226252>.
- Sameni A., Nassif A.B., Opathella C., Venkatesh B. A modified Newton-Raphson method for unbalanced distribution systems. *2012 International Conference on Smart Grid (SGE)*, 2012, pp. 1-7. doi: <https://doi.org/10.1109/SGE.2012.6463955>.
- De Vas Gunawardena A.P.S.G., Ranatunga N.T., Samarathunga L.L., Weerawansa S.D.T., Jayatunga U. Three phase asymmetrical power flow algorithm using current injection technique. *2016 Electrical Engineering Conference (EECon)*, 2016, pp. 37-42. doi: <https://doi.org/10.1109/EECon.2016.7830932>.
- Kumar A., Jha B.K., Singh D., Misra R.K. A New Current Injection Based Power Flow Formulation. *Electric Power Components and Systems*, 2020, vol. 48, no. 3, pp. 268-280. doi: <https://doi.org/10.1080/15325008.2020.1758846>.
- Ahmadi H., Marti J.R., von Meier A. A Linear Power Flow Formulation for Three-Phase Distribution Systems. *IEEE Transactions on Power Systems*, 2016, vol. 31, no. 6, pp. 5012-5021. doi: <https://doi.org/10.1109/TPWRS.2016.2533540>.
- Wang Y., Zhang N., Li H., Yang J., Kang C. Linear three-phase power flow for unbalanced active distribution networks with PV nodes. *CSEE Journal of Power and Energy Systems*, 2017, vol. 3, no. 3, pp. 321-324. doi: <https://doi.org/10.17775/CSEEJPES.2017.00240>.
- Garces A. A Linear Three-Phase Load Flow for Power Distribution Systems. *IEEE Transactions on Power Systems*, 2016, vol. 31, no. 1, pp. 827-828. doi: <https://doi.org/10.1109/TPWRS.2015.2394296>.
- Bazrafshan M., Gatsis N. Comprehensive Modeling of Three-Phase Distribution Systems via the Bus Admittance Matrix. *IEEE Transactions on Power Systems*, 2018, vol. 33, no. 2, pp. 2015-2029. doi: <https://doi.org/10.1109/TPWRS.2017.2728618>.
- Petridis S., Blanas O., Rakopoulos D., Stergiopoulos F., Nikolopoulos N., Voutetakis S. An Efficient Backward/Forward Sweep Algorithm for Power Flow Analysis through a Novel Tree-Like Structure for Unbalanced Distribution Networks. *Energies*, 2021, vol. 14, no. 4, art. no. 897. doi: <https://doi.org/10.3390/en14040897>.
- Samal P., Ganguly S. A modified forward backward sweep load flow algorithm for unbalanced radial distribution systems. *2015 IEEE Power & Energy Society General Meeting*, 2015, pp. 1-5. doi: <https://doi.org/10.1109/PESGM.2015.7286413>.
- Segura S., da Silva L.C.P., Romero R. Generalised single-equation load flow method for unbalanced distribution systems. *IET Generation, Transmission & Distribution*, 2011, vol. 5, no. 3, art. no. 347. doi: <https://doi.org/10.1049/iet-gtd.2010.0204>.
- González-Morán C., Arboleya P., Mohamed B. Matrix Backward Forward Sweep for Unbalanced Power Flow in  $\alpha\beta 0$  frame. *Electric Power Systems Research*, 2017, vol. 148, pp. 273-281. doi: <https://doi.org/10.1016/j.epr.2017.03.026>.
- Balamurugan K., Srinivasan D. Review of power flow studies on distribution network with distributed generation. *2011 IEEE Ninth International Conference on Power Electronics and Drive Systems*, 2011, pp. 411-417. doi: <https://doi.org/10.1109/PEDS.2011.6147281>.
- Subrahmanyam J.B.V., Radhakrishna C., Pandukumar K. A simple and direct approach for unbalanced radial distribution system three phase load flow solution. *Research Journal of Applied Sciences, Engineering and Technology*, 2010, vol. 2, no. 5, pp. 452-459.
- Abul'Wafa A.R. A network-topology-based load flow for radial distribution networks with composite and exponential load. *Electric Power Systems Research*, 2012, vol. 91, pp. 37-43. doi: <https://doi.org/10.1016/j.epr.2012.04.016>.
- Şeker A.A., Gözel T., Hocaoglu M.H. BIBC Matrix Modification for Network Topology Changes: Reconfiguration Problem Implementation. *Energies*, 2021, vol. 14, no. 10, art. no. 2738. doi: <https://doi.org/10.3390/en14102738>.
- Kersting W.H. *Distribution System Modeling and Analysis*. 4th Ed. CRC Press, 2017. 546 p.
- Dugan R.C. A perspective on transformer modeling for distribution system analysis. *2003 IEEE Power Engineering Society General Meeting (IEEE Cat. No.03CH37491)*, 2003, pp. 114-119. doi: <https://doi.org/10.1109/PES.2003.1267146>.
- Chen T.-H., Chen M.-S., Inoue T., Kotas P., Chebli E.A. Three-phase cogenerator and transformer models for distribution system analysis. *IEEE Transactions on Power Delivery*, 1991, vol. 6, no. 4, pp. 1671-1681. doi: <https://doi.org/10.1109/61.97706>.
- Schneider K.P., Chassin D., Chen Y., Fuller J.C. Distribution power flow for smart grid technologies. *2009 IEEE/PES Power Systems Conference and Exposition*, 2009, pp. 1-7. doi: <https://doi.org/10.1109/PSCE.2009.4840078>.
- IEEE PES Test Feeder. Available at: <https://cmte.ieee.org/pes-testfeeders/> (Accessed 22.05.2022).
- GridLAB-D. Available at: <https://sourceforge.net/projects/gridlab-d/> (Accessed 22.05.2022).

Received 15.08.2022  
Accepted 13.11.2022  
Published 06.05.2023

M. Kadri<sup>1</sup>, Associate Professor of Electrical Engineering,  
A. Hamouda<sup>2</sup>, Doctor of Electrical Engineering, Professor  
S. Sayah<sup>1</sup>, Doctor of Electrical Engineering, Professor,  
<sup>1</sup>Department of Electrical Engineering, QUERE Laboratory,  
Farhat Abbas University, Setif 1, 19000, Algeria,  
e-mail: kadri\_moussa@yahoo.fr;  
samir.sayah@univ-setif.dz (Corresponding Author)  
<sup>2</sup>Optics and Precision Mechanics Institute, QUERE Laboratory,  
Farhat Abbas University, Setif 1, 19000, Algeria,  
e-mail: a\_hamouda1@yahoo.fr

#### How to cite this article:

Kadri M., Hamouda A., Sayah S. Efficient method for transformer models implementation in distribution load flow matrix. *Electrical Engineering & Electromechanics*, 2023, no. 3, pp. 76-82. doi: <https://doi.org/10.20998/2074-272X.2023.3.11>

G. Srinivasan, V. Mahesh Kumar Reddy, P. Venkatesh, E. Parimalasundar

## Reactive power optimization in distribution systems considering load levels for economic benefit maximization

**Introduction.** The need for electrical energy has been increased sharply due to hasty growth in industrials, social and economic improvements. From the previous studies, it has been agreed that almost 13 % of the total power generated is wasted as heat loss at distribution level. It has been extensively recognized that the node voltage profile along the distribution system can be enhanced under steady state power transfer controlled by proper reactive power compensation. Capacitors have been acknowledged as reactive power compensating device in distribution systems to achieve technical and economical benefits. **Novelty** of this work is the application of Archimedes optimization algorithm for reactive power optimization in distribution systems so as to obtain an improved solution and also a real 94-bus Portuguese network and modified 12-bus network has been taken and validated for three different load levels which are totally new. **Purpose** of the proposed work is to maximize the economic benefit by reducing the power loss and capacitor purchase cost at three different load conditions subject to satisfaction of equality and inequality constraints. **Methods.** The economic benefit has been validated using Archimedes optimization algorithm for three load levels considering three distribution systems. **Results.** The computational outcomes indicated the competence of the proposed methodology in comparison with the previously published works in power loss minimization, bus voltage enhancement and more economical benefit and proved that the proposed methodology performs well compared to other methods in the literature. References 17, tables 6, figures 6.

**Key words:** reactive power compensation, distribution system, power loss minimization, economic benefit, Archimedes optimization algorithm.

**Вступ.** Потреба в електроенергії різко зросла через стрімке зростання промисловості, соціальних та економічних поліпшень. З попередніх досліджень було встановлено, що майже 13 % усієї електроенергії, що виробляється, витрачається марно у вигляді втрат тепла на рівні розподілу. Загальновізвано, що профіль напруги вузла вздовж розподільчої системи може бути поліпшений при передачі потужності в режимі, що встановився, керованої відповідною компенсацією реактивної потужності. Конденсатори були визнані як пристрої компенсації реактивної потужності в розподільчих системах для досягнення технічних та економічних переваг. **Новизна** цієї роботи полягає у застосуванні алгоритму оптимізації Архімеда для оптимізації реактивної потужності в розподільчих системах з метою отримання покращеного рішення, а також було взято та перевірено реальну португальську мережу з 94 шинами та модифіковану мережу з 12 шинами для трьох різних рівнів навантаження, які абсолютно нові. **Мета** запропонованої роботи полягає в тому, щоб максимізувати економічний ефект за рахунок зниження втрат потужності та вартості купівлі конденсатора за трьох різних режимів навантаження за умови дотримання обмежень рівності та нерівності. **Методи.** Економічний ефект було підтверджено з використанням алгоритму оптимізації Архімеда для трьох рівнів навантаження з урахуванням трьох систем розподілу. **Результати** розрахунків показали компетентність запропонованої методології порівняно з раніше опублікованими роботами в галузі мінімізації втрат потужності, підвищення напруги на шині та більшої економічної вигоди, а також довели, що запропонована методологія добре працює порівняно з іншими методами в літературі. Бібл. 17, табл. 6, рис. 6.

**Ключові слова:** компенсація реактивної потужності, розподільча система, мінімізація втрат потужності, економічний ефект, алгоритм оптимізації Архімеда.

**Problem definition.** Now-a-days modern distribution systems (DSs) are becoming large and difficult causing reactive currents to raise losses result in increased ratings for distribution components. The power loss and the reduction in bus voltages in the DS are disturbing the whole power system performance which can be effectively controlled by proper position and sizing of reactive power compensating device thereby reduction in economical loss.

It is widely recognized that installation of shunt capacitors reduces a portion of power loss of the DS, which in turn increase the overall efficacy of the power delivery. The other benefits such as sub-station power factor improvement, better power flow control; enhancement in bus voltage profile; system stability improvement; reduction in total kVA demand and feeder capacity release can be possible only when the capacitors are located at optimal locations with appropriate capacity [1]. Hence optimal capacitor placement problem is a complex, combinatorial, mixed integer and non-linear programming problem with a non-differential objective function due to the fact that the costs of the capacitor varies in discrete manner. Selection of appropriate nodes and determination of optimal capacitor sizing are the two main steps to obtain the best result in capacitor allocation problem.

**Related past publications.** Polar bear optimization algorithm (PBOA) as optimization method, optimal

allocation and sizing of capacitors has been presented in [2]. Application of Clonal Selection Algorithm (CSA) for optimal capacitor placement problem has been presented in [3]. Loss sensitivity constant based optimization of capacitor allocation problem using analytical method has been proposed in [4]. Water cycle algorithm (WCA) and grey wolf optimizer (GWO) as optimization tools, optimal capacitor placement and sizing has been analyzed in [5]. Six test systems were considered to prove the efficacy of the proposed method. Optimal reactive power optimization in radial DS using Weight Factor based Improved Salp Swarm Algorithm (ISSA-WF) has been reported in [6]. In [3-6] was discussed reactive power optimization considering 3 load levels.  $P_{Loss}$  reduction cost and capacitor investment cost are taken as objective function [2-6]. Reduction in  $P_{Loss}$ ,  $Q_{Loss}$  and voltage stability maximization as objective, optimal allocation and sizing of real and reactive power compensation devices using CSA as optimization tool has been performed in [7].  $P_{Loss}$  reduction, voltage stability maximization, profit maximization as objective, allocation of capacitors using Loss Sensitivity Factor (LSF) has been presented in [8]. CSA has been utilized to find out the necessary sizing. Chu and Beasley Genetic Algorithm (CBGA) as optimization method, reduction in  $P_{Loss}$  and capacitor cost as objective, reactive power compensation

© G. Srinivasan, V. Mahesh Kumar Reddy, P. Venkatesh, E. Parimalasundar

using capacitors has been suggested in [9].  $P_{Loss}$  reduction as objective, optimal allocation of capacitors using Mixed-Integer Second-Order Cone Programming (MI-SOCP) has been done in [10].  $P_{Loss}$  minimization, voltage stability enhancement and capacitor cost reduction as objective, optimal location of capacitors using LSF has been done in [11]. Appropriate sizing of capacitors are done by Modified Teaching Learning Based Optimization (MTLBO) algorithm. Reactive power compensation in radial DS using Particle Swarm Optimization (PSO) and Dice Game Optimizer has been presented in [12]. However it is to be noted that the reactive power compensation using PSO (4 nodes) exceeds the total maximum reactive power demand of the DS taken for evaluation.

**Proposed work.** In this study, Archimedes Optimization Algorithm (AOA) which is powerful in solving wide range of optimization problems has been engaged to solve the objective function due to its merits such as good convergence acceleration, lower plainly of stuck in local optima, accelerated process in getting excellent solutions and has higher feasibility and efficiency in producing global optima. Capacitor sizes in discrete steps are taken for validation. No sensitivity factor (based on loss or voltage) has been utilized to select the most appropriate buses for reactive power compensation. Single objective function comprising capacitor purchase cost with cost based  $P_{Loss}$  reduction has been evaluated under three load levels subject to maintain all the constraints within its permissible limits. The proposed method has been tested and evaluated with the help of the modified 12-bus test system, standard IEEE 33 bus system and 94-bus Portuguese DSs using MATLAB coding.

The **purpose** and **contribution** of this work is to yield a better solution for reactive power compensation. Taking into consideration the above published studies, the contributions of this work include:

1. Suggestion of futuristic AOA to solve the objective function (with decreased / increased load demand);
2. Utilizing a new modified 12-bus test system for reactive power optimization;
3. Considering 3 load levels for capacitor allocation and sizing for 94-bus Portuguese DS.

**Problem of statement.** The objective function is to obtain maximum economic benefits by optimal placement and sizing of shunt capacitors in the radial DS while satisfying both system equality and inequality constraints.

Objective function is:

$$\text{Minimize} = \left( \frac{K_C \times \sum_l^{TCN} Q_C(l)}{K_{P_{loss}} \times (TP_{Loss}^{BO} - TP_{Loss}^{AO})} \right), \quad (1)$$

where  $K_C$  is the cost of capacitor (discrete), \$;  $Q_C(l)$  is the capacity of capacitor at  $l^{\text{th}}$  node, kVAr; TCN is the number of capacitor nodes;  $K_{P_{loss}}$  is the cost of real power loss, \$;  $TP_{Loss}$  is the total real power loss, kW; AO means after optimization; BO means before optimization.

Subject to equality constraints:

$$Q_{MS} - \sum Q_D + \sum_l^{TCN} Q_C(l) - TQ_{Loss}^{AO} = 0, \quad (2)$$

where  $Q_{MS}$  is the reactive power from main source, kVAr;  $Q_D$  is the reactive power demand, kVAr;  $TQ_{Loss}$  is the total reactive power loss, kVAr.

Inequality constraints are:

$$Q_C(l)^{\min} \leq Q_C(l) \leq Q_C(l)^{\max}; \quad (3)$$

$$V_i^{\min} \leq V_i \leq V_i^{\max}; \quad (4)$$

$$\sum_l^{TCN} Q_C(l) \leq \left( \sum Q_D + TQ_{Loss}^{AO} \right), \quad (5)$$

where  $V_i$  is the voltage at  $i^{\text{th}}$  node (p.u);

$$TP_{Loss} = \sum_{m=0}^{TNB} P_{Loss(m, m+1)};$$

and

$$P_{Loss(m, m+1)} = \frac{P_m^2 + Q_m^2}{|V_m^2|} \times R_{(m, m+1)},$$

where  $R_m$  is the resistance of the branch  $m$ ;  $P_m$  is the real power of the branch  $m$ , kW;  $Q_m$  is the reactive power of the branch  $m$ , kVAr;  $TNB$  is the total number of branches.

Practical capacitors are available in standard capacities which are the multiple integer values of the smallest size denoted as  $Q_C^0$ . The per kVAr cost of the capacitor changes across its sizes which are available commercially. The available capacitor sizes are typically taken as

$$Q_C^{\max} = A \times Q_C^0. \quad (6)$$

Thus for each capacitor installation node, the sizes are  $A$  times that of capacitor size (i.e)  $\{Q_C^0, 2Q_C^0, 3Q_C^0, \dots, A Q_C^0\}$ , where  $A$  is an integer multiplier.

In this paper, recursive function and a linked-list data structure designed power flow [13] has been used which have advantages of solving power balance equation for radial nature of DS, low  $X/R$  system and also the ability to update easily to accommodate the reconfiguration technique and embedded generation.

**Solution methodology.** In [14] proposes a population based metaheuristic optimization algorithm called AOA inspired by the law of physics called as Archimedes' principle. In order to find global optimal solutions, AOA keeps a population of solutions and examines a huge area. Hence this work considers AOA as optimization tool to solve capacitor allocation problem anticipates that AOA maintains a good balance between exploration and exploitation. Similar to other population based algorithms, AOA begins the search procedure with initial Solution Vectors (SVs) with random volumes, densities, and accelerations. Also each object is set with its arbitrary location in fluid. During the evaluation process, AOA updates the density and volume of every object in every iteration and based on the condition of its collision with any other adjacent object the acceleration is being updated. The updated new solution vectors (density, volume, acceleration) replace the existing positions. The mathematical model of AOA is discussed below.

**Process 1.** Initialize the SVs randomly using (7):

$$ob_d = BL_d^{\min} + \left[ rand \times (BL_d^{\max} - BL_d^{\min}) \right], \quad d = 1, 2, 3, \dots, (7)$$

where  $ob_d$  is the  $d^{\text{th}}$  object in a SV of  $N$  objects;  $BL^{\min}$  and  $BL^{\max}$  are the minimum and maximum values of the search agent respectively;  $rand$  is the  $M$  dimensional vector randomly generates number between 0 and 1.

Equation (8) indicates the acceleration initialization of  $d^{\text{th}}$  object. Estimate the object with the best fitness value:

$$ac_d = BL_d^{\min} + \left[ rand \times (BL_d^{\max} - BL_d^{\max}) \right] \quad (8)$$

**Process 2.** The volume and density for each object  $d$  for the iteration  $IT+1$  is updated using (9). Assign  $x^{bt}$ ,  $de^{bt}$ ,  $vo^{bt}$  and  $ac^{bt}$ :

$$\begin{cases} de_d^{IT+1} = de_d^{IT} + \left[ rand \times (de_d^{bt} - de_d^{IT}) \right]; \\ vo_d^{IT+1} = vo_d^{IT} + \left[ rand \times (vo_d^{bt} - vo_d^{IT}) \right]; \end{cases} \quad (9)$$

where  $vo^{bt}$  and  $de^{bt}$  are the volume and density connected with the best object established so far;  $IT$  is the current iteration.

**Process 3.** During the commencement of process in AOA, collision between the objects occurs and drives the objects towards the equilibrium state after a specified period done by a transfer operator (TO), which changes search from exploration to exploitation as given in (10). The value of TO increases gradually towards 1:

$$TO = \exp\left[\frac{IT - IT_{\max}}{IT_{\max}}\right], \quad (10)$$

where TO is transfer operator.

In the same way, density decreasing factor  $g$  also helps AOA in achieving global to local search with respect to time using (11):

$$g^{IT+1} = \exp\left[\frac{IT - IT_{\max}}{IT_{\max}}\right] - \left[\frac{IT}{IT_{\max}}\right], \quad (11)$$

where  $g^{IT+1}$  decreases with respect to time which gives the capability to converge in previously recognized promising value. To achieve a good balance between the exploration and exploitation process, appropriate control of this variable must be confirmed.

**Process 4.** As already discussed, collision between the object occurs, if the value of TO is less than or equal to 0.5. Select a Random Material (MR) and update object's acceleration for iteration  $IT + 1$  using (12):

$$ac_d^{IT+1} = \frac{de_{MR} + vo_{MR} \times ac_{MR}}{de_d^{IT+1} \times vo_d^{IT+1}}, \quad (12)$$

where  $de_d$ ,  $vo_d$  and  $ac_d$  are the density, volume, and acceleration of object  $d$ ;  $ac_{MR}$ ,  $de_{MR}$  and  $vo_{MR}$  are the acceleration, density, and volume of MR respectively. It is significant to state that TO is less than or equal 0.5 conforms the exploration during one third of iterations. However, if TO value is greater than 0.5 no collision between objects occurs and hence update the object's acceleration for iteration  $IT+1$  using (13):

$$ac_d^{IT+1} = \frac{de^{bt} + vo^{bt} \times ac^{bt}}{de_d^{IT+1} \times vo_d^{IT+1}}, \quad (13)$$

where  $ac^{bt}$  is the acceleration of the best object.

**Process 5.** To calculate the percentage of change, normalize the acceleration using (14):

$$ac_{d-nor}^{IT+1} = b \times \frac{ac_d^{IT+1} - ac_{\min}}{ac_{\max} - ac_{\min}} + k, \quad (14)$$

where  $b$  and  $k$  are the range of normalization and set to 0.9 and 0.1, respectively. The left-hand side of (14) regulates the % step that each agent will change. The value of acceleration is high when the object  $d$  is far away from the global optimum, which indicates that the object will be in the exploration phase; or else, in exploitation phase. Under

normal case, the acceleration factor starts with larger value and moves towards the lower value with time.

**Process 6.** If the object  $d$  is in exploration phase, the updation has been done using (15) and if the object  $d$  is in exploitation phase then updation has been done using (16)

$$x_d^{IT+1} = x_d^{IT} + P_1 \times rand \times ac_{d-nor}^{IT+1} \times g \times (x_{rand} - x_d^{IT+1}); \quad (15)$$

$$\begin{aligned} x_d^{IT+1} &= x_{bt}^{IT} + F \times P_2 \times rand \times ac_{d-nor}^{IT+1} \times \\ &\times g \times (T \times x_{rand} - x_d^{IT+1}), \end{aligned} \quad (16)$$

where  $T$  increases with respect to time and directly proportional to TO and is defined as  $T = P_3 \times TO$ ;  $F$  is the flag to change the direction of motion. The value of  $F$  is +1 for  $P$  is less than or equal to 0.5, otherwise -1.

The value of  $P$  is calculated as:

$$P = 2 \times rand - P_4. \quad (17)$$

Below is the pseudo code for AOA [14].

---

```

Set the population size (N), total number of iterations (Itmax)
Fix the value for P1, P2, P3 and P4 as 2, 6, 2 and 0.5 as
mentioned in [13].
Initialize the population, random positions, densities,
acceleration and volumes using (7) and (8)
Evaluate the initial population and select the one with the best
fitness function value
Set the iteration count IT=1
while (IT < ITmax) do
for each search agent 'd' do
Update density and volume of each object using (9)
Update TO and 'g' using eqn. (10) and (11) respectively
if TO ≤ 0.5 then (Exploration phase)
update the acceleration using (12) and normalize acceleration
using (14)
update the position using (15)
else (Exploitation phase)
update acceleration using (13) and normalize acceleration using
(14)
update direction flag 'F' using (17)
update the position using (16)
end if
end for
evaluate each object and select the one with the best fitness
function value
set IT = IT+1
end while
return object with the best fitness value
end of procedure

```

---

**Test parameters, results and discussions.** To prove the usefulness of the proposed optimization algorithm (AOA), in minimizing the  $P_{Loss}$  with enhancement in bus voltage and maximizing the economic benefit, 3 radial power DSs such as modified 12-bus, IEEE 33-bus and Portuguese 94-bus DS have been considered in this work. The single-line diagrams of all the test systems before optimization (BO) are shown in Fig. 1–3.

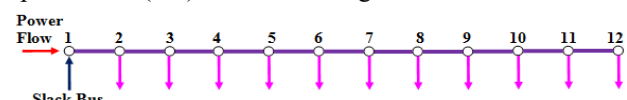


Fig. 1. Indian 11 kV, 12-bus system (BO)

For all the test cases, bus number 1 has been considered as substation bus/slack bus whose bus voltage is fixed as 1 p.u. The remaining buses are considered as load buses and capacitor will be installed in any of the potential load nodes that require compensation.

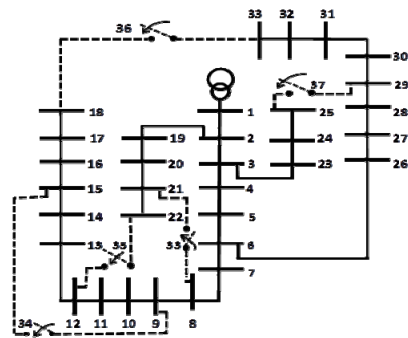


Fig. 2. IEEE 33-bus test system (BO)

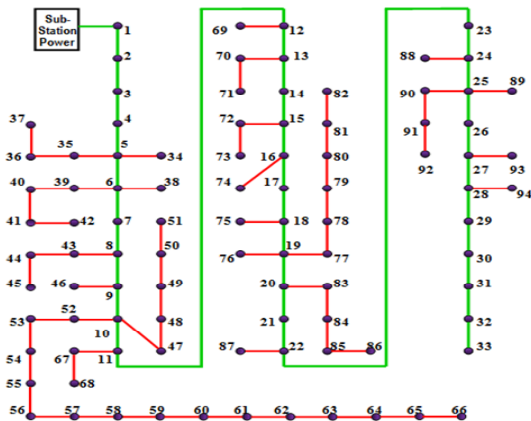


Fig. 3. Real 94-bus Portuguese test system (BO)

In this work, maximum number of nodes for capacitor installation is limited to 3 for all the test systems. The algorithm parameters details such as agent size and number of iterations are selected as 800 and 100 respectively. The variables used to calculate the net savings per annum are power loss cost \$168/kW/year and the cost data pertaining to commercially available capacitor sizes (\$/kVAr) used in this work has been taken from [9]. Table 1 reveals the parameter results pertaining to BO.

**Modified 12-bus test system.** First radial test system is a modified 12-bus single feeder Indian DS which has 12 nodes and 11 branches. Further details of this DS can be found in [15, 16]. However, similar to [17], the loads on each bus are multiplied by five (both active and reactive power). The base kV and base MVA are 11 kV and 100 MVA respectively.

Table 2 reveals the results obtained by the proposed method under 3 load levels After Optimization (AO). Verifying Table 1 and 2, it is obvious that the power loss has reduced between 47.5 % and 61.5 % by injecting 86.4087 %, 93.5 % and 85.4276 % of the total ( $Q_D + Q_{Loss(AO)}$ ) respectively. The minimum bus voltage has enhanced by 5.1522 %, 11.832 % and 32.273 % respectively at bus number 12. Considering the cost factor, the change in power loss cost ( $\Delta P_{Loss}$ ) cost is \$12561.2424, \$37174.77 and \$112947.93 respectively. Thus the total economical benefit is found to be between 47 % and 61 % compared to BO.

Table 1

Parameter details of test systems under 3 different load levels – BO				
Load level	Load demand, kVA	$P_{Loss} + j Q_{Loss}$ , kVA	Bus voltage, p.u.	Cost of $P_{Loss}$ , \$
<b>Modified 12-bus DS</b>				
50 %	1087.5 + j 1012.5	153.0848 + j 59.2462	0.8443 (12)	25718.2464
75 %	1631.2 + j 1518.8	420.1375 + j 161.9583	0.7387 (12)	70583.1
100 %	2175 + j 2025	1090.7 + j 416.8654	0.5689 (12)	183237.6
<b>IEEE 33-bus test DS</b>				
50 %	1857.5 + j 1150	48.7903 + j 33.0487	0.9540 (18)	8196.7704
100 %	3715 + j 2300	211 + j 143.135	0.9038 (18)	35448
160 %	5944 + j 3680	603.4843 + j 410.2165	0.8360 (18)	101385.362
<b>Real 94-bus Portuguese DS</b>				
50 %	2398.5 + j 1161.95	79.6036 + j 110.9393	0.9299 (33)	13373.405
100 %	4797 + j 2323.9	361.67636 + j 503.7688	0.85413 (33)	60761.63
160 %	7675.2 + j 3718.24	1155.5 + j 1595.2	0.7242 (33)	194124

Table 2

Performance of AOA – modified 12 bus system – all the 3 load levels			
Parameter details	50 % load levels	75 % load levels	100 % load levels
$P_{Loss}$ (AO), kW	78.3155	198.8591	418.3909
$P_{Loss}$ reduction, %	<b>48.842</b>	<b>52.6681</b>	<b>61.64</b>
Capacitor nodes, kVAr	300 (4)	450 (4)	900 (5)
	300 (7)	600 (7)	600 (8)
	300 (10)	450 (10)	450 (10)
$V_{min}$ , p.u	0.8878	0.8261	0.7525
$P_{Loss}$ cost (AO), \$/year	13157.004	33408.3288	70289.6712
Cost of capacitor, \$(/kVAr-year)	315	359.7	410.55
Net savings, \$	12246.242	36815.0712	112537.3788
Economic benefit, %	<b>47.61694</b>	<b>52.1585</b>	<b>61.4161</b>

Figure 4 shows the graph of the bus voltages before and after optimization. From Fig. 4, it is visible that drastic fall in voltages are evidenced from bus number 1 to 5 and 7 to 9 compared to other buses both BO and AO.

Two ways of comparison (IEEE 33-bus) have been given from Tables 3 to 5 – one based on  $P_{Loss}$  reduction and the other based on economic benefits.

**IEEE 33-bus test system.** The next DS is a renowned system which has 33 nodes, 32 main branches and 5 looping branches as shown in the Fig. 2. The details pertaining to IEEE 33-bus can be taken from [10]. The base kV and base MVA of this test system are 12.66 kV and 100 MVA respectively. For this DS the comparison have been shown in 2 ways. First one based on  $P_{Loss}$  reduction alone and second one based on  $P_{Loss}$  as well as economic benefit.

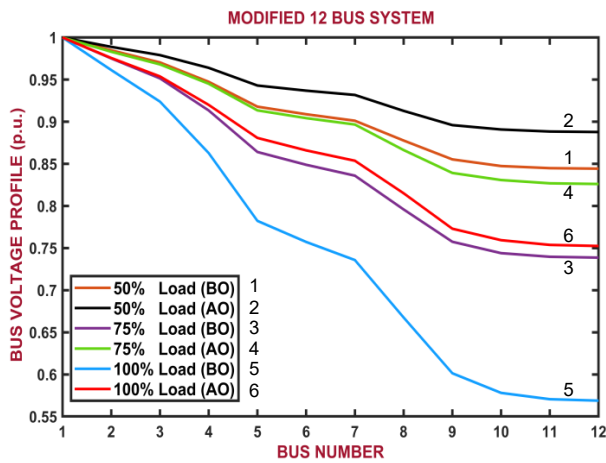


Fig. 4. Bus voltage – modified 12 bus – all load levels

From Tables 3 to 5, it is obvious that the  $P_{Loss}$  has reduced by around 32.1 %, 34.4 % and 36.945 % respectively after optimal reactive power support of 77.543 %, 83.03 %

and 86.174 % of the total ( $Q_D + Q_{Loss(AO)}$ ), at 3 optimal nodes considering 3 load levels. The bus voltage has enhanced by 1.4465 %, 3 % and 6.746 % respectively. The change in the  $P_{Loss}$  cost is found to be \$2630.93, \$12194.112 and \$37456.858 and the net annual financial benefits are between 28 % and 36.5 %.

Tables 3–5 discuss the comparison between AOA and other methods in the literature for 50 %, 100 % and 160 % load levels individually [2-10]. Considering 50 % load level and from Table 3, AOA achieves better performance compared to [2-5] in terms of  $P_{Loss}$  reduction and economic benefit. Taken into consideration the cost factor, AOA achieves more than 1 % compared to [5]. However, AOA equals ISSA-WF. Considering 100 % load level and from Table 4, AOA achieves better performance in terms of  $P_{Loss}$  reduction and net economic benefit compared to [2, 6-10]. From Table 4, it is witnessed that the difference in  $P_{Loss}$  reduction and economic benefit are minuscule compared to [6, 9, 10]. Finally, under 160 % load level and from Table 5, the performance of AOA is better than [3-6].

Table 3

Performance of AOA – IEEE 33 bus – 50 % load –  $P_{Loss}$  and economic based comparison

Parameter details	PBOA [2]	CSA [3]	Analytical [4]	GWO [5]	WCA [5]	ISSA-WF [6]	AOA
$P_{Loss}$ (AO) /	48.7868 /	32.0895 /	33.04 /	32.42 /	32.43 /	33.13 /	33.13 /
$P_{Loss}$ (BO), kW	35.03134	47.0709	47	47.07	47.07	48.7903	48.7903
$P_{Loss}$ reduction, %	28.195	31.8273	29.8	31.12	31.1	32.097	<b>32.097</b>
Capacitor size, kVAr/nodes	125 (13)	150 (12)	300 (14)	300 (5)	300 (5)	300 (6)	300 (6)
	72 (28)	100(24)	250 (30)	150 (12)	150 (12)	150 (14)	150 (14)
	162 (29)	600 (30)	170 (32)	300 (29)	300 (29)	450 (30)	450 (30)
$V_{min}$ , p.u	0.966	0.9678 (18)	0.9734 (18)	0.9694 (18)	0.9687(18)	0.9678 (18)	0.9678 (18)
$P_{Loss}$ cost (AO), \$	–	–	–	5446.56	5448.24	5565.84	5565.84
Cost of capacitor, \$(/kVAr-year)	–	–	–	285	285	293.85	293.85
Net savings, \$	–	–	–	2176.2	2174.52	2337.08	2337.08
Economic benefit, %	–	–	–	27.52	27.49856	28.5122	<b>28.5122</b>

Table 4

Performance of AOA – IEEE 33 bus – 100 % load –  $P_{Loss}$  and economic based comparison

Parameter details	PBOA [2]	CSA [7]	CSA [8]	CBGA [9]	ISSA-WF [6]	MI-SOCP [10]	AOA
$P_{Loss}$ (AO) /	135.1018 /	138.54 /	138.65 /	138.416 /	138.511 /	138.416 /	138.416 /
$P_{Loss}$ (BO), kW	202.6774	210.99	210.99	211	211	210.987	211
$P_{Loss}$ reduction, %	33.33	34.338	34.286	34.4	34.355	34.395	<b>34.4</b>
Capacitor size, kVAr/nodes	318 (6)	495(11)	450 (11)	450 (12)	450 (12)	450 (12)	450 (12)
	294 (13)	500(24)	400 (24)	450 (24)	600 (24)	450 (24)	450 (24)
	709 (29)	946(30)	950 (30)	1050 (30)	1050 (30)	1050 (30)	1050 (30)
$V_{min}$ , p.u	0.9365 (18)	0.9321 (18)	0.9321 (18)	0.93 (18)	0.93093 (18)	–	0.9309 (18)
$P_{Loss}$ cost (AO), \$	–	–	–	23253.888	23269.9	23253.888	23253.888
Cost of capacitor, \$(/kVAr-year)	–	–	–	467.10	485.25	467.10	467.10
Net savings, \$	–	–	–	11727.012	11692.9	11692.9	11727.012
Economic benefit, %	–	–	–	33.0823	32.9861	32.98607	<b>33.0823</b>

Table 5

Performance of AOA – IEEE 33 bus – 160 % load –  $P_{Loss}$  and economic based comparison

Parameter details	CSA [3]	Analytical [4]	GWO [5]	WCA [5]	ISSA-WF [6]	AOA
$P_{Loss}$ (AO) /	393.2709 /	384 /	364.82 /	368.56 /	381.1067 /	380.5268 /
$P_{Loss}$ (BO), kW	575.3682	575.36	575.36	575.36	603.4843	603.4843
$P_{Loss}$ reduction, %	31.64883	33.21	36.5927	35.943	36.849	<b>36.945</b>
Capacitor size, kVAr/nodes	550 (12)	840 (14)	1200 (5)	1050 (5)	600 (13)	600 (12)
	100 (24)	650 (30)	450 (13)	600 (12)	1050 (24)	1050 (24)
	1050 (30)	520 (32)	1200 (29)	1050 (29)	1650 (30)	1650 (30)
$V_{min}$ , p.u	0.8528 (18)	0.9	0.8982 (18)	0.8982 (18)	0.8924 (18)	0.8921 (18)
$P_{Loss}$ cost (AO), \$	–	–	61289.76	61918.08	64025.926	63928.5024
Cost of capacitor, \$(/kVAr-year)	–	–	521.85	610.8	689.85	689.85
Net savings, \$	–	–	34848.87	34131.6	36669.5844	36767
Economic benefit, %	–	–	36.0529	35.3108	36.16852	<b>36.2646</b>

Figure 5 reveals the bus voltage profiles of IEEE 33 bus test system under three different load levels. From Fig. 5 it is evident that bus voltage has improved well in all the load buses.

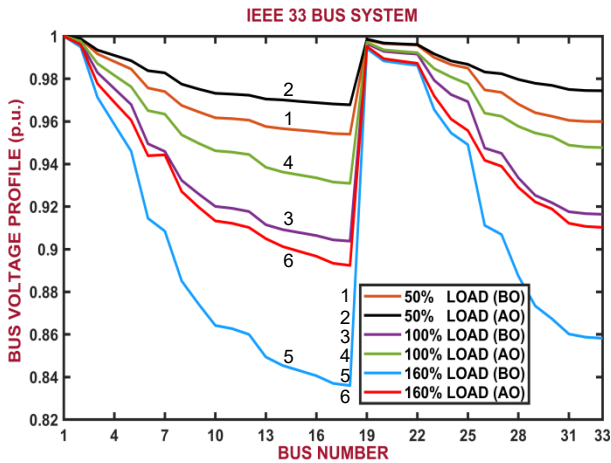


Fig. 5. Bus voltage – IEEE 33-bus – all load levels

**Portuguese 94-bus test system.** Final test system taken for evaluation is a real 94-bus Portuguese DS which has 94 nodes, 93 branches and 22 laterals. The base kV and base MVA of this test system are 15 kV and 100 MVA respectively. The line and load data for this real test system can be viewed in [11].

From Table 6 it is observable that the  $P_{Loss}$  has reduced between 21 % to 34 % after reactive power injection of above 95 % of the total ( $Q_D + Q_{Loss(AO)}$ ), at 3 optimal nodes considering 3 load levels. The difference in bus voltage enhancement is found to be between 3 % and 16.75 %. The change in power loss cost ( $\Delta P_{Loss}$ ) after reactive power compensation is \$2854.488, \$15871.296 and \$65333.352 respectively considering 3 load levels. Thus the net annual economic benefit is found to be between 19 % and 33.3 %. By comparing the  $P_{Loss(AC)}$  with [11], AOA achieves better performance.

Figure 6 shows the graph of the bus voltages before and after compensation. From Fig. 6, it is observable that enhancement of bus voltage is better in all the buses.

Table 6

Performance of AOA – Portugal 94-bus – all load levels –  $P_{Loss}$  based comparison

Parameter details	GA [11]	PSO [11]	TLBO [11]	MTLBO [11]	AOA		
					50% load levels	100% load levels	160% load levels
$P_{Loss(AO)} / P_{Loss(BO)}$ , kW	279.1 / 362.858	301.5 / 362.858	278.98 / 362.858	269.91 / 362.858	62.613 / 79.6036	268.386 / 362.8578	766.611 / 1155.5
$P_{Loss}$ reduction, %	23	16.91	23.1	25.63	<b>21.3444</b>	<b>26.035</b>	<b>33.6555</b>
Capacitor size, kVAr/nodes	450 (65) 450 (73) 600 (84) 250 (87)	650 (58) 450 (73) 450 (84) 300 (90)	800 (59) 450 (72) 500 (83) 300 (90)	850 (58) 400 (72) 500 (84) 250 (89)	450 (19) 150 (25) 450 (57)	750 (10) 750 (20) 900 (58)	900 (15) 1200 (20) 1500 (57)
$V_{min}$ , p.u.	0.9094	0.9124	0.9039	0.9065	0.9584	0.9065	0.8454
$P_{Loss}$ cost (AO), \$	46888.8	50652	46868.64	45344.88	10518.984	45088.848	128790.648
Cost of capacitor, \$(kVAr-year)	–	–	–	–	302.7	578.7	670.2
Net savings, \$	–	–	–	–	2551.788	15292.596	64663.152
Economic benefit, %	–	–	–	–	<b>19.08106</b>	<b>25.16818</b>	<b>33.31023</b>

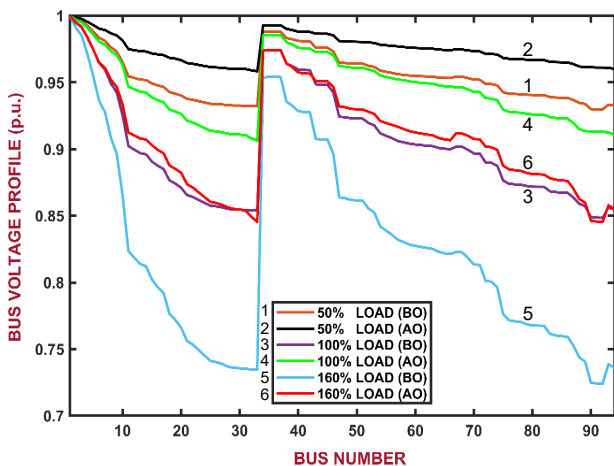


Fig. 6. Bus voltage – Portugal 94-bus – all load levels

**Conclusions.** In this paper, a new powerful swarm intelligence algorithm has been utilized to solve the cost based objective function which is the combination of power loss  $P_{Loss}$  cost with capacitor investment cost so as to get more economic benefits under 3 different load levels. The merits of adopting Archimedes optimization algorithm for this problem have already been discussed. The proposed method has been successfully applied to a

new modified 12-bus, standard IEEE 33-bus test system and a real 94-bus Portuguese test systems. Following are the key points which are worth noted:

1. No sensitivity factor based optimal node selection for reactive power compensation has been adopted in this paper.
2. Considering modified 12-bus system, an overall  $P_{Loss}$  reduction (under 3 load levels) of around 49 % to 62 % with economical benefit of 47.6 %, 52 % and 61.4 % have been observed. Regarding standard IEEE 33 bus system, the overall  $P_{Loss}$  reduction is found to be between 32 % and 37 % with economical benefit of 28.5 % to 36.246 % have been witnessed. Finally, considering practical 94-bus test system, the  $P_{Loss}$  reduction under 3 load levels are seemed to be between 21 % to 34 % with economical benefit of 19 % to 33.3 % are evidenced.

3. Considering the standard IEEE 33-bus system and 94-bus real Portuguese system, the performance has been analyzed and compared to the recent methods presented in the literature. It is obvious that the difference in  $P_{Loss}$  reduction and economic benefit achieved by the proposed method are found to be better and significant. Hence Archimedes optimization algorithm has been recommended to be another strong and efficient method to solve capacitor allocation problem in terms of  $P_{Loss}$  reduction, bus voltage enrichment and economic benefit.

**Conflict of interest.** The authors declare that they have no conflicts of interest.

#### REFERENCES

1. Soma G.G. Optimal Sizing and Placement of Capacitor Banks in Distribution Networks Using a Genetic Algorithm. *Electricity*, 2021, vol. 2, no. 2, pp. 187-204. doi: <https://doi.org/10.3390/electricity2020012>.
2. Saddique M.W., Haroon S.S., Amin S., Bhatti A.R., Sajjad I.A., Liaqat R. Optimal Placement and Sizing of Shunt Capacitors in Radial Distribution System Using Polar Bear Optimization Algorithm. *Arabian Journal for Science and Engineering*, 2021, vol. 46, no. 2, pp. 873-899. doi: <https://doi.org/10.1007/s13369-020-04747-5>.
3. Tamilselvan V., Muthulakshmi K., Jayabarathi T. Optimal capacitor placement and sizing in a radial distribution system using clonal selection algorithm. *ARPN Journal of Engineering and Applied Sciences*, 2015, vol. 10, no. 8, pp. 3304-3312.
4. Bansal A.K., Sharma M.P. A Novel Analytical Technique for Optimal Allocation of Capacitors in Radial Distribution Systems. *Journal of Engineering and Technological Sciences*, 2017, vol. 49, no. 2, pp. 236-246. doi: <https://doi.org/10.5614/j.eng.technol.sci.2017.49.2.6>.
5. Kola Sampangi S., Thangavelu J. Optimal capacitor allocation in distribution networks for minimization of power loss and overall cost using water cycle algorithm and grey wolf optimizer. *International Transactions on Electrical Energy Systems*, 2020, vol. 30, no. 5, art. no. e12320. doi: <https://doi.org/10.1002/2050-7038.12320>.
6. Srinivasan G., Lokasree B.S. Siting and Sizing of Capacitors in Distribution Systems for Annual Cost Savings Using ISSA-WF. *2021 Innovations in Power and Advanced Computing Technologies (i-PACT)*, 2021, pp. 1-8. doi: <https://doi.org/10.1109/i-PACT52855.2021.9696659>.
7. Salimon S.A., Adepoju G.A., Adebayo I.G., Adewuyi O.B., Amuda S.O. Simultaneous Placement and Sizing of Distributed Generation Units and Shunt Capacitors on Radial Distribution Systems Using Cuckoo Search Algorithm. *Current Journal of Applied Science and Technology*, 2021, vol. 40, no. 12, pp. 43-58. doi: <https://doi.org/10.9734/cjast/2021/v40i1231380>.
8. Salimon S.A., Baruwa A.A., Amuda S.O., Adeleke H.A. Optimal Placement and Sizing of Capacitors in Radial Distribution Systems: A Two-Stage Method. *Journal of Engineering Research and Reports*, 2020, vol. 19, no. 2, pp. 31-43. doi: <https://doi.org/10.9734/jerr/2020/v19i217229>.
9. Riaño F.E., Cruz J.F., Montoya O.D., Chamorro H.R., Alvarado-Barrios L. Reduction of Losses and Operating Costs in Distribution Networks Using a Genetic Algorithm and Mathematical Optimization. *Electronics*, 2021, vol. 10, no. 4, art. no. 419. doi: <https://doi.org/10.3390/electronics10040419>.
10. Montoya O.D., Gil-González W., Garcés A. On the Conic Convex Approximation to Locate and Size Fixed-Step Capacitor Banks in Distribution Networks. *Computation*, 2022, vol. 10, no. 2, art. no. 32. doi: <https://doi.org/10.3390/computation10020032>.
11. Rahiminejad A., Foroughi Nematollahi A., Vahidi B., Shahrooyan S. Optimal Placement of Capacitor Banks Using a New Modified Version of Teaching-Learning- Based Optimization Algorithm. *AUT Journal of Modeling and Simulation*, 2018, vol. 50, no. 2, pp. 171-180. doi: <https://doi.org/10.22060/miscj.2018.14594.5111>.
12. Belbachir N., Zellagui M., Setoul S., El-Bayeh C.Z., Bekkouche B. Simultaneous optimal integration of photovoltaic distributed generation and battery energy storage system in active distribution network using chaotic grey wolf optimization. *Electrical Engineering & Electromechanics*, 2021, no. 3, pp. 52-61. doi: <https://doi.org/10.20998/2074-272X.2021.3.09>.
13. Venkatesh B., Ranjan R. Data structure for radial distribution system load flow analysis. *IEE Proceedings - Generation, Transmission and Distribution*, 2003, vol. 150, no. 1, pp. 101-106. doi: <https://doi.org/10.1049/ip-gtd:20030013>.
14. Hashim F.A., Hussain K., Houssein E.H., Mabrouk M.S., Al-Atabany W. Archimedes optimization algorithm: a new metaheuristic algorithm for solving optimization problems. *Applied Intelligence*, 2021, vol. 51, no. 3, pp. 1531-1551. doi: <https://doi.org/10.1007/s10489-020-01893-z>.
15. Balakishan P., Chidambaram I.A., Manikandan M. Improvement of power quality in grid-connected hybrid system with power monitoring and control based on internet of things approach. *Electrical Engineering & Electromechanics*, 2022, no. 4, pp. 44-50. doi: <https://doi.org/10.20998/2074-272X.2022.4.06>.
16. Das D. Novel method for solving radial distribution networks. *IEE Proceedings - Generation, Transmission and Distribution*, 1994, vol. 141, no. 4, pp. 291-298. doi: <https://doi.org/10.1049/ip-gtd:19949966>.
17. Aman M.M., Jasmon G.B., Mokhlis H., Bakar A.H.A. Optimal placement and sizing of a DG based on a new power stability index and line losses. *International Journal of Electrical Power & Energy Systems*, 2012, vol. 43, no. 1, pp. 1296-1304. doi: <https://doi.org/10.1016/j.ijepes.2012.05.053>.

Received 22.07.2022  
Accepted 06.11.2022  
Published 06.05.2023

G. Srinivasan<sup>1</sup>, Professor,  
V. Mahesh Kumar Reddy<sup>2</sup>, Assistant Professor,  
P. Venkatesh<sup>3</sup>, Assistant Professor,  
E. Parimalasundar<sup>3</sup>, Associate Professor,  
<sup>1</sup>Department of Electrical and Electronics Engineering,  
Thamirabharani Engineering College, Thachanallur,  
Tirunelveli – 627358, Tirunelveli, Tamilnadu, India,  
e-mail: prof.gsrinivasan@gmail.com (Corresponding Author)  
<sup>2</sup>Department of Electrical and Electronics Engineering,  
Kandula Srinivasa Reddy Memorial College of Engineering,  
Yerramasupalli, Kadappa – 516003, Andhra Pradesh, India,  
e-mail: vmahesh@ksrmce.ac.in  
<sup>3</sup>Department of Electrical & Electronics Engineering,  
Sree Vidyanikethan Engineering College,  
Tirupati, AP – 517102, India,  
e-mail: venkatesh.p@vidyanikethan.edu;  
parimalasundar.e@vidyanikethan.edu

#### How to cite this article:

Srinivasan G., Mahesh Kumar Reddy V., Venkatesh P., Parimalasundar E. Reactive power optimization in distribution systems considering load levels for economic benefit maximization. *Electrical Engineering & Electromechanics*, 2023, no. 3, pp. 83-89. doi: <https://doi.org/10.20998/2074-272X.2023.3.12>

**Матеріали приймаються за адресою:**

**Кафедра "Електричні апарати", НТУ "ХПІ", вул. Кирпичева, 2, м. Харків, 61002, Україна**

**Електронні варіанти матеріалів по e-mail: [a.m.grechko@gmail.com](mailto:a.m.grechko@gmail.com)**

**Довідки за телефонами: +38 067 359 46 96 Гречко Олександр Михайлович**

**Передплатний індекс: 01216**